Experimental and Numerical Investigation of Fiber Reinforced Laminated Composites Subject to Low-Velocity Impact

by

Solver I. Thorsson

A dissertation submitted in partial fulfillment
of the requirements for the degree of
Doctor of Philosophy
(Aerospace Engineering)
in The University of Michigan
2017

Doctoral Committee:

Professor Anthony M. Waas, Co-Chair
Associate Professor Veera Sundararaghavan, Co-Chair
Professor Carlos E.S. Cesnik
Mostafa Rassaian, Boeing Research & Technology
Professor Nickolas Vlahopoulos

Solver I. Thorsson

solitor@umich.edu

ORCID iD: 0000-0002-3743-2961

To my family

ACKNOWLEDGEMENTS

I would like to extend my sincere thanks to all the people that have supported and encouraged me during my studies at the University of Michigan. Thank you to my loving wife Ashley for her devoted support and love throughout my PhD journey. Thank you to my entire family for their continuing love and support. Special thanks go out to my parents, Hanna and Thor, and my great uncle Sölver.

I am deeply grateful to my advisor, Professor Anthony Waas, and his excellent guidance and support towards my research. His passion and knowledge in the field of composite materials is absolutely inspiring. I will truly miss our many technical discussions.

I would like to thank the members of the Composite Structures Lab for the day to day technical dialogue which I greatly benefitted from. Special thanks go out to my friends and comrades in the lab, Brian, Jaspar, Nhung, Alastair, Sunil and Stewart, who I shared many good moments with conducting experiments and other lab activities.

I will forever have fond memories of my time spent in Ann Arbor and the countless people I was fortunate enough to cross paths with. My heartfelt appreciation to my close friends, Greg, Ryan, Francisco, Ari, Kyle, Riddhiman, Moritz, Sebastian, Anmeen, Justin, Jeanette, Thor and Gretel, and many more. I would like to thank the members of the University of Michigan and University of Washington lunch groups. During our uplifting lunch breaks many great illuminating discussions over matters both highly technical and some not so technical were had.

I am grateful to Prof. Anthony Waas, Prof. Veera Sundararaghavan, Prof. Carlos Cesnik, Prof. Nickolas Vlahopoulos, and Dr. Mostafa Rassaian for serving as my committee members. Their feedback and suggestions on improvements to the dissertation thesis are greatly appreciated.

I am thankful for the support and assistance provided by the faculty and staff of the University of Michigan Aerospace Department and the University of Washington Aeronautics and Astronautics Department. Among them are the graduate administrators, Denise Phelps and Patrick Gibbs. Our technical staff for their machining and other assistance, Thomas Griffin, Chris Chartier, Terry Larrow, Marty Stenzel, Aaron Borgman, David McLean, Dzung Tran and Jack Ross. And many more who helped through the process.

Lastly, I would like to express my gratitude to The Boeing Company for their financial support. Furthermore, I would like to thank my Boeing technical contacts, Dr. Mostafa Rassaian, Salvatore Liguore, Dr. Joseph Schaefer, Dr. Brian Justusson, and Dr. Hamid Razi for their invaluable insight and positive feedback on my work.

TABLE OF CONTENTS

LIST OF FIGURES

Figure

LIST OF TABLES

Table

LIST OF APPENDICES

Appendix

ABSTRACT

Foreign object impact on composite materials continues to be an active field due to its importance in the design of load bearing composite aerostructures. The problem has been studied by many through the decades. Extensive experimental studies have been performed to characterize the impact damage and failure mechanisms. Leaders in aerospace industry are pushing for reliable, robust and efficient computational methods for predicting impact response of composite structures. Experimental and numerical investigations on the impact response of fiber reinforced polymer matrix composite (FRPC) laminates are presented. A detailed face-on and edge-on impact experimental study is presented. A novel method for conducting coupon-level edge-on impact experiments is introduced. The research is focused on impact energy levels that are in the vicinity of the barely visible impact damage (BVID) limit of the material system. A detailed post-impact damage study is presented where non-destructive inspection (NDI) methods such as ultrasound scanning and computed tomography (CT) are used. Detailed fractography studies are presented for further investigation of the through-the-thickness damage due to the impact event. Following the impact study, specimens are subjected to compression after impact (CAI) to establish the effect of BVID on the compressive strength after impact (CSAI). A modified combined loading compression (CLC) test method is proposed for compression testing following an edge-on impact. Experimental work on the rate sensitivity of the mode I and mode II inter-laminar fracture toughness is also investigated. An improved wedge-insert fracture (WIF) method for conducting mode I inter-laminar fracture at elevated

loading rates is introduced. Based on the experimental results, a computational modeling approach for capturing face-on impact and CAI is developed. The model is then extended to edge-on impact and CAI. Enhanced Schapery Theory (EST) is utilized for modeling the full field damage and failure present in a unidirectional (UD) lamina within a laminate. Schapery Theory (ST) is a thermodynamically based work potential material model which captures the pre-peak softening due to matrix microcracking such as hackling, micro fissures, etc. The Crack Band (CB) method is utilized to capture macroscopic matrix and fiber failure modes such as ply splitting and fiber rupture. Discrete Cohesive Zone Method (DCZM) elements are implemented for capturing inter-laminar delaminations, using discrete nodal traction-separation governed interactions. The model is verified against the impact experimental results and the associated CAI procedures. The model results are in good agreement with experimental findings. The model proved capable of predicting the representative experimental failure modes.

CHAPTER I

Introduction

1.1 Foreign Impact on Composite Laminates and the Associated Modeling Challenges

Composite laminates are widely used in many industrial applications because they offer an attractive strength to weight ratio as well as application specific tailoring of the material lay-up. The use of composites in the aerospace industry is rapidly increasing and slated to be a mainstay in many future platforms. Once a composite structure is in service it is likely to be subjected to impact from different sources, such as bird impact, collision with another vehicle or tool drops during maintenance, to name a few. The last example given belongs to the category of low-velocity (or low-energy) impacts. Low velocity impacts can cause internal damage while showing minimal surface damage. This type of damage generally falls in the category of Barely Visible Impact Damage (BVID). The internal damage could initially be negligible. However, if it goes unnoticed it could grow under repeated load cycles and possibly result in a catastrophic structural failure. The compressive strength after impact (CSAI) of a structure subject to BVID impact has been shown to be lower than that of the pristine structure [2, 3, 23], depending on the level of impact force and impact energy. A significant amount of work has been conducted on the impact of

laminated composites where the majority of the research has been on the impact response, impact damage mechanisms and extent of damage, as well as the structural strength after impact. Work in the field was summarized and reviewed by Abrate in 1991 and 1994 [2, 3] and by Davies and Olsson in 2004 [23]. Some of the relevant work in the field will be summarized next, this is by no means an exhaustive summary.

Joshi and Sun [61] studied the impact on a strip with a spherical indenter. Experimental results showing detailed damage plots were presented. A plane-strain based model was introduced to study the event. Matrix cracking at the mid-plane of the laminate were shown to be driven mainly by transverse shear stresses. Jih and Sun [58] studied the delaminations induced by a low velocity (large mass) impact on composite laminates. Curing stresses were found to have a significant effect on delamination estimates in crossply laminates with multiple ply stacking. Delamination footprint predictions using static value fracture toughness were found to agree well with experiments.

Potti and Sun [92] studied the penetration and delamination in thick composite laminates. A static punch curve was used for predicting the penetration process of thick laminates. They reported that delamination grows with increasing impact velocity up until the ballistic limit. Past the ballistic limit the delamination areas were seen to decrease. A ring element model utilizing a critical shear strain criterion accurately captured the delamination areas for different impact velocities.

Sankar and Kwon [104] studied the static indentation-flexure and low-velocity impact of simply supported circular graphite/epoxy laminates. Testing was done with two different indenter radii, three different laminate stacking sequences and three different plate radii. Static tests showed significant differences between failure loads for traditional quasi-isotropic laminates than for cross-ply laminates of the same thickness. The quasi-isotropic laminates showed a larger peak force, however the cross-ply showed a more gradual damage growth.

Springer et al. [33] studied the delaminations in composite plates under transverse impact loads. Multiple material systems were used in the impact study. The results showed the variance of many impact variables such as the effect of impactor velocity, impactor mass and diameter, difference in ply angle mismatch and so forth. The data was compared to results from the Finn-Springer model [34], agreement between experiments and model were reported as reasonable.

In the work by Hallet et al., [44] the rate effects of carbon fiber T300/914 material were investigated at impact strain rates. The material was seen to have a small rate-dependence. The experiments were also modeled using LS-DYNA3D, results showed good agreement with initiation while propagation of damage was captured incorrectly. The experimental data of a cross-ply composite laminate subjected to three point bend impact using a gas gun was also investigated [43]. High speed photography was used to capture the locations, initiation and growth, of matrix cracking and delaminations.

In other studies, Hallet et al. [48] conducted a numerical study of impact on a composite laminates using a 3D Finite Element (FE) model implemented in LS-DYNA3D. In-plane and through-the-thickness failure criteria were utilized, delamination was modeled by an in-plane failure criteria. The reported results were in good agreement with experiments. In a more recent study [20] the impact and CAI behavior of variable angle tow (VAT) laminates was studied numerically. Cohesive elements were used to predict delamination, a bi-linear cohesive law was used. Ply-splitting was modeled using cohesive contact between in-plane elements. Impact results were then used for the initial damage state of the laminate subject to virtual CAI. The study gave good insight into the impact damage and CAI of VAT laminates, further experimental study would be essential.

Takeda et al. [122] used small diameter fiber Bragg grating (FBG) sensors to monitor the delamination growth of laminated composites during a low-velocity impact

event. The method was found to be effective to capture to the extent of delamination in a laminated structure subject to impact.

Hu et al. [49] introduced a new cohesive modeling method where stable delaminations of transversely loaded laminates can be predicted with a reasonably coarse mesh. A pre-softening zone was introduced ahead of the crack tip where the penalty stiffness and cohesive strengths of the elements would be degraded with increasing separation. The onset displacement was not altered using this method and the fracture toughness was kept constant. The cohesive model was verified with simple benchmark problems before being applied to an impact problem. Delamination footprint captured by the impact model showed good agreement with experimental data.

Devivier and Wisnom [27] proposed a simple measurement technique, deflectometry, for detecting impact damage in composite laminates. The method uses high quality surface slope measurements (provided by the deflectometry method) to accurately capture the locations and extent of damage in the composite laminate. Results showed great agreement with damage extent gathered from ultrasound scanning. In previous work by Kim, Wisnom et al. [64] the virtual fields method (VFM) had been used as an inverse method for obtaining the local loss of stiffness from full field measurements. The VFM method was shown to pick up the location of damage as well as giving a good estimate of the stiffness reduction in the impact damage area.

Zhang et al. [139] used quasi-static loading in their model to predict low-velocity impact results. Cohesive elements were inserted in potential damage zones to capture in-plane matrix cracking and delaminations. A contact stiffness was introduced in to the cohesive formulation to model contact induced friction. Matrix cracks were found to play an important role in capturing delaminations correctly. The model, using quasi-static loading, showed good agreement with experimental data.

Yashiro et al. [134, 135] investigated the high-velocity impact response and damage of composite laminates, both experimentally and numerically. In part I the ex-

perimental results were presented in detail. The damage mechanisms were studied by utilizing fractography as well as soft X-ray photography. Part II presented the numerical modeling of the high-velocity impact event. A smoothed particle hydrodynamics (SPH) model was introduced, which allows for large deformations, contact and separation of objects. Cohesive layers were introduced to capture delaminations. Two way symmetry was utilized when the problem was modeled and therefore only 1/4 of the experimental setup was modeled. Caution should be taken when assuming symmetry in an impact problem, as is mentioned later on. Numerical results showed good agreement with experimental findings.

The effect of ply clustering and mismatch angles between adjacent plies (dispersed stacking sequence) in laminates under low-velocity impact and CAI have been investigated [35, 108]. A reduction in impact peak load was seen with introduction of clustering. The CSAI of laminates with ply clustering was higher than those without, with impact energies kept consistent. The study of mismatch angles between adjacent plies showed that by reducing the mismatch angle the low-velocity impact response and CSAI could be improved. Lowering the mismatch angle resulted in less indentation, smaller number of delaminations however larger in extent at some interfaces. Increase in CSAI was seen with a lower mismatch angle.

Further study on dispersed stacking sequences has been done both experimentally and numerically [69, 71]. A stacking sequence design method was proposed, where the axial and bending stiffness of the laminate is kept constant while the layup is adjusted for more dispersed ply angles. A traditional laminate layup was compared to two alternative layups produced by the design method. The laminates were subject to low-velocity impact and CAI. No clear benefit of dispersing the stacking sequence was seen. The traditional laminate showed a higher CSAI than the two alternatives.

Shi and Soutis [111] recently published a brief introduction and overview of damage theories of composite materials as well as introducing an FE impact model for

predicting the impact response and damage. Cohesive elements were used in-plane to capture ply splitting that is observed in experiments. Reasonable agreement with experiments was achieved.

Due to the high demand from industry to quantify and accurately predict impact damage and the post-impact strength of the structure, there is renewed interest in developing models to capture the impact damage event and to predict CSAI, the latter being sensitive to the impact damage state. It is therefore necessary that the effects of the impact damage be captured correctly to have a reasonable chance of predicting the CSAI [84]. Analytical models have been proposed for quick assessments of impact peak loads, duration and the onset of failure as well as delamination growth during impact [82, 83] as well as for quasi-static loading [132]. These models are good for initial calculations and assessments however when it is needed to predict the full damage extent of the laminate accurately, on a ply and interface level, numerical methods are needed. Such a task is important for predicting the CSAI strength accurately.

The FE method has now become a mainstay in the stiffness and strength analysis of aerospace load bearing components and assembled structures. The FE method allows for modeling individual damage and failure mechanisms, at the ply level in a composite material, as well as the interaction between the two. Furthermore, with the adoption of multi-scale analysis and parallelization of commercial FE codes, the ability to assess fiber-matrix scale (micromechanics) damage and its influence at the macroscopic level is becoming mature [136, 137], and computational run times are increasingly becoming amenable to use by industry. Many damage and failure modeling techniques have been introduced previously that capture the impact event to a good extent. Some relevant and up to date models will be summarized below and used as discussion for the remainder of the paper, by no means an exhaustive list.

Bouvet et al., [11–13, 47, 101] introduced a discrete 3D FE model which utilizes

cohesive elements to model both inter-lamina delamination as well as intra-lamina matrix cracking. Compressive and tensile fiber failure was implemented using the crack band model by Bazant [9]. Due to the nature of the modeling technique, a fiber-orientated mesh is needed and therefore would prove difficult for modeling non-traditional laminates of arbitrary ply angles. Symmetry was utilized and therefore only half of the problem was modeled, but caution should be taken when assuming symmetry. At the first sign of damage in the structure, which necessarily may not be symmetric, the assumed symmetry is broken. Therefore this assumption should not be used for modeling impact damage in composites, particularly when it is needed to introduce randomization of material properties. Furthermore, if one takes account of the cure cycle, in the presence of unavoidable manufacturing induced imperfections, then it is likely that the form of residual stress (and strain) state that is present will destroy the assumed symmetry in the problem, to begin with.

Bouvet's 3D FE model was shown to correlate well with experimental results for a $[0_2, 45_2, 90_2, -45_2]_s$ laminate subject to impacts at different energies. Delamination patterns on a ply by ply level were captured with great accuracy. The method was then extended to include compression after impact (CAI), and shown to be in agreement with experimental results. It is noteworthy to mention that the original development of the model was intended for simulating the impact event to understand the failure mechanisms that are required for accurately capturing the impact response and damage. Therefore, as mentioned by the authors, due to mesh sensitivity, the method is better suited for simulations instead of predictions. Two additional non-quantified material constants related to the indentation are also needed. Since those values were not measured accurately, a reference impact problem is required to calibrate those values.

Falzon et al., [29] also introduced a 3D FE model utilizing continuum damage mechanics (CDM) and the built in cohesive contact for inter- and intra-lamina damage

and failure, respectively. The cohesive contact is available in the commercial software ABAQUS. The model accounts for fiber compressive and tensile failure. Shear non-linearity due to matrix micro cracking is modeled as well as matrix compression, tension and shear failure. The model was made mesh objective by correctly calculating the characteristic length and adjusting the fracture toughness accordingly. The model showed good agreement with the overall experimental load response and the projected delamination area. In-plane matrix damage was over predicted, spanning a large area of the laminate in some plies. Calibration of the model was done by using in-situ strength values, and better agreement for damage was achieved but the load response started to deviate from the experimental results. Compression after impact for the laminate coupon was also simulated and showed an overall good agreement with experimental results.

Lopes et al. [70] introduced a high-fidelity computational model for simulation of low-velocity impact damage in composite laminates. A continuum damage approach was introduced for capturing intra-lamina damage coupled with intra-ply cohesive elements for ply splitting. Cohesive elements were used for capturing delaminations. A structured mesh aligned with the fiber direction of each ply was utilized for capturing ply splitting and delamination interactions. An element erosion criteria and intra- and inter-laminar friction allowed for capturing permanent indentation due to fiber splitting.

While much work has been done in the field, there is still an immense requirement for further improved prediction capabilities. The major push from industry is a model that can be used for any arbitrary laminate stacking, and layup angles, ranging from thin to thick, all while keeping the computational time as low as possible. During the development of computational tools, it is easy to loose sight of the practical utility of the developed model. In many cases, there is a tendency to attack simple problems for model development and trouble shooting, however, the complexity of a larger

problem may not be amenable to being produced through an induction process of building up from a set of smaller problems. While the simple model problems provide insight, interaction between different and multiple damage and failure mechanisms renders extensions to real problems difficult. The ability to break-up and reduce a problem to a set of simpler problems does not imply that one can construct the whole from the reduced parts. Interestingly, the impact damage and CAI problem of composites, falls into this problem class. It is the *interactions* between different mechanisms that dictate the outcome of the impact and CAI problems. In physics, a similar discovery led to the award of the Nobel prize to the American Physicist, P.W. Anderson [4]. High fidelity and computationally efficient models of the impact and CAI problems need to be advanced to solve real problems from industry. With the growth of laminated structures of very high ply counts with limited amount of ply stacking, as well as with increasing interest in non-traditional laminates and automated fiber placed structures, it is necessary to develop robust computational tools for impact and CAI predictions. Much remains to be done in this field.

In the following introduction sections, impact damage mechanisms and inspection methods will be reviewed as well as the computational methods currently being developed. The focus will be on currently used damage measuring techniques. Impact modeling will be overviewed in a general sense, with the scope being currently developed models and the requirements for moving forward.

1.1.1 Impact Damage Mechanics

Laminated composite structures subject to low-velocity (low-energy) impact have a set of rich and intriguing failure mechanisms. While the structures' surface can show minimal signs of the impact event, the internal structure can have extensive damage showing a combination of interacting intralaminar (fiber and matrix) and interlaminar (delamination) failure modes. The impacted surface will show indentation, as well

as, depending on impact energy, signs of compressive matrix failure and/or fiber kinking of the top most layers, Figure 1.1. The compressive failure on the surface will initiate at the impactor-laminate contact boundary and travel outwards parallel to the fiber direction in case of matrix failure and perpendicular to the fiber direction for fiber compressive failure. Depending on layup, boundary conditions and material properties, the surface matrix cracks can be driven by fiber failure in the second layer and therefore traveling in an orientation neither parallel nor perpendicular to the fiber direction of the first layer, as presented in Figure 1.1.

The back surface (non-impactor side) of the laminate will be in tension and therefore it can show signs of splitting of the outer back surface ply, and in some cases fiber rupture can be achieved if the flexural deflection is large enough. In recent studies, the in-situ out-of-plane deflection has been recorded as a function of time, using an angled mirror placed beneath the specimen and using alignment optics to record images of speckled back surface. 3D digital image correlation is used to attain full field out-of-plane displacement fields [123]. Such information is valuable in identifying the temporal evolution of damage on the laminate response modeled using the FE method, where mechanism based models are favored over empirical ones.

The most commonly used method for identifying the internal damage of an impacted laminate is ultrasound scanning (C-scanning). High-quality ultrasound scanning requires the specimen to be submerged in an ionized water tub with the measuring probe. The water acts as a transfer medium for the sound waves before reaching the specimen. In-situ ultrasound scanning techniques have been developed where the specimen does not need to be submerged in a tub, instead a thin water layer is applied to surface prior to scanning. The in-situ ultrasound results are however far less detailed and simply give a good estimate of the impact area. Recent advances by Pelivanov et al. using a high-frequency fiber-optic laser-ultrasound scanner which does not require a transfer medium and is therefore desirable for in-situ evaluation of

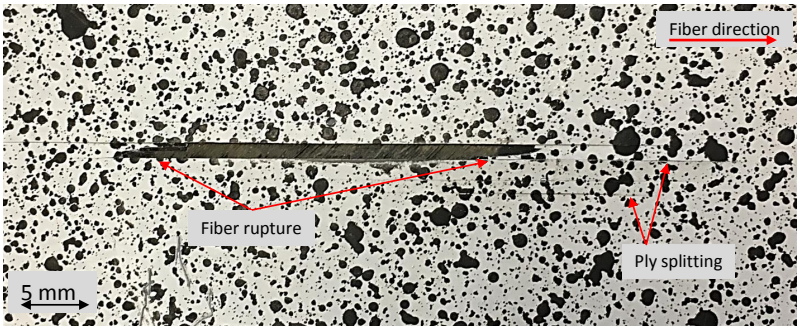

a) General back surface damage (non-impacted side). Speckled for DIC purposes.

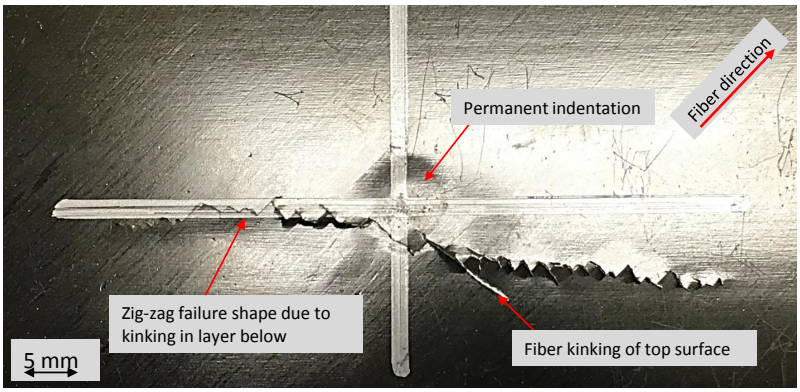

b) General front surface damage (impacted side).

Figure 1.1: Surface damage for a 20J impact, 24kg mass.

damage. The method has been used effectively in accessing thermal induced damage [87] and impact induced damage [86] in composite materials.

Utilizing the ultrasound method on impacted laminates provides the user with step-wise delamination patterns, where the delamination depth can also be acquired. Figure 1.2 shows a general ultrasound result [126]. Figure 1.2 (a) shows a depth contour which shows the depth of each delamination, while Figure 1.2 (b) and 1.2 (d) show the signal intensity for the front and back surface, respectively. Figure 1.2 (c) shows the through-the-thickness damage of a section traversing vertically through the center of the impact. The widely reported conical shape of the delaminations [2, 23] can be observed. Due to the physics of the method, the top most (from the measuring probe) damage will overshadow anything underneath.

Delamination shapes are often referred to as being "peanut" shaped and orientated in the fiber direction of the lower ply of the interface [2, 23]. The delamination shapes

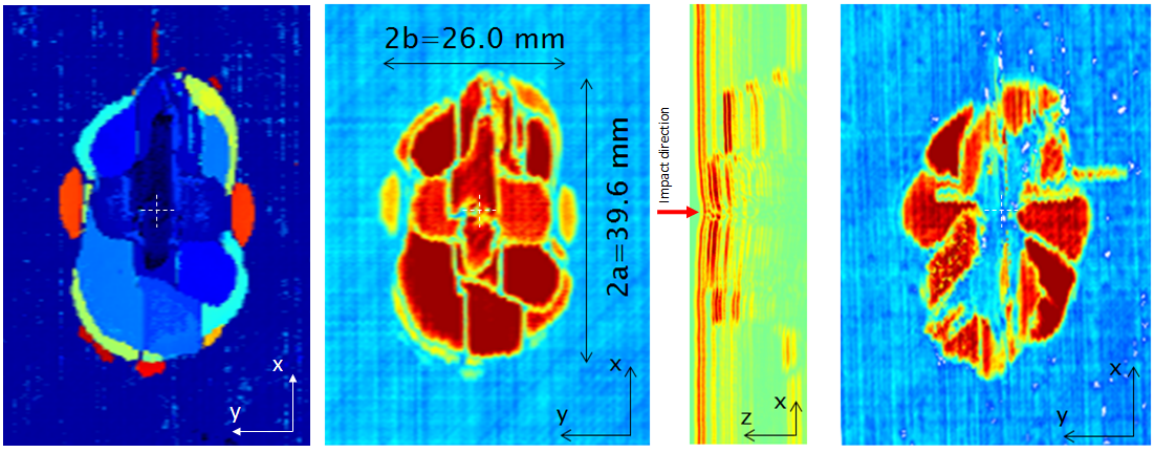

Figure 1.2: Ultrasound results for a 20J impact, 24kg mass.

at each interface are often estimated from ultrasound results and the unknowns are extrapolated following the peanut shape trend. Abrate reported in his second impact review that several investigators had described delamination shapes being bounded by splitting in the top ply of the interface [3].

These delamination patterns were reported as early as 1991 by Clark and Saunders [17] and in 1993 by Hull and Shi [52], where the delaminations are shown to have two general trends. The first one being between plies with a 90 difference in angle, where the shape is somewhat like the peanut shape with a non-delaminated area in the center which is bounded by splitting of the top ply and therefore perpendicular to the elongated orientation of the delamination, Figure 1.3(a). The second is for plies with a 45 difference in angle, where the shape is more like a propeller, following sharp boundaries formed by the splitting of both, top and bottom layers, Figure 1.3(b).

Fractography has been a widely utilized inspection method for investigating through-the-thickness impact damage. By sectioning the specimen through the center of the impact and polishing accordingly, the through-the-thickness damage can be seen in detail. The downside of this method is, of course, the destructive nature of it. Figure 1.4 shows a microscopic images of a general impact damage. The interaction be-

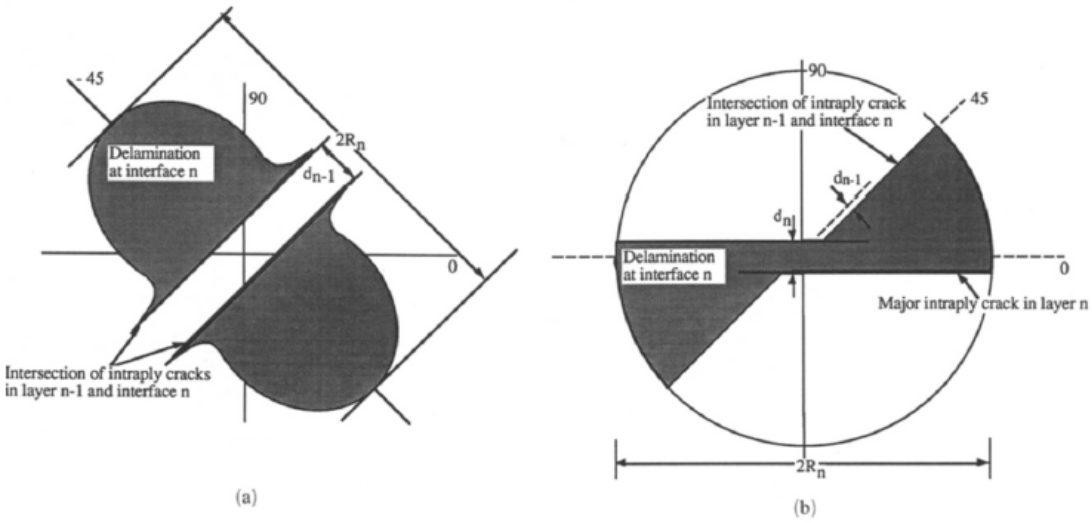

Figure 1.3: Ply splits interacting with delamination growth [52].

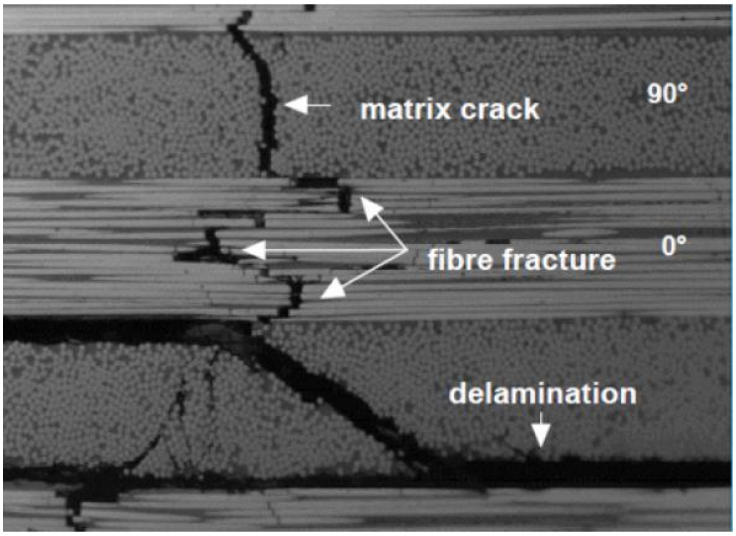

Figure 1.4: Microscopic image of typical impact damage [23]. Shear matrix crack interacting with a delamination can be seen, as shown in [124]. The ply thickness is approximately, 0.2-0.3 mm.

tween an intralaminar matrix crack and interlaminar delaminations can be observed in close detail. Delamination induced by matrix cracking was observed and modeled in a simplified case study by Thorsson and Waas et al.[124].

Micro computed tomography (microCT) is currently the most advanced technique

for visualizing the internal damage of a composite structure. MicroCT scanning allows for 3D renderings of the impacted laminate to be produced and visualized at will. Delaminations can be visualized, interface by interface, and through-the-thickness sections can be produced on the fly. The size restrictions of the scanned part are consistently being reduced with further advances. With the newest microCT machines, the scanning of a full sized impact coupon (100mm by 150mm by Thickness) can be achieved with high detail and accuracy. Very clear details of delamination shapes, matrix crack and fiber failure locations can be identified. Figure 1.5 shows a snapshots gathered from a microCT scan of the same impacted specimen as shown in Figure 1.2.

The top most pictures show the through-the-thickness view of the impacted specimen.The delamination and ply split interaction can be seen clearly when the interface layers are observed. A lot of ply splitting can be seen with crack lengths varying in lengths. Delaminations bounded by these intra-laminar splitting can be observed with good detail, sharp transitions from delaminated to intact areas. This is the same failure mechanism as was shown in Figure 1.3. Fiber rupture can also be captured in great detail, as can be seen in the center image of Figure 1.5. A sectional view is also demonstrated, where the interaction between intra-laminar through-the-thickness shear cracks and delaminations can be seen. The section visualization gives an exceptional view of the amount of matrix cracking and delaminations the 20J impact caused on this particular coupon. The through-the-thickness section around the impact is riddled with cracks and delaminations.

1.1.2 Computational Methods

1.1.2.1 Introduction

Early FE models for predicting impact on laminated composites were limited to damage and failure in the interface layers by cohesive zone modeling [15, 16, 25, 97].

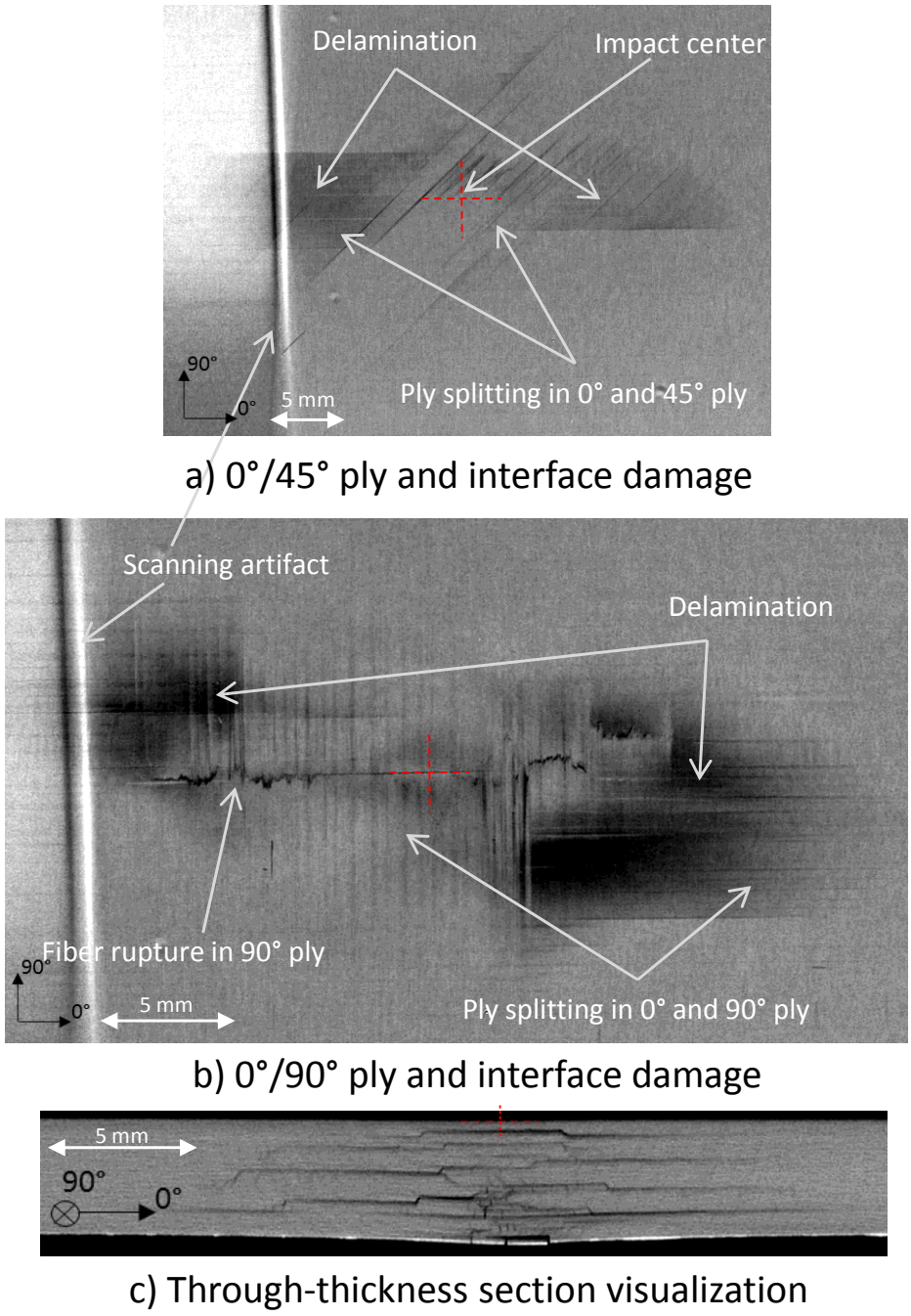

Figure 1.5: Sample of a microCT result from a 20J impacted specimen.

With increasing computational power and knowledge of the impact damage mechanism more improved models have been developed in the last decade to include in-plane failure modes such as fiber tensile and compressive failure, and matrix dominated ten-

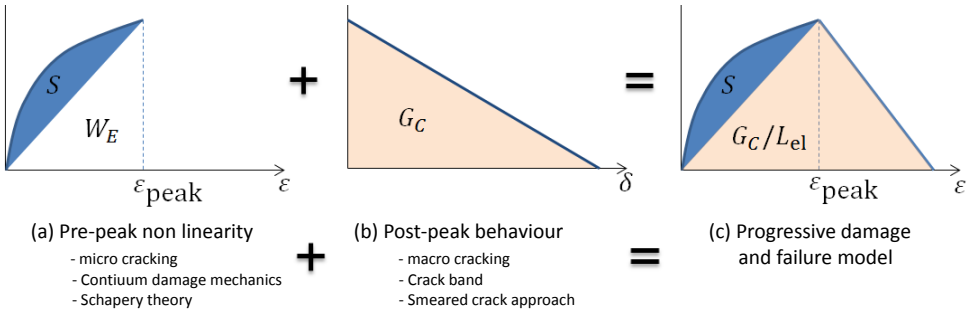

Figure 1.6: Progressive damage and failure modeling schematic as used in EST [88].

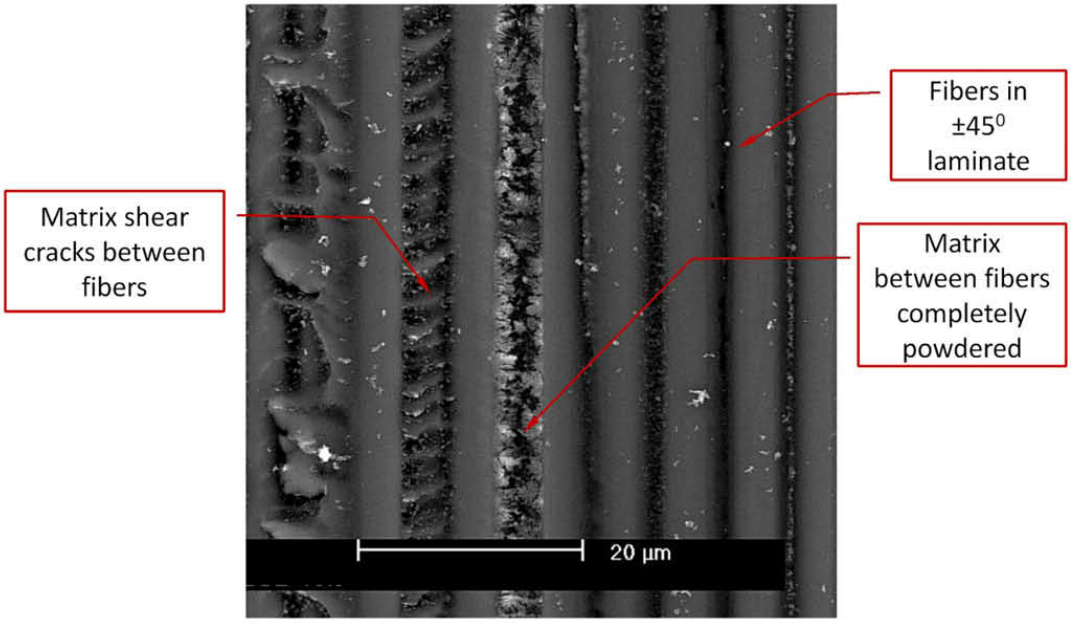

Figure 1.7: Micro cracks in a +/-45 laminate subject to tensile loading [77].

sion, compression and shear failure modes.

There are two main differences between the general FE scheme being used by different investigators. On the one hand there are full 3D models and on the other hand 3D shell theory based models, utilizing plane stress assumptions. Both methods have the same principal idea, each lamina is modeled with an individual layer and the layers are then connected together using cohesive elements or other cohesive methods that will be discussed later. The shell theory approach is desired due to computational efficiency while constraining the intralamina damage and failure modeling to the 1-2 plane. The through-the-thickness shear failure cannot be modeled directly using

a shell theory approach, yet the effect of it can be captured using a first order (or higher order) shear deformation theory. The 3D approach, while computationally more burdensome, allows for modeling of failure modes in each plane (1-2, 1-3 and 2-3).

Damage and failure modeling techniques usually combine a pre-peak response model and a post-peak softening model, Figure 1.6. Pre-peak nonlinear response due to matrix micro damage (micro cracks, micro fissures, shear banding etc.), Figure 1.7, is handled through degradation of the matrix related moduli, E_{22} and G_{12} with respect to in-plane modes. In this pre-peak regime, the tangent stiffness of the assumed stress-strain response is positive, thus, there are no issues related to mesh objectivity. Micro cracks are initiated predominantly by shear loading of the matrix, growth is effected by transverse loading as well and therefore both the transverse and shear moduli are degraded. Micro-damage is usually modeled using continuum damage mechanics (CDM) or Schapery Theory (ST) [105], a thermodynamically based work potential theory. The degradation scheme is backed out from coupon level experimental data. For example, the degradation of the shear moduli with evolving micro-damage is backed out from a tensile or compressive test of a $\pm 45^{\circ}$ coupon. Obtaining the other parameters is also conveniently carried out with coupon level testing, see for example results by Sicking and Schapery, [106, 112].

Initiation of failure (or transition from damage to failure), which leads to post-peak softening, is initiated by a stress or strain failure initiation criterion such as Hashin-Rotem [45], Mohr-Coulomb, Puck [95, 96] or LaRC0 criteria [24, 91], or any other established failure criteria. Ultimately, micromechanics modeling, such as that reported in, [75, 76] or an analytical sub-scale model, such as reported in, [137], are favored over these transition criteria to establish a sound multi-scale framework that can be used for this class of problems.

Failure modeling (post-peak) is carried out using discrete and non-discrete meth-

ods. Discrete failure modeling is achieved by introducing sharp discontinuities at a macroscopic crack surface. This can be done by utilizing zero-thickness cohesive elements to model intra-laminar failure modes and by using nodal/element enrichment methods such as eXtended finite element method (X-FEM), [30, 31, 109, 110], Variational multi-scale cohesive method, [103], continuum decohesive finite element method (CDFE) [79, 93], the methods of Yang and co-workers which is based on an extension of CDFE,[32] or the method based on X-FEM, [54]. However, the aforementioned methods are still too early on in their development to be able to handle impact of composite laminates, and it is unclear if they will yield computationally efficient schemes. In this regard, the paper by Oliver [81], provides a good discussion.

Failure modeling can also be done using non-discrete, smeared methods. The most commonly used and known method is the Bazant-Oh Crack Band (CB) model [9]. The CB model introduces a characteristic length parameter in the failure evolution to ensure a mesh independent solution. This is because the effects of the cracking are smeared over a characteristic band of known size and this length scale in conjunction with the energy release rate associated with softening and details of the pre-peak response provide a well-posed problem in the softening regime. Mixed mode failure can be achieved by utilizing a mixed mode failure criterion such as a power law criterion and this is commonly used for mode I, II and III matrix failure. Recently, an objective, novel mixed-mode criterion which leads to the simultaneous vanishing of crack face tractions has been reported by Nguyen and Waas [78].

By combining pre-peak damage response due to micro cracking and post-peak softening response due to macroscopic failure on the lamina scale, the full extent of lamina level damage and failure can be captured. The transition from damage to failure requires further study. At present, criteria are used to establish this transition. In the future, micromechanically informed transition criteria are likely to replace the traditional (such as the Hashin-Rotem [53]) transition criteria. In the following

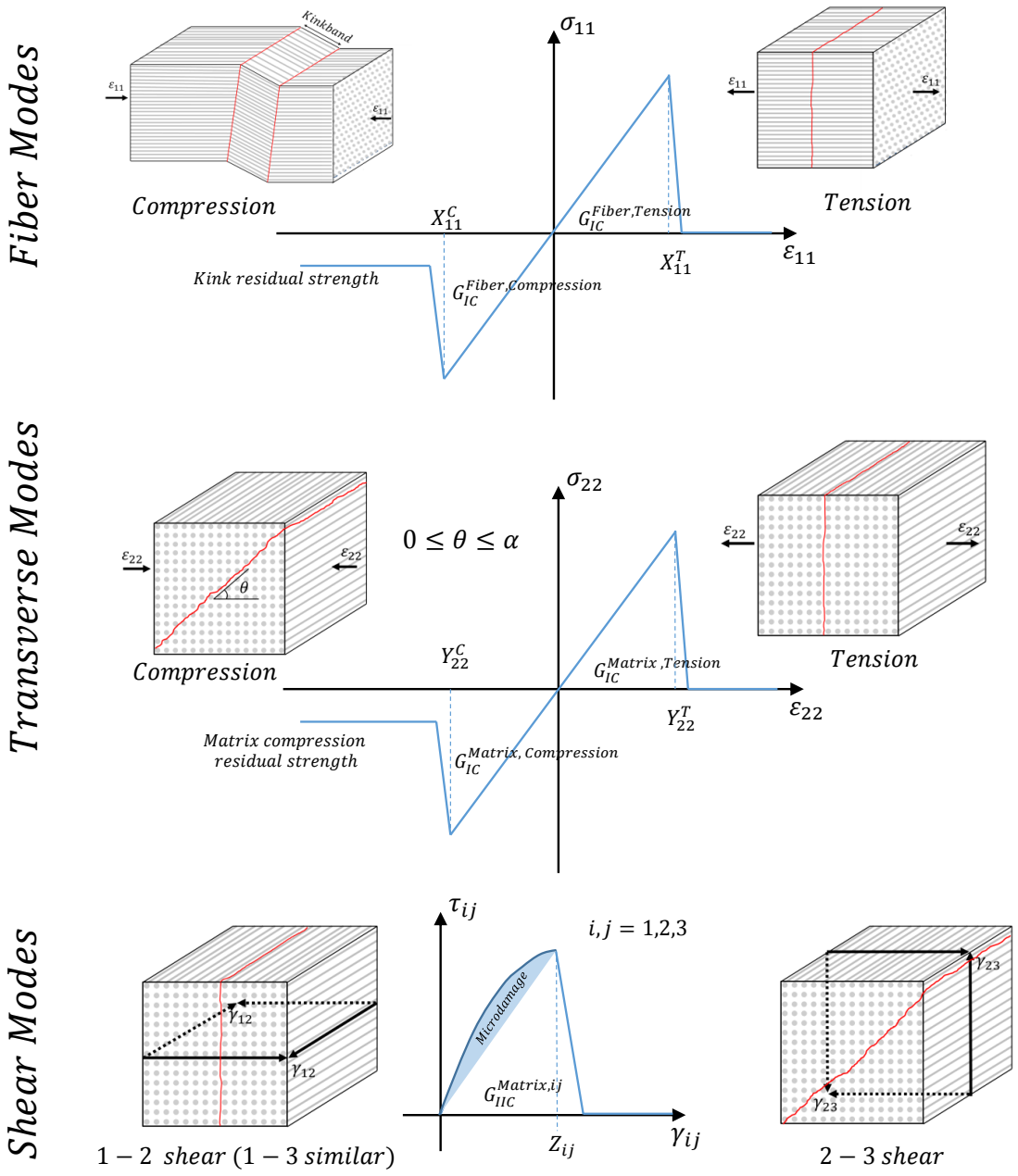

Figure 1.8: Intra-laminar failure modes for uni-directional composite plies.

subsections, the modeling of intra- and inter-laminar failure modes and the interaction between the two will be discussed. Emphasis will be placed on recent models, as well as what is required to move forward in modeling capabilities.

1.1.2.2 Intra-laminar Damage and Failure

The failure modes observed in composite laminates are summarized in Figure 1.8 with respect to the in-plane modes (1-2) as well as showing the matrix out-of-plane shear mode. Some of these failure modes can also be seen in the microscopic image in Figure 1.4. In the most common impact studies, the important intra-laminar failure mechanisms to capture, in no particular order, are, fiber breaking, transverse tensile failure, matrix in-plane shear (1-2 and 1-3 planes, which are usually assumed to be the same although that is not the case, and a discussion is beyond the scope of this paper) and matrix out-of-plane shear (2-3 plane). The transverse compressive failure mode, although not considered as a major mode of failure, should still be accounted for in most models. The fracture angle can range between $0^\circ - 55^\circ$ depending on the multi axial state of stress as shown by Puck et al., [95, 96].

The compressive failure modes, for both fiber and matrix compression, have a residual strength associated with them, as shown in Figure 1.8. The residual compressive strength after fiber kink banding and matrix crushing are very difficult to measure experimentally and therefore these values are usually estimated from calibration simulations. Combined experimental and micromechanics based studies on the residual strengths would be highly beneficial for further improving computational models, especially impact models.

Fiber kinking has been shown to be the result of a combination of initial fiber misalignment, multi-axial loading and matrix non-linear shear response [8, 107]. Micromechanics models have been developed with those sensitivities in mind to accurately predict the fiber kinking phenomena on a single lamina level scale [7] and a multilayered composite laminate [94]. The progressive kink development has also been captured [22]. Impact models tend to simplify the failure mode by introducing a fiber compressive failure strain (or stress). The fiber compressive failure strain can be acquired experimentally or by backing it out with a formulation based on matrix

shear non-linearity, such as the Considere construction, [22]. This simplified approach has shown good agreement with experimental data.

These four failure modes (fiber breaking, transverse tensile failure, matrix in-plane and out-of-plane shear failure) are the most commonly referred to modes of failure when experimental studies on transversely (we refer to this as face-on impact) impacted composite structures are reported. However, by altering the material properties of the structure, for instance by making the material of the structure tougher, the impact response can be altered in a manner where other failure modes become more influential. It is therefore necessary to capture fiber kinking and matrix compressive failures as well as the rest of the failure modes, as a function of the properties of the constituents (lamina level, or fiber and matrix level with an understanding of interfaces). This will result in a more diversified, robust and predictive model.

As mentioned before, by utilizing a 3D modeling approach one can model each of the failure modes. When a shell theory is used for laminae, the out-of-plane failure modes are lost, and the largest sacrifice will be the matrix out-of-plane shear mode, (2-3 plane), see Figure 1.8, bottom right. However the shell models have shown to be successful for capturing the bending response and failure, by utilizing only the in-plane failure modes (modeling of each layer individually, and connecting the layers through cohesive elements), and therefore having reasonable satisfaction of the plane-stress condition, [60, 126].

1.1.2.3 Inter-laminar Damage and Failure

Inter-laminar failure or delaminations appear due to three common modes, mode I (peel) and modes II and III for shear, Figure 1.9. Delaminations are modeled using interface elements referred to as cohesive elements. The cohesive element connects two surfaces together, with the separation governed by a traction-separation law. Bilinear traction separation laws are the most commonly used, see Figure 1.9. A separate law

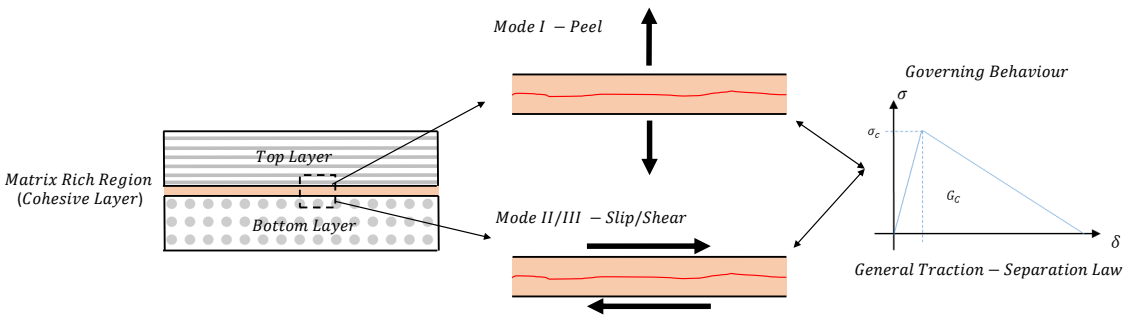

Figure 1.9: Inter-laminar failure modes.

can be defined for Mode I, Mode II and Mode III delaminations. Mode mixity is commonly captured by the use of a power law. As previously mentioned, however, the work of Nguyen and Waas, [78] for mixed mode failure is appealing, where the crack face tractions vanish simultaneously at crack growth without undergoing a sudden jump to zero as in the power law models.

Cohesive elements can be of multiple formulations which separate into continuum elements and discrete nodal elements (1D nonlinear elements). Continuum elements are beneficial when modeling a finite thickness cohesive layer but when the layer thickness decreases the computational cost rapidly increases due to diminishing element size. Discrete nodal elements such as Virtual Crack Closure Technique (VCCT) and Discrete Cohesive Zone Method (DCZM) elements have been utilized to model zero and finite thickness cohesive layers. The benefit of having discrete nodal traction-separation elements is that the degrees of freedom are uncoupled (one to one connection between two opposing surface nodes or Gauss points). The discrete nodal element is therefore more computationally efficient than the continuum elements. Cohesive contact, a surface based traction-separation behavior has been introduced in the commercial finite element code ABAQUS. The cohesive contact is very attractive due to not having to define any cohesive elements but instead merely a contact behavior between the two surfaces at the interface.

Many problems have been solved using cohesive elements with good results, how-

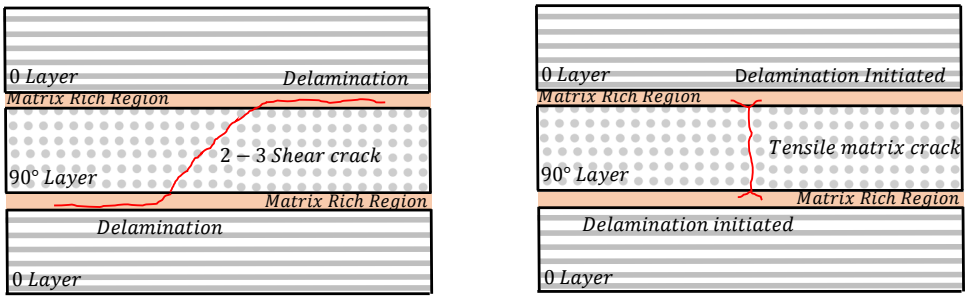

a) Delamination caused by out of plane shear matrix crack b) Tensile matrix crack initiating delamination

Figure 1.10: Intra- to inter-lamina failure interaction.

ever when the face-on impact problem is analyzed, the results are not as good as one would hope for. The general shape of the delaminations are captured while the "sharp" and abrupt change from intact to delaminated areas cannot be achieved successfully thus far, except by manual insertion of in-plane cohesive elements (a-prior in selected locations) However this method becomes highly mesh sensitive and computationally heavy. This does not necessarily need to be a deficiency but is merely a result of the modeling approach. Interactions between intra- and inter-laminar failure modes need to be clearly understood and implemented in the FE models, and this topic is further discussed in the next section.

1.1.2.4 Intra- to Interlaminar Interaction

Once the intra- and inter-lamina damage and failure modeling is achieved, the most important modeling aspect is the interaction between these two modes. This is a challenging task for modelers. The interaction between a delamination initiated from an in-plane matrix crack and the propagation of that delamination must be captured. Figure 1.10(a) shows a schematic of an out-of-plane shear matrix crack interacting with the interface layer and causing a delamination to grow due to shear. Figure 1.10(b) shows a tensile matrix crack which then initiates a delamination at the interface but the crack will not grow without shear loading. The next frame of this picture (given that load is continuously applied) is that a second matrix crack

would form, and then a third and so forth due to shear lag effects, as has been shown in many studies, see for example, Meyer and Waas [75].

The interaction of in-plane and out-of-plane damage and failure modes is a subtle thing but of very high importance for capturing the impact induced damage correctly. There are many challenges to be overcome in a numerical model to accurately capture this event. While it is tempting to duplicate the exact details of a crack and how it meanders through a structure, such a detailed model may lead to a computationally intractable model. Understanding and capturing the main effects of these damage modes on the task at hand (i.e. predicting stiffness loss, predicting strength, predicting fatigue life of an impact damaged structure and so on) is a much more attainable and important goal for design purposes. Yet, some test cases may be needed to ascertain the importance of various details of damage modes, and this remains to be clarified.

Failure mode interactions can be captured with a micro-mechanics model on the fiber and matrix scale, such as that reported by Meyer and Waas, [75], however, those models are not suitable for a laminate level event. With the correct interactions modeled, the "sharp" and abrupt change from intact to damage areas could be captured with a "smeared" modeling approach, as was mentioned previously. This aspect needs a significant amount of further study. In order to capture the interaction between a matrix crack and delamination of adjacent layers, a model experiment with sandwich composites, subjected to three-point bend loading, under static and impact conditions was recently reported in Thorsson and Waas [124]. In that study, the authors were able to re-produce the experimentally observed result of matrix crack initiation and subsequent growth leading to delamination. However, much remains to be done to extend those findings to laminates in a 3D setting, where curved crack fronts and curved delamination fronts are the norm.

1.1.3 Conclusion

An overview of the challenges facing the resolution of face-on impact damage to composite laminates and CAI predictions have been provided. The impact damage mechanics have been presented with a focus on currently used experimental techniques for estimating, measuring and visualizing the damage extent due to impact. The shapes and trends of impact damage, as previously reported in literature, is shown to be more complex than a lot of models are being bench marked against. Resolution of the interaction of intra-lamina and inter-lamina failure mechanisms are shown to be a challenging task.

Industry needs a computationally efficient model. While high-fidelity is desirable, computational efficiency with respect to capturing the important details of the impact event and subsequent prediction of CAI is important. For this task, the important coupon level material properties have to be identified. The state of the art modeling techniques and their predictive capability for modeling of laminate impact damage and CAI have been discussed. The necessary lamina level failure modes that need to be incorporated into models have been discussed, and the inter-lamina failure modes and techniques necessary have also been discussed. The importance of the interaction of the two, intra- and inter-lamina failure, has been highlighted as being a challenging yet important task. The authors feel that there is much work remaining to gain full understanding of the impact damage prediction event and the assessment of CAI. Micromechanics based modeling as a tool to gain insight on failure modes and their interactions is encouraged.

1.2 Objective and Organization of the Thesis

This dissertation contains experimental and computational work on FRPC laminates subject to impact and CAI. The main motivation for the impact work, both

experimental and numerical, arises from industry needs. There is a growing need for efficient and effective computational models for predicting the impact response and post-impact state of composite laminates. It is furthermore required that the computational model is robust and easily applicable to non-trivial stacking sequences as well as containing a ply count which is relevant to real problems. The computational model was therefore designed to be efficient by using plane stress shell elements in combination with cohesive elements for capturing ply interfacial slipping due to through-the-thickness shear mismatch. The model combines the EST material model developed by Pineda and Waas [88–90] and the DCZM element first introduced in a 2D form by Xie and Waas [131] and later extended to 3D by Gustafsson and Waas [40–42]. EST is able to capture the full field damage and failure of a UD lamina in the 1-2 plane. EST captures the pre-peak non-linearity due to matrix micro-cracking using ST. Failure initiation is controlled by a Hashin-Rotem [45] strain based failure criteria, including mixed mode matrix failure. Post-peak strain softening due to failure is modeled using the Bažant-Oh CB model. Failure modes that are accounted for are matrix transverse and shear cracking as well as fiber rupture. The DCZM element is a node based traction-separation element which captures delamination due to mode I and mode II loading. Mixed mode failure is handled by a first order power law.

The organization of the thesis is as follows. Chapter II will focus on the face-on impact and CAI experimental work. First a high fidelity impact study on IM7/8552 laminated composites is presented. Next a BVID impact study and CAI is presented on a second material system. In Chapter III an experimental approach for conducting edge-on impact and CAI is presented. An edge-on BVID study is presented with detailed impact failure mode investigation. In Chapter IV a study on rate sensitivity of inter-laminar mode I and mode II fracture toughness of FRPC's is presented. First a Modified Wedge Insert Fracture (MWIF) method is introduced for conducting experimental mode I fracture at elevated rates. MWIF method correction factors

applicable to the Modified Beam Theory (MBT) fracture toughness calculations are presented along with experimental results. Next the mode II fracture testing and results are presented.

In Chapter V the details of the computational intra-laminar material model (EST) and inter-laminar cohesive element (DCZM) are introduced. Chapter VI then introduces the face-on impact and CAI modeling strategy. The impact and CAI model are compared to experimental results presented in Chapter II. Chapter VII presents the edge-on impact and CAI model, using the same modeling strategy as in the face-on impact model. The model results are compared against experimental data from Chapter III. Chapter VIII then concludes the dissertation with final remarks, a summary of the research findings including best practices and modeling guidelines, suggested future work and contributions of the thesis.

1.3 Unique Contributions in this Thesis

The impact failure mechanisms in laminates of industry standards are rich and intriguing. The damaged/failed state of the structure shows a combination of interacting intralaminar (fiber and matrix) and interlaminar (delamination) failure modes. The interaction of in-plane and out-of-plane damage and failure modes is a subtle thing but of very high importance for capturing the impact induced damaged correctly. It is therefore necessary to develop a computational tool that is able to capture these effects accurately. A secondary requirement arrives from the industry, where computational time is one of the biggest factors. High-fidelity experimental data is of high importance for accurately validating and improving the developed impact model. The thesis focuses on both the experimental and numerical investigation of low-velocity face-on and edge-on impact of FRPC's, with the main focus on BVID events. The unique contributions of the thesis are as follows:

1. Detailed experimental (real time) results for face-on and edge-on impact and CAI of aerospace laminates has been conducted. Different lay-ups and material systems were investigated. In-situ out-of-plane deformations were captured using high speed imagery and 3D DIC methods. Detailed post impact CT scans showing detailed interior damage mechanisms.

2. Introduced a new experimental method for conducting coupon level edge-on impact and CAI. The method allows for a drastic reduction in experimental costs (material, setup and preparation). Evaluation of the edge-on impact damage on the stringer of a stiffened panel is captured using a simple laminate coupon.

3. Developed a new experimental method for quasi-static, intermediate and elevated rate mode I fracture characterization using a modified wedge-insert fracture experimental configuration. Detailed analysis and validation of the method were conducted.

4. Introduced a new robust and efficient, finite element based, mesh objective formulation and model that virtually predicts the face-on impact response and CSAI of FRPC's. A continuum shell based model utilizing an in-plane progressive damage and failure material model and discrete cohesive elements was introduced. The model successfully captured several failure mechanisms accurately, such as top face kinking, delamination jumps, and moderate interaction between intra- and inter-laminar failure modes, in a unified model.

5. Extended the shell element model to predict edge-on impact responses and CSAI of FRPC's. Limited FE modeling of edge-on impact has been reported in literature, especially for realistic aerospace laminates. The model showed good promise for capturing the edge-on response, as well as showing good agreement for CSAI.

CHAPTER II

Face-on Impact Experimental Work

2.1 Introduction

In this chapter the experimental results for face-on impact and CAI are presented. Face-on impact and CAI of fiber reinforced polymer matrix composites has been studied by many, as was reviewed in Chapter I. With computational models being developed and utilized for impact and CAI predictive capabilities it is important to have the necessary experimental data to evaluate these models. It is tempting to choose laminate stacking sequences which introduce ply clustering and therefore result in a limited number of critical interfaces. These laminates subject to impact will show simplified failure modes and their interactions. While experiments on such laminates are good for initial model validation it is clear that more realistic laminate designs, in accordance with industry design guidelines, are required. It is also important to look to the future and what the industry design allowable may develop to include. Non-traditional laminate (NTL) stacking sequences containing ply angles of any arbitrary degree are a continuously increasing interest in industry, although it is not at the level of being used for structures in service at the current time.

It is therefore necessary to not only gather indepth experimental data for impact and CAI but to do so for laminates with ply counts and stacking sequences of relevance. In this chapter two different impact studies on different material systems

are presented. First an impact study of a 20 ply specimen with a industry standard layup ([50/40/10]) and material (IM7/8552) is presented. The nomenclature ([50/40/10]) refers to 50% of 0° plies, 40% of ±45° plies and 10% of 90° plies. Impact was conducted at a fixed impact energy of 25J while varying the impact velocity by changing the mass. A thorough post-impact investigation using ultrasound and microCT scanning, which clearly maps the damage extent and failure mechanisms observed, is presented. A rich combination of in-plane fiber and matrix failure in combination with delamination was seen in great detail. Out-of-plane deflection of the back surface of the impacted specimen during the impact event are captured using a set of two high speed cameras in a stereo setup.

Next a BVID impact study is presented. Impact at varying impact energies was conducted on specimens containing a traditional laminate (TL) stacking sequence to establish the BVID limit of the material system and layup. Ultrasound and microCT scanning results are presented for the coupon impacted at the BVID limit. Out-of-plane deflection of the back surface of the coupon is presented. Impact peak loads for NTL coupons impacted at the BVID limit are compared against the TL results. The NTL coupon layups were designed to have the bending and axial stiffness as close as possible between the different layups. Finally the compression after impact experimental results for the TL and NTL laminates are presented.

The above results are the foundation of the development and evaluation of the FE model development presented in Chapter VI. The detailed experimental results presented in this chapter are essential in establishing the predictive capability using impacts for different materials as well as multiple different impact conditions.

2.2 High-Fidelity Impact Study

A detailed face-on impact study was conducted on the readily available IM7/8552 laminated composite material system. The goal of this study was to investigate the

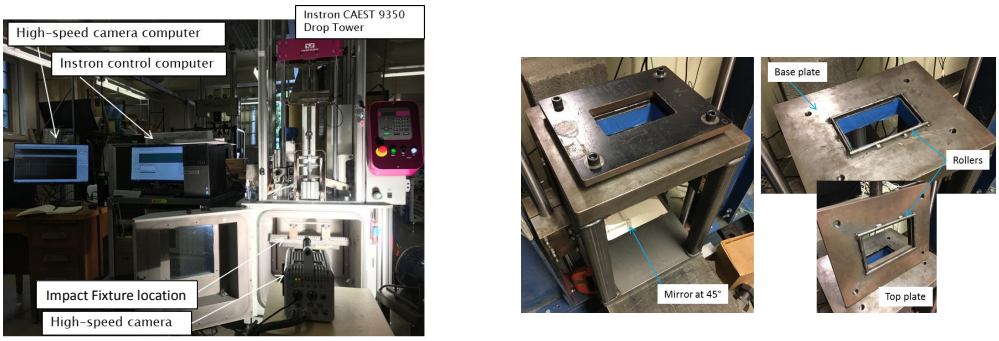

(a) Instron CAEST 9350 drop tower setup. Different impact fixture shown and only 1 camera.

(b) Face-on impact fixture.

Figure 2.1: Face-on Impact Experimental Setup.

impact failure mechanisms in depth and acquire important data for impact modeling verification. The material system is different from the one in the BVID study later in the chapter, therefore giving a second material system as additional data for the impact modeling. The composite laminate chosen for this study was a 20 ply laminate, layup $[0/45/0/90/0/-45/0/45/0/-45]_s$. The laminate chosen is a [50/40/10] laminate which is commonly used in Aerospace industry. This stacking sequence, when subject to impact, would show typical delamination patterns while also being subject to fiber failure. This would give rich insight into the failure mechanisms of composite laminates subject to face-on impact while not simplifying the problem away from industry standards. The specimens were scanned using ultrasound C-scanning methods to verify that they are in a pristine condition prior to impact.

Face-on (transverse) impact tests were carried out on an Instron Dynatup 9350 drop tower test system, Figure 2.1. The impact energy was chosen to be 25J in accordance to ASTM D7136 standard which suggests 6.7 J of impact energy per mm of the specimen thickness. The impact energy was kept constant while impacts were conducted with different impact masses, therefore varying the impact velocity. This would allow for establishing if the change in impact velocity (within the low-velocity

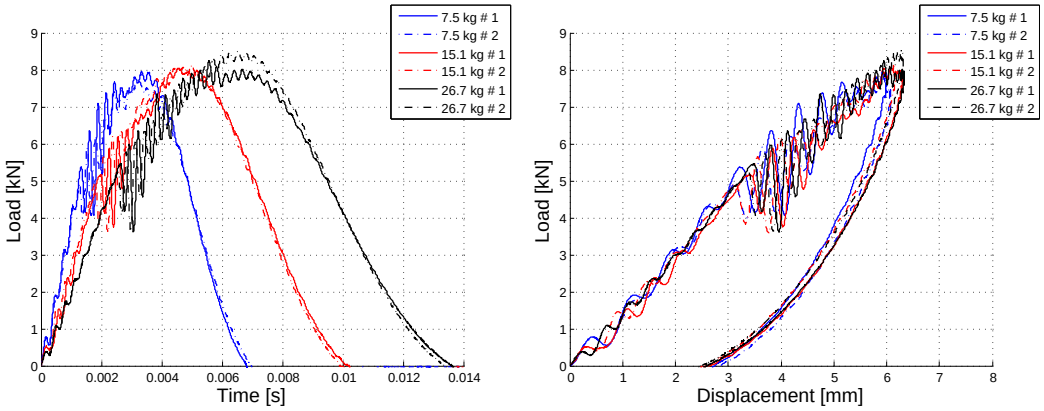

(a) Load vs. time

(b) Load vs. displacement

Figure 2.2: IM7/8552 results for varying impact mass.

bound) would have any effect on the response of the structure. The impact mass was chosen in accordance to the drop tower limitations, ranging from the minimum impact mass to the maximum impact mass with an additional impact velocity chosen in between. The impact masses that were studied are 7.5 kg, 15.1 kg and 26.7 kg. This resulted in impact velocities of 2.58 m/s, 1.82 m/s and 1.37 m/s for the low to high impact masses, respectively. A hemispherical impactor with a diameter of 20 mm was used for this impact study (note that the impact conditions are different than the BVID impacts presented in the next chapter).

The specimen dimensions are 150 mm by 100mm (in accordance to ASTM D7136) with the zero degree orientated in the longitudinal direction. The specimen nominal thickness was 3.72 mm, giving an average ply thickness of 0.186 mm. The impact fixture design draws from the ASTM D7136 standard while minimal changes have been made. Instead of clamped boundary conditions the specimen is simply supported in the form of rollers which outline a "picture-frame" boundary condition on both sides of the specimen (top and bottom). The rollers have a diameter of 6.35 mm and are positioned 6.35 mm away from the edges of the specimen. The picture-frame boundary dimensions (where the rollers are in contact with the specimen) are therefore 137.3 mm by 87.3 mm.

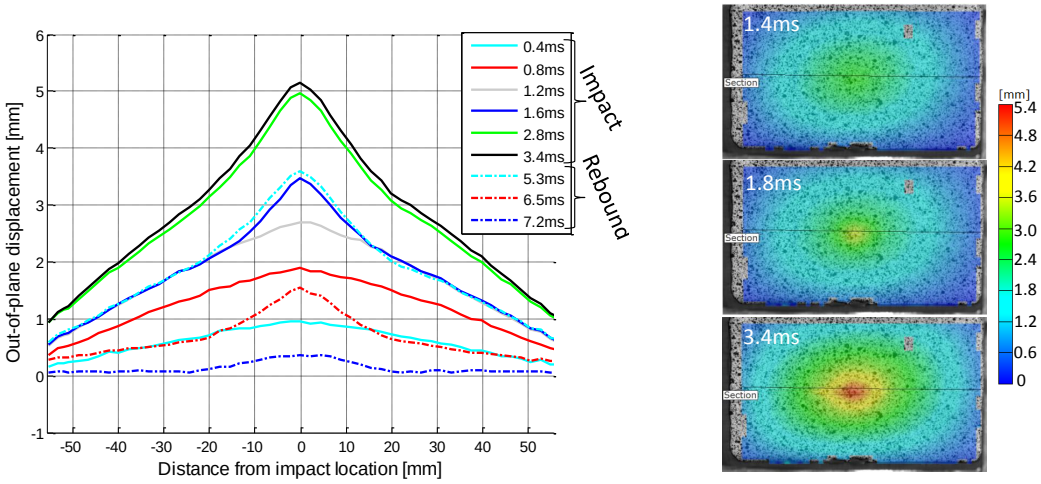

(a) Deflection of a section on the back surface, section showed on contour plots.

(b) Deflection contours at 1.4ms, 1.8ms and 3.4ms into the impact.

Figure 2.3: DIC results showing the out-of-plane deformation of the back surface during the impact and rebound.

Two Photron SA-X highspeed cameras were used in a stereo setup to record the back surface of the specimen during impact. A mirror was placed below the specimen, orientated at 45°, to allow for the back surface of the specimen to be observed during impact. Camera resolution was set to 768 pixels by 448 pixels which allowed a recording rate of 25,000 frames per second, which results in roughly 175 images of the 7.5kg impact event. The resolution and recording rate are coupled by the buffer memory of the cameras, a higher resolution will result in a reduced frame rate capability. Frame rate and resolution is chosen on a test basis in order to maximize the quality of data achieved. Applying black and white speckles to the back surface of the specimen enables Digital Image Correlation (DIC) techniques to be utilized to acquire the full-field strains on the back surface as well as the out-of-plane deflection during the impact event (after careful calibration of the system stereo system). The commercially available DIC program ARAMIS is used.

Impacts were carried out on multiple specimens to ensure repeatability, the experiments proved very repeatable as can be seen in Figure 2.2. The load-time response of the laminates can be seen in Figure 2.2(a) and the load-displacement response in

Figure 2.2(b). The load-time histories show a trend that would be expected with the increases in impact duration being directly proportional to the change in impact velocity. The load-displacement history shows that all three impact cases share the same response. Therefore it is concluded that the flexural response of the laminated coupon does not change with impact velocity (given that the impact energy is constant) within the low-velocity impact regime studied here.

A significant failure event can be seen in all impact cases at roughly 5kN. When the images from the highspeed cameras were investigated, matrix splitting in the back surface ply could be seen initiating at this failure event and then growing to a maximum at the impact peak load. The load-displacement curves, Figure 2.2(b), show a substantial energy dissipation due to impact damage as represented by the area under the curves (for a fully elastic impact the loading and unloading curves would coincide).

The out-of-plane displacement of the specimen back surface during impact can be seen in Figure 2.3. The results are plotted at time intervals of interest for the 7.5 kg impact event (test 1). The figure shows the out-of-plane deflection of a section traveling along the longitudinal direction of the laminate through the impact center, Figure 2.3(a). The impact event is shown in solid lines and the rebound event in dotted lines. It is very interesting that the back surface deflection captures the major failure event that occurs at 5kN in the experiments. For the 7.5 kg impact it is at roughly 1.4ms into the impact event. The back surface shows a smooth contour prior to the failure event, and once the failure is initiated a sharp gradient can be seen. This sharp gradient forms due internal damage dispersing through the laminate underneath the impactor. This damage relaxes the global deformation of the laminate by more local deformation. Further damage and failure details can be seen in the microCT study, Chapter 2.2.2.

It is interesting to note that at the time of zero force being transmitted and

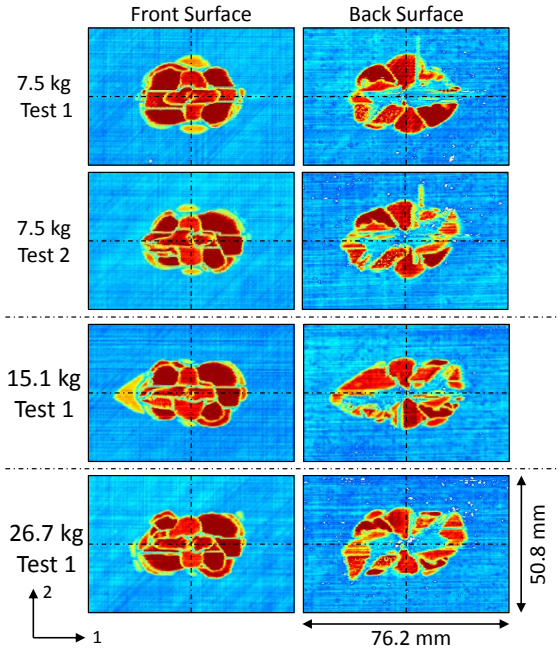

Figure 2.4: Ultrasound C-scanning results for the 7.5 kg impacts and one specimen of the 15.1 kg and 26.7 kg.

the impactor has effectively rebounded, at $t \approx 7ms$, the back surface deflection has rebounded and shows a permanent deformation of $\approx 0.36mm$. Yet the impactor is still $\approx 2.6mm$ below the initial contact plane, permanent indentation was only in the range of $\approx 0.2mm$. This would imply that a part of the structure is relaxing back at a slower rate than the back surface and impactor.

Post-impact inspection of the specimen with the naked eye showed very minimal damage. A slight dimple and ply split can be seen on the impacted side as well as a few cracks due to splitting on the back surface. To further evaluate the damage extent and failure mechanisms due to the impact event the specimens were subject to further non-destructive inspection (NDI). In the following chapters the results from ultrasound scanning (C-scanning) and micro computed tomography (microCT) scanning will be presented.

2.2.1 Ultrasound Scanning

Ultrasound scanning (C-scanning) is a widely used method for establishing the damage extent (or footprint) of the impact damage. The method allows for visualizing the locations of damage within the structure by sending high frequency sound waves through the specimen and monitoring the reflections that are sent back. The waves rebound when they change from one medium to another (mediums of different densities) similar to light refraction and transmission. When the waves hit voids/air pockets in the specimen the signal is rebounded to due to sudden change in medium. These voids are caused by delamiantions or other type of failure modes in the structure. The intensity of the rebounded signal can be used to identify damaged areas. The time that it takes for the rebounded wave to reach the sensor can also be used to back out the depth at which the signal rebounded. The downside of the method is that it requires a medium between the specimen and the sensor (and signal producer). De-ionized water is commonly used as a medium but ionized water can also be used to produce relatively good quality scans. Due to these limitations the method usually requires a tub of water which the specimen will be set into prior to scanning, which puts size limitations on the method and in-situ inspection becomes difficult. Hand-held ultrasound monitors have been introduced where water is sprayed on the surface prior to scanning being performed. The sensor is carefully moved over the surface of the structure manually. The results from these hand-held ultrasound devices are sufficient for identifying damage in the structure while the high quality of the results seen in the submerged scanning can not be captured.

Recent advances by Pelivanov et al. [86, 87], using a high-frequency fiber-optic laser-ultrasound scanner shows great promise. The method does not require a transfer medium and is therefore highly desirable for in-situ evaluation of damage. The method has been used effectively in accessing thermal induced damage [87] and impact induced damage [86] in composite materials.

Each of the impacted specimens was subject to ultrasound scanning to achieve the extent of damage and its repeatability. The machine used was a Mistras UPK-T36 immersion ultrasound system, and the water used as a transfer medium was not de-ionized. The impacted specimens were scanned from both the impacted and non-impacted sides. The signal intensity results for the scanned specimens (both specimen sides) can be seen in Figure 2.4, the back surfaces images have been mirrored about the specimen layup 90° axis for better comparisons with the surface scans.

The damage trends observed for the different impact energies are very much alike. An astonishing resemblance between the two 7.5 kg impacts can be seen, the back surface damage contours are almost identical. Some scatter can be seen in back surface damage. The 15.1 kg test shows a spear-head like delamination traveling out close to the back side. While a similar trend can be observed in the other tests, in this particular case delamination seems to have grown further than the other three. Internal ply splitting can be seen by the sharp and clear boundaries between delamination shapes. The existence of ply splitting on the back surface can clearly be seen in the scans of the back surface, although the method does not capture the finer details on the surface due to these splits. The scans show signs of either fiber rupture or matrix failure, a straight crack along the 90° direction can be seen in the 7.5 kg impact scans. This would point to fiber failure in a 0° layer or a ply split in the 90° layer within the laminate (this should become more clearer in the microCT scanning in chapter 2.2.2).

As previously mentioned the depth of the damage areas can be achieved from the ultrasound scanning data. Figure 2.5 shows the depth contour for the 7.5 kg test 1 as well as showing the through-the-thickness (often called B-scans) results at chosen sections of the laminate. These results clearly show how the damage event closest to the signal source overshadows any damage that could be underneath.

The damage footprint, when estimated as an ellipse, was measured for the impacts.

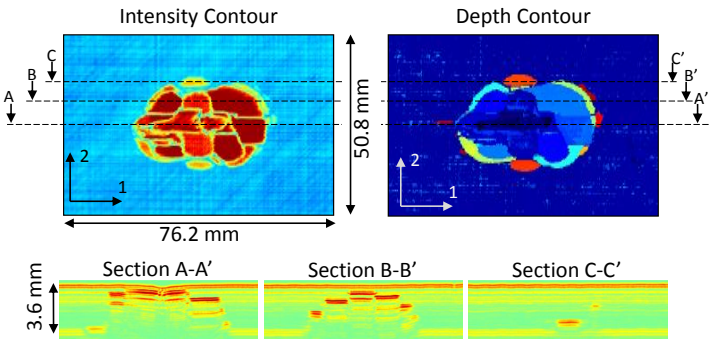

Figure 2.5: Ultrasound result for 7.5 kg impact test 2 showing intensity and depth contours as well as through-the-thickness visualization.

The damage area for the 7.5 kg impacts was $(1261 \pm 177) mm^2$, for the 15.1 kg impacts it was $(1300 \pm 68) mm^2$ and for the 26.7 kg it was $(1127 \pm 113) mm^2$, where variability is reported as standard deviation. It can therefore be seen that the damage extent for all tests was within the experimental bounds. The overall average damage footprint was found to be $1234 \pm 152 mm^2$.

The ultrasound C-scanning proved to be highly useful for establishing the extent of damage as well as some of the delamination patterns due to the impact event. The scans also gave insight into ply splitting and possible fiber ruptures. In the next chapter, a specimen will be studied using X-ray microCT to allow visualization of the damage in more detail as well as ply-by-ply through-the-thickness view.

2.2.2 X-ray micro-Computed Tomography

X-ray micro-Computed Tomography (microCT) scanning was carried out to give more insight about the damage extent and failure mechanisms within the impacted laminate. Since the impacted specimens show very similar impact results (as well as repeatability within impact cases) it was decided that only one of the impact coupons would need to be investigated further. The 7.5 kg impact was chosen due to modeling purposes, with the impact duration being the shortest of the three cases it would be the most time-efficient impact experiment to predict. More details can be seen in

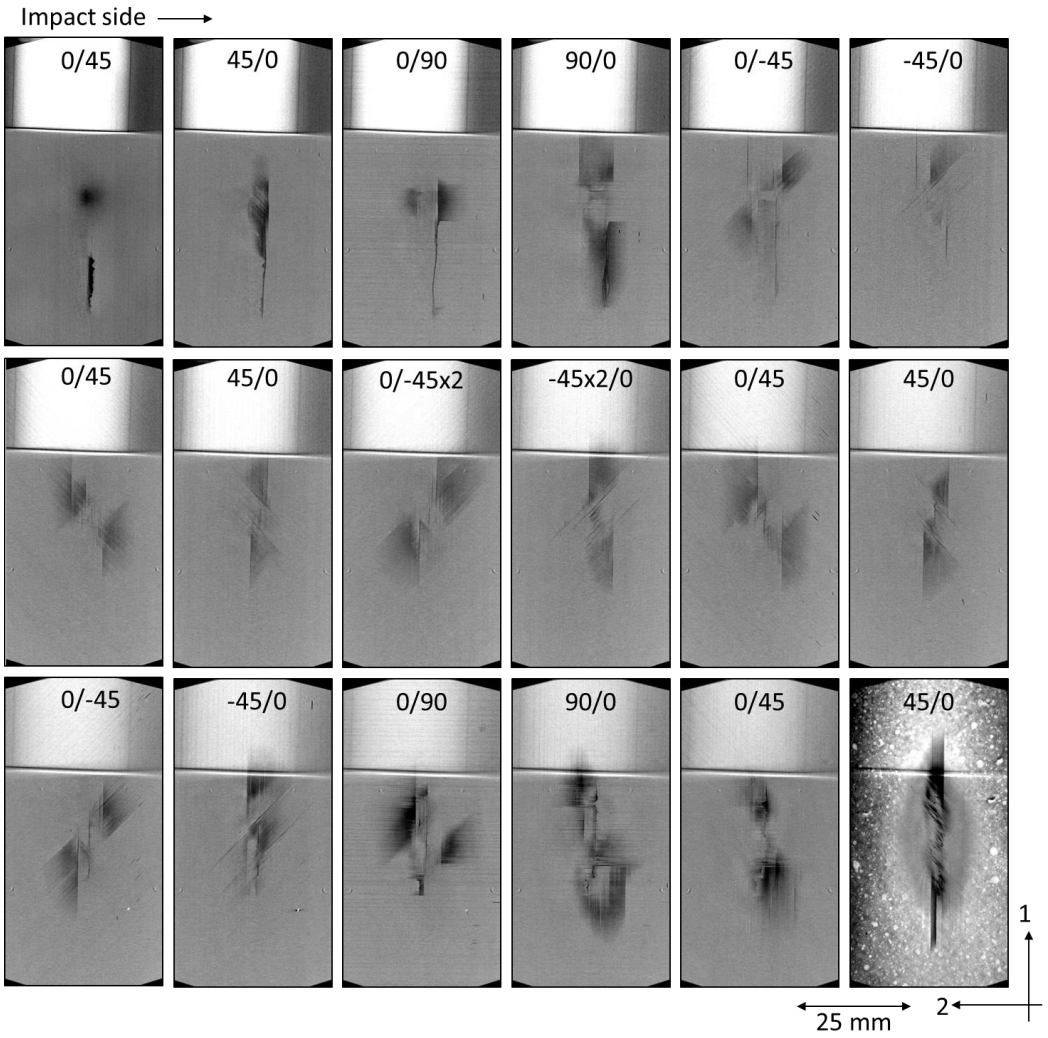

Figure 2.6: CT scan results for the impacted laminate. Each image shows an interface and the adjacent plies. Note that the white area which fades as the back surface is approached is an artifact of the scan, it is a part of the specimen fixture used in the CT machine.

Chapter VI. Test 3 of the 7.5 kg impacted specimens was used for the CT scanning investigation.

The data gathered from CT scanning can be used to generate sectional slices through the specimen (X, Y and Z planes) as well as reconstructing the data into a voxel (3D volume element) representation of the raw CT data. Resolution of 24.3 microns was used for scanning the coupon giving a voxel cube with length, width and height equal to 24.3 microns. The microCT machine used is a NSI X5000 CT system.

Voltage was set to 100kV, current to 250 μA, frame rate was set to 4 4 Hz and the projections were a total of 2250. The 3D representation is a great tool for visualizing the damage mechanisms and extent of damage seen in the laminate, however it is difficult to present such results on paper. Therefore the planar slices will be used for presentation purposes.

Figure 2.6 shows the through-the-thickness slices (1-2 plane) which show the overall damage extent on a ply-by-ply level. However each slice usually shows some effects of the adjacent interface layers or plies due to any permanent deformation (or misalignment of the slice plane which has been minimized in these results) due to the impact. Higher resolution microCT images can be seen in Appendix B Each thickness slice shown in Figure 2.6 shows an interface layer and the adjacent plies, resulting in 18 images (due to stacking of the two midplane layers) which represent the full extent of damage in the impacted laminate. The results show the internal damage through the depth very clearly, compared to the C-scanning method, as expected. Extensive ply splitting and delaminations bounded by the ply splits can be seen through the entire thickness of the laminate. The top most layers (plies 1-3) show a large crack running in the 0° direction causing splits and fiber failure depending on the ply orientation. These cracks are caused by kinking of the 3rd layer (90°) and as a result ply splits occur and fiber ruptures occur in the adjacent plies, depending on orientation. Extensive fiber rupture can also be seen past the midplane, fiber rupture can be seen in the bottom most non-zero layers (plies 15, 17 and 19) due to tensile loading caused by the specimen deflection. The bottom most ply (0° orientation) shows extensive ply splits formed due to tension in the "2" direction, where the splits extend up to about 50 mm. The obscure crack observed in the C-scanning results (see Figure 2.4) is visible in the microCT scans and proved to be a split in layer 17 (90°).

The cross-sectional views for the 2-3 and 1-3 planes can be seen in Figure 2.7 top and bottom, respectively. The image contrast has been sharpened for represen-

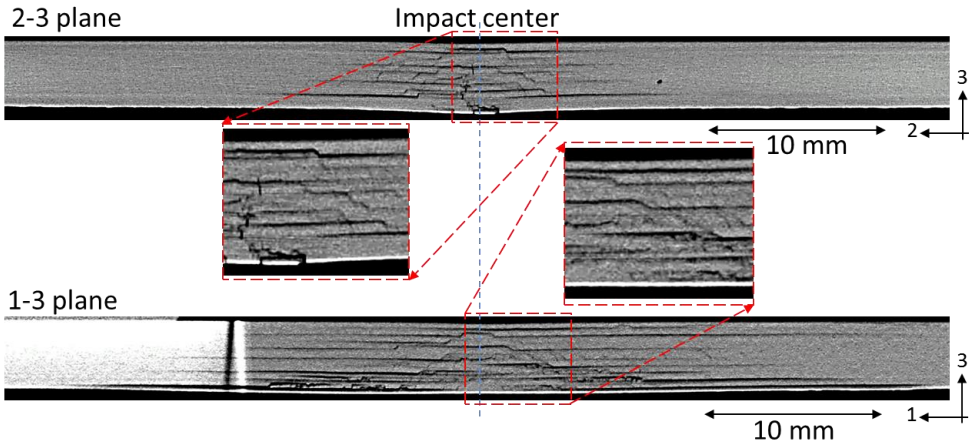

Figure 2.7: CT scan results for the impacted laminate. The two images show the planar sections through the impact center for the 2-3 plane (top) and 1-3 plane (bottom).

tation purposes, making cracks and delaminations more visible to the reader. The sectional views are very useful for getting a clear view of the migration of damage through-the-thickness of the structure. Interaction between in-plane matrix cracks and delaminations can be visualized in good detail. The interaction between matrix (through thickness) shear cracks and delamination was studied in a simplified problem, a sandwich composite beam under three point bend loading at different rates. The study results are shown in Appendix A, which corresponds to a published paper by Thorsson et al. [124]. The cross-sectional views of the impacted specimen also show the typical conical shape of the damage extending through-the-thickness, as has been reported in literature. In the amplified images it can be seen that there is a significant amount of matrix cracking that can not be observed so easily due to CT scanning limitations, in this case it is most likely the dimensions of the coupon as well as the resolution achieved. Further improvements to the CT scanning could be achieved however the results achieved are sufficient for the study presented here. In the following subchapter (Chapter 2.3) details from a microscopic fractography study which shows matrix cracks and delamination interactions in great detail will be presented.

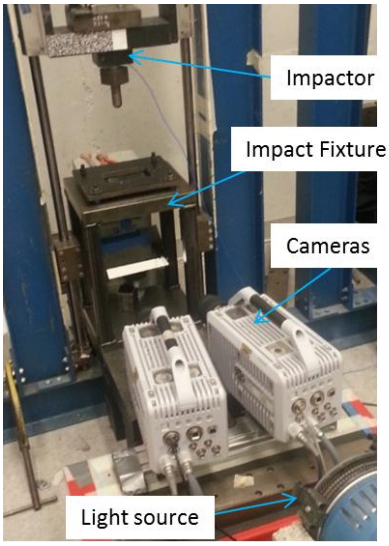

Figure 2.8: Experimental setup for the BVID impact study.

2.3 Barely Visible Impact Damage (BVID) Study

A BVID and CAI study was conducted on PMC laminates of different stacking sequences. A study on TL coupons which contain traditional ply angles (0°, ±45 and 90° angles only) was conducted to establish the BVID limit for the material system. The TL chosen for this study was a 20 ply laminate with stacking sequence [45/90/-45/0/0/-45/0/45/0/45/-45/0/45/0/-45/0/0/-45/90/45], the layup is symmetric except for the midplane layers. A range of impact energies was used while keeping the impact mass and impactor diameter constant. The impact surface was observed while standing 5 feet away from the specimen. The BVID limit was established to be the lowest energy impact that corresponded to noticeable damage being observed. Post impact inspection was performed on the coupon impacted at the BVID limit using C-scanning, microCT scanning as well as microscopic fractography.

Once the BVID limit was identified, impact at the BVID energy was conducted on 10 different NTL specimens containing non-traditional ply angles (any arbitrary ply angle) and limited ply stacking. As previously mentioned, the NTL layups were designed to keep the bending and axial stiffness between different laminates as close as

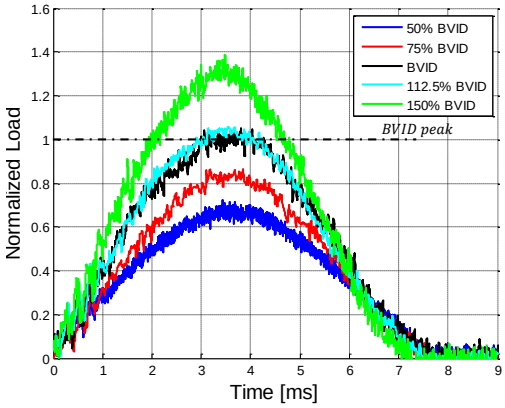

(a) Load vs. time

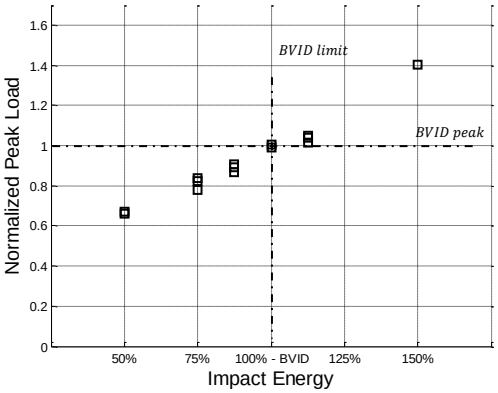

(b) Peak load vs. Impact energy

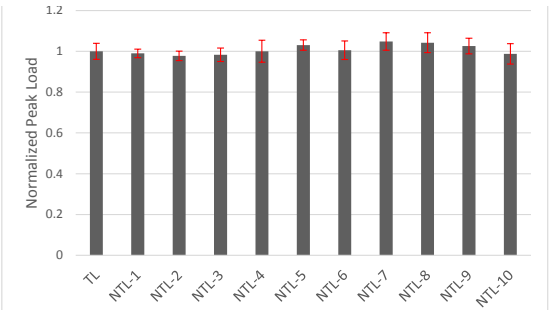

(c) Peak load comparisons for TL and NTL.

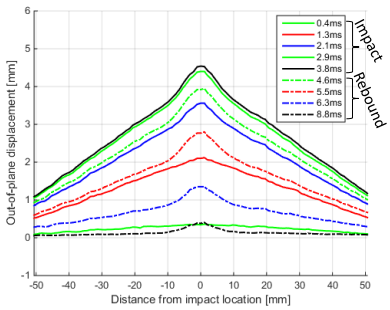

(d) Deflection of a section traveling in the specimen longitudinal direction through the impact center.

Figure 2.9: Impact response results for the BVID impact study on the TL coupons (a) and (b). TL vs. NTL load comparisons (c). Typical back surface deflection for a BVID impact (d).

possible. The surface damage was inspected and recorded for each impact, identifying it as below or above the BVID limit. Compression after impact was conducted on the TL and NTL coupons to establish the post-impact compressive strength and failure mode.

The following chapters will address the BVID impact and CAI study in detail. The results of these impacts and CAI are used for FE model validation.

2.3.1 BVID Impact Experiments

Face-on impact was conducted on an in-house built drop tower equipped with a Kistler piezo-electric load washer for collecting the load-time history. The experimen-

tal setup can be seen in Figure 2.8. Impact testing was done with the same impact fixture as presented in chapter 2.2, the fixture is an adjusted ASTM D7136 fixture (Figure 2.1(b)). Specimen dimensions are the same as in the previous study, 150 mm by 100 mm with the zero orientation traveling in the longitudinal direction of the specimen. Impact mass used was 9.7 kg, a hemispherical impactor with diameter 25.4 mm was used for the TL impact study while an impact weight of 21.6 kg was used for the NTL impacts. The variance in impact mass was due to changes being made to the drop tower between the impact experiments being conducted. The change in impact mass at such low impact velocities does not have an effect on the laminates impact response and damage as was shown in Chapter 2.2. The results presented have been normalized to the peak load of the BVID impact energy, the curves will be related to the BVID impact energy simply denoted by "BVID".

The back surface of the specimen was recorded during impact, as before. Two Photron FASTCAM SA-X high-speed cameras (105 mm SIGMA lenses) recording at 25,000 frames per second were used. The images were post-processed through the DIC program ARAMIS to establish the full field surface strain and displacement fields on the back surface.

Figure 2.9 shows the results gathered from the BVID study of the TL coupons. Figure 2.9(a) shows representative load-time histories for chosen impact energies around the BVID limit and Figure 2.9(b) shows the peak load as a function of impact energy for the tests conducted. The plots show the impact results for the BVID impact limit energy as well as impacts at $50\%, 75\%$ and 150% of the BVID limit. It can be seen that the peak load is increasing linearly with impact energy, for the impact energies studied. The load-time history for the impact at 50% energy of the BVID limit shows no significant damage event while the 75% impact starts showing slight signs of a failure event occurring at around 2.2ms into the impact event. The BVID impact shows the same signs of damage occurring at about 1.9ms into the

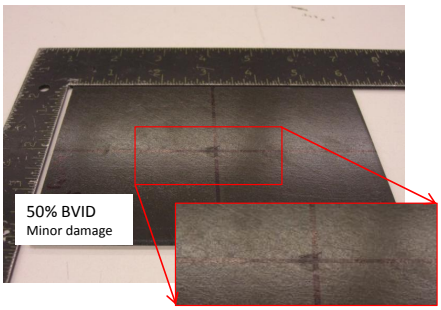

(a) 50% BVID showing no damage.

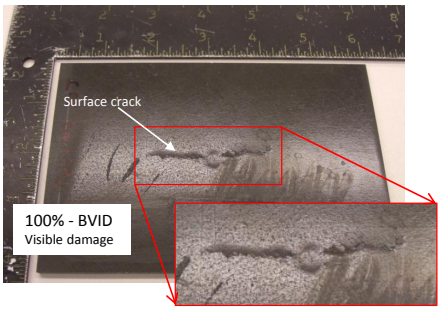

(b) 100% - BVID showing damage.

Figure 2.10: Impact surface damage for the TL BVID study.

impact. The impact conducted at 150% of the BVID limit showed a slight load drop around the same location as the BVID impact showed damage initiation, however the subsequent trend of the response curve did not show any other major failure events.

The typical back surface deflection can be seen in Figure 2.9(d). The plot shows, similar as in the previous chapter, the out-of-plane deflection of a section traveling in the specimen longitudinal direction through the center of the impact. A similar trend as was reported in Figure 2.2 can be seen, a failure event occurs which causes significant localized deflection.

With the BVID limit of the TL coupon, the NTL coupons were impacted at the BVID energy limit, with 3 coupon replicates for each layup being impacted to establish the repeatability of the results. A comparison of peak loads, normalized with respect to the TL BVID peak load, can be seen in Figure 2.9(c). The peak loads for the all laminate stacking sequences are very consistent, this was to be expected due to the design principle of the layups (near consistent bending stiffness). The results also showed great repeatability between coupon replicates. The standard deviation of all of the experiments was 3.2%.

When the impact surface of the laminates was investigated after impact it was seen that large surface cracks had formed on the impacted surface. Figure 2.10 shows the damage on the impacted surface for the 50% and BVID impacts. These cracks

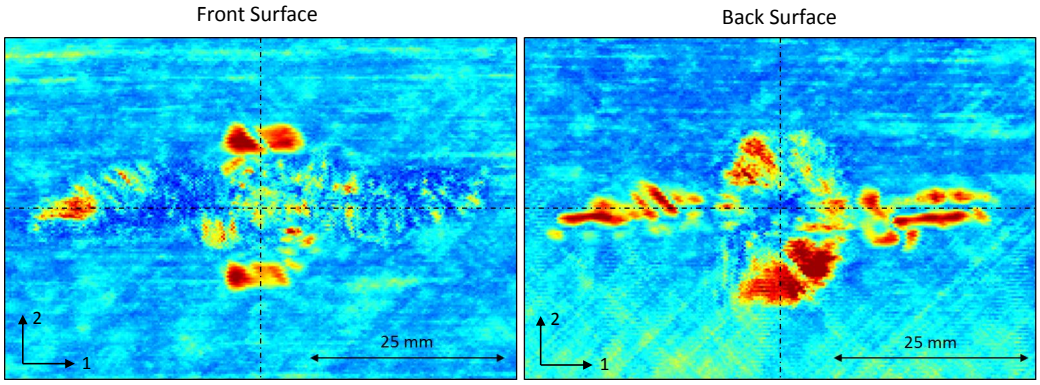

Figure 2.11: Ultrasound scan of a TL coupon impacted at the BVID limit.

form due to kink-bands in the top most layers, resulting in either fiber failure or splitting of the adjacent plies. This was also seen in the CT scans of the IM7/8552 impact study presented in the previous chapter (chapter 2.2). When the specimens are examined for BVID damage (standing 5 feet away) it is observed that the visibility of damage depends highly on the lighting (intensity and direction) of the surface. The lighting sets off a glare on the specimen surface, revealing any cracks due to the light reflecting off the un-even (damaged) surface. The BVID was established without any significant glare coming off the impacted surface.

Ultrasound scanning results for the TL coupon impacted at the BVID limit can be seen in Figure 2.11. The ultrasound results were not as clear as the ones achieved in the previous impact study (Figure 2.4). The ultrasound scan of the front surface showed a lot of influence from the damage in the upper most plies and was therefore not able to achieve an accurate picture of the damage. The back surface scan picks up the surface cracks (now on the far side away from the sensor) as well as capturing some of the delamination trends in the bottom most interfaces. The back surface also gets influenced and disturbed by the ply splitting observed on the back surface.

The X-ray CT results can be seen in Figures 2.12 and 2.13 for the planar and section views, respectively. In Figure 2.12 each interface of the laminate (neglecting interfaces between plies of the same orientation) is shown, the first two plies (45° and

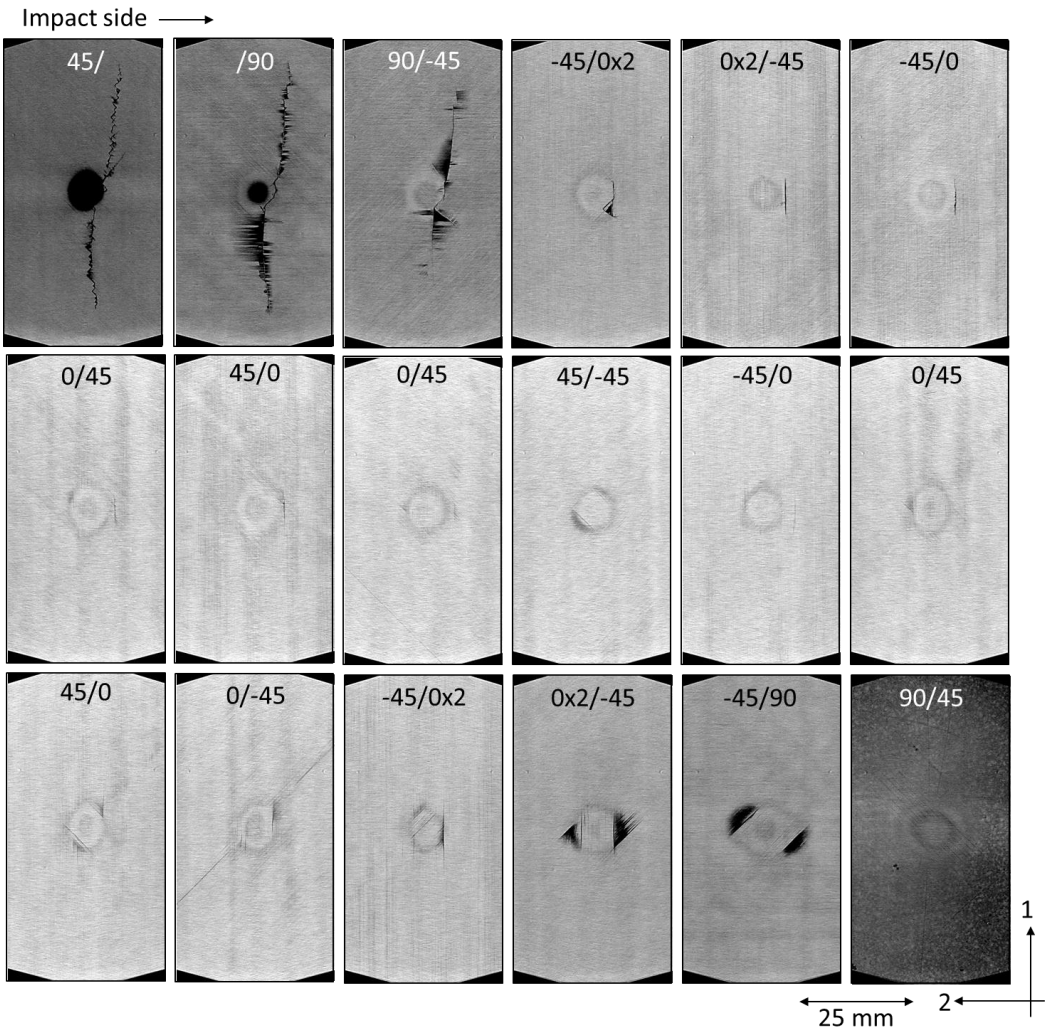

Figure 2.12: CT scan results for the TL impacted coupon at the BVID limit. Each image shows an interface and the adjacent plies, ply 1 (45°) and 2 (90°) are shown independent for better visualization.

90°) are shown independently due to the significance of the damage interaction. When the CT results are examined in detail, the limited results achieved by the ultrasound scanning becomes more clear. There is hardly any delaminations or major ply splitting visible within the center of the laminate. Each layer has dispersed ply splits close to the center however in most layers they are quite few and small. No significant delamination is observed in any of the central layers, apart from a small one being visible at the midplane most likely due to the 90° mismatch angle at that interface.

The top 2 plies show a large crack traveling along the 0° orientation, and the

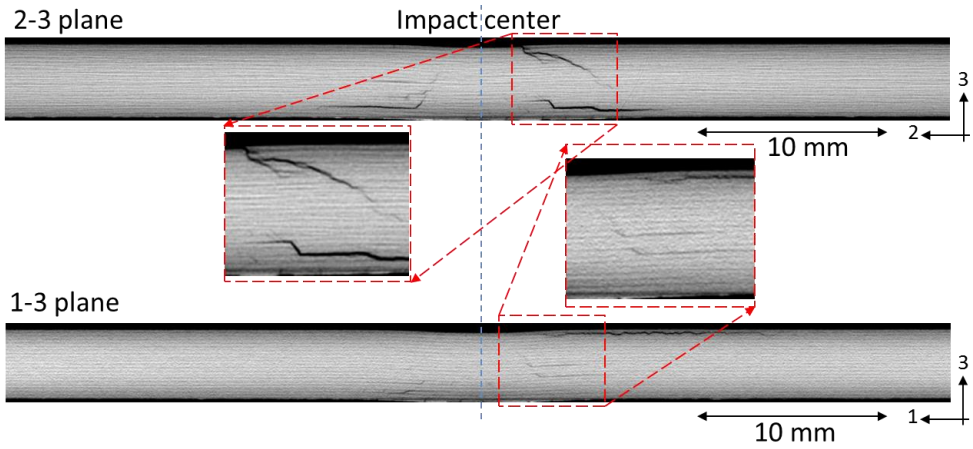

Figure 2.13: CT scan results for the TL impacted laminate at the BVID limit. The two images show the planar sections through the impact center for the 2-3 plane (top) and 1-3 plane (bottom).

crack is driven by fiber kinking in the second ply of the laminate (90° ply) which then initiates a zig-zag failure mode in the top layer (45° ply), similar as the previous study had shown. The zig-zag failure mode occurs when the macro crack in the 45° layer is driven by the fiber failure in the 90° layer. For the crack in the 45° ply to travel along the 90° crack it continuously transitions between ply splitting and fiber failure while following the crack path in the 90° layer below.

Fiber cracks propagating away from the center of impact, perpendicular to the fiber direction, can also be seen in the top 45° and −45° layers. A moderate amount of ply splitting and delaminations can be seen traveling along the large cracks, mainly driven by the fiber kink in the second ply. A crack traveling through multiple layers, initiating at the second layer kink, can be seen as far as layer 8.

Delaminations, interacting with ply splits, can be seen in the bottom most interfaces where the two large ply splits can be seen on each side of the impact center. The back surface shows long splits, similar to the previous impact study. The reader is advised to zoom in on the images on the computer format for better visualization. A large split is observed in the 15th layer (−45° ply), a crack of this size is not seen in any other ply except for the first 2 plies. The length of the crack could be caused

due to the ply below being a stack of two 0° layers. Further investigation would be required.

It is noteworthy to mention that a light circle can be seen traveling down the entire thickness of the laminate. The CT scan images do not show any signs of what the cause of it is however it is most likely caused by slight differences in thickness due to permanent indentation and/or matrix compressive behavior. The circle would therefore mark the "down slope" of the permanent indentation dimple caused by the spherical impactor. However, this effect was not observed in the previous impact study (Figure 2.6) and is therefore still an unknown.

The through-the-thickness planar cuts from the CT scanning can be seen in Figure 2.13. The top image shows the section in the 2-3 plane through the impact location and the bottom image shows the section in the 1-3 plane. The 2-3 plane shows the delaminations in the bottom layers in clear detail. The crack consisting of fiber and matrix failure traveling from the kink resultant crack down through almost half the laminate, can also be seen clearly, as was seen in Figure 2.6. Some delaminations that were not clearly visible from the planar slices can be seen when examined carefully. Through thickness matrix shear cracks seem to be visible through out the whole laminate thickness although they are hard to make out without observing the full resolution of the images. The 1-3 plane shows less damage through the thickness. The bottom layer delaminations are not orientated correctly for this section cut and only the end of it can be observed on one side. Further, small delaminations can be seen through the thickness. The large surface crack from the fiber kink can also be seen traveling along the section.

While the CT scanning proved successful in this study, the damage extent in the specimen was seen to be very minimal, apart from the top and bottom most plies. It was desired to get a more detailed look at the impact damage. A fractography study was conducted, a new specimen was impacted (due to CAI requirements) at

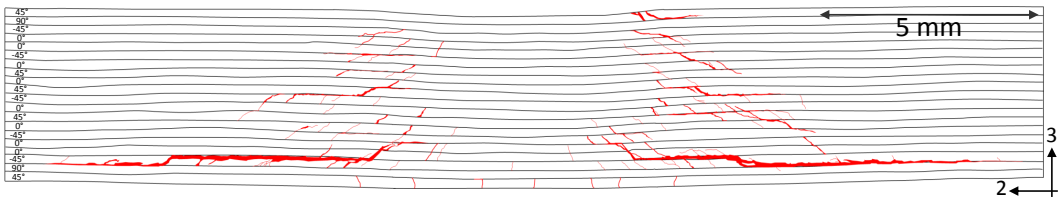

(a) Section through the impact center.

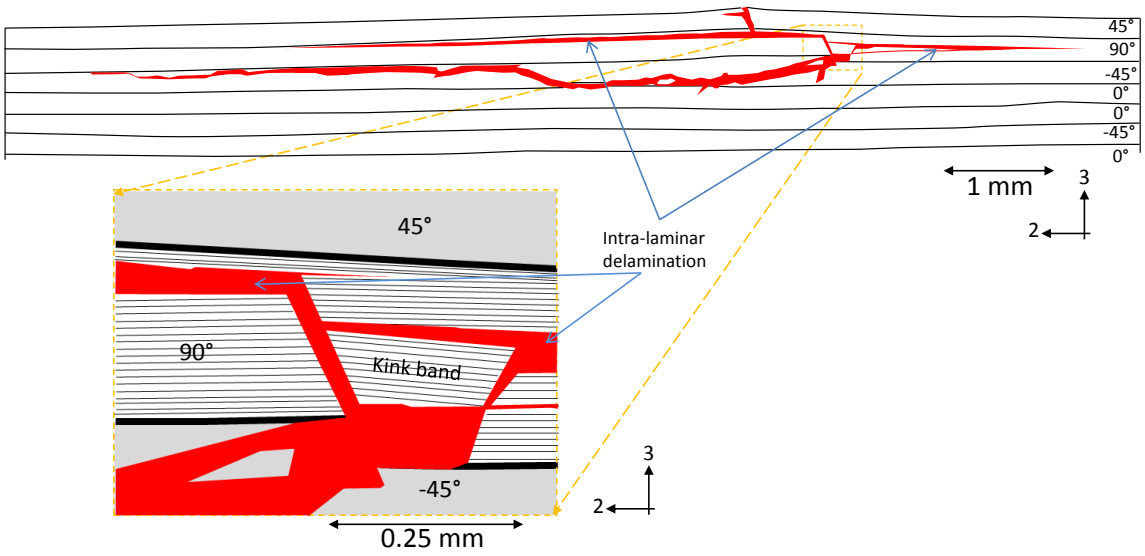

(b) Section through the kink band.

Figure 2.14: Sections showing damage in the 2-3 plane.

the 112.5% BVID impact energy. The specimen was sectioned using a wet saw with a diamond coated blade, making sure to account for the thickness of the saw. Two section cuts were made in the 2-3 plane, the first through the impact center and the second one away from the impact center but through the surface cracks to give a good view of the fiber kinking. The slices were then potted in epoxy and polished thoroughly for preparation for the microscopic study.

The microscopy results can be seen in Figure 2.14. Sketches of the sections were done for presentation purposes. The sketches were made by directly tracing each crack, this was done because the damage extent would be more visible in a presentation format. Figure 2.14(a) shows the 2-3 plane through the impact center. The

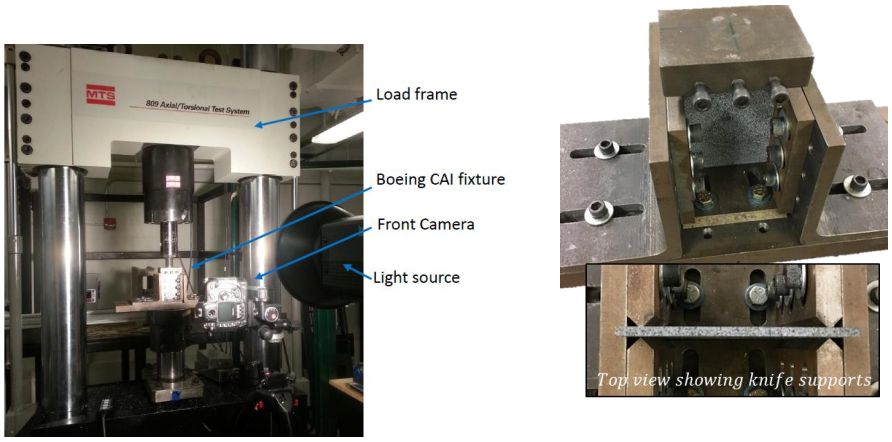

(a) CAI Experimental setup. (b) CAI fixture.

Figure 2.15: Experimental setup and fixture used for the face-on impact CAI.

figure here was assembled from 54 microscopic images to create a complete image of the section. It can be seen that the overall damage extent is repeatable between the two different impact tests (although the higher impact energy shows a larger extent, the shape is conserved) when compared to the CT scanning results in Figure 2.13. The microscopic image however shows the damage in much more detail, with hair fine matrix cracks which are not visible in the CT images clearly seen in the microscopic images. From the microscopic image it is clear that matrix cracks and delaminations exist through out the entire thickness of the impacted coupon.

The section (2-3 plane) at the kink band can be seen in Figure 2.14(b). The main image shows the overall damage extent due to the fiber kink in the 90° ply, while the smaller images then show the kink band in more detail. The resultant failure modes are quite interesting. On one hand an intra-laminar delamination can be seen in the 90° causing failure in the 45° layer (top) as well as the top part of the now delaminated 90° ply. On the other hand the kink causes a large matrix crack in the $-45°$ layer below which transitions into a delamination traveling away from the kink band origin.

2.3.2 Compression After Impact Experiments

Compression after impact testing was done in accordance to ASTM D7137 standard for measuring compressive strength after face-on impact. The experimental setup can be seen in Figure 2.15(a). Testing was done on an MTS 809 Axial/Torsional load frame with a 444kN load capacity. Loading rate was set at 0.01 mm/s. Two Nikon D5300 digital single lens reflex (SLR) cameras (24.2 mega pixels) equipped with a 105 mm SIGMA lens were used for recording. The cameras recorded the back and front surface of the specimen during loading at a rate of 1Hz. Specimen front surface was sprayed with white and black speckles (back surface was already speckled) to allow for DIC measurements. The full field surface displacement and strain fields during loading were obtained. Displacements over the entire gage length of the specimen was collected from the DIC data by monitoring the change in length between two points on opposite sides of the specimen (top and bottom). This measurement acts as a digital extensometer, with an average gage length of approximately 90mm. These measurements were then used for constructing the load-displacement histories.

The CAI fixture can be seen in Figure 2.15(b). The specimen is supported with sliding blocks on the top and bottom, constraining any rotation of the specimen and assisting with accurately end loading the specimen and minimizing misalignment. The height of the top and bottom blocks is 12.7 mm and they extend the entire width of the specimen. Knife support blocks are used as anti-buckling guides. The knife supports slide into the specimen at each side, the distance from the edge is 6.35 mm. The buckling guides are in place to constrain the specimen from buckling failure, however in some cases (depending on material, layup and so forth) the final failure mode can be caused by buckling. When the specimen has been impacted, the non-symmetric (about the mid-plane) damage such as delamination and/or permanent deformation can cause premature buckling. This failure is not uncommon for CAI specimens, and this will be further discussed later.

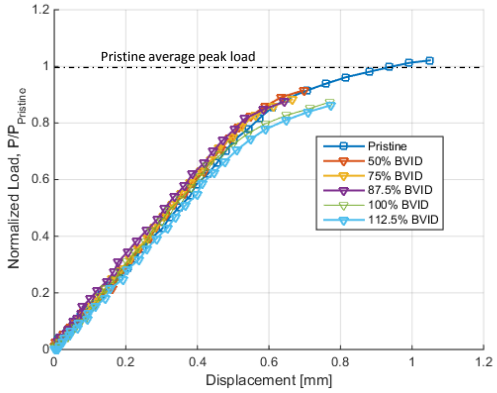

(a) Load vs. displacement curves for the TL CAI coupons.

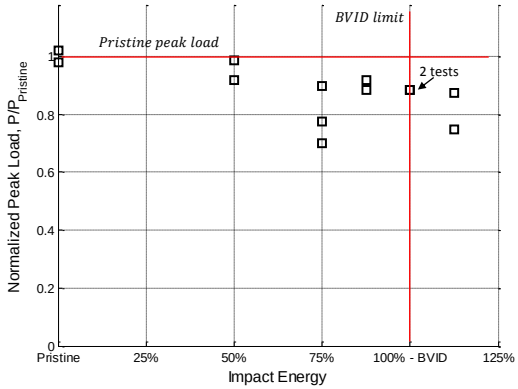

(b) Normalized CAI peak load vs. impact energy for TL coupons.

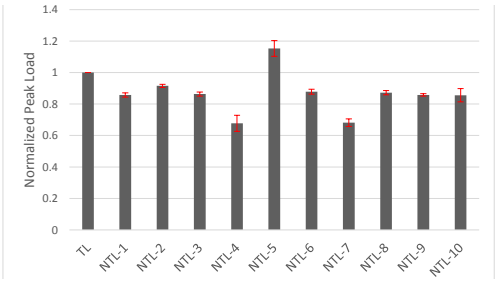

(c) CAI peak load comparisons for TL and NTL. The loads have been normalized w.r.t. the average TL BVID CAI peak load.

Figure 2.16: CAI experimental results for the TL and NTL coupons.

The experimental results for the TL BVID study as well as comparison of compression peak loads for all coupons can be seen in Figure 2.16. Representative load-displacement response curves for the TL specimens can be seen in Figure 2.16(a). Tests that experienced end failure due to mis-alignment were disregarded purposely. Figure 2.16(b) shows the compression peak loads of the TL coupons as a function of impact energy. From the two figures we see that the load-displacement response of the impacted specimens is quite repeatable, the global stiffness is not affected by the impact event. It was also observed that the main specimen failure, even the pristine, was due to buckling. While the specimens impacted below the BVID energy showed a lower peak load than the pristine failure loads, the specimens followed the same trends prior to failure. At impact energies at or above the BVID limit buckling was

seen to initiate earlier. The CAI event can be seen in detail in Figure 2.17(a) where the load-displacement response curve of a BVID impacted specimen is shown along with surface strain contours (surface shown is the backside of the impacted specimen). The strain contour shows the strain in the loading direction, with clear buckling of the specimen resulting in a failure through the middle of the impact location. The buckling direction of the specimen is consistently in the direction of the impact, which is another sign of the buckling being caused by the impact damage. Figure 2.17(b) shows typical post CAI specimen damage/failure.

From the peak load vs. impact energy plot, Figure 2.16(b) it can be seen that an impact at or below the BVID limit can cause a drop in the compressive strength of more than 10%. The impacts at 50% of the BVID impact energy, which had shown very minimal surface damage (Figure 2.10(a)), showed a large variance in peak loads with one test showing a 1.3% drop while the second one had an 8% drop in compressive strength.

The average CAI peak loads for the TL and NTL coupons are compared in Figure 2.16(c). We can see that the experimental results are very repeatable for the CAI tests conducted at the BVID limit alone. The NTL laminates have an overall lower compressive strength after impact than the TL coupon. No significant conclusion can however be drawn from that result, it can not be said that the TL are more resistant to impact. For that to hold true the knockdown factor in compressive strength would need to be compared between the TL and NTL coupons. The NTL impact was conducted for evaluation of the computational models.

2.4 Conclusion

Low velocity face-on impact and CAI of PMC laminates has been investigated in detail. First a thorough impact study was conducted on IM7/8552 laminates of a traditional stacking sequence. Effect of impact velocity and mass on the impact

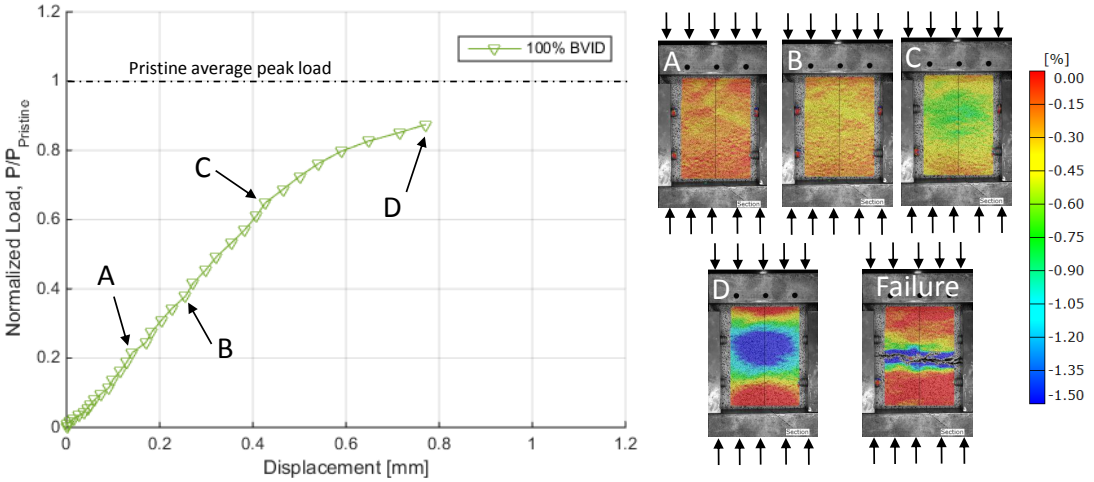

(a) Load displacement response and strain contours during loading.

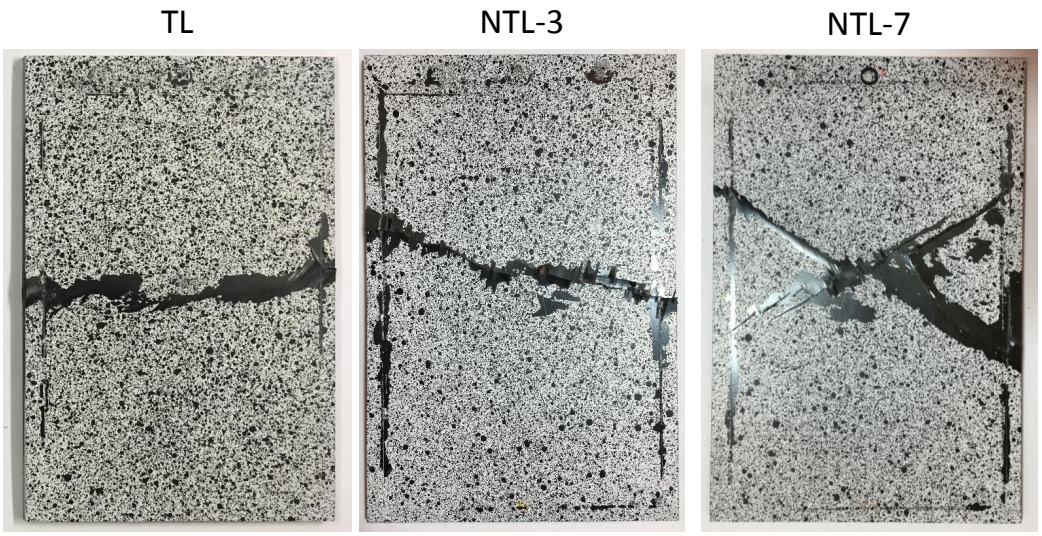

(b) Typical CAI failure modes.

Figure 2.17: CAI event shown in detail (a) and typical failure modes shown in (b).

response was studied by impacting the specimens at a fixed energy level of 25J while the impact mass was varied (7.5 kg, 15.1 kg and 26.7 kg) and therefore varying the impact velocity. Experimental results were very repeatable throughout. A major damage event was seen from the load history, this event was also noticed from the DIC data of the back surface deflection. The damage event caused a significant increase in local deformation of the coupon.

A thorough post impact study was conducted to establish the damage extent and failure mechanisms caused by the impact event. Ultrasound scanning and microCT scanning gave detailed insight into the rich impact failure mechanisms. The results showed fiber kinking, fiber tensile rupture as well as a step-wise delamination pattern interacting with in-plane matrix cracking. The impact velocity (and mass) did not prove to have an effect on the impact event at the energy range tested.

In this chapter, a BVID study was conducted on PMC laminates of TL and NTL stacking sequences. The purpose of the investigation was to produce experimental data for FE model validation. Impacts at different energies (fixed mass) was performed on TL coupons to establish the BVID limit. The BVID limit was established by examining the impact damage by 5 feet away, once the damage became barely visible the limit was set. The TL coupon impacted at the BVID limit was subject to ultrasound and microCT scanning to establish the internal damage extent.

The microCT scans showed large fiber kinks in the second layer which spread into further fiber and matrix failure in plies 1 and 3. Next to no delamination was visible in the coupon until the bottom layers, where limited delamination and ply splits were visible. In order to get a more accurate measure of the through-the-thickness damage extent, non-affected by the resolution of the microCT, a fractography study was conducted. The microscopic fractography study showed very fine matrix cracking and minor delaminations that the microCT was unable to capture (at the scanning resolution). However it was concluded that the microCT gave a reasonable picture of the overall damage extent by capturing the larger and therefore more significant failures. The bottom most layer showed significant ply splitting. With the BVID limit established, impacts on NTL coupons was carried out at the established BVID limit.

CAI study was conducted on the TL and NTL coupons. The effect of different impact energies on the CSAI was investigated for the TL laminates, some variance

was seen in the experimental data. It was established that impacts at or slightly below the BVID limit could cause a 10% or more drop in compressive strength of the coupon. The TL coupons commonly experienced failure due to global buckling, including the pristine coupons. The impact coupons impacted at the BVID limit and above showed a change in pre-peak behavior caused by premature buckling.

The conclusion of this chapter is that the impact damage caused by face-on impact at and below the BVID limit could have a significant effect on the load carrying capability of the structure. The surface damage visibility depends greatly on the lighting condition and inspection angle. While C-scanning methods are sufficient for establishing the overall damage extent, the method is not capable of capturing fiber failure which gets over shadowed by delaminations. The existence of fiber failures will have a significant effect on the load carrying capability of the structure. It is therefore important that the more detailed NDI such as microCT is carried out where it is applicable.

CHAPTER III

Edge-on Impact Experimental Work

3.1 Introduction

In this chapter the experimental results for edge-on impact and CAI are presented. Face-on impact and CAI of fiber reinforced polymer matrix composites has been studied by many, as was reviewed in Chapter I. With computational models being developed and utilized for face-on impact and CAI predictive capabilities it is important to have the necessary experimental data to evaluate these models further for edge-on impact and CAI predictions. BVID due to edge-on impact is usually easier to detect than the face-on impact. However, if a BVID event goes unnoticed the impact damage could grow under repeated load cycles, similar to the face-on impact BVID, and possibly cause a catastrophic failure during service.

While face-on impact on composite laminates has been thoroughly studied [12, 27, 33, 35, 48, 59, 69, 71, 92, 104, 108, 111, 134, 135, 139] and widely accepted industry standards have been established (ASTM D7136 and D7137 etc.), the same cannot be said about edge-on impact. The investigation of edge-on impact has been limited. Edge-on impact is most prone to occur on the edge of a stringer on a stiffened panel. Numerous studies have been conducted on skin (face-on) impacts and compression after impact of skin-stringer (or stiffened) composite panels [6, 36–39, 56, 129, 130]. The most typical impact locations that have been studied are on the skin side at the

middle of the stringer flange and at the flange root connections. Detailed ultrasound and fractography inspection for skin impacts at different locations have been presented by Greenhalg et al. [37].

Edge-on impact on a skin-stringer panel and compression after impact was studied by Li and Chen [68]. Two different types of stiffener geometries were studied, T shaped and I shaped stiffener webs. The compressive strength after impact was reported to be sensitive to the impact damaged stiffeners.

The impact damage due to near-edge and edge-on impact on glass fiber reinforced epoxy laminates using a spherical indenter was investigated and found to show a significant amount of damage [72]. The effect of BVID edge-on impact on a composite laminate stringer using a spherical indenter as well as the compressive strength after impact was reported by Rhead et al. [99], where a cylindrical indenter was recommended for further research.

Due to the high demand from industry to quantify and accurately predict impact damage and the compressive strength after impact of the structure, which has been shown to be highly sensitive to the impact damage state and shape [84], it is therefore necessary to understand the edge-on impact failure modes correctly, and develop models to assess the structural integrity after edge-on impact.

In this chapter the response of a 20 ply polymer matrix composite (PMC) laminate subjected to low-velocity edge-on impact is studied at impact energies in the BVID regime. Impacts are performed with a cylindrical impactor, and specimens are impacted at two different angles, 0° and 45° with respect to the impacted edge. The laminate investigated has a traditional stacking sequence consisting of 0°, 90° and ±45° ply angles. The layup of the laminate is [45/90/−45/0/0/−45/0/45/0/**45/-45**/0/45/0/−45/0/0/ − 45/90/45], symmetric except for the switch in the mid-plane layers. Post-impact damage inspection was done by visual inspection of the specimen surfaces as well as ultrasound C-scanning being used to acquire the full damage extent of the

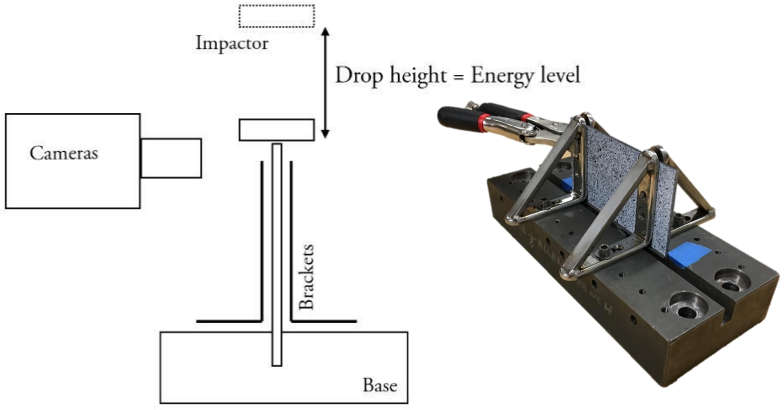

Figure 3.1: 0° Edge-on impact experimental fixture.

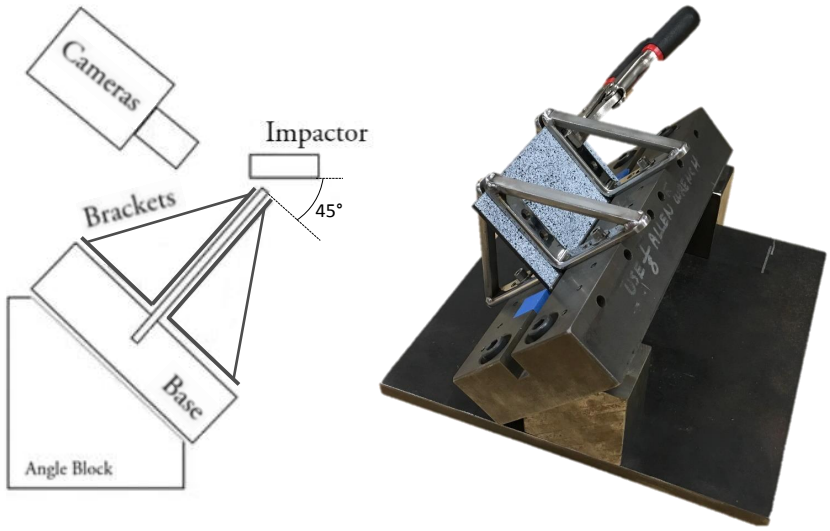

Figure 3.2: 45° Edge-on impact experimental fixture.

impact. Optical microscopy was performed on chosen damage sections for a few of the impact energies. The industry standard for compression after impact (CAI) proved to be insensitive to the impact damage. Therefore a new approach for conducting CAI was introduced using an adjusted version of the Combined Loading Compression (CLC) standard for compressive testing.

3.2 Experimental Procedure

A fixture for coupon level edge-on impact that would resemble a stringer impact was designed, Figure 3.1. Edge-on impacts at 0° and 45° with respect to the edge of the specimen were desired for this study. The fixture was designed to accommodate specimen dimensions in accordance to the industry standard for face-on impact and CAI, ASTM D7136 and D7137, respectfully. Therefore the specimen dimensions were chosen to be 150 mm by 100 mm where the impact would be conducted on the longitudinal edge of the specimen.

The specimen is inserted into a channel, a steel bar is inserted and tightened to the specimen to produce a uniform clamped boundary condition. Depth of the channel is 19mm and extends the entire length of the specimen. Brackets are used to suppress out-of-plane displacements away from the impacted area. These lateral supports act as a method of resembling the length of the actual stiffener. C-clamps are applied to the top of the brackets to ensure full contact between the brackets and specimen during the impact event. For the 45° edge-on impact the fixture was mounted on 45° angle blocks, Figure 3.2. The fixture was then mounted on to a heavy steel base plate to ensure no unwanted motion would be obtained due to the 45° tilt of the fixture.

Edge-on impact and CAI experiments were carried out on the composite laminates at different impact energies. The composite layup of the specimens is $[45/90/-45/0/0/-45/0/45/0/\mathbf{45/\text{-}45}/0/45/0/-45/0/0/-45/90/45]$, which is symmetric except for the midplane plies. Specimen thickness is 3.84 mm. Impacts were performed on an in-house built drop tower, and the impact load was captured using a Kistler 9104A piezo-electric load washer inserted between the impact sled and the impactor. A cylindrical steel impactor with a diameter of 12.7 mm was used for all impacts, a mass of 25 kg was used to produce low velocity impacts. The impactor was positioned so that the impact location was centered between the lateral support brackets.

For digital image correlation (DIC) purposes the specimen surface was speckled with matte black and white spray paint, giving an even distribution of black and white on the surface. Two Photron SA-X high speed cameras were utilized in a stereo setup to record the speckled surface of the specimen during the impact event. The commercially available DIC software, ARAMIS, was used for camera stereo calibrations and post-processing of the images. The DIC post-processing allows for the full field in-plane strain and displacement fields to be acquired as well as the out-of-plane displacement of the specimen being acquired through the 3D correlation of the stereo setup cameras.

Due to the nature of the impact, the energy required for inducing BVID is significantly lower than the 7.6 J per mm of thickness as recommended by ASTM D7136 for face-on impact. Preliminary studies with a coarser impact energy interval was conducted to acquire the energy range desired for the BVID impact study presented in this chapter. Once a relevant impact energy which induced damage in the BVID range was achieved, multiple impacts in the vicinity of that energy were conducted. Impacts at 0° and 45° angles were carried out at even energy level integrals which will be referred to as E1-E5.

Compression after impact testing was initially performed in accordance to the ASTM D7137 standard for measuring compressive strength after face-on impact. Minor adjustments were made to the experimental procedure, which will be described in chapter 3.4.1. The method proved to be insensitive to the impact damage induced by the edge-on impact and therefore a different approach for CAI was introduced. Adjusted Combined Loading Compression (CLC) experimental procedure was introduced for conducting the edge-on CAI as described further in chapter 3.4.2. The CAI testing was performed on an MTS 809 axial/torsional load frame with a 444.8kN load capacity. Loading rate was chosen to be 0.01 mm/s to satisfy quasi-static loading conditions. Two Nikon D2Xs digital cameras with a 105 mm SIGMA lens recording

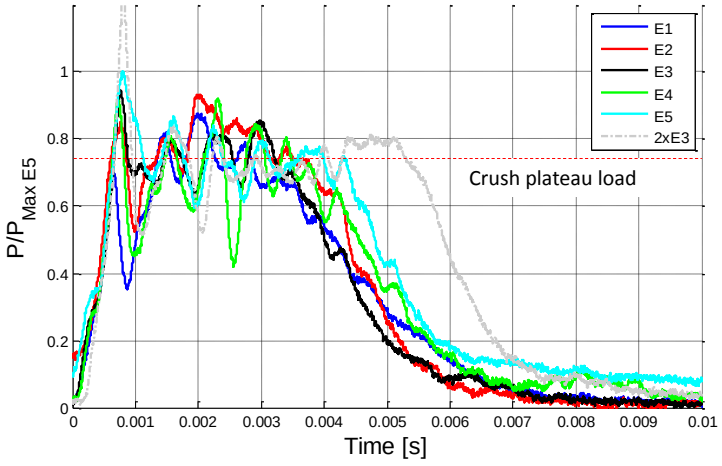

Figure 3.3: 0° Edge-on Impact load-time histories.

at 1Hz were used to capture the front and back surface of the specimen during loading. For the CLC test, the front (impacted) and back (non-impacted) edges of the specimen were viewed due to the fixture limiting the view of the specimen sides. The specimen was prepared accordingly for DIC measurements, similar as for the impact event. Displacements over the length of the gage section were collected from the DIC data, and the average of the front and back displacements was used for constructing the load-displacement curves.

3.3 Impact Results

3.3.1 0° Edge-on Impact

0° Edge-on impact experiments were carried out at crude energy intervals to establish the impact energy range desired for BVID impact studies. It was found that the damage extent due to edge-on impact is easily detectable with the naked eye from a few feet away from the structure/specimen, even at very low energies of impact. This is due to the local nature of the impact, with minimal global elastic deformation. The impact energy is absorbed by localized failure mechanisms. The failure mechanisms observed are of the splaying and fragmentation nature as can often be

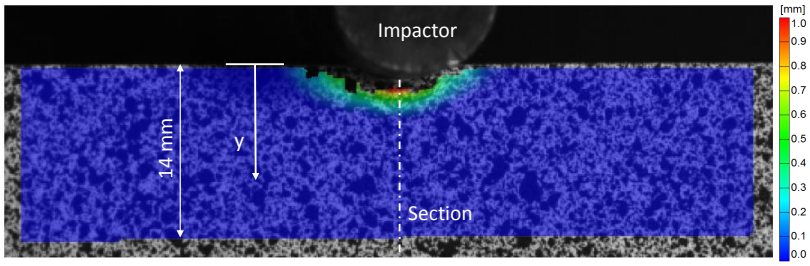

(a) Out-of-plane displacement contour plot

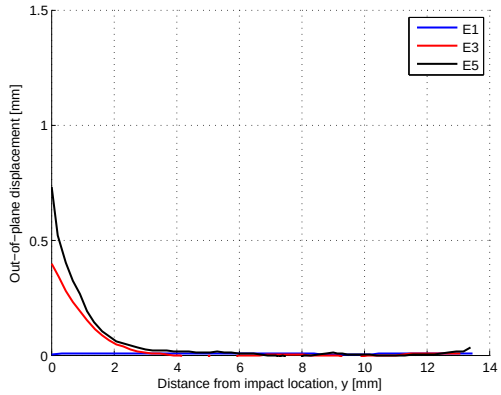

(b) t=0.001s

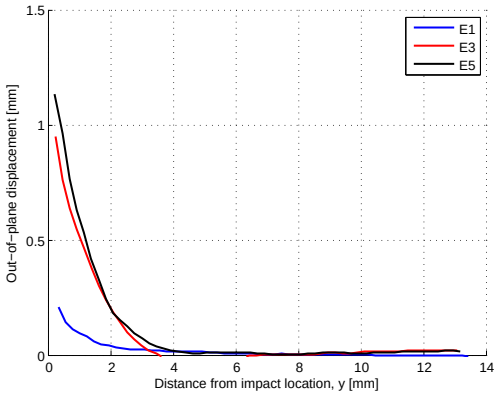

(c) t=0.002s

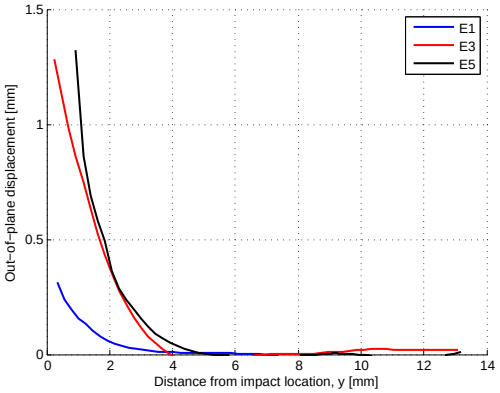

(d) t=0.003s

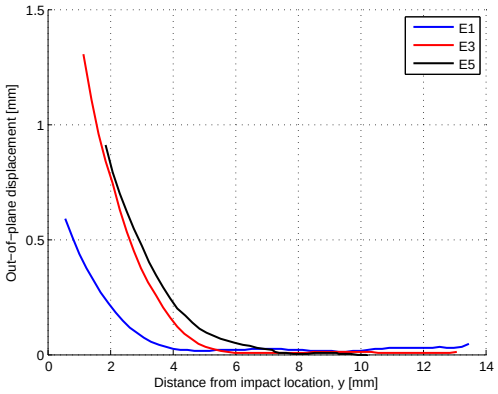

(e) t=0.004s

Figure 3.4: 0° Edge-on impact event. Out-of-plane displacement in detail for energy levels E1, E3 and E5.

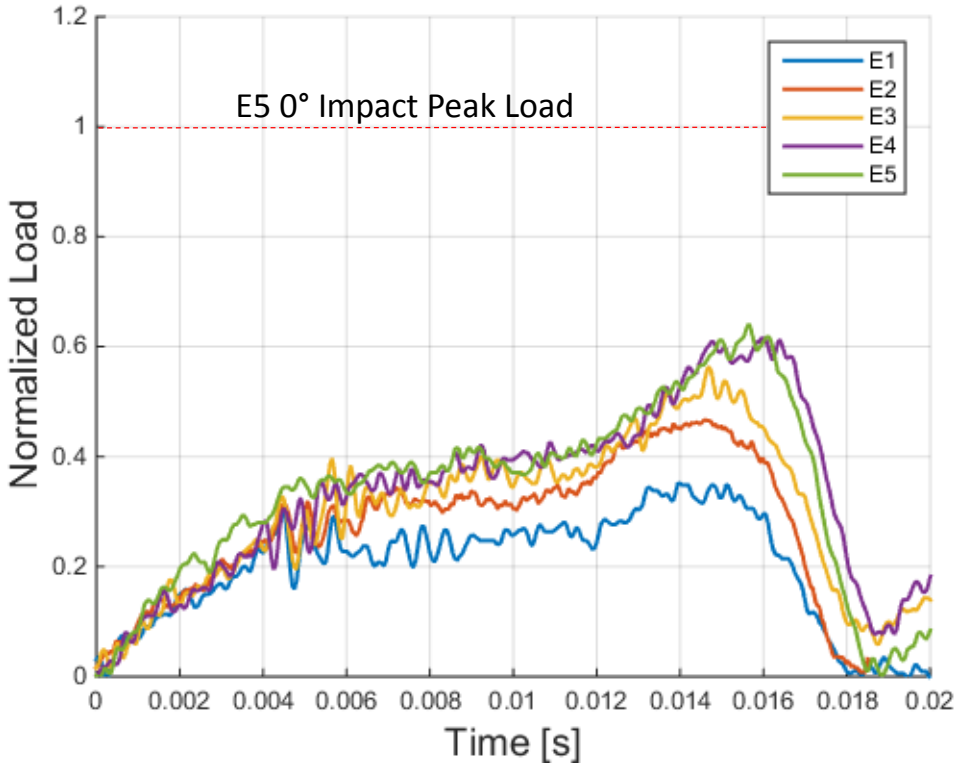

Figure 3.5: 45° edge-on impact load-time histories, normalized with respect to E5 0° peak load.

seen in crushing problems [51]. The impact damage mechanisms will be explored in detail in chapter 3.3.3. The lower range of impact energies will be the main focus of this study.

Representative load-time histories for the 0° edge-on impact for energies E1-E5 can be seen in Figure 3.3. The general trend to be expected is that with increasing impact energy the peak load and impact duration will increase, and this trend is partially correct for the edge-on impacts reported here. It is generally observed that the initial peak load increases with increasing impact energy level. The initial peak load followed by a large load drop is identified as the initiation of significant damage in the composite specimen. The crush plateau "load", identified as the load history past the initial damage event and prior to the impactor rebound, is seen to be fairly constant for the energy levels tested (within experimental bounds). This is similar

to what is observed in crush testing of composite tubes [51]. Overall the load-time histories for the 5 energies tested are very similar, this is due to the energy increment being very small. An impact event with energy twice the amount of E3 has been plotted for reference, showing how the impact plateau load is consistent while the initial peak is increased. While the load-time histories show great resemblance, the specimen deformation response and damage extents show significant differences, as will be discussed in chapter 3.3.3.

The 0° edge-on impact is a highly localized event. By visualizing the displacement and strain contours on the surface of the specimen during impact it can be seen that deformation only occurs in a highly localized area underneath the impactor. Away from the impactor, the specimen shows minimal surface strains or out-of-plane displacements. Figure 3.4 shows the impact event in more detail.

The full-field out-of-plane displacement contour is shown for a general energy level in Figure 3.4(a). The out-of-plane displacement contour is taken at the peak of impact, right before the impactor rebounds (typically around 0.004s in to the impact). The out-of-plane displacements of a section traveling vertically down from the impactor (as shown on the contour) are shown for intervals of 0.001 seconds for energy levels E1, E3 and E5 (Figure 3.4(b)-3.4(e)). The sections furthermore show how localized the impact event is as well as the large difference in out-of-plane deformation between the lower energy levels and the higher ones. It is noteworthy to mention that the curves are cut short due to correlation being lost underneath the impactor. This is due to a combination of optical lighting/viewing difficulties as well as excessive local distortion of the surface.

3.3.2 45° Edge-on Impact

Impacts at 45° were conducted on the adjusted impact fixture as shown in Figure 3.2. The impact energies were kept consistent between the 0° and 45° impacts,

therefore impact energies E1-E5 were studied. Impact damage was originally deemed minimal for all energy levels but further investigation showed that the impact behavior was more related to impact failure mechanisms seen in face-on impact than the 0° edge-on impact. Delaminations and transverse shear matrix failure induced by interlaminar shear during bending, is observed.

The experimental load-time histories for impact energies E1-E5 can be seen in Figure 3.5, where the curves have been normalized with respect to the E5, 0° impact peak load. Similar to before, the impact peak load and duration is seen to increase with increasing impact energy. The difference between the energy levels is more significant than that of the 0° impacts. The 45° impact response is driven by elastic deformation due to bending of the specimen. The damage events are not seen to be as significant as the global response of the structure as the 0° impact case. The impact duration is also three times longer than that of the 0° impacts. The initiation of a significant damage event in the specimen is seen at roughly 0.005s, as the contact edge significantly deforms due to the localized compressive load. The small plateau-like region of the load curve is thought to be due to continuous crushing underneath the impactor. The sudden increase in peak loads seen at roughly 0.012s is thought to be due to arrest of the crushing and initiation of loading of the bottom most layers of the laminate in tension and therefore showing the stiffening in the impact response as the specimen is loaded.

Similar to the previous chapter, the impact event for impact energies E1, E3 and E5 has been shown in more detail in Figure 3.6. The contour plot can be seen in Figure 3.6(a) where a large global deformation of the structure can be seen. The out-of-plane displacement, moving away from the camera in this case, is shown for a section at different time increments throughout the impact event. This can be seen in Figure 3.6(a). Figures 3.6(b)-3.6(e) show the difference in bending for impact energies of E1, E3 and E5. The cameras were positioned closer to the impact event

for energies E1 and E3 and therefore the section lengths are roughly 7 mm in length. This trend can however be seen for the bending vs. impact energy. It can be seen how a significant bending deformation is induced in the specimen causing a large portion of the impact energy to be absorbed by elastic deformation of the specimen.

3.3.3 Damage Extent

Non-destructive inspection (NDI) of the specimens was performed post impact for establishing the impact damage extent. First, the visible damage on the edge of the specimen was inspected. Indentation could easily be seen on all impacted specimens while no visible delaminations were seen for the 45° impacts. A dial indicator with ball diameter 1 mm and a resolution of 0.0254 mm (0.001 inches) was used for indentation depth measurements. The indentation depth was measured as the maximum permanent deformation by indentation parallel to the impact direction. A caliber with resolution 0.01 mm was used for surface delamination measurements. The indentation depths and surface delamination lengths can be seen in Figure 3.7. It can be seen that both the indentation depth and surface delamination lengths follow a linear trend with increasing impact energy. The impacted edges of specimens impacted at E1, E3 and E5 energy levels for the 0° and 45° impacts can be seen in Figure 3.8.

Ultrasonic C-scanning was performed on impact energies E1, E3 and E5 to measure the extent of internal damage as well as the area of damage for the three impact energies for both 0° and 45° impacts. The ultrasound C-scanning results did not prove to be as good as previously achieved for face-on impact results [126]. The impact damage area is small and has high out-of-plane permanent deformation. Due to these effects, the ultrasound scanning results only proved useful for measuring the total damage area and no detailed delamination trends were able to be seen. Location (through thickness) and shapes of the delaminations are difficult to capture. The post-processed ultrasound C-scanning results can be seen in Figure 3.9, where it

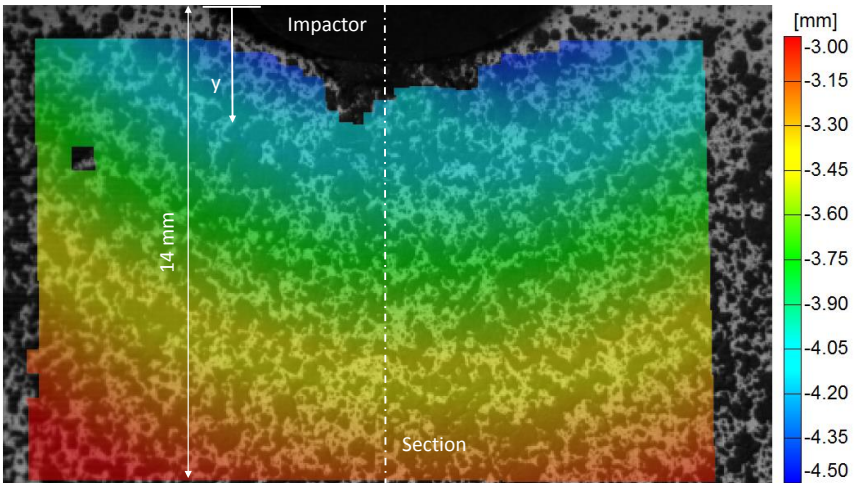

(a) Out-of-plane displacement contour plot

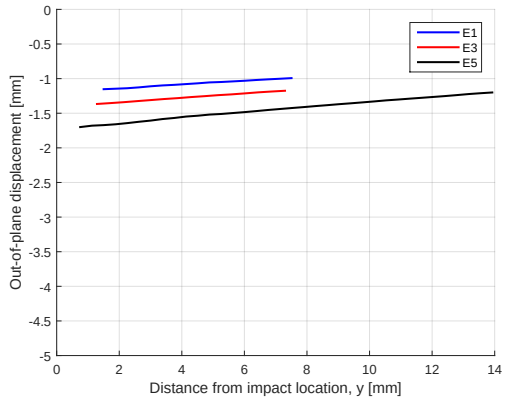

(b) t=0.004s

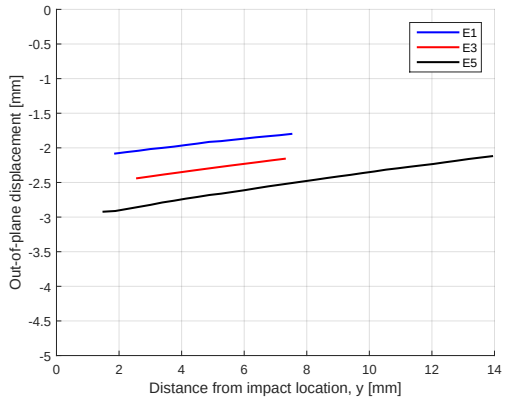

(c) t=0.008s

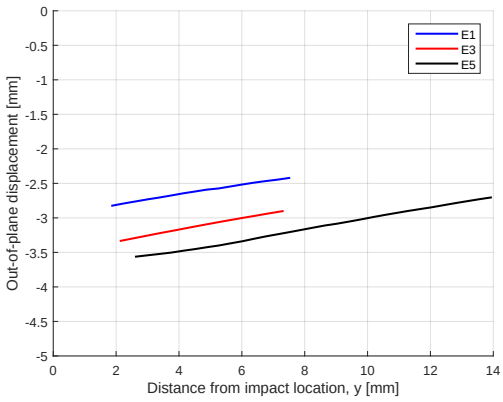

(d) t=0.012s

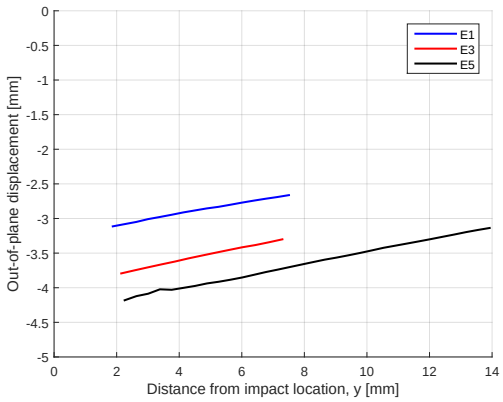

(e) t=0.016s

Figure 3.6: 45° Edge-on impact event out-of-plane displacement in detail for energy levels E1, E3 and E5.

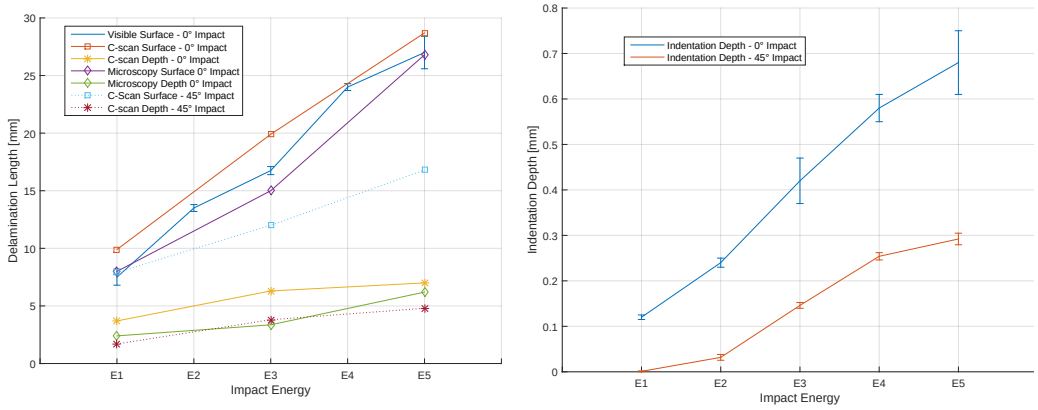

(a) Delamination measurements.

(b) Indentation depths.

Figure 3.7: 0° and 45° Edge-on impact indentation and delamination measurements.

can be seen that the delamination area grows drastically with increasing energy. The surface delaminations (x-direction) can be seen growing with a steady rate while the depth delaminations (y-direction) could be interpreted as approaching an asymptotic value. Further investigation at higher impact energies would need to be conducted to establish that. The ultrasound results showed that the 45° impacts produce a significant amount of delamination which could not be seen on the impacted edge, although lower than the 0° impacts, the damage extent is quite significant. The delamination measurements achieved from C-scanning and compared to surface measurements can be seen in Figure 3.7(a).

Three additional 0° impacts were performed at E1, E3 and E5, and these specimens were not to be used for CAI and instead were used for sectioning of the specimen. This allowed for evaluation of the damage mechanisms observed underneath the impactor. The sectioning would also be used to evaluate the accuracy of the ultrasonic C-scanning method as well as the surface delamination measurements achieved by visual inspection. A wet tile saw with a diamond coated blade was used for sectioning the specimens, and the cut was made vertically down the impact center of the specimen edge. The thickness of the blade (1.7 mm) was accounted for when making the cut. The specimens were then potted, polished and prepared for microscopic study. The

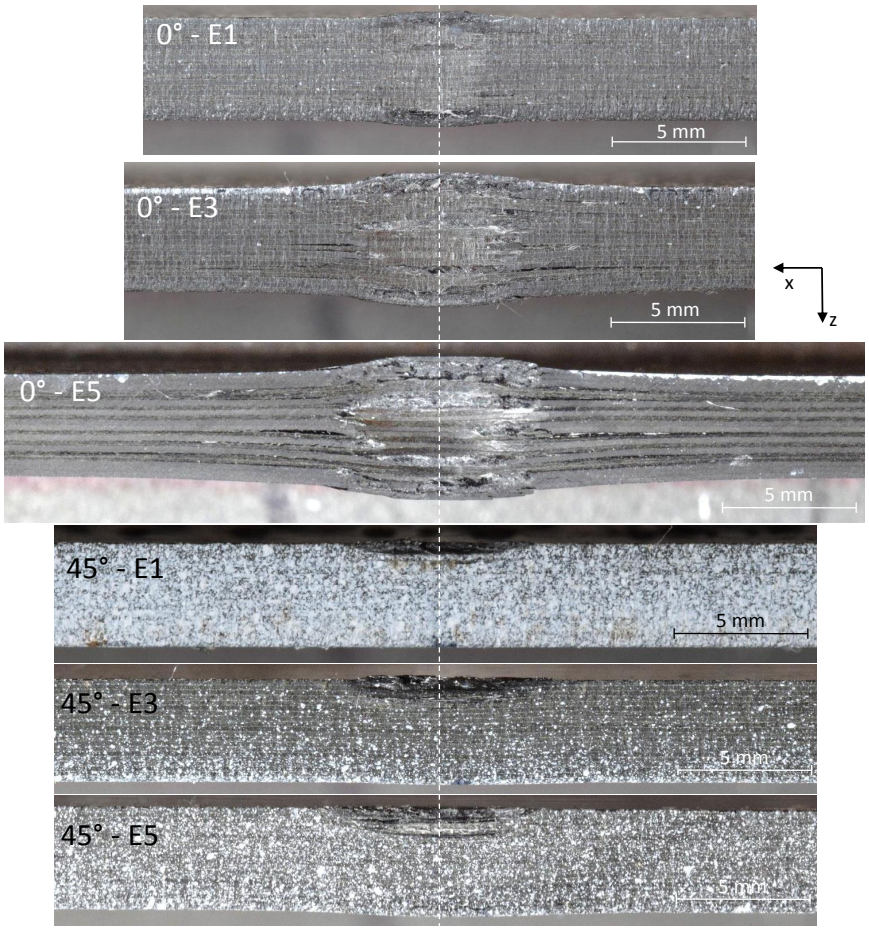

Figure 3.8: Impacted edge for the 0° and 45° impacts for energies E1, E3 and E5.

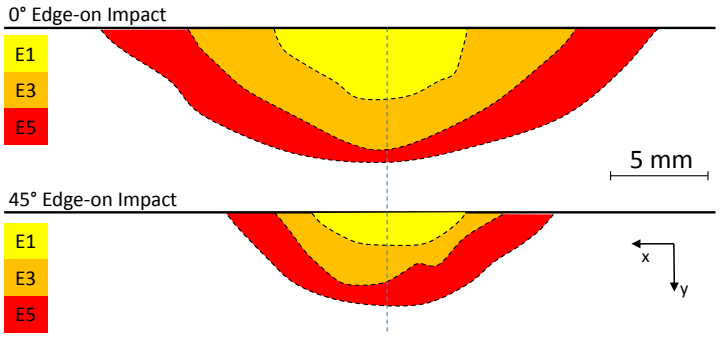

Figure 3.9: Post-processed 0° and 45° edge-on impact ultrasound C-scan results for energies E1, E3 and E5.

microscopy specimens were prepared so that both the horizontal (surface) and vertical delaminations could be investigated.

The microscopic images of the horizontal and vertical surfaces for the three energy levels can be seen in Figure 3.10. The figure shows the damage extent on the horizontal edge (left) and the vertical edge (right). The horizontal surface shows the delaminations which were also observed from visual inspection while the vertical edge shows the damage depth. It can be seen from the sectioning that the damage increases significantly for the increasing impact energy. Impact energy E1 produces minimal damage, and delaminations can be seen in the outer most 0° layers as well as shear matrix cracking being present in the vertical section. The layers of the laminate which lay within the outer most 0° layers show no significant damage.

Impact at E3 energy level shows a significant increase in horizontal damage extent while the vertical damage is fairly similar. A large intra-laminar delamination can be seen within the outer most 0° ply on the top side, while the other side shows intra-laminar matrix damage within the -45° layer. Intra-laminar matrix damage can be seen initiated in the $+45^\circ$ center layer. The most noteworthy failure mode observed here, which was not observed by visual inspection of the impacted (horizontal) edge are the transverse shear cracks showing a shear lag effect in the top most -45° layer. These cracks formed due to the excessive bending of the outer most layers, made possible by the large delamination during the impact event.

The E5 impact energy case shows the further propagation of similar failure modes and damage locations as in the E3 case with addition of extensive damage formed in the center of the laminate. The delaminations in the outermost layers (both intra- and inter-laminar) extend even further while new delaminations are observed at the 0° layers throughout the laminate. Both the horizontal and vertical surfaces views show large matrix cracks traveling through multiple outer layers. These shear cracks are commonly seen in crushing problems where fragmentation is encountered [51].

The outer layers fail due to a combination of tensile and through-the-thickness shear while the inner layers fail due to high compressive stresses. In this case the top most 11 layers followed, in one direction, while the bottom 9 moved together in the opposite direction. This is most likely caused by the slight non-symmetry of the layup due to the +45/-45 center of the laminate. This behavior could also be further induced by structural imperfections and any experimental misalignment.

Maximum delamination measurements from the microscopic images proved to be lower than that of the visual inspection and ultrasound scanning. Surface delaminations measured from the images were multiplied by two, assuming a mirrored damage extent about the impact center. The surface delamination measurements were approximately similar to the other two methods, while the depth delaminations were under predicted quite significantly. The reason for the under predicted length measurements can be justified due to the cutting and polishing of the specimen. The smallest offset of the cut in addition to polishing can have a large effect on the measured delamination lengths.

It has been shown that the impact damage due to 0° and 45° edge-on impact is quite significant for BVID impact events. Visible delaminations on the impacted edge (horizontal) are sufficient for establishing a lower bound measure of the damage extent for the 0° impact case while the 45° impact will require through thickness techniques for identifying the damage extent. It is therefore concluded that the damage extent due to a foreign object impact cannot be estimated by surface inspection alone. It is therefore necessary to utilize the appropriate through-the-thickness inspection techniques to identify the total extent of edge-on impact damage.

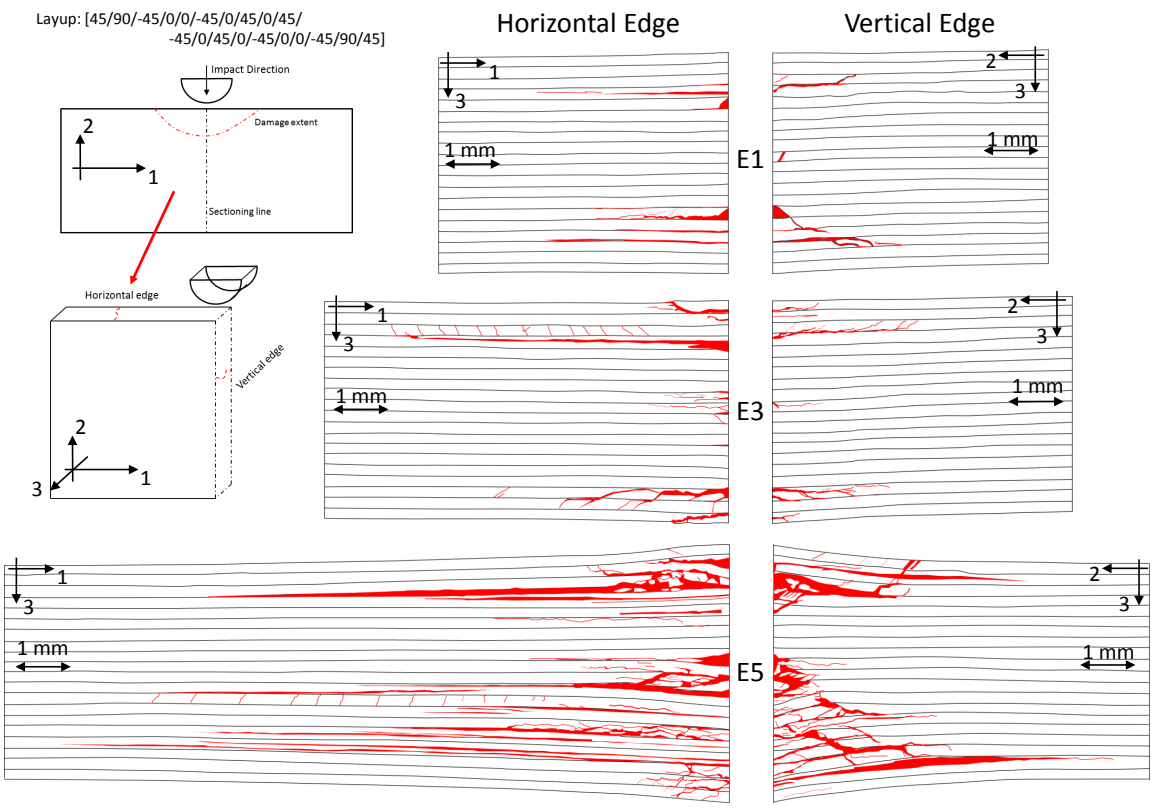

Figure 3.10: Microscopic images of the 0° impacted specimens for energies E1, E3 and E5.

3.4 Compression After Impact

3.4.1 Boeing Compression After Impact

Original design of the edge-on impact fixture was to accommodate specimens in accordance to ASTM D7136 and D7137 standards for face-on and CAI, respectfully. ASTM D7137 standard is also recognized as the Boeing CAI standard. The Boeing CAI fixture was intended for evaluation of the compressive strength after impact (CSAI) of the edge-on impacted specimens. Testing was conducted on the 0° edge-on impacted specimens. Due to the location of the impact damage not being in the center of the laminate (as is the case for face-on impact) the fixture needed slight adjustments to accommodate the edge-on impacted specimens and to allow for unconstrained damage growth.

The experimental setup can be seen in Figure 3.11. The solution to un-constraining the impacted edge was to relax the anti-buckling guides in the area of the damage. From examination of the impact damage produced, the anti-rebound supports were relaxed 25 mm in both directions of impact location, total of 50 mm, as shown in Figure 3.11. This will allow the specimen to locally deform out-of-plane due to the delaminations caused by the impact event. Preliminary testing showed that the edges of the knife supports were digging in to the specimen, therefore the edges were ground down to initiate the knife supports in a smooth manner.

Representative experimental load-displacement plots and a typical specimen failure can be seen in Figure 3.12. It was established that the compressive strength was unaffected by the impact damage. While the load-displacement response had a reasonable variance between tests it was not seen to be an effect of the impact damage. Furthermore, it was seen from the DIC results that for the impact energies studied, the final failure was always governed by global buckling of the specimen followed by structural failure in the post-buckling regime. 3D DIC was utilized for one of the specimens, E1, where the out-of-plane motion of buckling was captured, as is shown in Figure 3.12. It was therefore concluded that the Boeing CAI experimental procedure is not sensitive to the damage induced by a BVID edge-on impact event.

In the next section, will go in to details on the suggested CAI experimental method for edge-on impact and the results achieved will be presented.

3.4.2 Combined Loading Compression After Impact

The ASTM D7137 industrial standard for compression after impact testing proved to be insensitive to the impact damage induced by the edge-on impact event. It is therefore necessary to introduce a different method for measuring the compressive strength after edge-on impact. The Combined Loading Compression (CLC) fixture in accordance to ASTM D6641 standard was the prime candidate. The CLC fixture

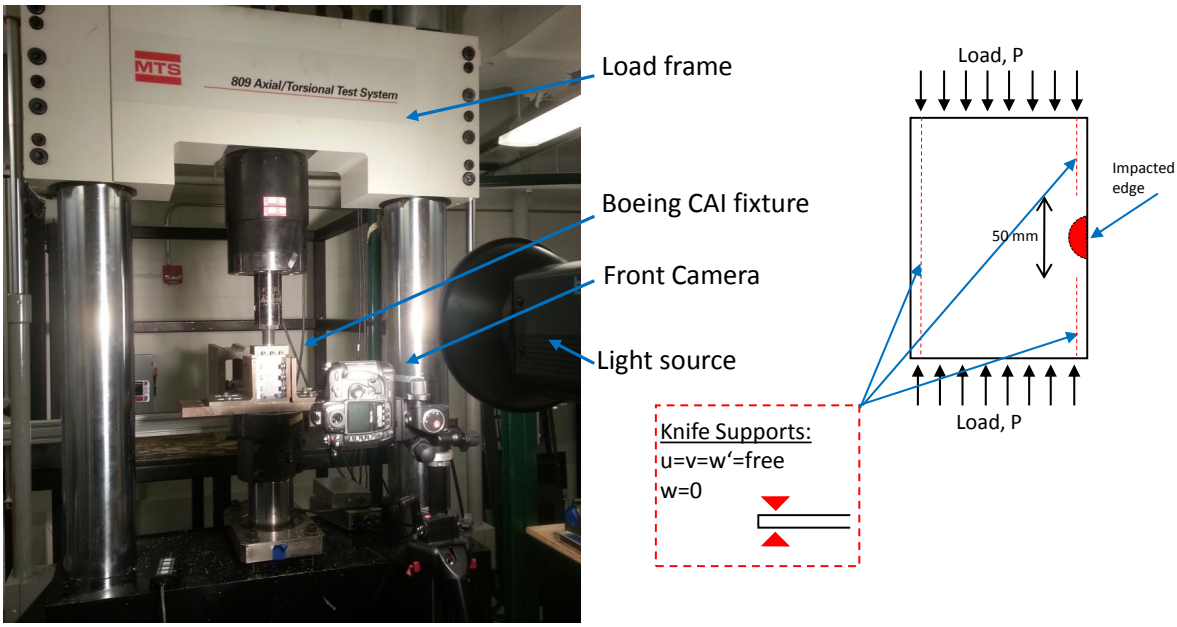

Figure 3.11: Boeing CAI experimental setup (right) and relaxed boundary condition schematic (left).

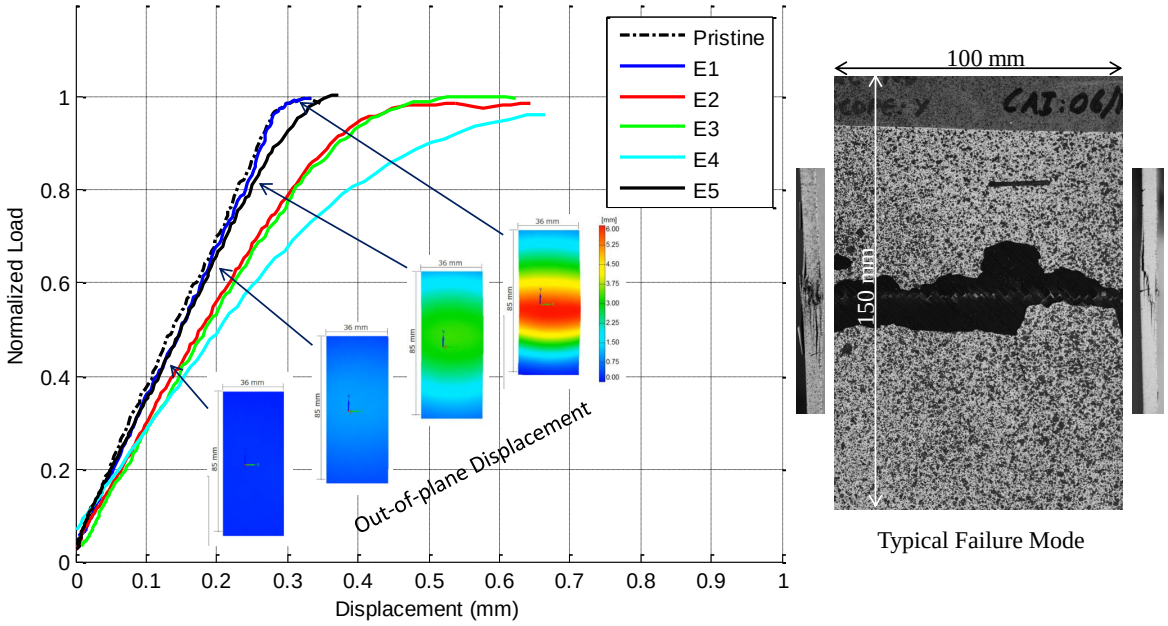

Figure 3.12: Boeing CAI representative load curves and failure mode.

allows for a combination of end-loading and shear loading of the specimen by adjusting the clamping pressure accordingly. End-loading of the specimen was desired for the CAI and therefore the bolts were only hand tightened.

The standard specimen length and gage lengths for CLC testing is 140 mm and 13 mm, respectively, with a width of 12 mm. From the evaluation of damage extent from the 0° and 45° edge-on impact experiments, the damage can be seen exceeding the gage length and width of the standardized CLC specimen dimensions. Adjustments to the CLC experimental setup are therefore needed to keep the impact damage confined within the gage section of the specimen. It was decided that a gage length of 50 mm and a specimen width of 25 mm would be suitable. Maximum delamination length was seen to be 29 mm while the delamination depth was seen to not exceed 7 mm, Figure 3.7(a). Achieving a gage length of 50 mm in the conventional CLC fixture would require specimen length of 178 mm. However, the impact specimens are only 150 mm long and therefore 14 mm by 25 mm shims were machined to match the thickness of the specimens. The shims were placed on the top and bottom of the specimen in the CLC fixture to act as load extensions, where this extension allows for the desired 50 mm gage length to be achieved.

With the new approach for compression after edge-on impact in place and preliminary testing proving successful, the specimens were all sized down to 150 mm by 25 mm strips, and the excess material was used for pristine CLC testing to acquire the baseline. The CLC fixture did not allow for observing the surface of the specimen during loading, due to the guiding columns blocking the view. Instead, the cameras were used to record the edges of the specimen, and the front (impacted) and back (non-impacted). The specimen edges were speckled for DIC post-processing purposes. The experimental setup and a schematic for the loading can be seen in Figure 3.13.

Representative load-displacement curves for the 0° edge-on impacted specimens can be seen in Figure 3.14(a). The loads have been normalized with respect to the pristine (non-impacted) compressive failure load. It can be seen that the CLC experimental method is quite sensitive to the edge-on impact damage. The experimental peak load for the highest 0° impact energy, E5, drops down to roughly 60 percent

of the pristine compressive failure load. The peak load is seen to follow a downward trend with increasing impact energy, Figure 3.15. It can be seen that the CSAI agrees well with the damage measurements, and the 0° impact shows an overall lower CSAI than the 45° impacts, while they seem to be converging to very similar values with increasing impact energies. The lowest impact energy, E1, at a 45° impact angle is not seen to have an effect on the compressive strength of the specimen. This can be related to the findings of no significant damage in the specimen besides the very minimal crushing of the impacted edge, Figure 3.8 and 3.9.

The CLC loading event for the E2, 0° impacted specimen can be seen in detail in Figure 3.14(b). The impacted and non-impacted edges of the specimen are shown at chosen intervals (Figure 3.14(a)) during the loading event as well as the axial strain contour being displayed on the side of each image. It can be seen in stage A that the strain in the specimen is quite uniform. At points B and C, the strain on the non-impacted edge is still uniform while the impacted edge shows strain concentrations. The impacted area is seen bulging out quite significantly prior to failure. At point D, the final failure mode is shown. The reader should be aware that DIC artifacts can be seen in the strain contours close to the edge of the specimen, and these effects should not be mistaken for strain concentrations.

3.5 Conclusion

Experimental results for PMC laminates subject to low-velocity BVID edge-on impact have been presented. Traditional laminate specimens were impacted at 0° and 45° angles with respect to the impacted edge. Results were reported for five different impact energies in the BVID regime. In-depth inspection of the impact damage was conducted by visual inspection of the specimen surfaces as well as ultrasound C-scanning and optical microscopic sectioning studies. The 0° impact event was shown to be a highly localized event while the 45° impact allowed for significant global

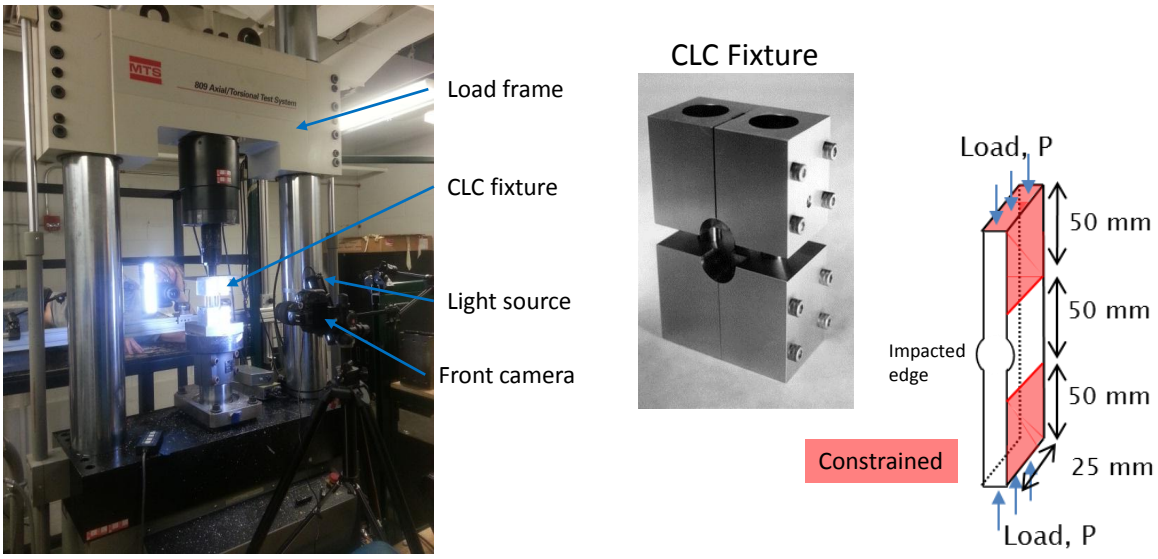

Figure 3.13: CLC experimental setup and schematic of CLC loading.

deformations through bending of the specimen. The impact damage due to 0° impact angle was seen to be more significant than that of the 45° impact angle. In addition to that the 0° impacts showed clear delaminations on the impacted edge of the specimen while the 45° impact delaminations were hidden from the naked eye and only emerging with the use of ultrasound techniques.

CAI testing was conducted using an adjusted version of the industry standard for CSAI testing, the standard was found to be insensitive to the impact damage. A modified CLC experimental method was then introduced for CSAI measurements for edge-on impacted specimens. The modified CLC method proved successful and showed high sensitivity to the impact damage induced by both the 0° and 45° impact events. It is concluded that the use of the CLC fixture would also allow for smaller impact specimen dimensions or for impact to be conducted twice on the same specimen, once on each side opposite to each other. This would however need to be investigated further for the 45° impacts due to the effect a smaller sized specimen would have on the impact response and damage due to the constraining of the bending deformation.

The conclusion of this study is that the BVID due to edge-on impact can cause

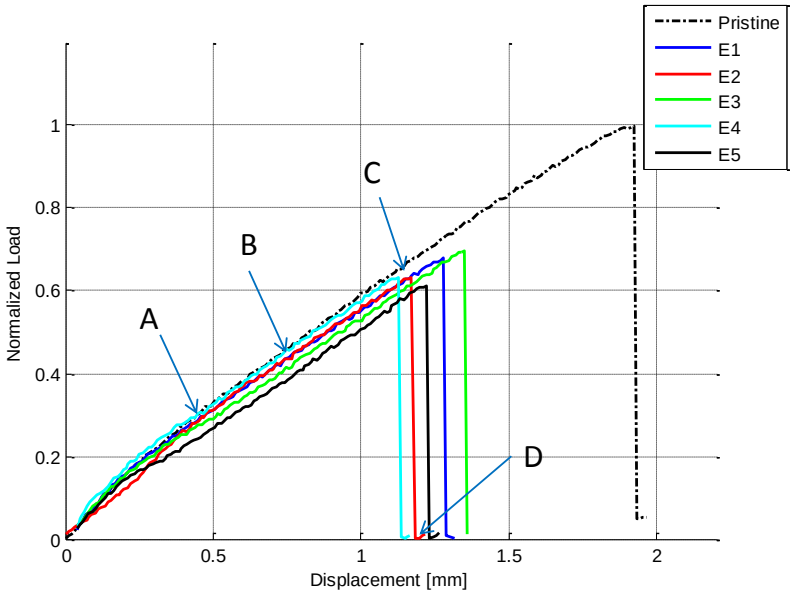

(a) CLC load-displacement curves for 0° edge-on impact.

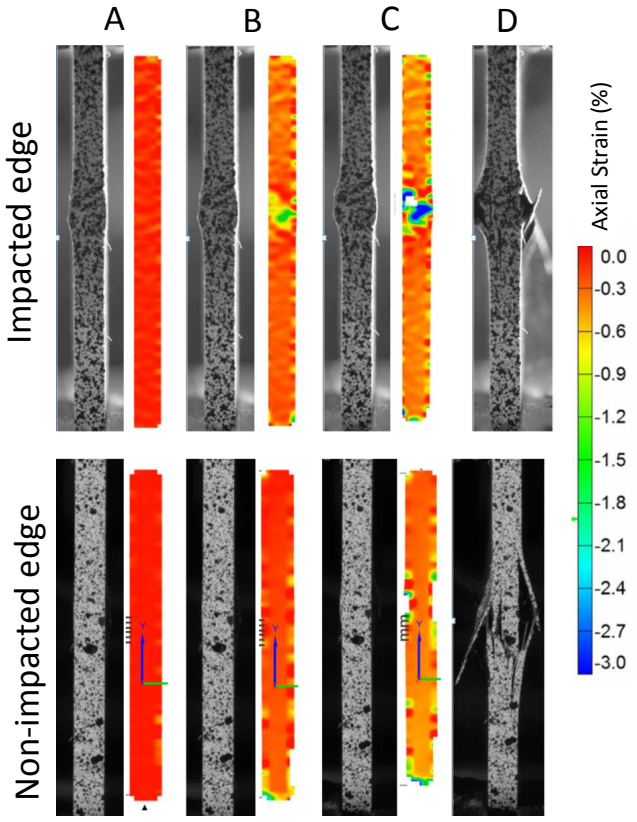

(b) Images and axial strain contour of the impacted and non-impacted edge of E2 specimen during the loading invent.

Figure 3.14: CLC load-displacement curves for 0° edge-on impacted specimens as well as detailed look of the failure mode for E2 specimens.

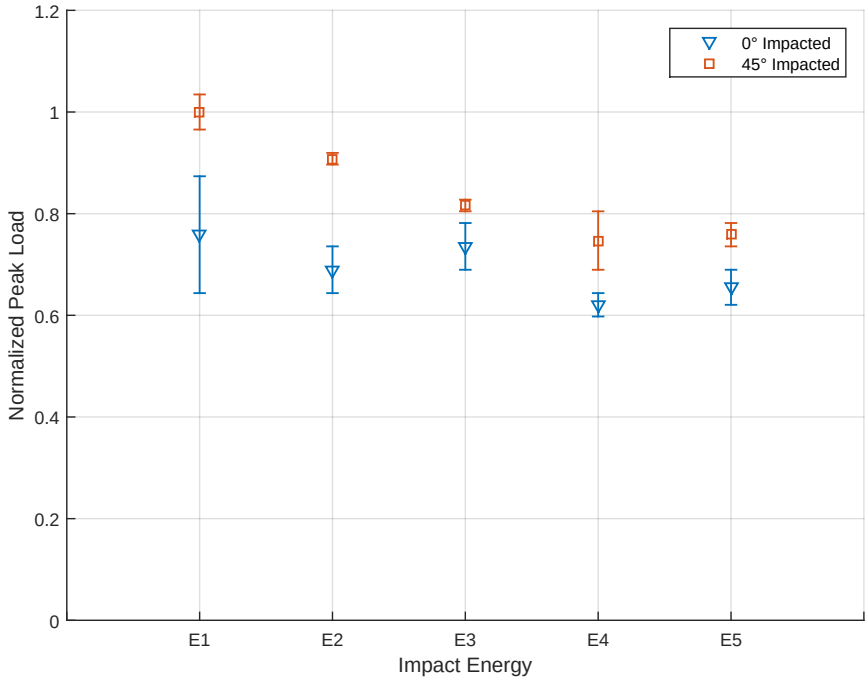

Figure 3.15: CLC experimental peak loads for 0° and 45° impacted specimens.

significant internal damage resulting in a drastic drop in compressive strengths of the structure. The visibility (to the naked eye) of the damage is shown to be dependent on the angle of the impact as well as the elastic deformation of the structure. It is shown that through-the-thickness inspection of the structure is necessary to capture the total extent of damage from edge-on impacts at oblique angles.

CHAPTER IV

Rate Dependence of Mode I and Mode II Interlaminar Fracture Toughness

4.1 Introduction

Composite laminates are increasingly used in applications where performance can be directly related to weight as is the case in the aerospace and automotive sectors. The attractiveness of composites comes from the high strength to weight ratio and the ability to tailor the structure specifically to each application. In many structural applications, composite laminates do not achieve the maximum performance due to delamination seen near highly loaded joints and in fatigue applications. In many high performance applications, highly loaded joints can experience a range of loading rates that vary in frequency and amplitude, and could have a large effect on the performance. To be able to accurately predict performance, such as during impact where the structure will experience different strain rate distributions, it is important to understand the rate-dependence of damage and fracture properties. While the impacts studied in this thesis are low-velocity impacts and the global loading rate of the structure is not considered high-rate. Locally, the material can experience a wide range of strain rates. Face-on impact FE model results, presented in Chapter VI, were studied in detail to investigate the lamina strain rates and interface separation rate.

It was observed that the local strain-rates ranged as high as 100 strain/s underneath the impactor as well as on the back surface. Furthermore, mode II nodal separation was seen to reach rates in the range of 100 mm/s underneath the impactor. For the edge-on impact model results, presented in Chapter VII, the mode I nodal separation rate was found to be in the range of 1300 mm/s and mode II separation rate in the 600 mm/s range. The lamina level strain rates underneath the impactor were seen to be quite high, ranging up to 1400 strain/s for the highest energy model.

Mode I and mode II interlaminar fracture at elevated rates is the focus of this chapter. Standards exist for quasi-static mode I and mode II interlaminar fracture toughness testing. No standards for elevated rate testing has been broadly accepted. A significant amount of research has been done in the past to understand the fracture of cohesively bonded structures and interlaminar fracture of composite laminates at increased rates of loading for mode I fracture [10, 21, 26, 63, 65, 73, 113, 119, 120], and mode II fracture [18, 66, 80, 114, 121, 128].

Daniel et al. [21], reported a decrease in fracture toughness for a graphity/epoxy double cantilever beam (DCB) specimen when loaded in a hydraulic load frame up to a tip opening rate of 8.5 mm/s. Smiley et al. [113], tested graphite/PEEK and graphite/epoxy materials using DCB specimens and loading them at a rate of up to 670 mm/s. Smiley introduced an expression for the crack tip opening rate as a measure for G_{IC} rate dependence. The material systems showed a sudden decrease in fracture toughness at a critical loading rate as well as different fracture behavior being observed as a function of loading rate.

Kusaka et al. [65], reported a stepwise drop in mode I interlaminar fracture toughness when specimens were tested up to rates of 20 m/s by wedge-insert fracture (WIF) using a split Hopkinson pressure bar (SHPB) system. Sun et al. [119, 120], conducted extensive testing at elevated rates using DCB specimens as well as conducting wedge-insert fracture testing at different rates. A transition in behavior (ductile-brittle) was

observed at the higher loading rates. The drawbacks of the wedge-insert approach is the friction between the specimen and the wedge as it is driven between the two arms. An extensive review was recently reported by May [74], on the current advances in measuring the rate-dependent mode I fracture toughness of composite materials. May reported the wedge insert fracture method as being the most promising method (as of yet) for achieving mode I interlaminar fracture at elevated rates. Being able to use DCB specimen configurations is an upside while achieving symmetric loading (pure mode I) are the main attractive aspects of the method.

At the time of this chapter being written, and after completion of the experimental work, as reported in [125]. The author came across the work of Xu and Dillard [133]. Xu and Dillard introduced the modified WIF in a similar manner as described in this chapter. The method was introduced to investigate the rate effects on the impact resistance of electrically conductive adhesives. Testing was done using a drop tower and applied loading rates of up to 1600 mm/s were achieved. The experimental procedure did not involve measurement of the impact loads and instead a displacement based calculation for the fracture energy [10] was used. No fracture energy corrections were implemented for the wedge loading.

The standardized method, End-notched flexure (ENF) for conducting mode II inter-laminar fracture has been shown to be successful at conducting at-rate testing. The experimental setup does not introduce any un-symmetric loading due to at-rate effects, as is seen in the mode I DCB test configuration. Due to this the research conducted on at-rate mode II inter-laminar fracture testing has been limited to the ENF method. While multiple different apparatus has been used, hydraulic load frames [114], drop tower apparatus [18, 121] and Split-Hopkinson pressure bars [66, 128].

In this chapter the modified wedge-insert fracture (MWIF) method for conducting mode I interlaminar testing on composite laminates with standardized specimen geometries is introduced and validated. The drawback of the conventional WIF method,

friction, has been removed in the MWIF by driving a wedge in between rollers attached to the specimen arms. This removes the surface to surface friction between the wedges and the crack surfaces, and allows for accurate measurement of the mode I interlaminar fracture toughness. The MWIF method introduced for mode I fracture (Figure 4.1) produces an additional axial force to the beams. This additional term will cause the two beams to be both loaded in compression as well as producing a moment which results in additional bending strains. A correction factor for the mode I fracture toughness calculation has been introduced into the modified beam theory (MBT) method.

Experimental results on the rate-dependence of interlaminar mode I fracture in polymer matrix composite (PMC) laminates obtained using the wedge insert method are presented. The method is successfully verified against established and accepted ASTM standard test methods at quasi-static rates. The MWIF method is shown to be capable of producing mode I fracture for G_{IC} calculations at quasi-static rates. Testing at elevated rates shows a reduction in fracture toughness for initiation of crack growth and further along in the crack propagation. The fracture behavior is seen changing from ductile-stable behavior to a brittle-unstable/stable behavior. The typical increase in G_{IC} with crack growth due to bridging was seen to decrease drastically with increasing rate.

4.2 Mode I: Modified Wedge Insert Fracture Method

The MWIF configuration was designed for use on a drop tower testing apparatus but can be adjusted for other at-rate loading configurations such as a Split Hopkinson Pressure Bar for instance. A schematic of the MWIF configuration can be seen in Figure 4.1. The method utilizes the same specimen dimension and preparation as the standardized DCB specimens used for mode I interlaminar fracture. Aluminum blocks are attached to the pre-cracked end of the specimen. Holes are machined with high

precision (slip fit tolerance) to fit hardened precision ground steel pins. Lubrication is added to the system and near frictionless roller bearing movement is achieved. Two wedges made from 7075-T6 aluminum are then inserted in between the two rollers, one wedge on each side of the beam. The wedge angle can be varied, and in this study a wedge angle of 90° was chosen so that the axial and vertical loading on the pin is of equal magnitude. By fixing the specimen at the intact end and driving the two wedges down, the rollers are forced to move up the wedge. As a result, the two arms of the DCB are pulled apart producing a mode I fracture.

Due to the nature of the loading, an additional axial force is applied to each roller. This additional axial force needs to be accounted for in the calculations for the mode I interlaminar fracture toughness, G_{IC}. The G_{IC} corrections are derived in the following subsection.

4.2.1 G_{IC} Corrections

The wedge angle has been fixed at 90° and therefore the axial and vertical loading on the pin will be equal in magnitude. Figure 4.1 shows a schematic of the method. The addition of the vertical force will cause a moment to be applied through a moment arm β as well as axially loading the beams. The elastic strain energy caused by

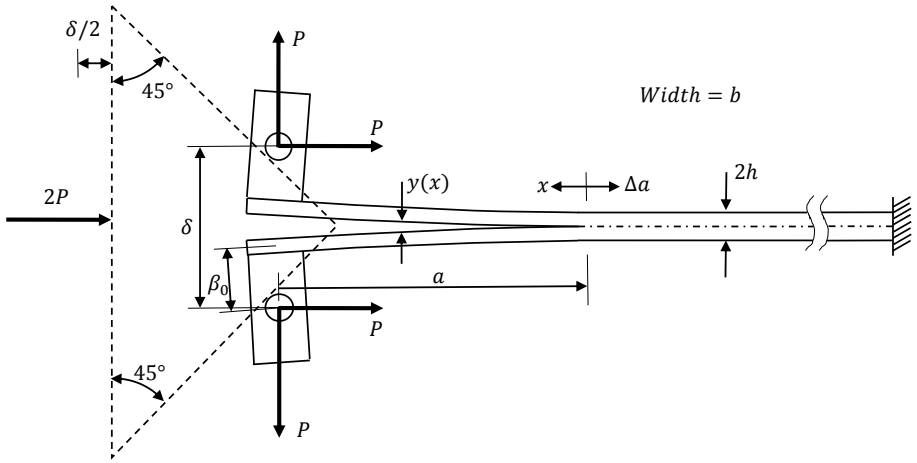

Figure 4.1: MWIF schematic.

the axial load, U_A, and the moment, U_M, in proportion to the elastic strain energy associated with the bending due to the end load, U_B, results in:

$$\frac{U_A}{U_B} = \frac{h^2}{4a^2} \tag{4.1}$$

$$\frac{U_M}{U_B} = \frac{3\beta^2}{a^2} \tag{4.2}$$

Where h is the thickness of the beam and a is the beam length. It can be seen that U_A is negligible when $h \ll a$ and that U_B accounts for $\approx 91\%$ of the total elastic strain energy. U_M accounts for $\approx 9\%$ of the total elastic strain energy at the initial configuration, $a = a_0$ and $\beta = \beta_0$. Contribution from U_M decreases rapidly as the delamination grows. The elastic strain energy caused by the axial load in the beams will therefore be considered insignificant, while the moment contribution is not.

From classical fracture mechanics the condition for crack growth is given by [14]

$$\frac{d}{da}(U_T - F + W) = 0 \tag{4.3}$$

where U_T is the total elastic strain energy, F is the work done by external forces and W is the energy required for crack formation. One can therefore determine the critical strain energy release rate, G_{IC}, as,

$$G_{IC} = \frac{dW}{da} = \frac{1}{b}\frac{d}{da}(F - U_T) \tag{4.4}$$

where b is the width of the specimen. The work done by external forces and elastic strain energy is, respectively,

$$F = P\delta \tag{4.5}$$

$$U = 2\left(\frac{P^2a^3}{6D} + \frac{P^2\beta^2a}{2D}\right) \tag{4.6}$$

Where P is the external load (horizontal and vertical) associated with each beam and δ is the tip opening displacement. Crack length is denoted by a , β is the moment arm and the flexural rigidity of the beams is denoted by D. The second term of the elastic strain energy is the additional term due to the moment caused by the wedge loading. From classical beam theory,

$$\delta = CP \tag{4.7}$$

where C is the compliance. For a DCB, the compliance is,

$$C = \frac{2a^3}{3D} \tag{4.8}$$

Now by combining eq. 4.5 and 4.6 into 4.4 and using the compliance relation in eq. 4.7, an equation for the mode I fracture toughness, G_{IC} is obtained,

$$G_{IC} = \frac{3P\delta}{2ba}\left(1 - \frac{\beta^2}{a^2}\right) \tag{4.9}$$

A secondary correction can be made to account for the change in length of the moment arm with increased bending. This can be done by relating β to the original moment arm length, β_0, and the beam tip rotation, θ_{tip}, where θ_{tip} can be expressed in terms of the tip deflection. The expression for β becomes,

$$\beta = \beta_0 cos(\theta_{tip}) = \beta_0 cos\left(\frac{3\delta}{4a}\right) \tag{4.10}$$

Finally, a simple equation to calculate G_{IC} for the MWIF method is achieved,

$$\boxed{G_{IC} = \frac{3P\delta}{2ba}\left(1 - \frac{\beta_0^2 cos^2\left(\frac{3\delta}{4a}\right)}{a^2}\right)} \tag{4.11}$$

4.2.2 Corrections for Elevated Rates

When elevated loading rates are being considered, there are two factors that need to be looked at, kinetic energy in the system and the definition of local rate (or crack tip rate). The inclusion of kinetic energy in the system will have an effect on G_{IC} calculations and needs to be accounted for. The crack tip opening rate varies from that of the applied loading rate and therefore a single test can give G_{IC} for multiple rates. First, the G_{IC} corrections will be introduced. The equation for the critical strain energy release rate now becomes;

$$G_{IC} = \frac{1}{b}\frac{d}{da}(F - U_T - T) \tag{4.12}$$

where T is the total kinetic energy in the system. The kinetic energy contribution to G_{IC} for a DCB can simply be calculated from the kinetic energy of a cantilever beam with applied tip displacement, the expression is,

$$\frac{dT}{da} = \frac{33\rho bh\dot{\delta}^2}{560} \tag{4.13}$$

where ρ is the density and $\dot{\delta}$ is the loading rate. It can be seen that for a quasi-static loading rate the kinetic energy contribution is negligible. The MWIF expression for G_{IC} at elevated rates can be expressed as

$$\boxed{G_{IC} = \frac{3P\delta}{2ba}\left(1 - \frac{\beta_0^2 cos^2\left(\frac{3\delta}{4a}\right)}{a^2}\right) - \frac{33\rho h\dot{\delta}^2}{560}} \tag{4.14}$$

Secondly, the crack-tip loading rate can be found at each crack length prior to crack propagation. The crack-tip loading rate at a distance x from the crack tip,

backed out using simple beam theory, is defined as

$$\dot{y}(x) = \frac{\dot{\delta}(3ax^2 - x^3)}{2a^3} \tag{4.15}$$

At the crack tip (x=0) the rate prior to crack propagation is zero ($\dot{y}(0) = 0$). The crack-tip loading rate will therefore be considered at a finite distance, ϵ, from the crack tip, following the example of Smiley et al. [113]. ϵ was chosen to be two ply thicknesses. The equation for the crack-tip loading rate becomes (given that $x = \epsilon \ll a$, Figure 4.1)

$$\dot{y}_{ct} = \frac{3\dot{\delta}\epsilon^2}{2a^2} \tag{4.16}$$

4.3 Mode I Fracture Experimental Results

MWIF Mode I interlaminar fracture tests were performed at quasi-static rates and elevated rates. The dimensions of the specimens were kept the same throughout the tests, both for the ASTM standardized DCB and MWIF tests. The specimen dimensions can be seen in Figure 4.2. The specimens used are 32 ply unidirectional laminates, $[0]_{32}$, with a manufactured interlaminar crack in the form of a teflon insert on one side of the specimen. The teflon is inserted at the mid-plane of the laminate. The length of the teflon insert is $76.2mm$ and therefore results in a $\approx 70mm$ initial crack length. The specimens were not pre-cracked further to produce a natural crack

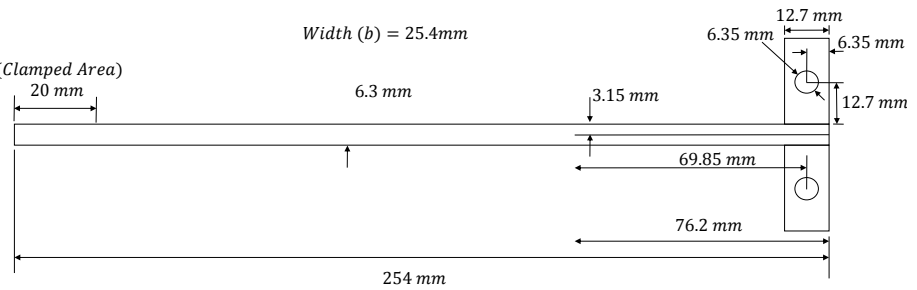

Figure 4.2: Specimen dimensions.

front. This can be done by pre-testing the specimen in fatigue, or by other means, until the crack propagates a small amount.

Quasi-static and intermediate rate testing was performed on a Shore Western hydraulic load frame with a displacement controlled loading rate of 0.01 mm/s and 50-100 mm/s for the quasi-static and intermediate rates, respectively. The quasi-static event was recorded using a Nikon D5300 digital camera with a 105 mm lens. The camera was recording at 0.2Hz. The intermediate rate tests were recorded using a Photron SA-X high-speed camera with a 105 mm lens recording at a rate of 2kHz, depending on loading rate. Resolution of the high-speed images are 1024 pixels by 512 pixels. The tip displacements of the two beams as well as the crack length were tracked digitally using a MATLAB script.

Elevated loading rate testing was conducted on a drop tower. The impactor mass was chosen to be high enough so that the kinetic energy of the impactor would be significantly larger than the energy put into the system as well as the energy dissipated by the mode I fracture. An impactor mass of 25 kg was used, and proved to be sufficient to achieve a smooth loading motion. The elevated loading rates ranged from 300-3600 mm/s. The elevated rates were recorded using the same camera setup as the intermediate rates, recording at a rate of 5-20kHz and a resolution of 1024 pixels by 512 pixels. Tip displacement as well as crack length were tracked in the same manner as for the quasi-static and intermediate rate tests.

G_{IC} calculations for stable crack growth were done using the MWIF modified beam theory (MBT) method described in the previous section. These G_{IC} values are therefore initiation values which are not representative of unstable crack growth. Any experimental variability is reported with the average value and the standard deviation (STD).

4.3.1 Quasi-static Rates: Method Validation

The MWIF method was verified at quasi-static rates by comparing it to ASTM D5528 standard for mode I interlaminar fracture. The specimen dimensions and preparation was kept the same between the two test configurations, Figure 4.2. The DCB method was therefore done using the same aluminum blocks and rods. The only difference is how the tip deflection is transmitted to the specimen. The MWIF method pushes the wedges in between the two rollers, producing an additional force term, while the DCB method pulls the two rods apart. The MWIF experimental fixture used in a hydraulic load frame can be seen in Figure 4.3

Figure 4.4 shows representative curves for the five tests conducted for the two test

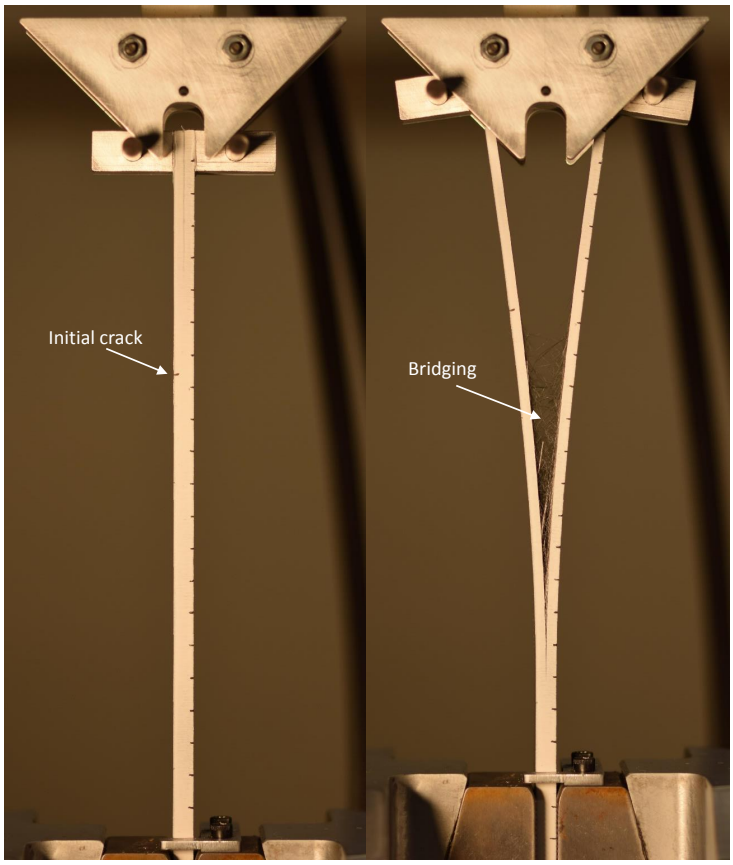

Figure 4.3: MWIF experimental fixture shown in the hydraulic load frame for a quasi-static test.

configurations. The plot shows load vs. tip displacement (δ), and crack length (Δa) vs. tip displacement for the two methods. It can be seen that the two methods agree very well with each other. Most importantly, the post-peak trends and crack growth are in very good agreement which is the early indication that the G_{IC} evaluation

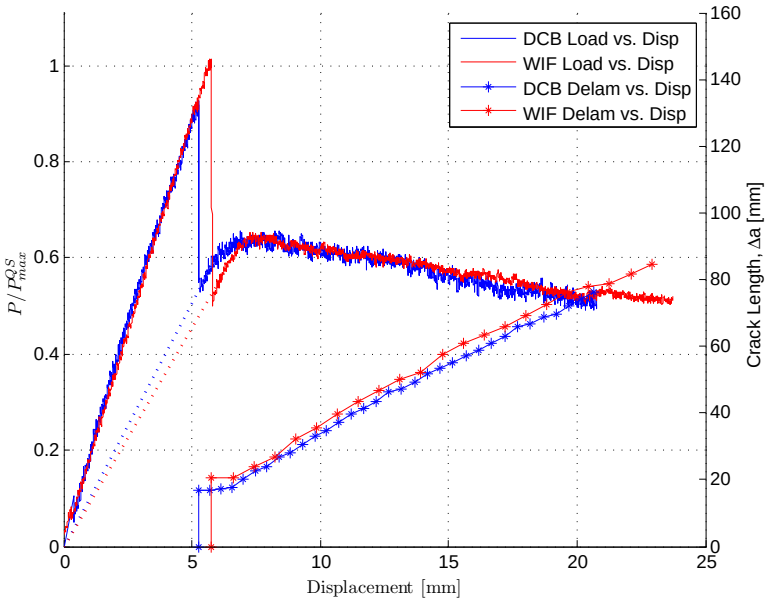

Figure 4.4: Load (solid lines) and crack length (stars) vs. displacement for the quasi-static WIF and DCB tests.

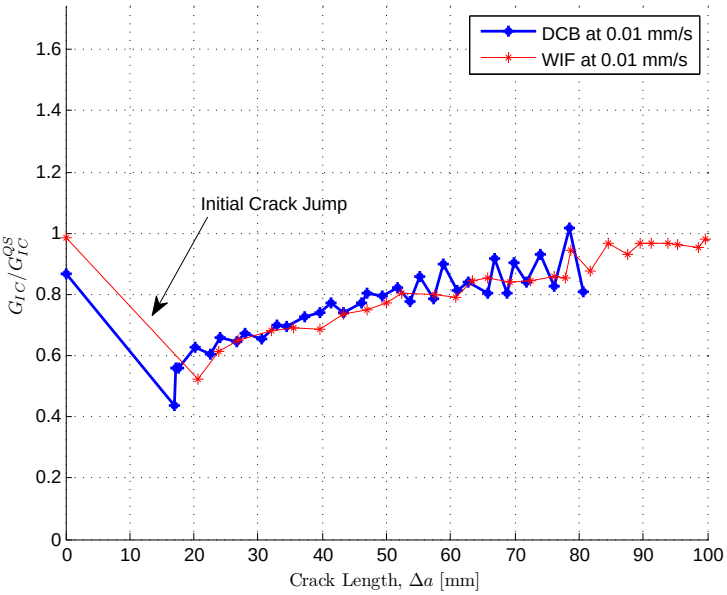

Figure 4.5: G_{IC} vs. crack length for the quasi-static WIF and DCB tests.

would agree as well. The peak load variation (Figure 4.4) is within the experimental bound that was seen for both methods, with the average peak load for the DCB tests having a STD of 7% and the MWIF test average peak load being $98.9\% \pm 0.7\%$ of the DCB average. While the MWIF showed a lower STD. Further testing would be required to confidently say that the method is more repeatable than the standardized DCB test. The average quasi-static MWIF peak load, denoted as P_{max}^{QS}, will be used as a reference from here onwards.

All tests showed an initial unstable (dynamic) crack growth. The average initial crack growth was $17.4 \pm 2.5mm$, including both methods. The difference in the load drops and unloading slopes (dotted lines) can be directly explained as being due to a difference in initial crack lengths. The higher the peak load the more energy will be dissipated during the unstable crack growth causing a longer initial crack growth. This, as a result, causes a larger load drop and a lower unloading slope which can be shown with simple beam theory calculations.

G_{IC} values for the representative quasi-static DCB and MWIF tests based on equation 4.11, where $\beta_0 = 0$ for the DCB test, can be seen in Figure 4.5. Values have been normalized with the average quasi-static value which will be denoted as G_{IC}^{QS} from here on out. This initial G_{IC} calculated for the unstable crack growth differed slightly between the two tests but is within the experimental bound observed, with a STD of 10%. The G_{IC} results for the stable crack growth are in good agreement. G_{IC} was seen increasing slightly with increasing crack growth, and this is a classic bridging behavior (Figure 4.3). It is therefore concluded that the MWIF method is adequate for capturing the mode I fracture desired for G_{IC} measurements.

4.3.2 Intermediate and Elevated Rates

Testing at elevated rates was categorized into two different sets of testing. Intermediate rate (50-100 mm/s) which was conducted on a hydraulic load frame and

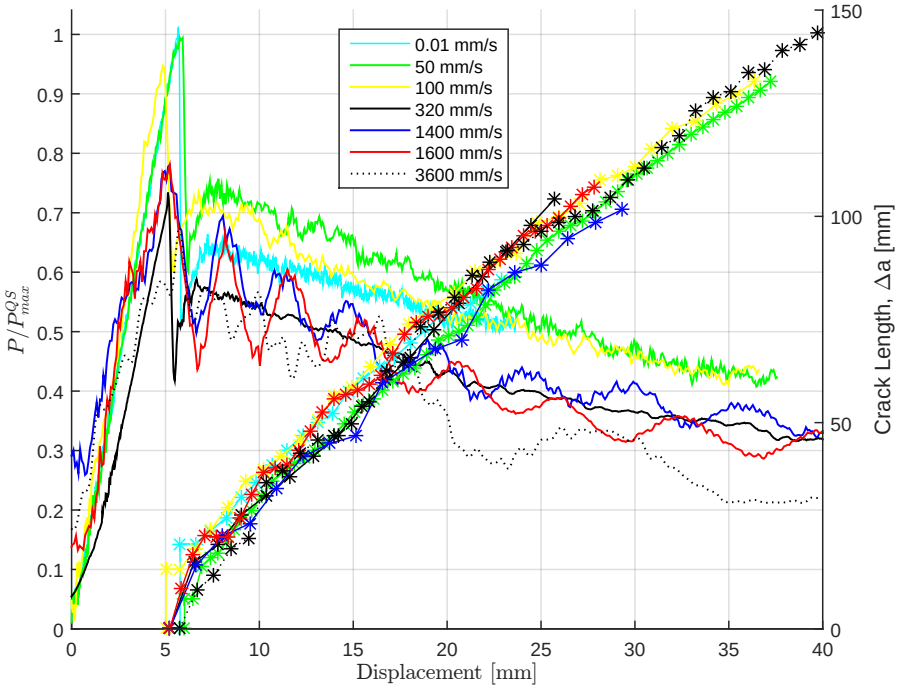

Figure 4.6: Load (solid lines) and crack length (stars) vs. displacement for all rates.

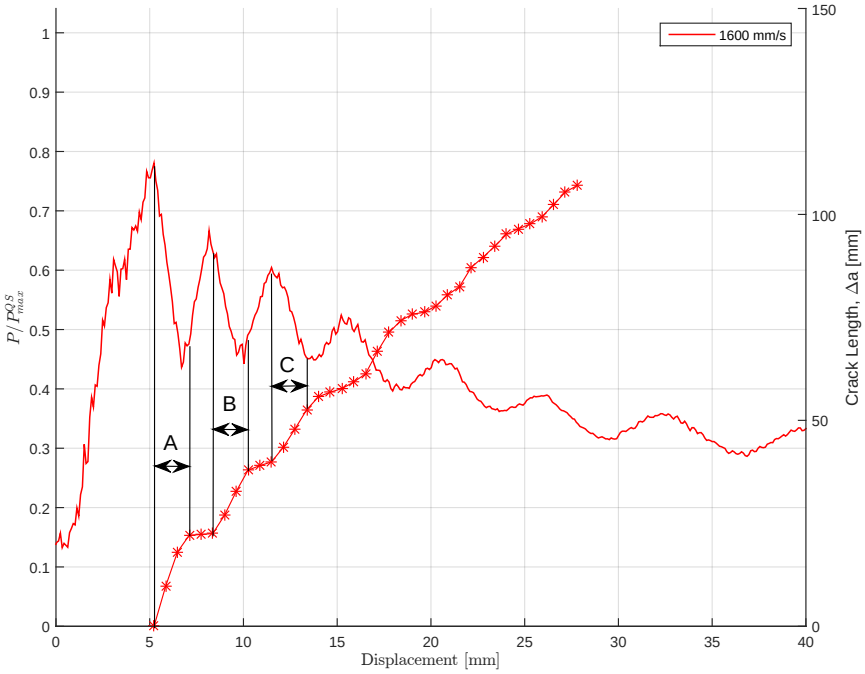

Figure 4.7: Load (solid lines) and crack length (stars) vs. displacement for a loading rate of 1600 mm/s.

elevated rates (300-3600 mm/s) done on a drop tower apparatus. Figure 4.6 shows the load and crack length (Δa) as a function of tip displacement (δ) for different tests representative of their rate. In a similar manner Figure 4.9 shows G_{IC} as a function of crack length (Δa). As was done in the quasi-static testing, the tip displacements (δ) and crack lengths (Δa) are measured from the images taken during the loading event. G_{IC} was calculated using equation 4.14, which accounts for the MWIF correction and the kinetic energy in the system.

The intermediate rates showed a slight difference from the quasi-static rates, with peak loads similar in all the tests, with an average load of $1.01P_{max}^{QS} \pm 3.2\%$. The post-peak response consistently showed an increased load which can partially be related to the shorter initial crack lengths. As the tip displacement increases they merge into the quasi-static results. The elevated rate tests showed a significant drop in peak load as well as the post-peak response. The average peak load for the elevated rates was $0.80P_{max}^{QS} \pm 7.0\%$, when the 300-3600 mm/s rates are lumped together for reference purposes. The load-displacement response at the highest rate (1400-3600 mm/s) showed a sudden change in fracture behavior, where the fracture transitioned from a ductile-stable behavior to a brittle-unstable/stable type behavior. This can be seen from both the load-displacement curves saw-tooth like shape as well as the crack length-displacement relations, showing crack velocities changing during the event. This is similar to the finding reported in [119, 120].

Figure 4.7 shows the 1600 mm/s test in more detail. By looking at the sections marked on the plot (A, B and C) we can see that the crack jumps a significant amount at an increased velocity. The crack can be seen jumping 22.5mm, 15.4mm and 17.8mm for section A, B and C, respectfully. During these spurts of crack growth the load can be seen to drop significantly. It is noteworthy to mention that the load drops are not vertical on the load-displacement curve as is seen in the lower rates, and this is due to the impactor moving at a rate closer to the crack propagation velocity.

While the crack length vs. displacement are shown to follow the same trend, the higher rate responses (above 320 mm/s) show the brittle-unstable/stable behavior. Figure 4.8(a) shows the crack length vs. time for the elevated rates testing (slower

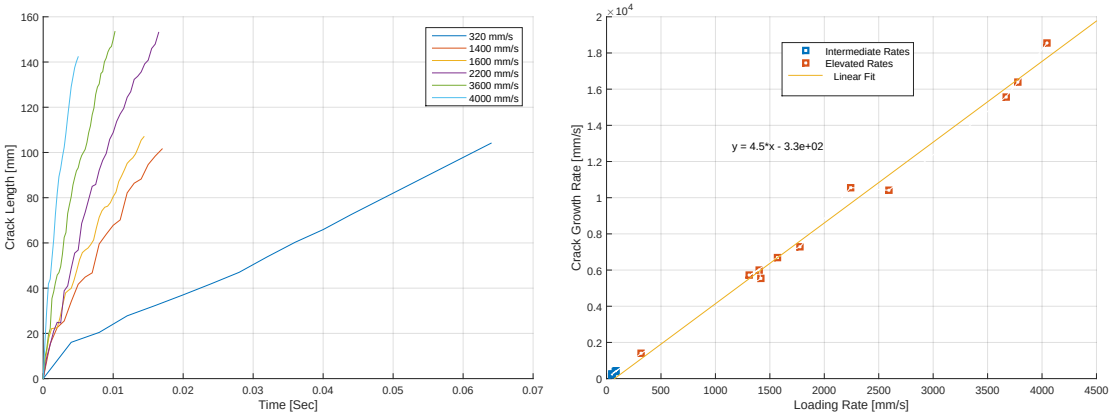

(a) Crack length vs. time

(b) Crack growth rate vs. loading rate

Figure 4.8: Figures showing the crack growth behavior and the relation to loading rate.

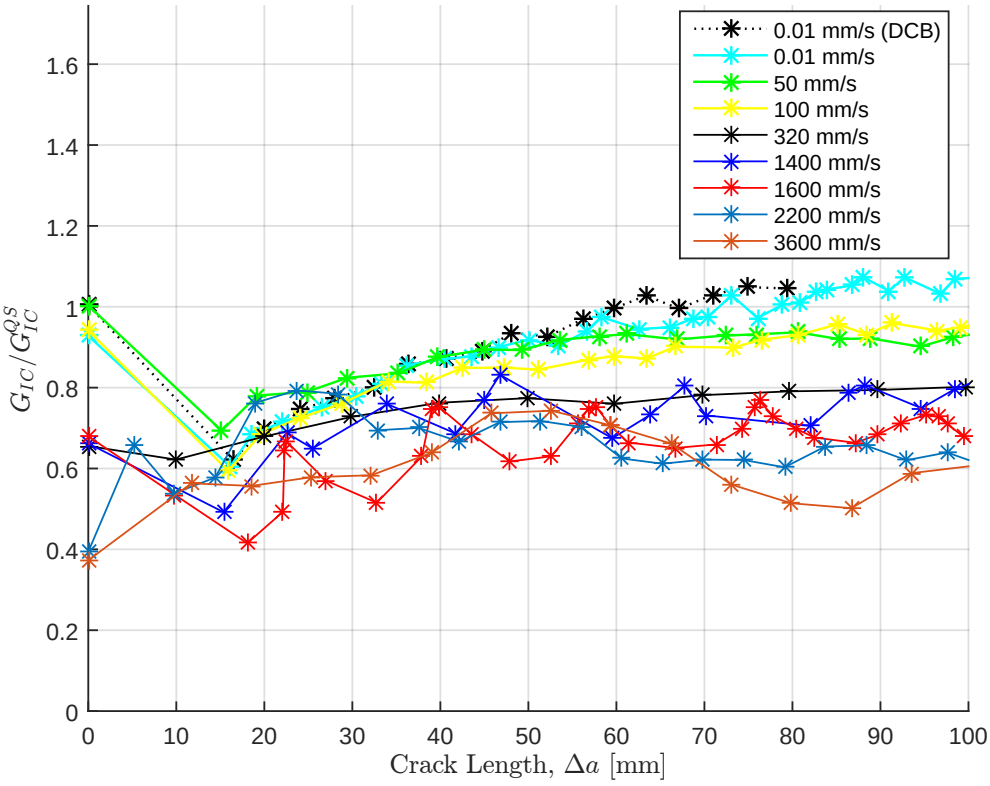

Figure 4.9: G_{IC} vs. crack length for all rates.

rates are not shown due to the significant time duration difference). The results here include tests up to a loading rate of more than 4000 mm/s, while the load-time history was not captured during this test and the applied displacement and crack growth could be measured. These results show in more detail how the crack jumping sets in at high rates as well as how the time duration (or wave lengths) of these velocity spurts gets larger with increasing rate. This can be seen clearly by observing the more linear trend of the higher rate curves. From this it could be drawn that as the rate is increased, a fully dynamic crack growth could be achieved, and at that point the length of the specimen could start having a significant effect on the test. Further investigation on this matter would need to be made.

Figure 4.8(b) shows the crack growth rate vs. loading rate for the intermediate rate and elevated rates testing. The crack rate is a global rate for the test estimated from a linear fit of the crack length vs. time plot and therefore neglecting the growth spurts. The intermediate and elevated rates showed a linear relation between the applied loading rate and crack growth rate where the crack growth rate is approximately 4.5 times the applied loading rate. The quasi-static loading however showed an average

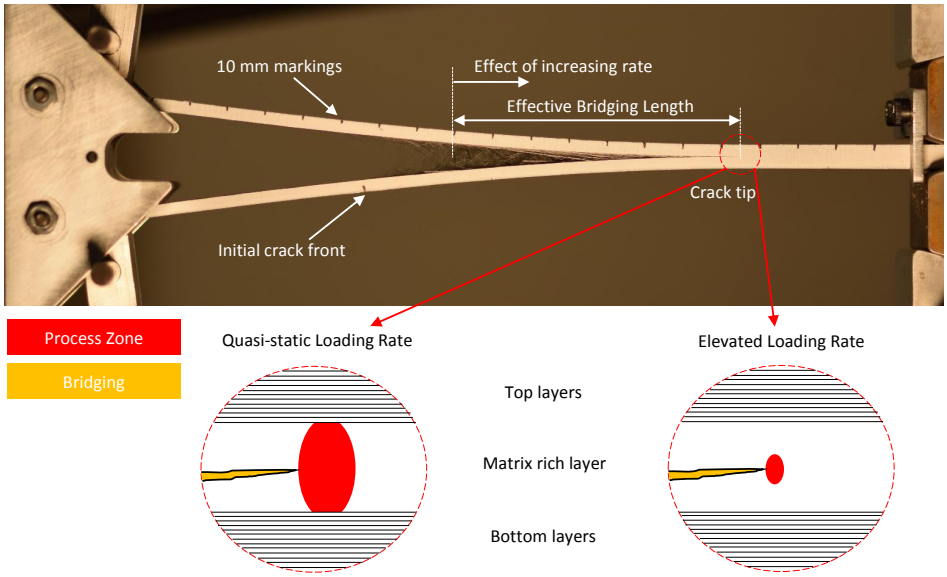

Figure 4.10: Effect of loading rate on bridging and process zone lengths.

ratio of 3.8 between the crack growth rate and applied loading rate, this is possibly an effect of the larger bridging and process zone. The crack growth to loading rate ratio is most likely dependent on a combination of multiple factors such as the loading rate, material properties, and as well the geometry of the structure.

G_{IC} results, averaged w.r.t. G_{IC}^{QS}, for the set of loading rates can be seen in Figure 4.9. The quasi-static and intermediate rate results are shown as average G_{IC} values over the five tests. Note though that here the fracture toughness measurements are compared only as a function of crack length (Δa) and the "far field" loading rate ($\dot{\delta}$). In the next section, the effect of (an estimated) local loading rate is investigated. The results show a clear dependant between G_{IC} and loading rate. As the rate was increased from 0.01 mm/s to 3600 mm/s, a drop of more than 60% was seen for initial G_{IC} and an average drop of roughly 40% for propagation. The initial reduction at increased loading rates can be explained by the localization and the decrease in process zone length as the system has insufficient time to effectively disperse the strain energy caused by the external work, Figure 4.10. While the G_{IC} values right after the initial load drop seem to agree across rates (within experimental margins), the resistance for further crack growth show a clear rate dependence. This rate dependence is thought to be a combination of two things. First, the decrease in process zone length and secondly the decrease in effective bridging length, Figure 4.10. The G_{IC} is seen to plateau at approximately 70-80 mm of crack growth for the quasi-static results while for the intermediate rates this plateau is seen to appear earlier and at a reduced toughness. The elevated rates show slight increase from the initial values before showing a plateau behavior when the effect of dynamic crack growth (which produced saw-tooth or oscillation behavior) is neglected. The extent and contribution of these effects are difficult to achieve experimentally but could be studied further with computational models.

4.3.3 Rate Dependence

The fracture toughness results were presented in the previous section as a function of crack length. In this section, G_{IC} will be looked at as a function of crack tip loading rate, $\dot{y}_{ct}$. While the far-field loading rates ranged from 0.01-3600 mm/s, when looking at the crack tip loading rates, the maximum was found to be roughly 0.17 mm/s. Figure 4.11 shows G_{IC} plotted against the local crack tip rate for each of the tests. Quasi-static tests are represented by squares, intermediate rate tests by diamond shapes and elevated rates are represented by triangles. Each color then represents a separate test. A clear trend can be seen between the intermediate and elevated rates tests, where with increasing rate the fracture toughness is reducing steadily. The quasi-static results at initial glance seem to lie outside of that trend.

However by investigating the results as initial and plateau G_{IC} values where the bridging effect is minimal for the initial values, and considered maximized for the plateau values more insight into the behavior can be had. The initial value where the bridging effect is minimal was considered from Figure 4.9 to be the values calculated

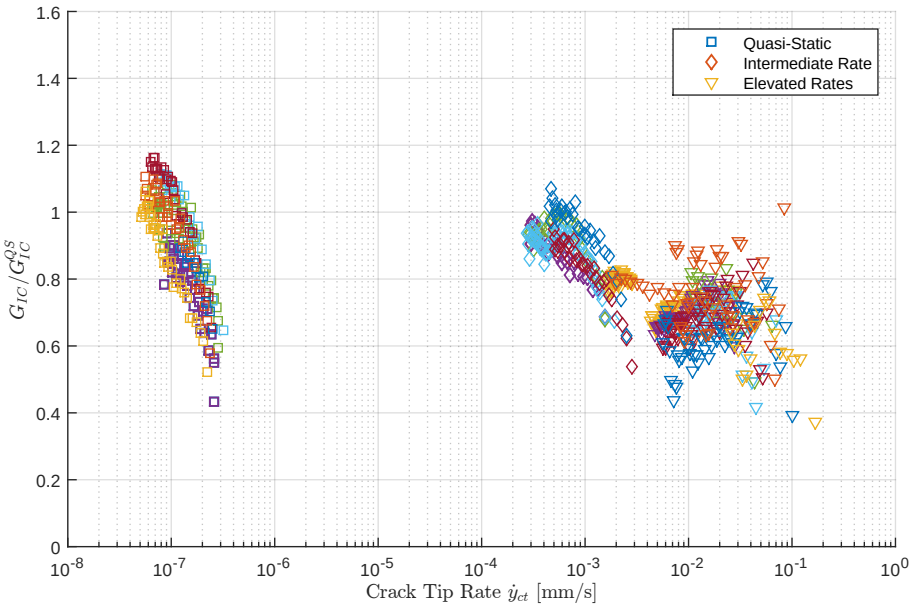

Figure 4.11: G_{IC} as a function of crack tip rate $\dot{y}_{ct}$.

for crack lengths (Δa) shorter than 40 mm. The plateau values, where bridging is considered significant, is considered for crack lengths (Δa) below 40 mm. For the initial values only, Figure 4.12, it can be seen that the intermediate rate tests show

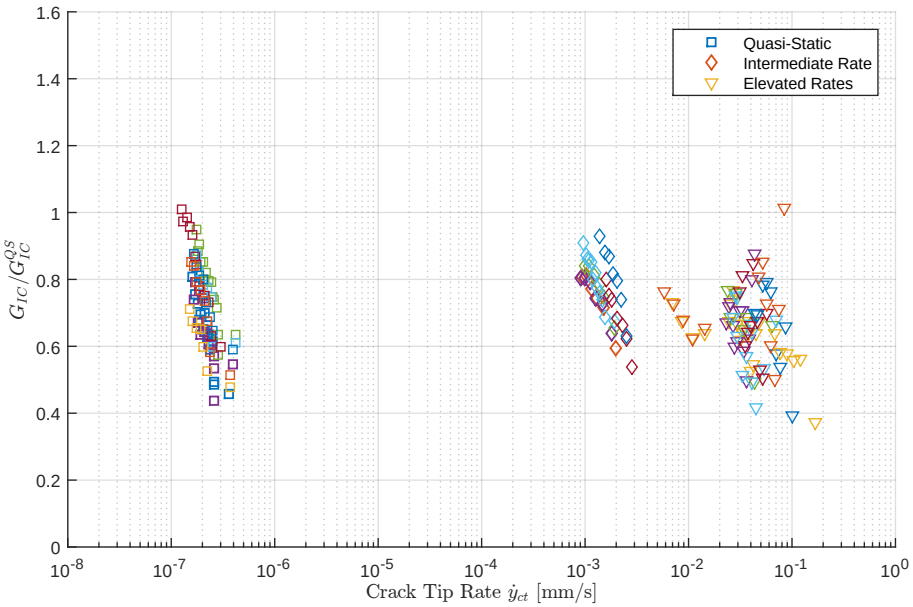

Figure 4.12: Initial G_{IC} measurements ($\Delta a < 40mm$) as a function of crack tip rate $\dot{y}_{ct}$.

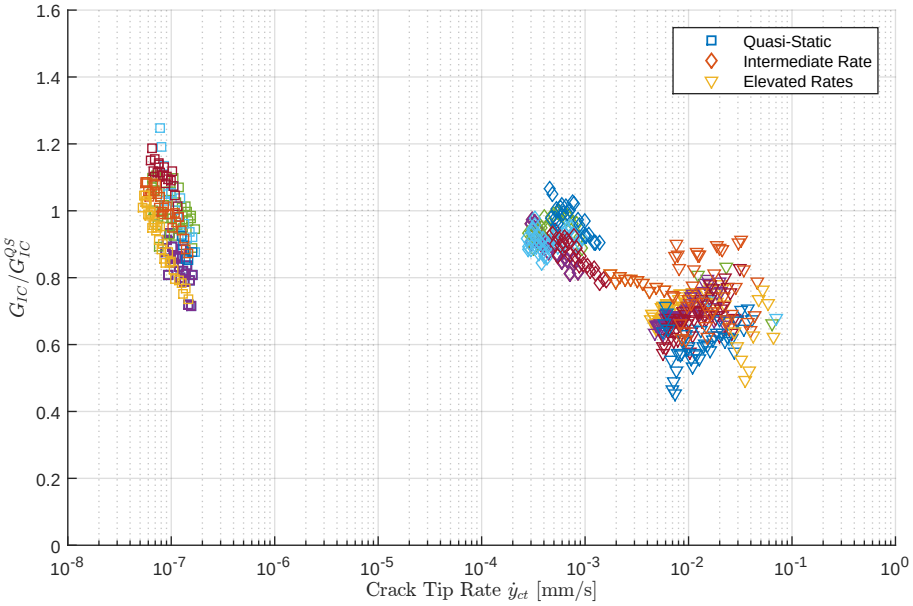

Figure 4.13: Plateau G_{IC} measurements ($\Delta a \geq 40mm$) as a function of crack tip rate $\dot{y}_{ct}$.

less scatter yet the average is fairly similar compared to the quasi-static values. As the loading is increased further the initial fracture toughness can be seen trending down slightly.

When the plateau values are considered, Figure 4.13, the results are more confined for each rate considered. The quasi-static results still show the biggest scatter, which is due to the highly effective bridging area while the elevated rates show little to effect from bridging (plateau through out). The same conclusion was drawn from Figure 4.9. It is clear from the plot that in the presence of a bridging behavior the fracture toughness of the structure becomes heavily dependent on the applied rate of loading.

Using the average mode I interlaminar fracture toughness for the quasi-static tests as G_{IC}^{QS} and using it as a reference, as has been done previously, the intermediate rates (when lumped together) have an average G_{IC} of about $0.92G_{IC}^{QS}$ and at the elevated rates it drops down below $0.37G_{IC}^{QS}$ for the initiation value of the highest rates achieved. These results are similar to trends that have been reported in literature [65, 113].

4.4 Mode II: End-Notched Flexure Tests

Mode II interlaminar fracture testing was performed with an End-Notched Flexure (ENF) configuration, where the quasi-static and intermediate testing were done on an hydraulic load frame (Shore Western, 35,000 lbs load capacity) while the elevated rates were performed on a drop tower (Instron CAEST 9850, 90kN load tub adjusted to 10% of operating value, or 9kN). The experimental setup (for the elevated rates) and test dimensions can be seen in Figure 4.14. The span length (2L) is 203.2 mm (8), bottom roller diameter is 25.4 mm (1) and the top roller diameter is 19.05 (3/4). The initial crack length (a_0) was fixed at 50 mm for all tests, with a variance of approximately +/- 1mm. G_{IIC} calculations were done in accordance to ASTM standard 7905, and further details will be shown in the following chapter. An additional term accounting

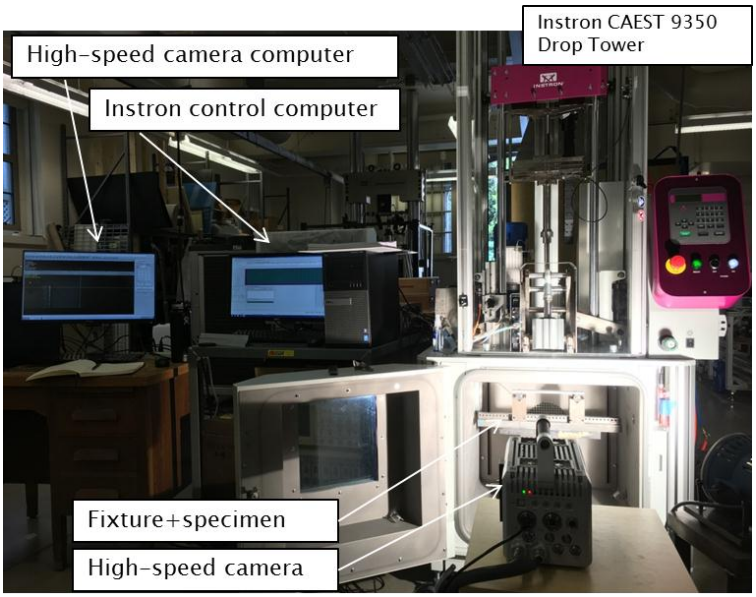

(a) Mode II elevated rate experimental setup.

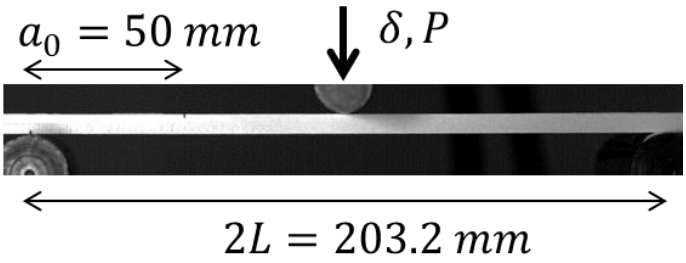

(b) Test dimensions.

Figure 4.14: Experimental configuration for the mode II fracture testing.

for the kinetic energy contribution is also described.

4.4.1 G_{IIC} Calculations

Mode II interlaminar fracture toughness, G_{IIC}, calculations were done in accordance to the Compliance Calibration (CC) method. G_{IIC} is calculated as follows,

$$\boxed{G_{IIC} = \frac{3mP_{Max}^2 a_0^2}{2b}} \tag{4.17}$$

Where P_{Max} is the experimental peak load, a_0 is the initial pre-crack length, b is

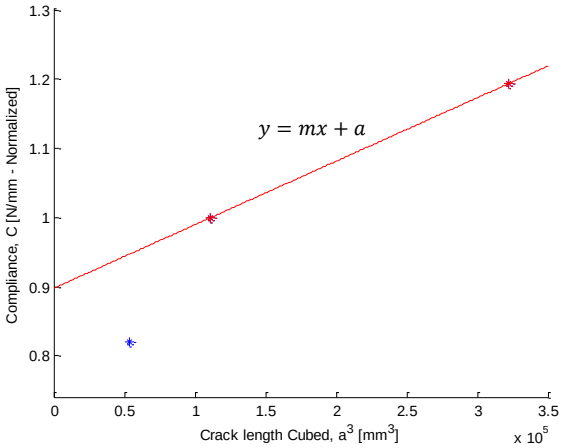

Figure 4.15: Compliance vs. crack length cubed - Compliance calibration plot.

the width of the specimen and m is the slope obtained from the calibration analysis. The kinetic energy also needs to be accounted for when the rate is increased. The kinetic energy for a beam under three point bend loading can be estimated as two cantilever beams with displacement δ. The kinetic energy term becomes similar to the mode I kinetic energy correction,

$$\boxed{G_{IIC} = \frac{3mP_{max}^2 a_0^2}{2b} - \frac{33\rho h\dot{\delta}^2}{70}} \tag{4.18}$$

where ρ is the density, h is half the thickness of the beams ($2h = thickness$) and $\dot{\delta}$ is the applied loading rate. We can see that the kinetic energy correction is four times larger than that of the mode I fracture.

4.4.2 Compliance Calibration (CC)

The compliance calibration method was done at quasi-static rates and then used onward in the intermediate rate and elevated rates testing. The stiffness (slope of the load-displacement relation) did not change noticeably between rates and therefore it was thought to be a good assumption. Calibration was done with the same specimen. A specimen was loaded up to 25% of the peak load observed in the preliminary

experiments. The pre-crack length, a_0, was tested at 35 mm, 50 mm (general testing length) and 65 mm, and the load displacement response were plotted and compliance C_0 was acquired. The compliance is defined as

$$\frac{1}{C_0} = \frac{\delta}{F} \tag{4.19}$$

with the compliance known for the three different initial crack lengths, the results can be plotted as compliance vs. crack length cubed, and the slope of the curve acquired is m, which is used in the G_{IIC} equation. The compliance plot can be seen in Figure 4.15, and the coefficient was initially found to be too high. First the initial crack lengths were measured from images to get a more accurate measurement, and they were corrected by slight amounts (1-2 mm). When actual test data was examined for compliance vs. initial crack length, the results matched closely with the CC estimate from the 50 mm and 65 mm crack lengths only. The coefficient from the CC, not including the shortest crack length, was therefore used in the experimental G_{IIC} calculations.

4.5 Mode II Fracture Experimental Results

Mode II interlaminar fracture tests were performed on ENF specimens both at quasi-static rates and elevated rates. The dimensions of the specimen were kept the same throughout the tests. The specimens used are 32 ply unidirectional laminates, $[0]_{32}$, with a manufactured crack in the form of a Teflon insert on one side of the specimen, same as the mode I fracture test specimens. The Teflon is inserted at the mid-plane of the laminate. The length of the Teflon insert is $76.2mm$ and therefore results in $\approx 50\ mm$ initial crack length. The specimens were not pre-cracked further to produce a natural crack front, similar to the mode I specimens.

Quasi-static and intermediate rate testing was performed on a Shore Western

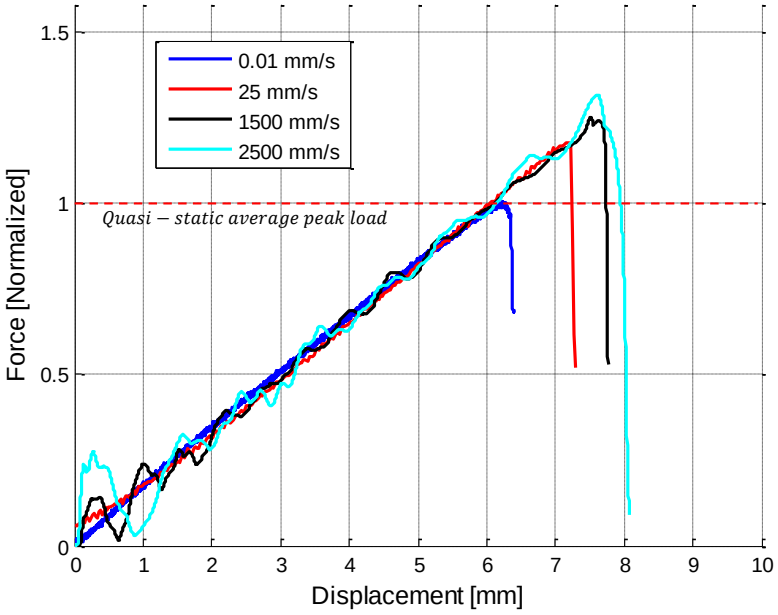

(a) Representative Load-displacement curves

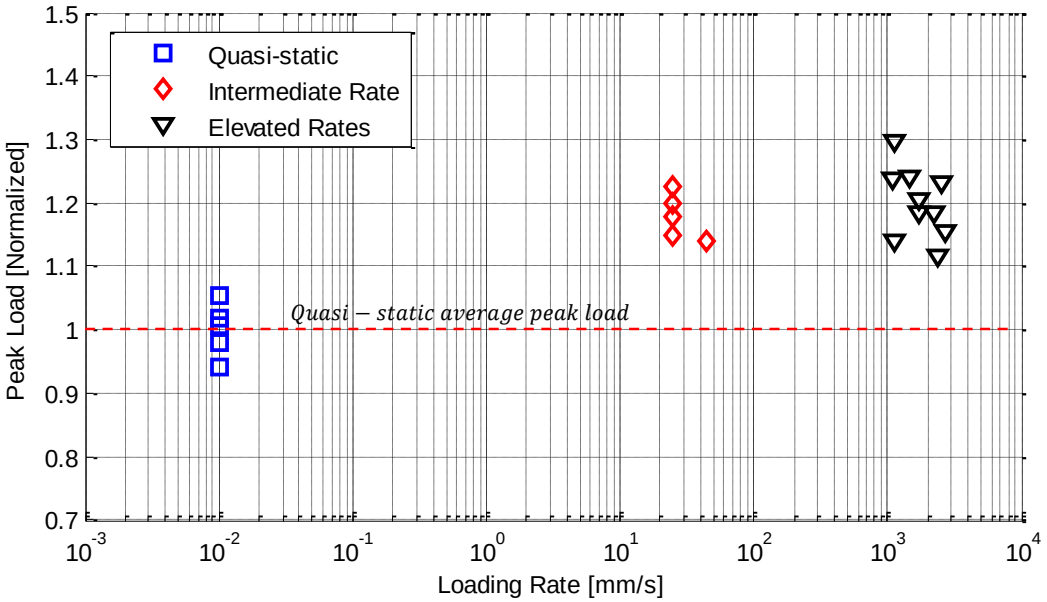

(b) Peak load vs. rate

Figure 4.16: Mode II experimental responses.

hydraulic load frame with a displacement controlled loading rate of 0.01 mm/s and $25 - 75$ mm/s for the quasi-static and intermediate rates, respectively. The quasi-static event was recorded using a Nikon D5300 digital camera with a 105 mm lens.

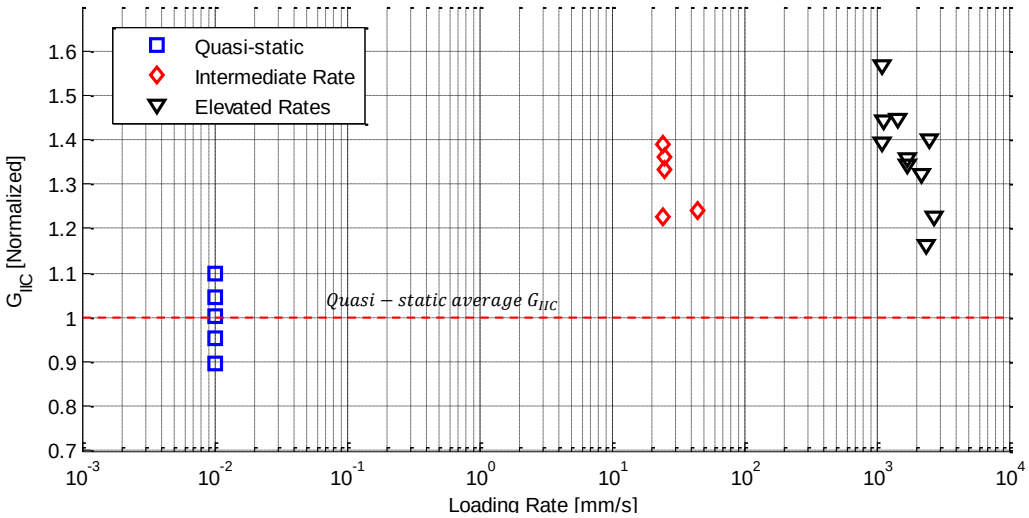

Figure 4.17: G_{IIC} as a function of loading rate.

The camera was recording at $0.2Hz$. The intermediate rate tests were recorded using a Photron SA-X high-speed camera using the same 105 mm lens recording at $4kHz$. The crack location was tracked using a MATLAB script.

Elevated loading rate testing was conducted on an Instron CAEST 9350 drop tower, Figure 4.14(a). The impactor mass was chosen to be high enough so that the kinetic energy of the impactor would be significantly larger than the energy put into the system and therefore the energy dissipated by the mode II fracture. This is done to ensure a nearly perfect ramp loading condition. An impactor mass of 19.4 kg was used, and proved to be sufficient to achieve a smooth loading motion. The elevated loading rates ranged from $1000-2800\ mm/s$. The elevated rates were recorded using the same camera setup as the intermediate rates, with images recorded at $20-30kHz$, depending on rate. The crack location and loading displacement was tracked using a MATLAB script.

Representative load-displacement response for the different rates can be seen in Figure 4.16(a), where load has been normalized with respect to the average quasi-static peak load. It can be seen that there is a reasonably big jump in peak load between 0.01 mm/s and 25 mm/s. The jump beyond that is less significant with

respect to the increase in rate. Figure 4.16(b) shows the normalized peak loads as a function of loading rate. The x-axis is plotted on a logarithmic scale to give a better visualization. The peak load jumps between the quasi-static and intermediate and then gets effected very little with increasing rate.

G_{IIC} calculations for crack growth initiation were done using the CC method, Eq. 4.17 and 4.18. The kinetic energy was accounted for in the intermediate and elevated rates G_{IIC} calculations. G_{IIC} as a function of loading rate can be seen in Figure 4.17, x-axis once again plotted on the logarithmic scale for better at-rate representation. It can be seen that the quasi-static results showed a variance of roughly 10%. Using the average quasi-static G_{IIC} result as a reference an average increase of $\approx 31\%$ for the intermediate loading rates is noted. The elevated rates show an increasing trend up to loading rate of 1437 mm/s, where G_{IIC} was seen to increase beyond 1.4 times the average quasi-static value. When the rate was increased further to 1700 mm/s and beyond an overall decreasing trend in G_{IIC} was observed.

From the testing conducted it is clear that a sudden change in behavior is observed at increasing loading rates. Initially an increasing trend is seen for G_{IIC} with loading rate. With the loading rate increased further a sudden shift to a downward trend is seen. At this point, it is unclear what the cause is and further work would be required to understand the behavior. Increasing the loading rate beyond 2800 mm/s would also be essential for the study.

4.6 Conclusion

Experimental results for mode I and mode II interlaminar fracture in polymer matrix composites at elevated rates has been presented. A novel method for conducting mode I fracture at elevated rates has been introduced. The MWIF method eliminates the frictional effects introduced between the wedge and beams in the conventional WIF method. This is achieved by inserting two wedges in between rollers

that are inserted into the conventional (aluminum block) DCB specimen. The aluminum blocks are machined to a high precision to allow the rollers to rotate freely (lubrication is added), similar to the conventional DCB method. The MBT method for mode I fracture toughness calculations has been extended to account for the extra loading factor that is introduced with the MWIF method. The MWIF method has been verified against established methods for mode I fracture in fiber reinforced polymer matrix composites at quasi-static rates and showed good agreement. Mode I fracture testing was performed at rates ranging from $0.01 - 3600\ mm/s$, utilizing a hydraulic load frame for rates up to $100\ mm/s$ and a drop tower for rates up to 3600 mm/s.

Intermediate rate testing ($50 - 100\ mm/s$) showed a slight decrease in G_{IC} while agreeing reasonably well with the quasi-static results ($0.01\ mm/s$) for the load-displacement response. The elevated rates ($300 - 3600\ mm/s$) showed a significant decrease in G_{IC}, most notably in the upper range as well as showing an overall load reduction in the load-displacement response. A downward trend for G_{IC} vs. rate was observed. The effect of bridging was seen to decrease significantly with increased loading rate.

The MWIF testing method presented in this chapter has been shown to agree well with established quasi-static methods. The method has been shown to be viable for conducting mode I fracture of polymer matrix composites at elevated rates. The authors feel that the experimental procedure is a good candidate for further study of mode I fracture toughness measurements at elevated rates and that the method can be extended for use with high-rate testing.

The ENF method was used to conduct testing at quasi-static, intermediate and elevated rates. Mode II fracture testing was performed at rates ranging from $0.01 - 2800$ mm/s utilizing a hydraulic load frame, for rates up to $50\ mm/s$ and a drop tower for rates up to $2800\ mm/s$. Intermediate rate testing ($25 - 50\ mm/s$) shows a significant

increase in G_{IIC}. The elevated rates ranging from $1000 - 1500$ mm/s showed only a slight increase in G_{IIC} compared to the intermediate rates while increasing the rate to 1700 mm/s and beyond resulted in a downward trend in G_{IIC}. Further study of the mode II fracture would be essential to understand the behavior further. Loading rates in excess of 3000 mm/s should be examined. Computational modeling of the testing would also give detailed information and knowledge into the fracture behavior of the system.

While it is clear that rate-effects are seen in the experimental procedure the effects of it could not be fully understood from the experimental findings presented in this chapter. For instance, the effect of rate on the process zone length and bridging on the initial G_{IC} values compared to the fracture toughness for a fully evolved bridging length. Furthermore, for the implementation into a FE framework the fracture behavior needs to be investigated with respect to the cohesive (traction-separation) laws. What kind of shape should the cohesive law take and how should the shape evolve with the rate of separation to capture the rate effects seen in the experiments. It would therefore be essential to conduct a further study, both experimentally and numerically, to investigate the fracture behavior at the different applied loading rates. This would also give valuable insight and information into the actual experimental loading rate vs. the local loading rate (or separation of the nodal connection in the cohesive element).

CHAPTER V

Finite Element Modeling of Impact

5.1 Introduction

In this chapter, the Enhanced Schapery Theory (EST) material model for progressive damage and failure modeling of lamina within a multidirectional laminate will be introduced. EST is a plane stress material model which captures the full field damage and failure of a lamina in the 1-2 principal material plane. EST captures the pre-peak matrix dominated non-linearity due to micro-damage using Schapery Theory (ST). Post-peak behavior is modeled using the Bazant-Oh Crack Band (CB) model. The material model was developed by Pineda and Waas [88–90] and implemented as a user material subroutine (VULT) for the commercial FE solver ABAQUS Explicit [1]. The model has proven itself, many times over, to be highly capable of capturing in-plane damage and failure in a computationally efficient manner [88, 89]. EST is a mixture of high-fidelity failure modeling and computational efficiency and was therefore ideal for the impact model requirements, as will be discussed in Chapter VI.

EST coupled with Discrete Cohesive Zone Method (DCZM) elements for capturing the inter-laminar failure modes due to mode I (peel) or mode II/III (slip/shear) loading allows for modeling of laminates under both in-plane and transverse loads. The DCZM is a discrete cohesive element, which uses nodal traction-separation laws. It is implemented in an 8 noded interface element which allows for modeling of zero and

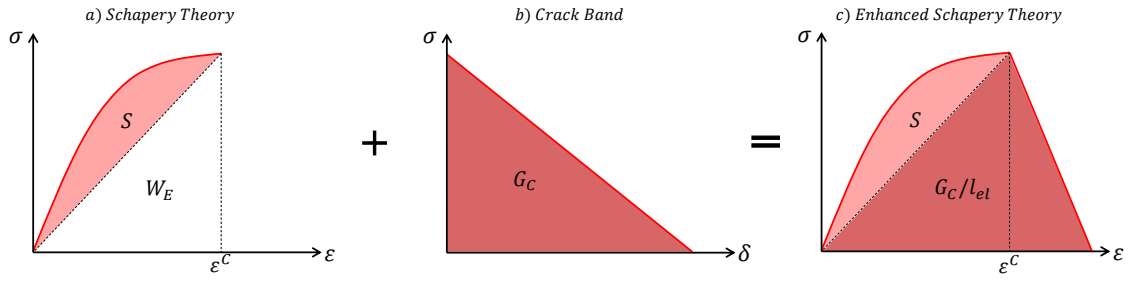

Figure 5.1: Schematic explaining the EST damage and failure model.

finite thickness cohesive layers. The element stiffness matrix is sparse and therefore computationally efficient. The DCZM element was first developed as a 2D formulation by Xie and Waas [131] and later extended to 3D by Gustafson and Waas [40–42]. The sensitivity of the cohesive law input parameters have been studied [42]. The shape of the cohesive law was also studied with respect to computational stability and efficiency [41].

In the following chapter, the intra-laminar progressive damage and failure model, EST, will be first introduced. Next the DCZM element for capturing inter-laminar fracture will be presented.

5.2 Intra-lamina Damage and Failure Model

As previously mentioned, EST combines ST [105, 106] and the Bažant-Oh Crack Band (CB) [9] model in order to capture the pre-peak (damage) and post-peak (failure) strain softening behavior of the material in the 1-2 plane. ST captures the pre-peak non-linearity due to matrix micro-cracking while CB captures the post-peak response due to macroscopic matrix cracks due to normal (tensile or compressive) and/or shear loading. CB also captures post-peak strain softening due to fiber failure in tension or compression. Failure initiation is handled through the Hashin-Rotem [45] strain based failure criteria. EST has been implemented as a plane-stress user defined material (VULT) model for use with shell elements (conventional and continuum

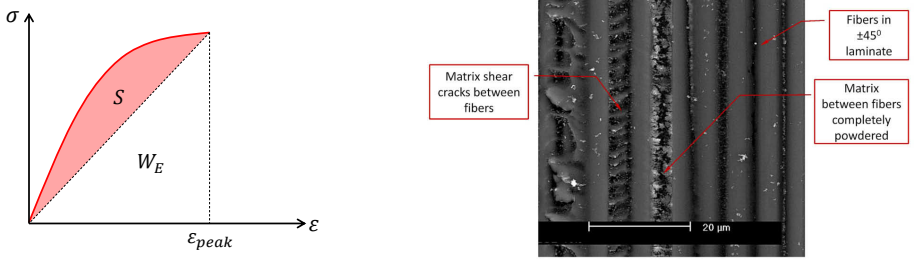

(a) Schapery theory schematic.

(b) Shear micro cracks present in a +/-45 tensile test [77].

Figure 5.2: Pre-peak non-linearity modeling and experimental details.

shells) in the ABAQUS Explicit solver.

In the following chapters the EST theory will be explained in a systematic manner. The pre-peak nonlinearity modeling approach (ST) will first be presented. The failure initiation criteria will be presented as well as the post-peak strain softening (CB) modeling details. The EST input parameters are reviewed in Chapter 6.2.3.

5.2.1 Pre-peak Non-linearity - Schapery Theory

ST [105, 106] is a thermodynamically based work potential model which captures the pre-peak non-linearity, Figure 5.3(a) due to matrix micro cracking on the fiber and matrix length scale. Matrix micro cracks are initiated by shear loading of the matrix, Figure 5.3(b). Matrix micro damage can occur due to hackling, shear banding, micro-fissures and fiber/matrix disbonds, to name a few. In this chapter, the theoretical derivation of the model will be summarized as implemented by Pineda and Waas [88–90].

The total work potential, W_T, can be expressed in terms of an elastic potential, W_E, and a dissipated potential, W_S. The dissipated potential has contributions from both ST and CB, as will be shown in the chapter on CB, Chapter 5.2.3. In this chapter, the dissipation potential will be referred to as simply the energy dissipated due to micro cracking, $W_S = S$. The total work potential, absent of macroscopic damage, becomes

$$W_T = W_E + S \tag{5.1}$$

where W_E and S are graphically represented in Figure 5.3. Schapery showed that the total work potential is stationary with respect to S, that is

$$\frac{dW_T}{dS} = 0 \tag{5.2}$$

Combining the above equations yield

$$\frac{dW_E}{dS} = -1 \tag{5.3}$$

By applying the second law of thermodynamics [100], the inequality can be achieved

$$\dot{S} \geq 0 \tag{5.4}$$

The inequality equation signifies that no healing of the material is allowed, and the time derivative of the dissipated energy is always positive and therefore S will always increase with time. The elastic potential can be written from classical lamination theory (CLT), making the assumption that $\nu_{12}\nu_{21} \ll 1$

$$W_E = \frac{1}{2}\left(E_{11}\epsilon_{11}^2 + E_{22}\epsilon_{22}^2 + G_{12}\gamma_{12}^2\right) + Q_{12}\epsilon_{11}\epsilon_{22} \tag{5.5}$$

Since the micro damage, S, is only accumulating in the matrix, it is assumed that the longitudinal modulus, E_{11}, is unaffected and remains constant. However, the transverse direction and shear moduli, E_{22} and G_{12}, respectively, are affected by the presence of micro damage in the matrix. The transverse and shear moduli are written in terms of the Schapery micro damage functions and the pristine moduli.

$$E_{22} = E_{220}e_s(S) \tag{5.6}$$

$$G_{12} = G_{120} g_s(S) \tag{5.7}$$

Where E_{220} and G_{120} denote the pristine transverse and shear moduli, respectively. $e_s(S)$ and $g_s(S)$ are the transverse and shear Schapery micro damage functions, respectively. The Schapery micro damage functions are acquired from mechanical testing (or a combination of mechanical testing and virtual simulations), this procedure is described in Appendix C.

By assuming that $Q_{12} = \nu_{12} E_{22}$ is independent of S and therefore remains constant, the Schapery micro damage evolution equation is found (by utilizing equations 5.3, 5.5 5.6 and 5.7).

$$\frac{1}{2}\Big(E_{220}\frac{de_s(S)}{dS}\epsilon_{22}^2 + G_{120}\frac{dg_s(S)}{dS}\gamma_{12}^2\Big) = -1 \tag{5.8}$$

Sicking and Schapery [106] showed that S varies in relation to ϵ^3 where ϵ is the applied strain in the experimental coordinate frame (applied tensile/compressive strain in most cases). A reduced damage variable, S_r was therefore introduced as,

$$S_r = \sqrt[3]{S} \tag{5.9}$$

Applying the reduced damage variable to the micro damage evolution equation results in,

$$\frac{1}{2}\Big(E_{220}\frac{de_s(S_r)}{dS_r}\epsilon_{22}^2 + G_{120}\frac{dg_s(S_r)}{dS_r}\gamma_{12}^2\Big) = -3S_r^2 \tag{5.10}$$

The above equation is an ordinary differential equation which can be solved with respect to the reduced damage variable, S_r. With the degradation of the transverse and shear moduli of a lamina, and after assuming plane stress conditions, and that $\nu_{12}\nu_{21} \ll 1$, the pre-peak stress-strain constitutive relation becomes

$$\begin{bmatrix} \sigma_{11} \\ \sigma_{22} \\ \tau_{12} \end{bmatrix} = \begin{bmatrix} E_{11} & \nu_{12}E_{22}e_s(S_r) & 0 \\ \nu_{12}E_{22}e_s(S_r) & E_{22}e_s(S_r) & 0 \\ 0 & 0 & G_{12}g_s(S_r) \end{bmatrix} \begin{bmatrix} \epsilon_{11} \\ \epsilon_{22} \\ \gamma_{12} \end{bmatrix} \tag{5.11}$$

5.2.2 Failure Initiation

Failure initiation, which marks the initiation of macroscopic matrix cracks or fiber failure is controlled by the Hashin-Rotem [45] strain based failure criteria. Failure initiation marks the activation of the post-peak crack band and in result a negative tangent stiffness. The fiber direction failure criteria for tension and compression are

$$\left(\frac{\epsilon_{11}}{X_T}\right)^2 = 1 \qquad \epsilon_{11} \geq 0 \tag{5.12}$$

$$\left(\frac{\epsilon_{11}}{X_C}\right)^2 = 1 \qquad \epsilon_1 < 0 \tag{5.13}$$

Where X_T and X_C are the fiber direction failure strains in tension and compression, respectively. Hashin and Rotem introduced mixed mode matrix failure criteria, the criteria depends on the normal (mode I) and shear strain. The mixed mode matrix failure criteria for tension and compression are

$$\left(\frac{\epsilon_{22}}{Y_T}\right)^2 + \left(\frac{\gamma_{12}}{Z}\right)^2 = 1 \qquad \epsilon_{22} \geq 0 \tag{5.14}$$

$$\left(\frac{\epsilon_{22}}{Y_C}\right)^2 + \left(\frac{\gamma_{12}}{Z}\right)^2 = 1 \qquad \epsilon_{22} < 0 \tag{5.15}$$

Where Y_T and Y_C are the transverse (mode I) failure strains of the lamina in tension and compression, respectfully. Z is the matrix shear (mode II) failure strain of the lamina. Furthermore, when either one of Eq. 5.12 or 5.13 is satisfied, that is fiber failure has occurred, the matrix failure modes are initiated at their current

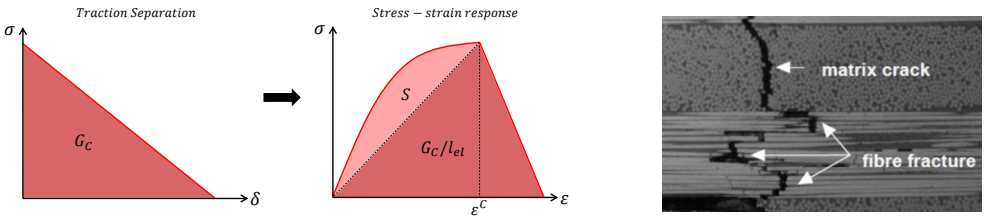

(a) Crack band schematic

(b) Matrix macro cracks and fiber rupture.

Figure 5.3: Post-peak strain softening modeling and experimental details.

tractions. However, matrix failure does not initiate fiber failure.

5.2.3 Post-peak strain softening - Crack band

The Bažant-Oh CB model is implemented as an extension to the ST model allowing modeling of the full in-plane damage and failure event of a fiber reinforced composite material. Once the failure criteria are satisfied the CB calculation is initiated. As previously mentioned, ST is utilized to model the pre-peak non-linearity due to matrix micro-cracking. CB captures the post-peak behavior due to failure. Failure occurs in the form of matrix transverse (tension and compression) and shear cracking as well as fiber failure in tension and compression.

The CB model is a smeared modeling method, meaning that the crack is smeared over the element in the form of degradation of the material moduli associated with the crack direction (1 for fiber failure, 2 and 12 plane for matrix failure). The post-peak strain softening is handled through traction-separation laws which are related to the stress-strain response by introducing a characteristic element length, introduced by Bažant [9]. More detail will follow later in the chapter.

The strain energy density, Eq. 5.1, now includes additional internal state variables (ISV) associated with the individual CB failure modes. The total strain energy density becomes

$$W_T = W_E + S + S_I^m + S_{II}^m + S_I^f \tag{5.16}$$

Where W_E is once again the elastic strain energy. S is the dissipated energy due to micro cracking from ST. S_I^m and S_{II}^m are the dissipations due to mode I and mode II matrix failure, respectively. S_I^f is the dissipation due to tensile/compressive fiber failure. At failure initiation the micro-cracks are considered to have transitioned into macro cracks and therefore the ST calculations are halted and the dissipation energy from ST becomes constant. At this point a crack is forming in the element and the transition from continuum to non-continuum response occurs. The element behavior is now calculated from the uncoupled CB traction-separation laws.

Applying the stationary principle to each individual ISV gives the following relations, similar to Eq. 5.3.

$$\frac{\delta W_E}{\delta S} = -1 \tag{5.17}$$

$$\frac{\delta W_E}{\delta S_I^m} = -1 \tag{5.18}$$

$$\frac{\delta W_E}{\delta S_{II}^m} = -1 \tag{5.19}$$

$$\frac{\delta W_E}{\delta S_I^f} = -1 \tag{5.20}$$

Where Eq 5.17 is simply the ST part and Eq. 5.18-5.20 are the CB associated stationary principles. As before, by applying the second law of thermodynamics, the following inequality equations are derived

$$\dot{S} \geq 0 \tag{5.21}$$

$$\dot{S}_I^m \geq 0 \tag{5.22}$$

$$\dot{S}_{II}^m \geq 0 \tag{5.23}$$

$$\dot{S}_I^f \geq 0 \tag{5.24}$$

These relations ensure the fact that none of the ISVs are able to decrease with time and therefore constraining any healing of the material. The energy potentials include the total energy available for dissipation (from crack growth) and a subtraction of the recoverable energy if the crack would be closed back up. The strain energy release rate (SERR) for each failure mode, assuming a triangular cohesive law, is

$$G_I^m = \frac{1}{2}\Big(t_{IC}^m + t_I^m\Big)\delta_I^m \tag{5.25}$$

$$G_{II}^m = \frac{1}{2}\Big(t_{IIC}^m + t_{II}^m\Big)\delta_{II}^m \tag{5.26}$$

$$G_I^f = \frac{1}{2}\Big(t_{IC}^f + t_I^f\Big)\delta_I^f \tag{5.27}$$

Where G_I^m and G_{II}^m denote the matrix fracture toughness for mode I and mode II, respectively. G_I^f denotes the fiber direction fracture toughness. t stands for the traction associated with each mode of failure (I and II) as well as for the matrix and fiber, m and f respectively. The subscript C denotes the critical cohesive traction (traction at initiation of failure). The potentials for each failure mode can be established from Eq. 5.25-5.27, by using a characteristic crack length (element length depending on direction of failure) as well as removing the elastic energy potential. The resulting

potentials are,

$$S_I^m = \frac{G_I^m}{l_{el,\theta}} - \frac{t_I^m \delta_I^m}{2l_{el,\theta}} \tag{5.28}$$

$$S_{II}^m = \frac{G_{II}^m}{l_{el,\theta}} - \frac{t_{II}^m \delta_{II}^m}{2l_{el,\theta}} \tag{5.29}$$

$$S_I^f = \frac{G_I^f}{l_{el,\theta+90}} - \frac{t_I^f \delta_I^f}{2l_{el,\theta+90^\circ}} \tag{5.30}$$

The crack length is denoted by the element length depending on the direction of the crack. Transverse/shear matrix cracks will grow parallel to the fibers and are therefore dependent on the element length in the fiber direction, denoted as $l_{el,\theta}$. Fiber failure will occur perpendicular to the fiber direction and therefore the crack length depends on the element length perpendicular to the fiber direction, denoted as $l_{el,\theta+90^\circ}$. Note that the latter part (subtractions) of Eq. 5.28-5.30 are simply the elastic strain energy of the crack. The tractions can be simply related to the secant stiffness and separation of the traction-separation law as follows

$$t_I^m = k_I^m \delta_I^m \tag{5.31}$$

$$t_{II}^m = k_{II}^m \delta_{II}^m \tag{5.32}$$

$$t_I^f = k_I^f \delta_I^f \tag{5.33}$$

The elastic strain energy of the crack can now be expressed in terms of the traction separation law secant stiffness and separations. Note that the secant stiffness is here expressed as a function of the associated potentials.

$$W_I^m = \frac{k_I^m \delta_I^{m^2}}{2l_{el,\theta}} \tag{5.34}$$

$$W_{II}^m = \frac{k_{II}^m \delta_{II}^{m^2}}{2l_{el,\theta}} \tag{5.35}$$

$$W_I^f = \frac{k_I^f \delta_I^{f^2}}{2l_{el,\theta+90}} \tag{5.36}$$

The total elastic strain energy density can now be expressed with the new dissipation potentials included,

$$W_E = \frac{1}{2}\big(E_{11}\epsilon_{11}^2 + E_{22}(S_r)\epsilon_{22}^2 + G_{12}(S_r)\gamma_{12}^2\big) + Q_{12}\epsilon_{11}\epsilon_{22} + \frac{k_I^m \delta_I^{m^2}}{2l_{el,\theta}} + \frac{k_{II}^m \delta_{II}^{m^2}}{2l_{el,\theta}} + \frac{k_I^f \delta_I^{f^2}}{2l_{el,\theta+90}} \tag{5.37}$$

By applying the stationary principle equations (Eq. 5.17-5.20) the ISV evolution equations are established.

$$\frac{1}{2}\Big(E_{220}\frac{de_s(S_r)}{dS_r}\epsilon_{22}^2 + G_{120}\frac{dg_s(S_r)}{dS_r}\gamma_{12}^2\Big) = -3S_r^2 \tag{5.38}$$

$$\frac{1}{2l_{el,\theta}}\frac{dk_I^m}{2S_I^m}\delta_I^{m^2} = -1 \tag{5.39}$$

$$\frac{1}{2l_{el,\theta}}\frac{dk_{II}^m}{2S_{II}^m}\delta_{II}^{m^2} = -1 \tag{5.40}$$

$$\frac{1}{2l_{el,\theta+90^\circ}}\frac{dk_I^f}{2S_I^f}\delta_I^{f^2} = -1 \tag{5.41}$$

Where Eq. 5.38 is simply the ST micro damage evolution equation derived in Eq. 5.10 using the reduced damage variable, S_r. It can be seen that the ISV evolu-

tion equations are completely uncoupled. A simple mixed mode energy criterion is implemented for capturing mixed-mode failure, as follows:

$$\frac{G_I^m}{G_{IC}^m} + \frac{G_{II}^m}{G_{IIC}^m} \geq 1 \tag{5.42}$$

Since the ISV equations are uncoupled, the dissipation potentials, S_I^m, S_{II}^m and S_I^f can be determined from Eq. 5.39-5.41 at the initiation of failure in terms of applied strain using the traction separation laws and kinematics.

First the derivation of the dissipation potentials, derived from equations 5.25-5.30, w.r.t. the associated separation will give the following relation

$$\frac{dS_I^m}{d\delta_I^m} = \frac{t_{IC}^m \delta_I^m}{2l_{el,\theta}} \tag{5.43}$$

$$\frac{dS_{II}^m}{d\delta_{II}^m} = \frac{t_{IIC}^m \delta_{IIC}^m}{2l_{el,\theta}} \tag{5.44}$$

$$\frac{dS_I^f}{d\delta_I^f} = \frac{t_{IC}^f \delta_I^f}{2l_{el,\theta+90^\circ}} \tag{5.45}$$

Where the tractions in the above equations are now the critical cohesive strengths, denoted by C as was shown before. Now from Eq. 5.39-5.41, using the above equations and the chain rule, an integral for the traction-separation secant stiffness is achieved

$$k_I^m = -\int \frac{t_{IC}^m}{\delta_I^{m^2}} d\delta_I^m \tag{5.46}$$

$$k_{II}^m = -\int \frac{t_{IIC}^m}{\delta_{II}^{m^2}} d\delta_{II}^m \tag{5.47}$$

$$k_I^f = -\int \frac{t_{IC}^f}{\delta_I^{f^2}} d\delta_I^f \tag{5.48}$$

The above integrals can be evaluated while applying the correct boundary conditions. The secant stiffness, k goes to zero when the critical separation of the traction-separation laws are achieved. Applying this boundary condition allows for the secant stiffness terms to be solved in terms of traction separation law parameters.

$$k_I^m = t_{IC}^m \left(\frac{1}{\delta_I^m} - \frac{t_{IC}^m}{2G_{IC}^m} \right) \tag{5.49}$$

$$k_{II}^m = t_{IIC}^m \left(\frac{1}{\delta_{II}^m} - \frac{t_{IIC}^m}{2G_{IIC}^m} \right) \tag{5.50}$$

$$k_I^f = t_{IC}^f \left(\frac{1}{\delta_I^f} - \frac{t_{IC}^f}{2G_{IC}^f} \right) \tag{5.51}$$

As previously mentioned, the transition from a continuum to non-continuum requires a relationship between the traction-separation and stress-strain response of the material. The strains in the post-peak regime, once failure is initiated, can be related to the traction separation by

$$\epsilon_{22} l_{el,\theta} = \epsilon_{22}^C l_{e,\theta} + \delta_I^m \tag{5.52}$$

$$\gamma_{12} l_{el,\theta} = \gamma_{12}^C l_{e,\theta} + 2\delta_{II}^m \tag{5.53}$$

$$\epsilon_{11} l_{el,\theta+90^\circ} = \epsilon_{11}^C l_{e,\theta+90^\circ} + \delta_I^f \tag{5.54}$$

where ϵ_{11}^C, ϵ_{22}^C and γ_{12}^C are the strains at failure initiation, when the appropriate Eq. 5.12-5.15 are satisfied. The traction separation law tangent stiffness can now be obtained as a function of the material strain,

$$k_I^m = t_{IC}^m \left(\frac{1}{(\epsilon_{22} - \epsilon_{22}^C) l_{el,\theta}} - \frac{t_{IC}^m}{2G_{IC}^m} \right) \tag{5.55}$$

$$k_{II}^m = t_{IIC}^m \left(\frac{2}{(\epsilon_{12} - \epsilon_{12}^C) l_{el,\theta}} - \frac{t_{IIC}^m}{2G_{IIC}^m} \right) \tag{5.56}$$

$$k_I^f = t_{IC}^f \left(\frac{1}{(\epsilon_{11} - \epsilon_{11}^C) l_{el,\theta+90^\circ}} - \frac{t_{IC}^f}{2G_{IC}^f} \right) \tag{5.57}$$

The equations above, Eq. 5.55-5.57, are used once the associated failure criteria are activated for calculating the traction-separation secant stiffness of the non-continuum. Eq. 5.31-5.33 and 5.52-5.54 can then be used to calculate the tractions on the crack surface and the separation (crack tip opening displacement). It is assumed that the stress state at each integration point is homogenous and that the stresses in the element are equal to the crack surface tractions. Finally, the longitudinal (E_{11}), transverse (E_{22}) and shear (G_{12}) moduli at the integration point can be calculated with the following equations,

$$E_{11} = \left[\frac{1}{E_{110}} - \frac{\epsilon_{11} - \epsilon_{11}^C}{t_{IC}^f \left(1 + \frac{t_{IC}^f l_{el,\theta+90^\circ}}{2G_{IC}^f} (\epsilon_{11} - \epsilon_{11}^C) \right)} \right]^{-1} \tag{5.58}$$

$$E_{22} = \left[\frac{1}{E_{22}^*} - \frac{\epsilon_{22} - \epsilon_{22}^C}{t_{IC}^m \left(1 + \frac{t_{IC}^m l_{el,\theta}}{2G_{IC}^m} (\epsilon_{22} - \epsilon_{22}^C) \right)} \right]^{-1} \tag{5.59}$$

$$G_{12} = \left[\frac{1}{G_{12}^*} - \frac{\gamma_{12} - \gamma_{12}^C}{2t_{IIC}^m \left(1 + \frac{t_{IIC}^m l_{el,\theta}}{4G_{IIC}^m} (\gamma_{12} - \gamma_{12}^C) \right)} \right]^{-1} \tag{5.60}$$

where E_{22}^* and G_{12}^* are the degraded transverse and shear moduli due to ST micro-damage at the initiation of failure. E_{110} is the pristine longitudinal moduli. A CB degradation parameter which relates the degraded shear moduli to the moduli values at the initiation of failure, E_{110}, E_{22}^* and G_{12}^* can be introduced. The failure parameter

has a minimum value of zero when no CB degradation has occurred, that is no macroscopic cracks have formed and a continuum can be assumed. A maximum value of one will on the other hand represent a fully cracked material with no global stiffness contributions in the associated direction of loading. The CB failure parameters are,

$$D_I^f = 1 - \frac{E_{11}}{E_{110}} \tag{5.61}$$

$$D_I^m = 1 - \frac{E_{22}}{E_{22}^*} \tag{5.62}$$

$$D_{II}^m = 1 - \frac{G_{12}}{G_{12}^*} \tag{5.63}$$

Finally the stress-strain constitutive relationship can be written up in terms of the CB failure parameters and the stiffness moduli at the initiation of failure. Assumptions are the same as before in Eq. 5.11. The non-continuum stress-strain constitutive relation becomes

$$\begin{bmatrix} \sigma_{11} \\ \sigma_{22} \\ \tau_{12} \end{bmatrix} = \begin{bmatrix} E_{11}(1-D_I^f) & \nu_{12}E_{22}^*(1-D_I^m) & 0 \\ \nu_{12}E_{22}^*(1-D_I^m) & E_{22}^*(1-D_I^m) & 0 \\ 0 & 0 & G_{12}^*(1-D_{II}^m) \end{bmatrix} \begin{bmatrix} \epsilon_{11} \\ \epsilon_{22} \\ \gamma_{12} \end{bmatrix} \tag{5.64}$$

It is important to understand that the above equation does not hold for a continuum. The formulation is merely for representation purposes for visualizing the CB traction separation degradation scheme as well as calculating the stress state to be passed back to the FE solver.

As a final remark, although the introduction of the characteristic element length allows for mesh objectivity to be achieved, there exists a maximum element length for the material model. The physics of the problem makes it clear that a maximum

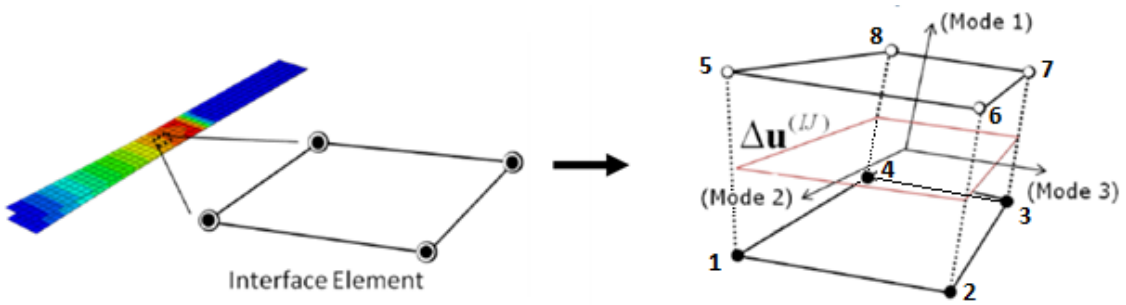

Figure 5.4: Schematic for DCZM element.

element length limit needs to be preserved to ensure that no snap-back occurs. Snap-back is a numerical behavior that occurs when the fracture toughness of the element is smaller than the internal strain energy of the element at failure initiation. For the element to be able to satisfy the correct fracture energy dissipation it is forced to reduce the displacement and therefore a non-physical snap-back occurs. A mesh objectivity study was done by Pineda and Waas [88] to illustrate this. The critical element length restrictions can be seen below for the longitudinal direction (fiber failure) and the transverse direction (matrix mode I and II failure).

$$l_{el,\theta+90^\circ} < min\left[\frac{2G_{IC}^{f,T}}{E_{11}X_T^2}, \frac{2G_{IC}^{f,C}}{E_{11}X_C^2}\right] \tag{5.65}$$

$$l_{el,\theta} < min\left[\frac{2G_{IC}^{m,T}}{E_{22}^* Y_T^2}, \frac{2G_{IC}^{m,C}}{E_{22}^* Y_C^2}, \frac{2G_{IIC}^{m}}{G_{12}^* Z^2}\right] \tag{5.66}$$

where the added superscripts of T and C denote tension and compression values, respectively.

5.3 Inter-laminar Damage and Failure Model

The Discrete Cohesive Zone Method (DCZM) element is utilized for capturing the inter-laminar failure modes through node to node cohesive traction-separation laws. The DCZM element is a 8 noded interface element which connects two surfaces

together through a nodal traction-separation law. A schematic of the element can be seen in Figure 5.4. The DCZM element can model cohesive layers of zero-thickness and finite thickness. For illustration purposes the entire formulation of the element is not presented here, instead the relation between a single nodal pair is presented, nodal pairs 1 and 5, see Figure 5.4. The formulation of a nodal pair can then easily be extended to include all 4 nodal pairs for the entire element formulation. The subscript 1-5 will be used to denote the nodal pair from here onwards.

The stiffness matrix of the nodal pair is as follows,

$$K_{1-5} = \begin{bmatrix} K_I & 0 & 0 & -K_I & 0 & 0 \\ 0 & K_{II} & 0 & 0 & -K_{II} & 0 \\ 0 & 0 & K_{III} & 0 & 0 & -K_{III} \\ -K_I & 0 & 0 & K_I & 0 & 0 \\ 0 & -K_{II} & 0 & 0 & K_{II} & 0 \\ 0 & 0 & -K_{III} & 0 & 0 & K_{III} \end{bmatrix} \tag{5.67}$$

Where K_I, K_{II} and K_{III} are the stiffness matrix terms corresponding to mode I, mode II and mode III loading directions, respectively. The force vector for the nodal pair is,

$$F_{1-5} = \begin{bmatrix} -F_{15}^{I} & -F_{15}^{II} & -F_{15}^{III} & F_{15}^{I} & F_{15}^{II} & F_{15}^{III} \end{bmatrix}^T \tag{5.68}$$

where the subscript denotes the nodal pair and the superscript denotes the direction. In a similar manner, the nodal displacements are noted as,

$$u_{1-5} = \begin{bmatrix} u_1^I & u_1^{II} & u_1^{III} & u_5^I & u_5^{II} & u_5^{III} \end{bmatrix}^T \tag{5.69}$$

The formulation above can be extended to include all 4 nodal connections and arrive at the DCZM elements contribution to the global stiffness matrix. The final

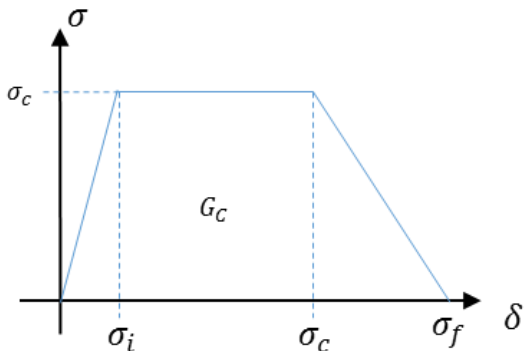

Figure 5.5: General trapezoidal cohesive law.

DCZM formulation becomes,

$$[K_{el}][u_{el}] = [F_{el}] \tag{5.70}$$

Where K_{el} would now be a 24x24 matrix and u_{el} and F_{el} would be 24x1 vectors due to the 8 nodes having 3 degrees of freedom each.

The element calculations are based on relative displacements of the nodal pairs, where the relative displacements for nodal pair 1-5 are calculated as follows,

$$\begin{bmatrix} \delta_I \\ \delta_{II} \\ \delta_{III} \end{bmatrix} = \begin{bmatrix} u_1^I - u_5^I \\ u_1^{II} - u_5^{II} \\ u_1^{III} - u_5^{III} \end{bmatrix} \tag{5.71}$$

where δ_I, δ_{II} and δ_{III} are the relative displacements of a single nodal connection for mode I, mode II and mode III, respectively. In the derivation to follow, a general nodal pair relative displacement will be used for demonstration purposes.

The element behavior is governed by a traction-separation (or cohesive) law. The cohesive law can be chosen as any arbitrary law. The trapezoidal/triangular law, Figure 5.5, is the most commonly used traction-separation law for toughened polymer matrix composites. The shape of the cohesive law can be tailored to represent the material behavior such as plastic deformation prior to strain softening or brittle-

stable fracture. The DCZM method can capture unloading as is shown in Figure 5.5. Energy dissipated, G, is the energy under the curve as shown in the figure. The traction separation law for each node is governed by the relative displacement of the nodal pairs. The trapezoidal/triangular separation law behavior will be demonstrated here in a general form, non-dependent on the mode of traction.

With the nodal separation known, the tractions can be calculated from the cohesive law properties,

$$\sigma(\delta) = \begin{cases} k^*\delta, & \text{if } \delta < \delta_i \\ \sigma_C, & \text{if } \delta_i \leq \delta < \delta_c \\ \sigma_C\left(1 - \frac{\delta - \delta_c}{\delta_f - \delta_c}\right), & \text{if } \delta_c \leq \delta < \delta_f \\ 0, & \text{if } \delta \geq \delta_f \end{cases} \tag{5.72}$$

Where δ is the relative nodal separation. k^* is the initial penalty stiffness prior to damage initiation and σ_C is the cohesive strength. δ_i is the separation at initiation of damage, δ_c is the initiation of failure which results in a traction reduction and a negative tangent stiffness. δ_f is the separation at complete failure at which the traction goes to zero.

The secant stiffness at any given point along the cohesive law can be calculated as,

$$k = \frac{\sigma(\delta)}{\delta} \tag{5.73}$$

where k is the secant stiffness. The critical nodal separations can be calculated directly from the cohesive law,

$$\delta_i = \frac{\sigma_C}{k^*} \tag{5.74}$$

$$\delta_c = \frac{\sigma_C}{k^*} + \alpha\frac{G_C}{\sigma_C} \tag{5.75}$$

$$\delta_f = (2-\alpha)\frac{G_C}{\sigma_C} \tag{5.76}$$

Where α is the trapezoidal coefficient. For a triangular cohesive law, α is set to zero so that $\delta_i = \delta_c$. The SERR at any given loading point is calculated as follows,

$$G = \begin{cases} \frac{1}{2}\sigma_C(\delta - \delta_i), & \text{if } \delta_i \leq \delta < \delta_c \\ G_c - \frac{1}{2}\sigma(\delta)\delta_f, & \text{if } \delta \geq \delta_c \end{cases} \tag{5.77}$$

The above derivation holds true for mode I, mode II and mode III. Mixed mode failure is governed by a 1st order power law,

$$\frac{G_I}{G_{IC}} + \frac{G_{II}}{G_{IIC}} + \frac{G_{III}}{G_{IIIC}} \geq 1 \tag{5.78}$$

The above calculations are implemented in a user element subroutine for ABAQUS Explicit (VUEL). At each increment the nodal displacements are given and from them the relative displacements are calculated from Eq. 5.71. During the first increment the critical separations are calculated, Eq. 5.74-5.78. With the critical separations known, the traction can be calculated using Eq. 5.77. Finally the SERR is calculated with Eq. 5.77. Once the above calculations have been done for mode I, mode II and mode III at a given nodal pair, the mixed mode criterion is checked, Eq 5.78. If this is satisfied, all tractions are set equal to zero. Finally the forces can be calculated from the tractions, where the area associated with each nodal pair is 1/4 of the total element area. The force vector in Eq. 5.68 is then assembled and the right hand side (RHS) vector can be updated accordingly and transferred back to the FE solver.

Element size restriction is governed by Irwin's characteristic fracture length [55]. The element size is recommended to be at least 4 times smaller. Irwin's characteristic

fracture length is defined as,

$$l_{el} = \frac{1}{4}\frac{KG_c}{\sigma_c^2} \tag{5.79}$$

where, K is the penalty stiffness, G_C is the critical fracture energy, and σ_C is the critical cohesive strength, as defined by the cohesive laws. The minimum result for the three modes (cohesive laws) would determine the element minimum length.

5.4 Conclusion

A FE modeling approach for predicting impact damage in composite laminates and the following CAI response has been introduced. An impact model using plane stress elements for modeling of each individual lamina was introduced. The progressive damage and failure model, EST, for modeling of intra-laminar damage and failure modes was presented. EST uses ST to capture the matrix moduli (E_{22} and G_{12}) degradation due to shear micro cracking. CB is implemented for capturing macroscopic failure phenomena such as ply splitting and fiber rupture. CB uses an element characteristic length for scaling the fracture toughness to achieve mesh objectivity.

Inter-laminar damage and failure (delaminations), are captured by using DCZM elements. The DCZM elements are discrete nodal traction-separation elements which allow modeling of zero and finite thickness cohesive layers. The method allows for any arbitrary cohesive law to be defined. In the study presented in this thesis, a triangular cohesive law is used. The DCZM element captures delaminations due to mode I (peel) and mode II/III (shear slipping) effects. A 1st order power law mixed mode criteria is used for crack growth.

A high fidelity, yet computationally efficient, model for capturing the impact and CAI response of a composite laminate has been introduced. The model allows for capturing the full range of damage phenomena experienced by the composite laminate

when subject to impact and CAI. The model presented in this chapter will be used in chapter VI for modeling face-on impact and CAI corresponding to experimental results presented in chapter II. In chapter VII the model is utilized for capturing the coupon level impact and CAI experiments presented in chapter III, for edge-on impact test.

CHAPTER VI

Face-on Impact and CAI Finite Element Modeling & Results

6.1 Introduction

In this chapter the proposed FE model for predicting the face-on impact and CAI response of FRPC's is presented. A lamina level model based on shell theory is introduced. EST coupled with DCZM elements allows for capturing lamina level damage and failure in the 1-2 plane and interface (or through-the-thickness)damage and failure, respectively. The goal of the research was to develop a robust and efficient computational model for predicting impact and CAI on FRPC's. It was desired that the model would be applicable to laminates of any arbitrary thickness and stacking sequences, not being limited to traditional layup angles of $0°$, $\pm 45°$ and $90°$. The model was initially developed for face-on impact (and CAI) but was later on evaluated for edge-on impact predictive capabilities as will be shown in Chapter VII.

The model was intended for industry purposes and would therefore need to be robust (as previously mentioned) as well as keeping the computational time as low as possible. Many models that have been introduced recently for impact modeling that utilize 3D elements [11, 29, 70, 111]. Models that use 3D elements can however be computationally inefficient due the critical element length often being very small

(limited by the ply thickness as well as element aspect ratios being prone to issues). Many researchers have overcome the element restrictions by implementing in-plane cohesive elements for capturing ply splitting. While this method can produce high quality results that often resemble reality to a high degree, the predictive capability of the models (and robustness) can be questioned. The implementation of in-plane cohesive elements is highly mesh sensitive due to ply cracking being limited to certain areas.

First the impact modeling method will be introduced as well as the consecutive CAI run and the process of importing the initial CAI damage state. Input properties required for the model are presented, IM7/8552 material data is provided. The impact model is then verified against the high fidelity impact results presented in chapter 2.2. Impact study was conducted on IM7/8552 laminates with a general [50/40/10] industry stacking sequence. Impacts were conducted at a fixed energy of 25J with three different impact masses. Extensive post-impact damage inspection was conducted using ultrasound and microCT scanning techniques. The EST and DCZM material input parameters are given with details of the impact model. The impact model results are compared to experimental data and is found to show great agreement for both the impact response as well as the impact damage mechanisms.

Experimental data collected in the BVID study presented in Chapter 2.3 is used for further validation of the impact model and CAI. The BVID study was conducted on a different fiber reinforced polymer matrix material system than the above mentioned impact experiments. A BVID impact and CAI study was conducted on traditional layup (TL) specimens to establish the BVID limit of the material system. Ten different non-traditional layup (NTL) specimens were impacted at the established BVID limit and the impacted specimens were then subject to CAI. The impact model showed exceptional agreement with both impact and CAI results for the entire set of 11 laminate layups studied.

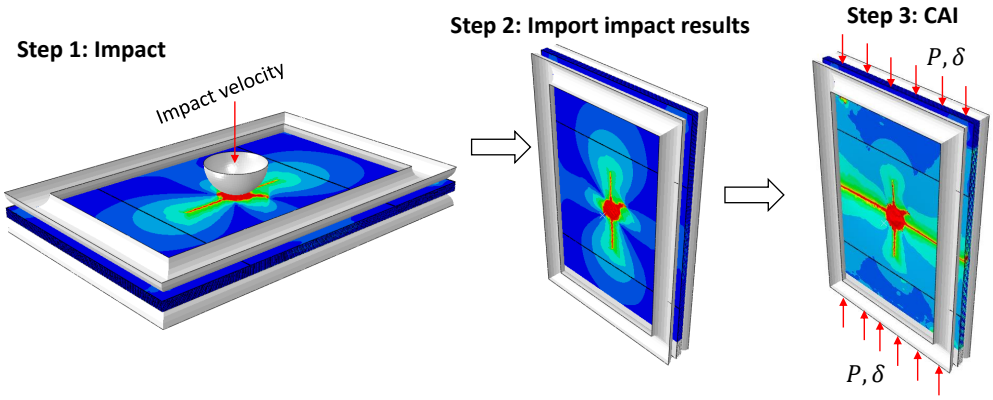

(a) Virtual impact and CAI steps.

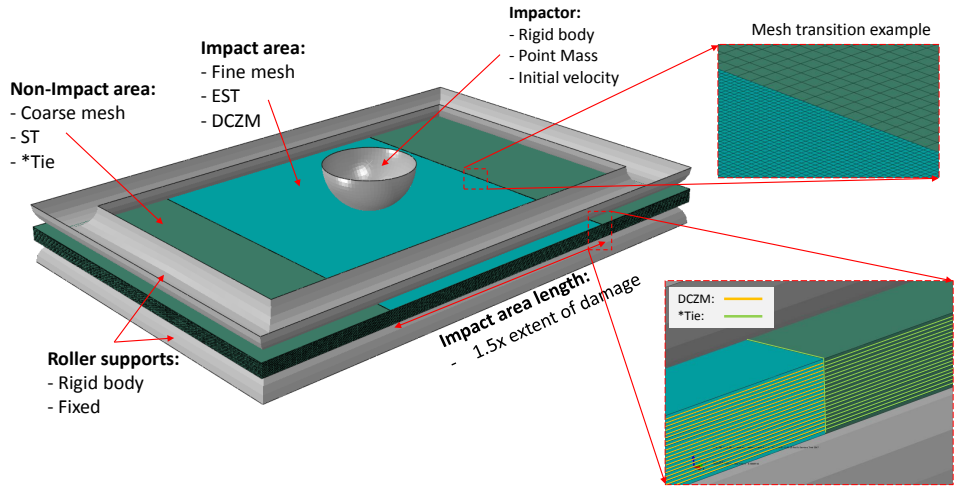

(b) FE model details.

Figure 6.1: FE modeling strategy showing steps (a) and model details (b).

6.2 Modeling Strategy

The model utilizes the Enhanced Schapery Theory (EST) material model and Discrete Cohesive Zone Method (DCZM) elements for modeling damage and failure in the intra-laminar and inter-laminar region, respectively. The two damage and failure modeling methods, EST and DCZM, have been presented in detail in chapter V. The model details can be seen in Figure 6.1(b). The impact and CAI events are captured using the same model for both experimental conditions. First the impact event is predicted and the impact damage is then used to predict the CAI experimental response,

Figure 6.1(a). The commercially available FE solver ABAQUS Explicit is used. The model approach utilizes 8 noded plane stress continuum shell elements with reduced integration (SC8R element in ABAQUS) for modeling each lamina individually. Continuum shells provide the benefit of having nodes on the top and bottom surface of the ply. This allows for capturing the traction separation relation of adjacent surfaces correctly without having to account for rotational degrees of freedom in the cohesive element formulation.

The model utilizes a "global-local" modeling technique to reduce computational cost. The "local" area is referred to as the "impact area" from here onwards. In the impact area (local model) the layers are connected by DCZM elements as well as the mesh being refined beyond the CB critical element size limit shown in Chapter 5.2. The full EST damage model is used in the impact area. Away from the impact area, the mesh is coarse and adjacent surfaces are connected by nodal tie constraints (*TIE). The CB model is suppressed in this area and therefore the element constraints are removed, ST is active and therefore any matrix moduli degradation due to micro damage evolution is captured. The impact area and non-impact area are modeled as separate continuum shell layers (in the same plane) which are connected by nodal tie constraints (*TIE), see Figure 6.1(b). This approach allows for a sudden transition from a refined mesh to a coarse mesh and therefore reduces the computational time.

The face-on impact model presented here has a mesh size of 0.5 mm by 0.5 mm in the impact area and 1.5 mm by 1.5 mm in other regions. The impact area was chosen to be sufficiently larger than that of the observed damage footprint of various low-velocity face-on impact experimental results. Caution should be taken when the impact area size is chosen. If the impact area is too small so that the impact damage is close to the boundary or even exceeds the boundary it will cause boundary effects to occur. The impact area was chosen to be 75 mm long, traveling in the longitudinal direction of the impact model. This length exceeded the damage extent of the impact

studies conducted in chapter II. The impact area was extended through out the width of the specimen in anticipation of the CAI failure modes.

Specimen dimensions are 150 mm by 100 mm, layups and thickness vary. The rollers are modeled as rigid shell elements. The rollers have a diameter of 12.7 mm and are positioned 6.35 mm in from the edge of the specimen. Impactor is also modeled using rigid shell elements with a point mass. A hemispherical impactor with a diameter of 20 mm and an impact mass of 7.5 kg was used for the IM7/8552 impact study. An impactor with diameter 25.4 mm and an impact mass of 21.6 kg was used in the BVID study.

Surface to surface contact is applied between the boundary rollers and the adjacent surfaces. Contact is also defined between the impactor and the top laminate surface. Frictional coefficient of 0.3 is used. The simulations were not seen to be sensitive to the frictional coefficient.

For the second step of the analysis, CAI, to be captured correctly the impact damage first needs to predicted correctly. The impact damage/failure state is to be used as the initial state of the CAI model. Further detail on the CAI initial damage import process is given in chapter 6.2.2. The rollers were imported directly and acted as the knife supports in the CAI experiments. The location of the roller to laminate contact is exactly the same as the knife supports in the CAI experiments. The only difference is that the roller diameter is larger than that of the knife supports. It was however deemed to be a reasonable assumption to use the roller supports in the CAI simulation. The bottom and top parts of the rollers do not effect the outcome of the CAI model. The CAI top and bottom experimental boundary conditions constrain any out-of-plane motion of 12.7 mm at the top and bottom of the laminate. The rollers lay well within the 12.7 mm boundary and are therefore not a concern. Once the impact results are imported over to the compression after impact model, and the virtual CAI is performed.

6.2.1 Continuum Shell Properties

The ABAQUS continuum shell element (as well as conventional shell element) is a displacement based Reissner-Mindlin plate theory element [50] and therefore accounts for through thickness shear deformations [1]. The transverse shear is linear through the thickness of the element, however to enable the shear calculations, the elements require shear correction factors. These values are normally calculated automatically by the ABAQUS solver, however when user subroutines are used with shell elements these values need to be defined specifically. The shear correction factors are input into ABAQUS as transverse shear stiffness values for the element section calculations. In addition to the shear correction factors, the thickness moduli (E_{33}) and effective thickness poisson's ratio need to be defined, $\nu_{effective}$. The effective poisson's ratio has no meaning when used in conjunction with the EST subroutine due to ϵ_{33} being calculated internally and not handled by the ABAQUS solver.

The thickness direction strains are calculated using simple stress-strain relations for a single lamina. While $\sigma_{33} = \tau_{23} = \tau_{31} = 0$ the strain in the thickness direction, $\epsilon_{33} \neq 0$, due to membrane stresses being non-zero. Solving for ϵ_{33} using the stress-strain relationship, the result becomes;

$$\epsilon_{33} = -\frac{\nu_{12}}{E_{11}}\sigma_{11} - \frac{\nu_{23}}{E_{22}}\sigma_{22} \tag{6.1}$$

The sections thickness moduli are estimated in accordance to the ABAQUS user manual [1]. The user manual recommends the use of twice the in-plane shear moduli, therefore, the thickness moduli of the shell section becomes;

$$E_{33} = 2G_{12} \tag{6.2}$$

For isotropic plates the transverse shear correction factor has been shown to be 5/6 [19]. However, for a composite laminate the transverse shear correction factors

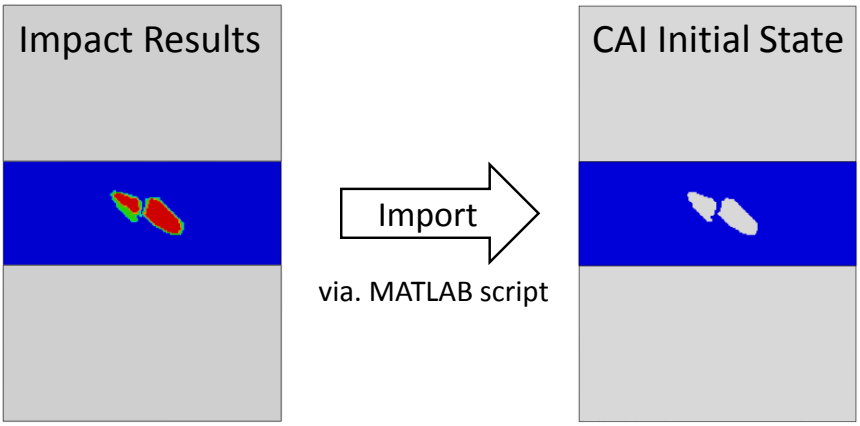

Figure 6.2: Schematic explaining the EST damage and failure model.

depend on which direction is being considered. For a transversely isotropic material, such as the case for a single lamina, the transverse shear stiffness become quite simple and they only depend on two material properties and the thickness of the layer [1]. Since the FE model introduced models each individual lamina as a separate continuum shell layer, the transverse shear stiffness values become,

$$\begin{aligned} K_{11}^{ts} &= \frac{5}{6} G_{12} t \\ K_{22}^{ts} &= \frac{5}{6} G_{23} t \\ K_{12}^{ts} &= 0 \end{aligned} \tag{6.3}$$

where 1 is the fiber direction and 2 is the transverse direction in accordance to the local coordinate system defined for the shell layer. The transverse shear stiffness is only updated at the pre-processing step of the ABAQUS Explicit solver and can therefore not be updated during the simulation. This is one of the major drawbacks of the shell model.

6.2.2 Compression After Impact Model

For the CAI prediction to be captured correctly the impact damage state needs to be captured as closely as possible. Once the impact results are at hand it is important that the damage in the CAI model is identical to that of the impact model. Previous studies by Olsson et al. [84], has shown that estimations or simplifications of impact damage areas is not a viable approach for predicting the CAI response of the laminate. Such artificially seeded damage areas are often represented as circular/elliptical delaminations or artificial "holes" in the laminate acting as degraded material properties due to impact damage. It is therefore required that the complex and rich damage and failure phenomena observed in the impact experiments, and captured by the FE impact model, is directly translated over to an FE model for the CAI response.

The ABAQUS command *Import was used for importing the impacted laminate over to the CAI model. The *Import is able to import any stress, strain and displacement state of the impact model as well as the user defined state variables from the user defined material model, EST in this case. The *Import command is however not able to import any results from user defined elements, DCZM elements in this case. The need for a separate approach for transferring over the inter-laminar damage state of the impact specimen was therefore required.

The inter-laminar damage state was imported by directly updating the input file. The results of the DCZM elements were output and a simple MATLAB script was written that would read in the DCZM results and then delete "failed" elements from the CAI input file. Figure 6.2 shows a representative import process. The gray area refers to no DCZM elements, blue is undamaged, red is fully 'failed while green is in between. The import criteria for "failed" elements is that if the mixed mode criterion is above 0.5, the element is considered sufficiently damaged to be removed form the CAI simulation. That is, if the following criterion is satisfied, the element will be

deleted from the CAI model.

$$\frac{G_I}{G_{IC}} + \frac{G_{II}}{G_{IIC}} + \frac{G_{III}}{G_{IIIC}} \geq 0.5 \tag{6.4}$$

It was found that rarely the elements were found to have initiated damage and were below a mixed mode failure index of 0.5 and therefore it was found to be an effective way of importing the damage state to the CAI simulation while keeping the delamination shapes unaffected.

In the experimental procedure, the CAI specimens are subject to quasi-static compressive loading. For faster computational times, mass scaling was used in the explicit FE solver. It was found that the model was reasonably sensitive to the mass scaling. Too high of a mass scaling can cause unstable behavior and failure at the initiation of loading. The model rate of loading was set to 2 mm/s and a variable mass scaling was used so that the stable time increment would not be smaller than $1e^{-5} - 2.5e^{-5}$ for any element. This combination proved to be very stable as well as the peak load predictions being converged at that stage.

6.2.3 Input Properties and Material Response

The in-plane and cohesive material models were explained in detail in Chapter V. The intra-laminar material response as modeled in the FE impact and CAI model can be seen in Figure 6.3. The compressive failure modes are shown here with their characteristic through-the-thickness failure response, however due to a plane stress model these failure modes are not captured in a physical manner but estimated through in-plane modes. The compressive matrix failure is modeled using a close to plateau crush strength (slight downward slope is used) at failure initiation, the reasoning behind this behavior is to capture progressive crushing as well as a way of bypassing the critical element size constraint introduced by CB. The face-on impact model was not seen to be sensitive to the matrix compressive failure mode and therefore this

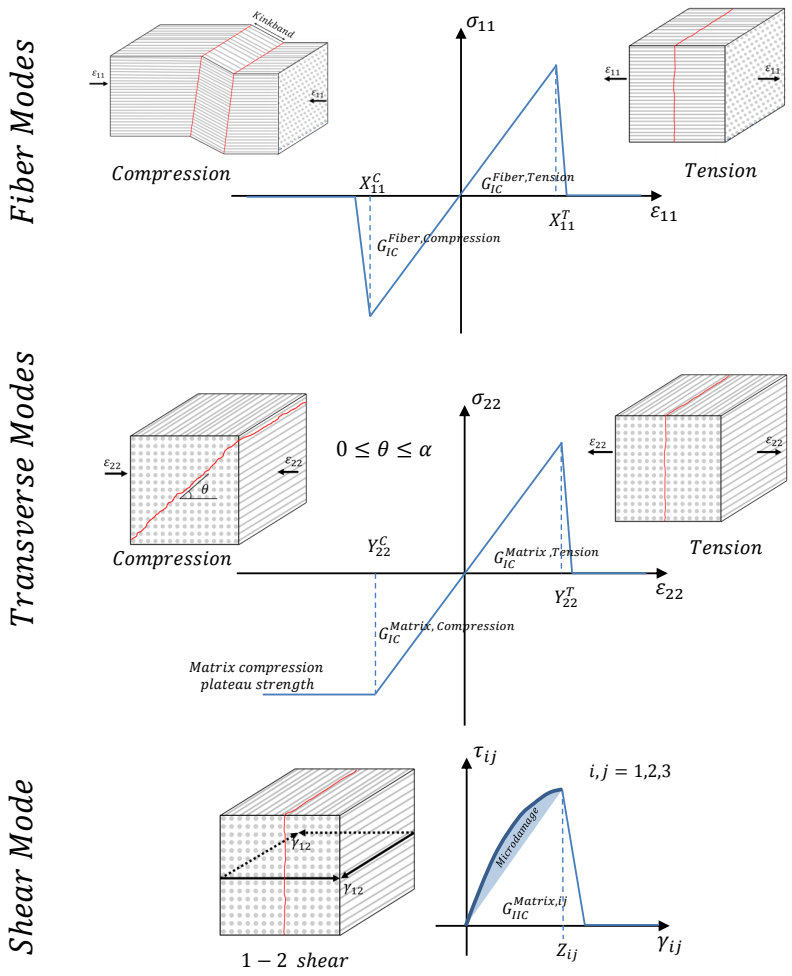

Figure 6.3: Intra-laminar material behavior as used in the FE model.

was deemed a reasonable assumption. For computational robustness and stability a residual stiffness is introduced at "full failure" of any mode. The residual strength was chosen to be lower than 1% for each mode of failure.

Material characterization of both materials used in this thesis was performed in house, experimentally or by inverse FE methods. The experimental procedures for the material characterization are described in Appendix C. The lamina elastic properties can be seen in Table 6.1. The longitudinal direction is referred to as the fiber direction.

The Schapery micro-damage functions can be seen in Figure 6.4. The Schapery shear micro-damage function, $g(s)$, was gathered from tension experimental data from $[\pm 45°]$ tensile specimens. The transverse micro-damage function was estimated

from inverse analysis of the [±45°] test. A hexagonally packed representative unit cell (RUC) micromechanics model is used for inferring the transverse stress-strain response. The in-situ matrix shear response is first backed out from the [±45°] tests using the concentric cylinder model (CCM) [77]. Plasticity theory is then used for calculating the equivalent stress-strain response of the matrix. Using the acquired matrix shear stress - shear strain response in the RUC micromechanics model will provide the transverse stress-strain response of the lamina. The downside of the approach is that the direction of loading is irrelevant and therefore the function in compression is assumed to be the same as in tension. The transverse micro-damage functions in tension and compression (separate functions) have been measured for the material system used in the BVID study using the approach presented by Schapery and Sicking [106, 112], and further details are shown in Appendix C.

Lamina fracture properties can be seen in Table 6.2. The fiber compressive failure strain was estimated using Considere's Construction [22], and the resultant failure strain was found to be 1.31% using a fiber misalignment angle of 1.2°. The value was later found to be quite high and better agreement with experimental results was achieved by using the experimentally measured fiber compressive strain of 0.97% as reported by Soutis et al. [67]. Effects of the compressive fiber failure strain value will be described later in the chapter. Fiber fracture toughness value in tension was backed out from inverse analysis of Single Edge Notched Tension (SENT) experiments modeled using EST. This value has proven to provide good agreement for multiple loading scenarios. The fiber fracture toughness in compression is however estimated from the tensile value and should therefore be used with care. The value in Table 6.2 was kept empty here since the material behavior post-peak was not driven by fracture energy. The transverse stress (σ_{22}) in the wake of compressive failure is kept at a constant plateau value in the case of progressive crushing behavior.

Inter-laminar fracture properties were measured at various rates using ASTM stan-

Table 6.1: IM7/8552 elastic lamina properties.

Fiber Direction Modulus (E_{11})	154,460 MPa
Transverse Direction Modulus (E_{22})	7,200 MPa
Shear Modulus (G_{12})	4,870 MPa
Poisson's Ratio (ν_{12})	0.340
Density (ρ)	$1.5e^{-9}$ tonne/mm^3

Table 6.2: IM7/8552 lamina fracture properties.

Fiber Tensile Failure Strain (X_{11}^T)	1.47%
Fiber Compression Failure Strain (X_{11}^C)	1.31% (0.97% [1])
Transverse Tensile Failure Strain (Y_{22}^T)	0.8%
Transverse Compression Failure Strain (Y_{22}^C)	4.62%
Shear Failure Strain (S_{12})	2.27%
Fiber Fracture Toughness in Tension (G_f^T)	40 N/mm
Fiber Fracture Toughness in Compression (G_f^C)	10 N/mm
Transverse Fracture Toughness in Tension (G_m^T)	0.384 N/mm
Transverse Fracture Toughness in Compression (G_m^C)	- N/mm
Shear Fracture Toughness (G_{IIC}^m)	1.335 N/mm

dards for Mode I and Mode II fracture toughness calculations, ASTM D5528 [116] and D7905 [118], respectively. The intra-laminar matrix fracture properties were assumed to be the same as the inter-laminar fracture properties due to experimental methods being unavailable for accurately measuring the intra-laminar fracture toughness. The cohesive strengths were gathered from peel off tests for Mode I, and single lap joint (SLJ) tests which were then used for backing out the cohesive strengths through inverse analysis. The penalty stiffness was chosen to be significantly higher than that of the transverse modulus of the material. While an infinitely large penalty stiffness would be desired, it is not possible to be used with a computational scheme. The stable time increment would approach zero for very large values. Therefore, a relatively high value, compared to the matrix material virgin stiffness was chosen. A value of 20,000 MPa/mm was used.

[1] Experimental value from Soutis et al. [67]

Table 6.3: IM7/8552 interlaminar fracture and cohesive law properties.

Cohesive Penalty Stiffness (k)	20,000 MPa/mm
Mode I Cohesive Strength (σ_C)	55 MPa
Mode II Cohesive Strength (τ_C)	72 MPa
Mode I Fracture Toughness (G_{IC})	0.384 N/mm
Mode II Fracture Toughness (G_{IIC})	1.335 N/mm

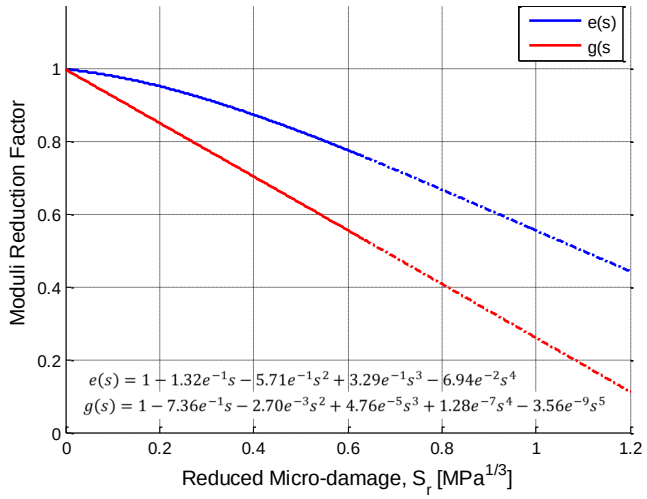

Figure 6.4: IM7/8552 Schapery Micro-damage curves

6.2.4 Computational Information

Computations were performed on an HPC cluster. The details of the computations can be seen in Table 6.4. The computational nodes used had 16 CPUS and a ram of 64gb. Parallel processing was used for both the face-on impact and CAI computations. Mass scaling was used in the CAI case, since it is a quasi-static loading rate, it was ensured that kinetic energies were negligible during the simulation. The CAI runs were limited to 8 nodes per job due to the *Import command in Abaqus requiring a large amount of ram for the pre-processing. It was therefore found that 8 CPU's were the maximum possible with the 64gb of memory that was available to the node, meaning that the pre-processing required at least 8GB of memory per CPU (it is believed that the pre-processing occurs on 1 CPU only, and therefore that is the limiting factor).

Table 6.4: Computational details for the face-on impact and CAI model.

Number of Elements	1,243,507	≈1,235,023
Number of DoF	4,087,383	≈4,083,906
Total step time (s) 0.0085	1	
Stable time increment (s)	$4e^{-8}$	$\approx 2.4e^{-6}$
Mass scaling used (Y/N)	No	Yes
Number of CPUS	48	8
Total run time (Hours)	15	53

6.3 High Fidelity Impact Modeling Results

The predicted impact response for the experimental results presented in Chapter 2.2 can be seen in Figure 6.5. The experimental results have been plotted as the maximum and minimum bound (gray area bounded by solid black lines) and an average impact response (dotted black line). It can be seen that the pre-peak response is captured quite accurately when examined with respect to both the load vs. time and load vs. displacement experimental response. The post-peak response deviates from the experimental results. As previously mentioned, in the experiments the load goes to zero when the rebounding impactor is still $\approx 2.6mm$ away from the initial contact position (zero point on the plot) while the back surface of the laminate relaxes to a permanent deformation of $\approx 0.37mm$. Comparing the back surface displacements of the model to experimental findings, Figure 6.6, reveals that the pre-peak displacements are slightly over predicted yet showing a reasonable agreement. The post-peak displacements however do not match up time-wise and it can be seen that the overall rebound of the FE model is slower than the experimental results.

Furthermore, by plotting the impactor and maximum back surface displacements from the experiments and model, more detail was revealed, Figure 6.7(a). The trends between impactor and back surface displacements seem to be similar between the model and experiments. The displacement is however over predicted for both cases. The plot furthermore shows that the predicted impactor displacements beyond $7ms$

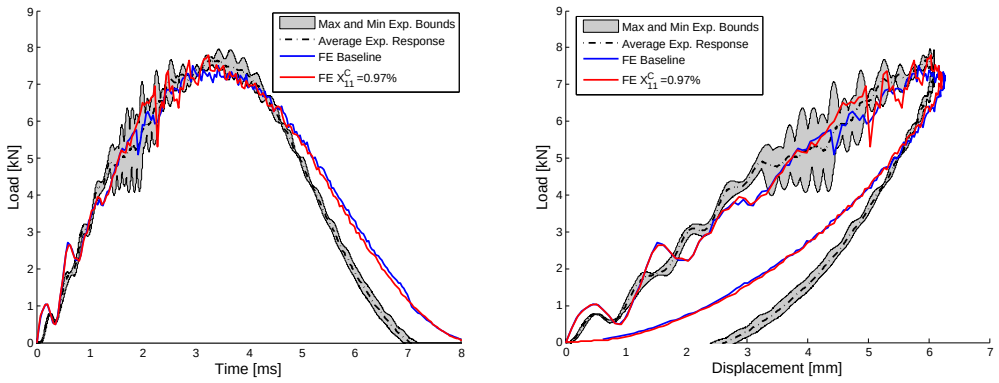

(a) Load vs. time comparison.

(b) Load vs. displacement comparison.

Figure 6.5: Impact model predicted impact response.

are not too far off from the experiments. Therefore the slower rebound respond of the model can be assumed to be from a material behavior that is incorrectly captured. This could be caused by multiple factors, and most likely a combination of friction between delaminated interfaces or between impactor and indentation crater (which was not seen to be sensitive in the shell model but possibly in a 3D model where through-the-thickness behavior is captured more accurately), crack debris, or non-conforming crack surfaces. Figure 6.7(b) shows the impactor kinetic energy comparison. The same trend can be seen as from previous results. Good agreement is achieved in the pre-peak regime. The impactor kinetic energy is brought to a halt correctly but the rebound over shoots resulting in roughly 75% increased kinetic energy at rebound.

The problem can be simplified by thinking of it as a simple mass and spring problem, Figure 6.8 where the spring can show a degradation in stiffness as well as permanent deformation due to the impact from the mass. When the spring now rebounds, it only rebounds a portion of the distance as well as the stiffness being lower. This results in the strain energy released dissipated from the spring to the rebounded mass being much smaller than it would be without the stiffness degradation and permanent deformation. As an effect, the mass rebound will be slower and shorter due to the reduced kinetic energy.

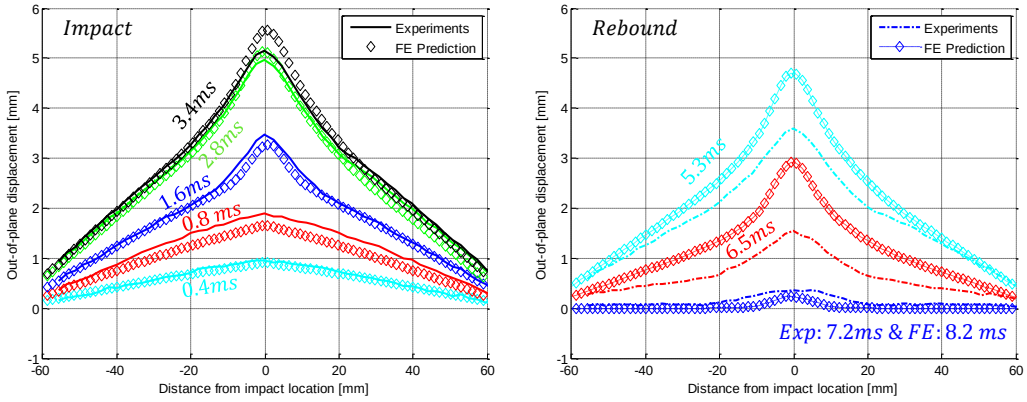

(a) Impact event, loading

(b) Rebound event, unloading

Figure 6.6: Out-of-plane displacements of the back surface of the laminate, experiments compared to FE results.

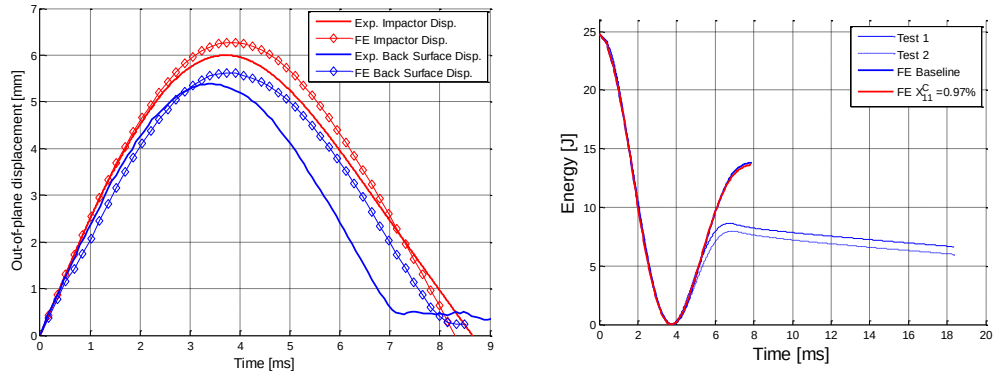

(a) Impact and maximum back surface displacement vs. time

(b) Impactor energy vs. time

Figure 6.7: Further comparison of experimental and FE model results.

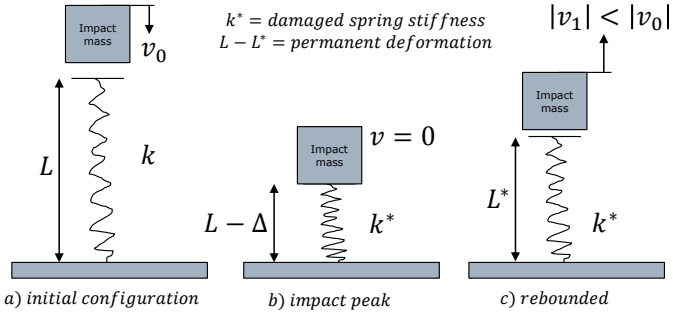

Figure 6.8: Simplified spring-mass impact model for demonstration.

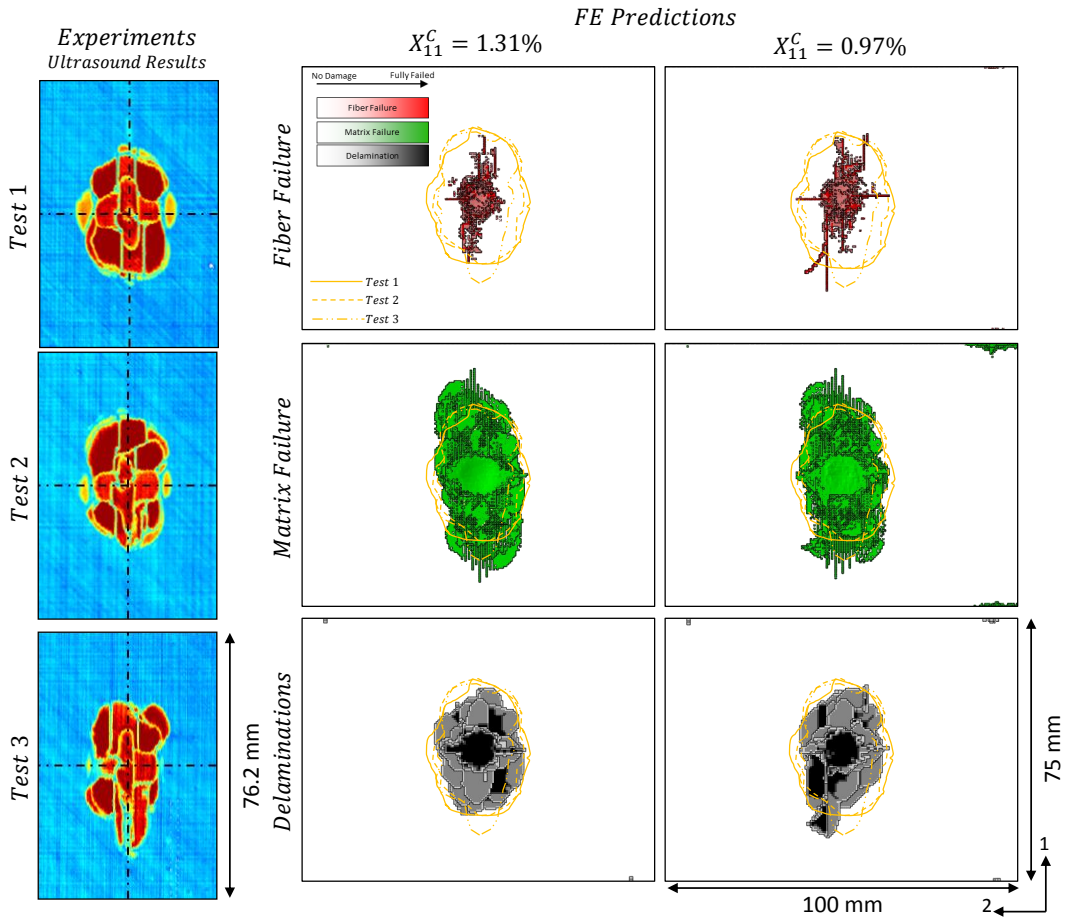

Figure 6.9: Comparison of ultrasound scan footprints to FE predicted footprints for fiber, matrix and delamination failure. Experimental footprint outlines is presented as yellow boundaries on top of the FE results.

The damage footprint for each of the predicted failure modes can be seen in Figure 6.9. The figure shows the fiber, matrix and delamination failure footprints for the initial and reduced X_{11}^C value. The ultrasound scan results from the experiments are shown on the left side for reference as well as the boundaries being over lapped on top of the FE model results for better comparisons. An overall good agreement was seen between the ultrasound results and the model. The FE baseline case fiber and delamination failure is within the experimental bounds. The fiber kinking in the top layers, which was observed in microCT scans, was achieved in the reduced X_{11}^C case The fiber and delamination failure extent now exceeds the results from test 1 and 2

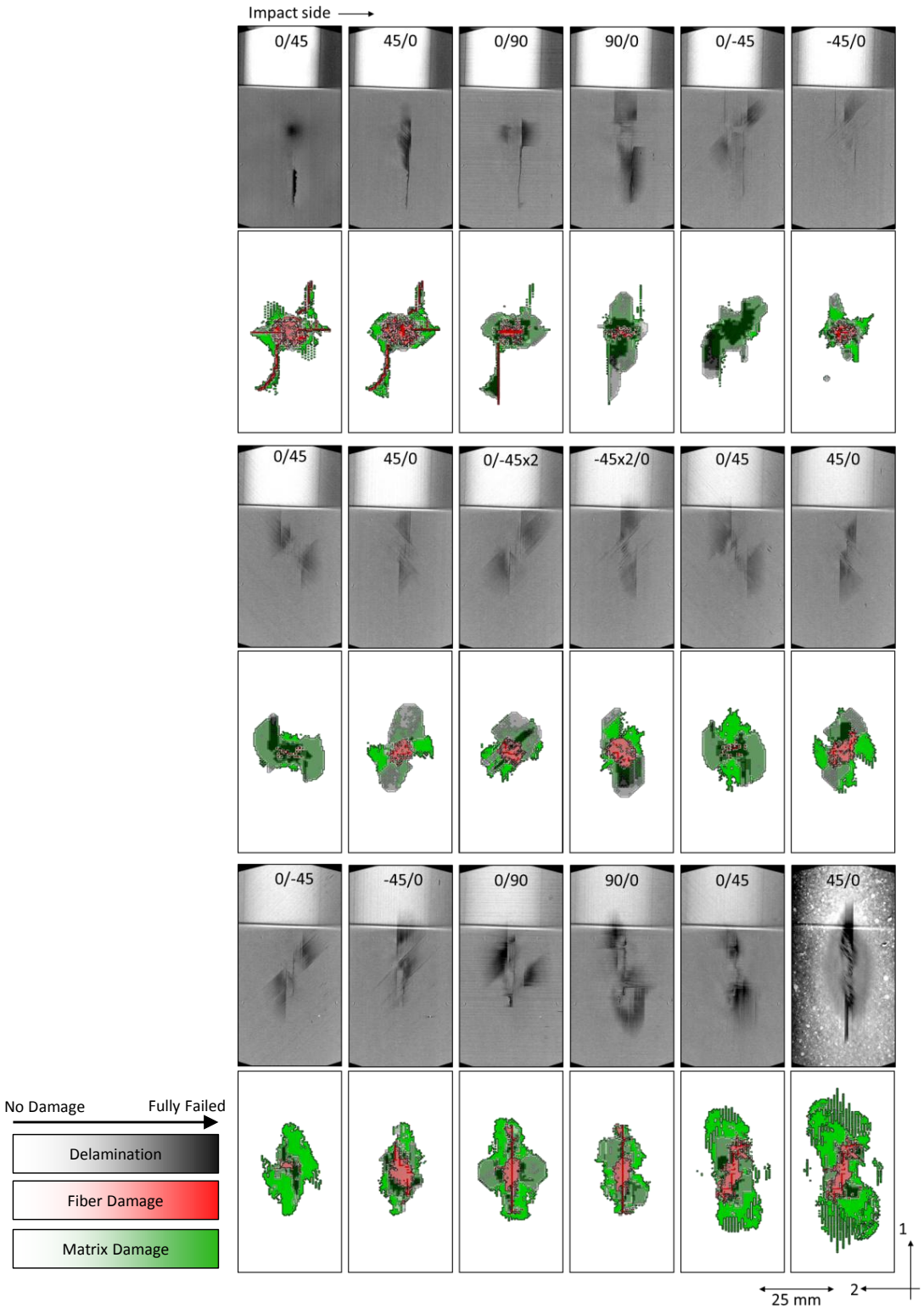

Figure 6.10: Comparison of microCT scans to FE model results.

while showing a fairly similar behavior to test 3. The specimen from test 3 was the one used for microCT scanning.

The matrix failure footprint is bounded by the back surface splitting. When compared to the ultrasound scan results, the model seems to over-predict the damage quite drastically. However, when compared to the microCT results it can be seen to be quite on par with the back surface splits of the impacted specimens, Figure 6.10.

The damage contours for each interface and the adjacent plies has been gathered in Figure 6.10 for comparison to the microCT data collected from the impacted specimen. The results from the microCT were best shown as the damage at an interface and the adjacent plies. This method is good for showing the estimated damage size and shapes. However, due to the method, some of the damage in either the top or bottom ply of the interface may be lost or be faint. When the entire set of interfaces is viewed, the results are quite good. More detailed microCT slices can be seen in Appendix B. The damage contours for the interfaces were collected from the model and assembled in a similar manner to the microCT images. Matrix failure is shown in green, delamination is represented by black color, and fiber failure is represented by red. Matrix failure is plotted first, the delamination failure is then plotted on top with a 25% transparency so not to overshadow the matrix failure areas. Fiber failure is then plotted last due to the significance of it as well as it having the smallest footprint.

An excellent agreement is seen between the microCT results and the FE model failure patterns, size and locations. The predicted delamination sizes are on par with the experiments as well as the delamination patterns. Delamination jumping between interfaces, bounded by in-plane splits, can be seen in interfaces 4 and 5 as well as other ones. When the fiber failure between the experiments and the model is examined it can be seen that a good agreement is achieved. Using the reduced compressive fiber failure strain, the top layer kinking was captured. The 4th ply, 90°, shows kink

failure that is accurately captured by the FE model (at a different location, as can be expected when comparing a perfect structure to a real structure with imperfections). The resulting kink in the 4th ply causes ply splitting in the adjacent layers as well as fiber kinking in the second ply, 45°. The 45° ply shows a zig-zag failure where fiber and ply splits take turns resulting in a crack orientated along the 0° direction. The model captures the fiber failure in the 45° ply, initiation is good but then it steers away from the 0° direction.

The model predicts fiber failure of different magnitudes in most plies. This seems to agree well with the experimental results where fiber failure can be seen in many plies when examined carefully, for example interface 11-13 show signs of fiber failure in the 45° plies. Closer to the bottom of the laminate in interfaces 14-18, extensive fiber failure can be seen. This failure is captured to a quite fine detail by the model. The straight fiber crack visible in the bottom 90° ply is represented in the model as well as the crack in the bottom most 45° layer having an oddly shaped fiber failure path which is captured to some extent by the model.

6.4 BVID Impact and CAI Modeling Results

6.4.1 BVID Impact Model Results

The predicted impact results for the BVID study on the TL specimens as well as the NTL specimens impacts can be seen in Figure 6.11. Figure 6.11(a) shows the load-time history predictions compared to the experimental results previously shown in Chapter 2.3.1. The load-time histories have been offset for better visualization The offset is $9ms$ for each impact curve above the 50% BVID limit impact. The impact model was successful at predicting the load-time history for multiple different impact energies. Furthermore, the model predicted the halted peak load growth that was seen in the 112.5% BVID impact energy case. The impact model was capable of

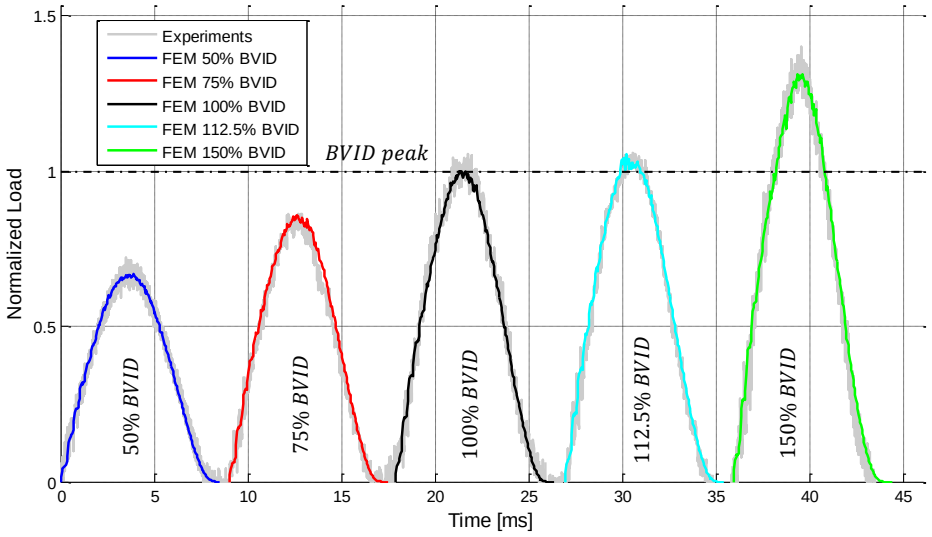

(a) Load vs. time comparison

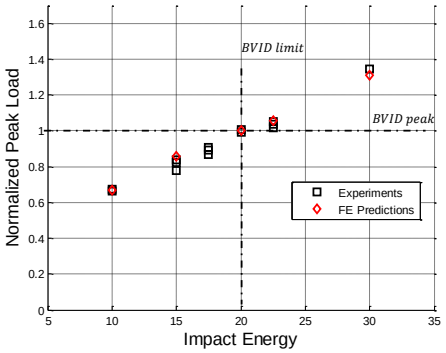

(b) Peak load vs. impact energy

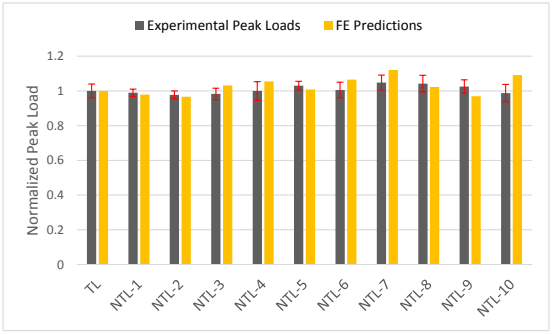

(c) Peak load comparisons for TL and NTL

Figure 6.11: Impact response results for the BVID impact study on the TL specimens (a) and (b). TL vs. NTL load comparisons (c). Typical back surface deflection for a BVID impact (d)

predicting the impact peak loads for each of the impact cases with great accuracy as can be seen in Figure 6.11(b).

The model results for the NTL impacts at the BVID impact limit are shown in Figure 6.11(c). An overall good agreement was seen between experimental and model results for the NTL impact cases. Roughly half of the impact peak loads are within the experimental bounds while the rest are not far off. It is worth noting that the exact same impact model was used, apart from some laminates being thinner by 1-2

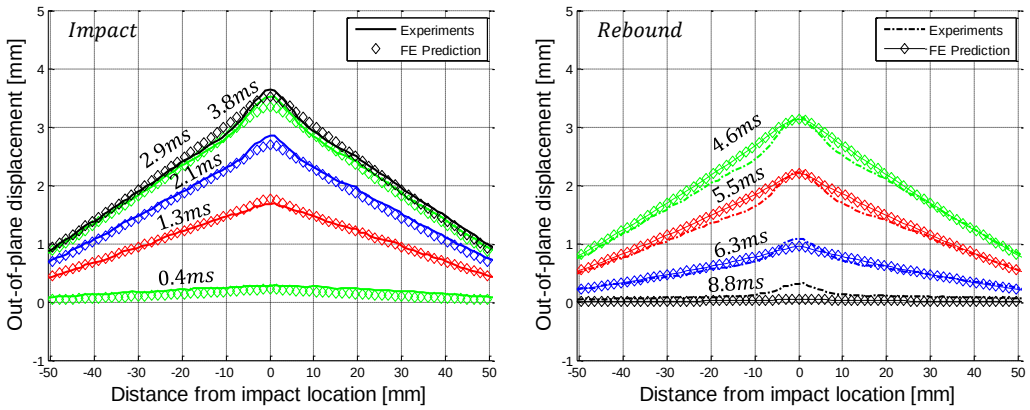

(a) BVID Impact event, loading

(b) BVID Rebound event, unloading

Figure 6.12: Out-of-plane displacements of the back surface of the TL laminate subject to BVID impact. Experiments compared to FE results.

plies. No mesh alignment was used for the non-traditional ply angles.

The predicted out-of-plane deflection of the back surface can be seen in Figure 6.12. The plots show the displacement of a section traveling through the impact center along the longitudinal direction of the specimen, similar to previously reported results. The model shows overall great agreement with experimental results. While the localized deformation is not captured, the sharp gradient of the shape is. Once the damage, which causes the localized deformation dimple, seen beyond the $2.1ms$ curve sets in, the model starts over predicting the displacement at $-20mm$ to $20mm$ from the impact center while either matching or slightly under-predicting the maximum deformation.

Damage/failure footprints for the BVID impacts can be seen in Figure 6.13. The figure shows the extent of in-plane fiber and matrix damage and failure as well as the delamination extent for the $50\% - 112.5\%$ BVID impact predictions. The extent of impact damage can be seen growing steadily with increased impact energy. Fiber failure in the top three layers $(45°/90°/-45°)$ is seen to increase drastically beyond the BVID limit. The same can be said for matrix failure. Fiber failure now propagates in two kinks traveling parallel to each other away from the impactor, and this type

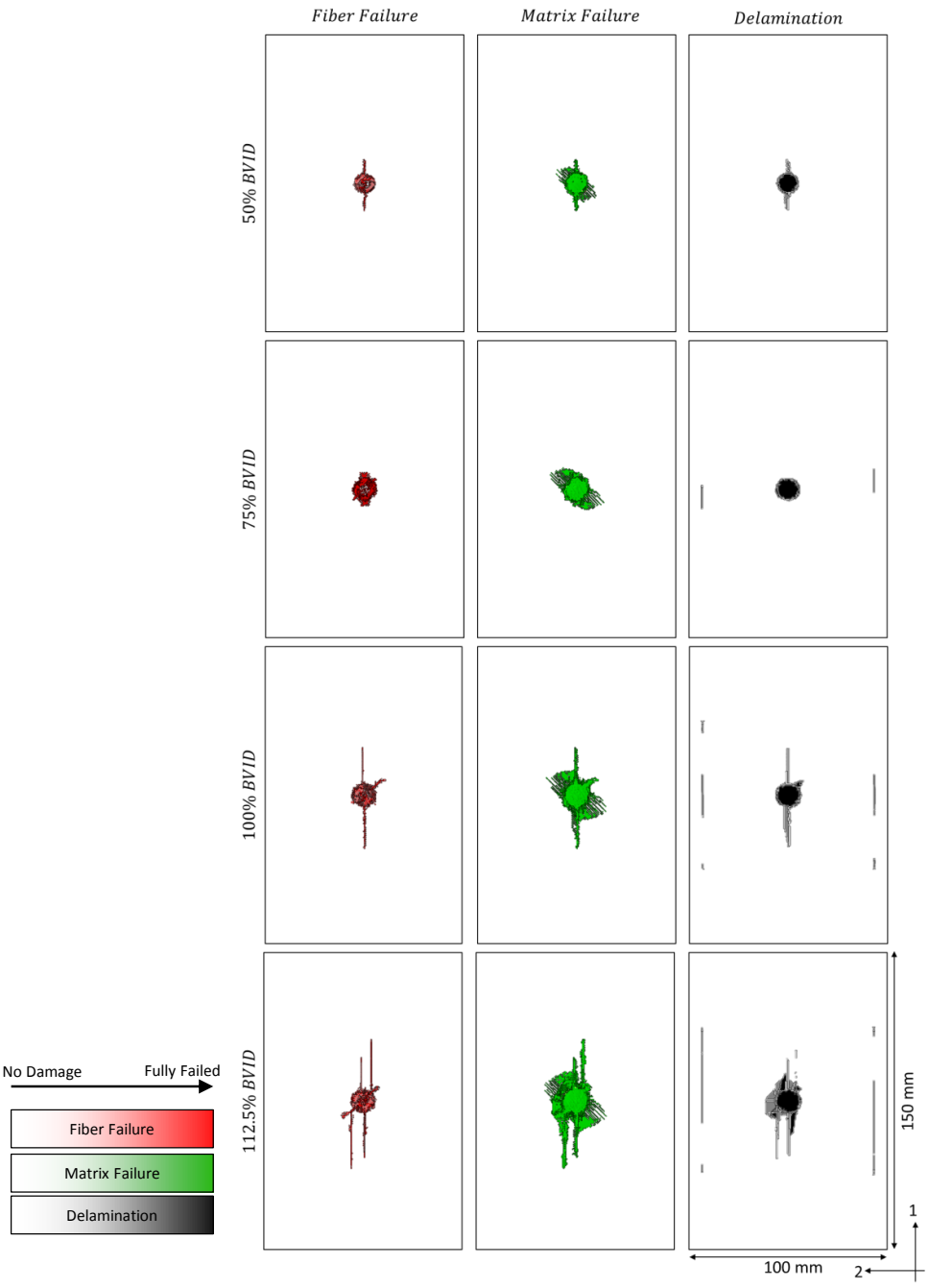

Figure 6.13: Impact damage footprints for the BVID impact study predictions. Footprints for fiber failure, matrix failure and delamination are shown.

of behavior was not observed in the experiments. Delaminations are growing in a similar manner. It is also notable that the 75% BVID case does not show any fiber failure at the top surfaces while the other energy cases do.

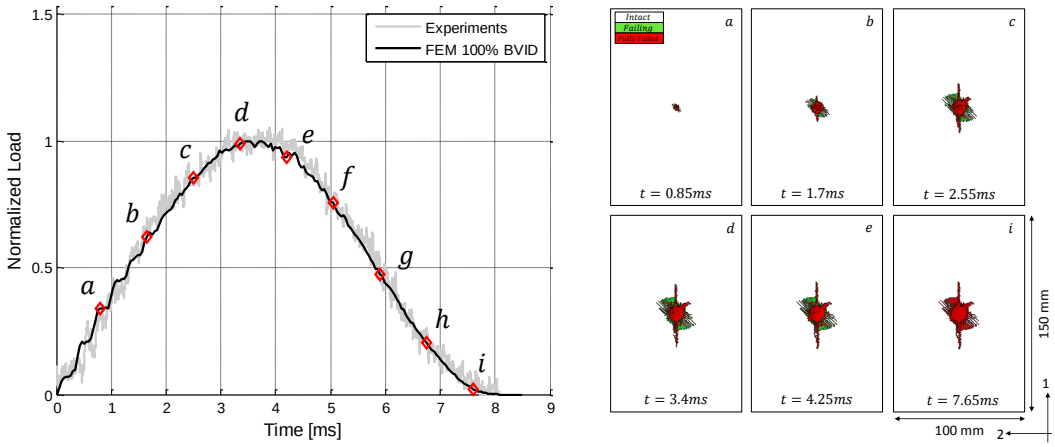

(a) BVID impact load curve in detail

(b) Damage footprint growth during impact

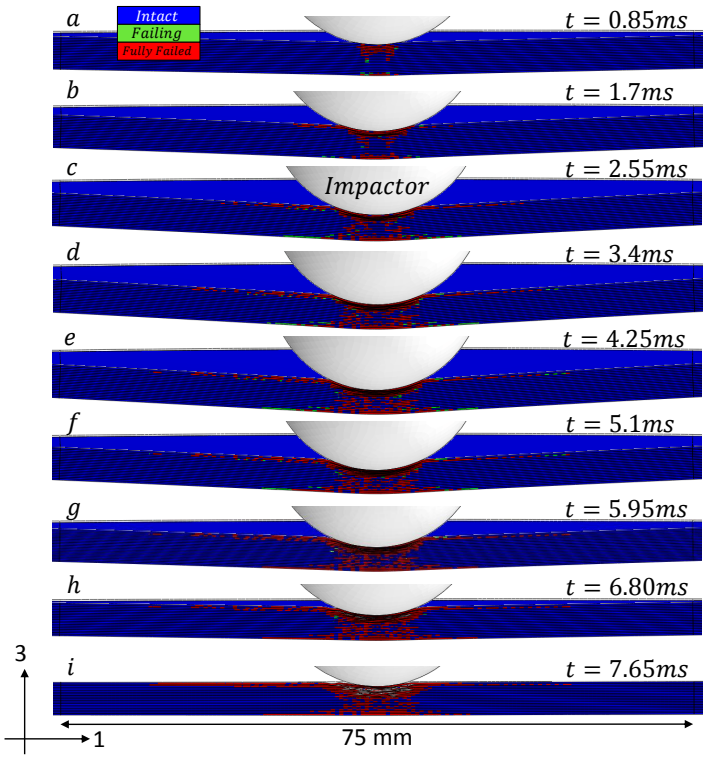

(c) Damage growth shown for a 1-3 plane section through the impact center

Figure 6.14: BVID impact model damage growth shown in detail, matrix failure is used as a reference of damage extent. Load curve with time intervals shown in (a), damage footprints in (b) and 1-3 section view of damage in (c).

Figure 6.14 shows the progressive damage and failure during the impact event. The figure shows the impact at the BVID limit. Time intervals have been marked

on the load-time history in Figure 6.14(a). Time intervals range from (a)-(i) with each time jump being $0.85ms$. Figure 6.14(b) shows the overall damage footprint at time intervals (a)-(e) and (i). The damage extent grows steadily until the peak load. At point (e), beyond the peak load, the extent of damage seems to have reached its final failed state. While some elements in the bottom most plies have yet to reach full failure, they do so during the rebound event. This effect is most likely caused by a combination of the element being close to full failure as well as dynamic effects. Finally in Figure 6.14(c) a section view is shown. A section in the 1-3 plane traveling through the impact center is shown at intervals (a)-(i). At the initiation of impact, (a), damage in the upper plies can be seen as well as initiation of matrix damage in the bottom two plies. As the impact event goes on, the fiber kink in the top plies can be seen initiating (b), and propagating in the following frames. Back surface damage initiates early on (a) and propagates to a maximum at (e), further energy dissipation is then seen until (g). Mid-plane damage seems to initiate early but propagation seems to be slower than that of the top and bottom plies.

As a final comparison of the predicted damage extent and failure modes, the results are compared to the experimental microCT scan results similar as in the previous chapter, Figure 6.15. The model results have been assembled to show the model results in a similar fashion as the visualization of the microCT results. That means that each interface and the adjacent plies are shown in a single image. Each failure mode is represented with a different color scale. Delamination is marked by white to black, fiber failure by white to red. Matrix failure is represented by two colors, one for the top ply and another for the bottom ply at each interface. The top ply matrix failure is shown in green and the bottom ply with yellow. The model shows great agreement with the experimental results. The top most plies accurately capture the fiber kinking in the second layer, 90° ply, which then results in zig-zag fiber failure and ply splits in the first and third layer, 45° and -45°, respectively.

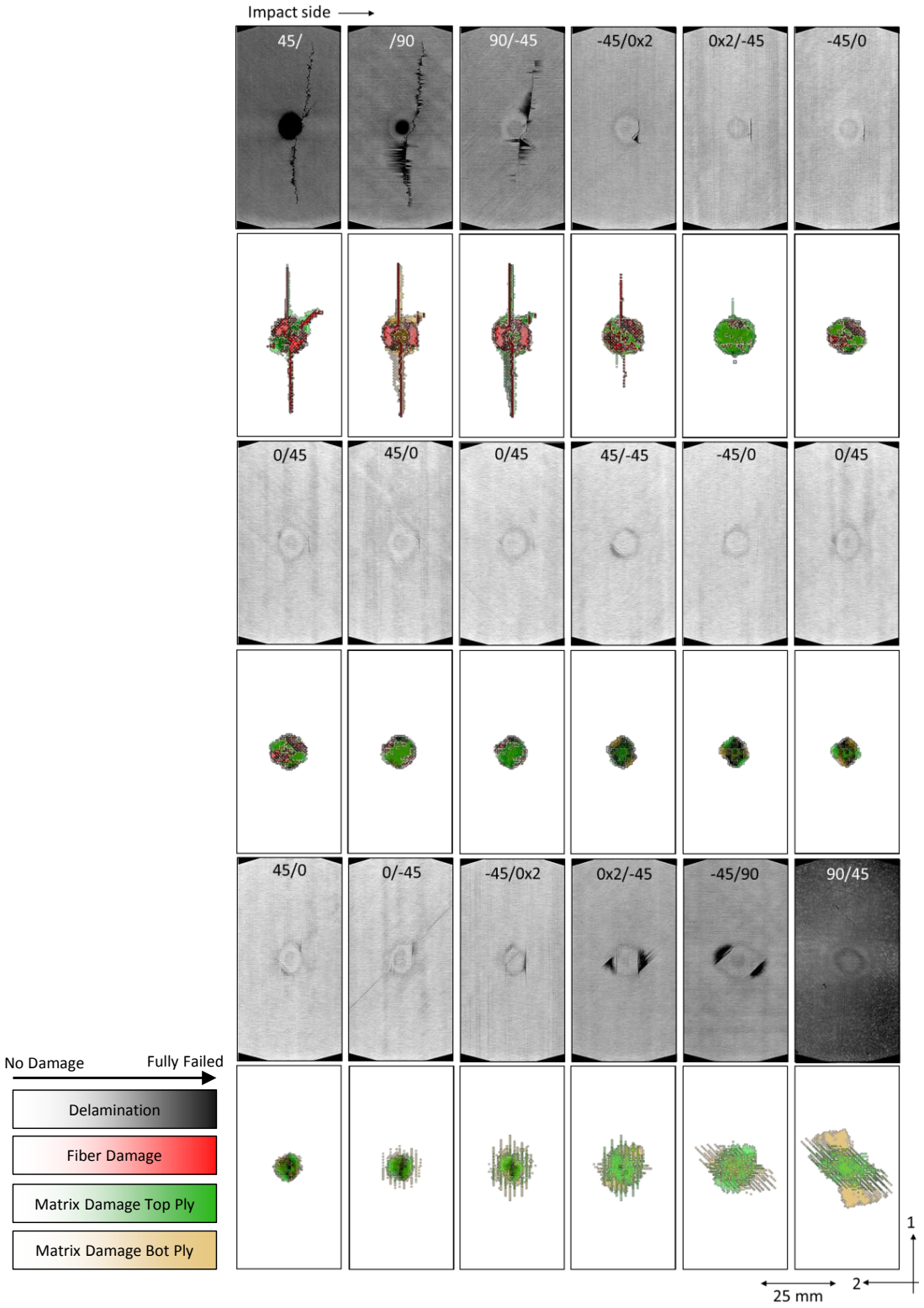

Figure 6.15: Comparison of microCT scans to FE model results for the BVID impact.

A few clear ply splits are seen in the experiment in interfaces 4-13. These ply splits are not "directly" seen in the model but instead a circular matrix failure area is observed in each ply as well as delamination in each interface. This circular area is fairly similar in size to the circles that were observed in the experiments, as was previously mentioned in Chapter 2.3.1. In the fractography results, Figure 2.14, through-the-thickness matrix cracks with varying sizes can be seen traveling the entire thickness of the specimen. These shear matrix cracks will end up resulting in delamination initiation and in some cases growth. It is therefore concluded that the impact model is capturing these through-the-thickness shear matrix crack formations in the 1-2 plane as mode I and mode II cracks, as well as delaminations. Although the cracks are not captured in a discrete manner since, as previously mentioned, the computational model uses a "smeared" method and therefore the cracks get smeared over the entire circular area.

As the bottom most plies are reached, the failure mode transitions from through-the-thickness shear modes of failure to a more tensile dominated matrix failure. Now the model can be seen predicting the ply splits to some extent. The model is seen to capture the characteristic crack spacing to some extent. This spacing can be seen both in the microCT scan as well as the microscopic image in Figure 2.14. The crack spacing dimensions should be taken with a grain of salt since results of such are typically very mesh dependent. The splitting on the back surface of the laminate, shown in the last interface, shows good agreement with experimental results.

The effect of elevated rate inter-laminar properties did not have a big impact on the results. By increasing the G_{IIC} value by up to 40%, the maximum increase shown in Chapter IV, the load-time history and damage footprints were almost identical. The mode I fracture toughness does not have a large effect on the model results and therefore the more drastic drop in G_{IC} did not have a big impact. It is possible that an impact event at a higher energy would show some significant difference, however

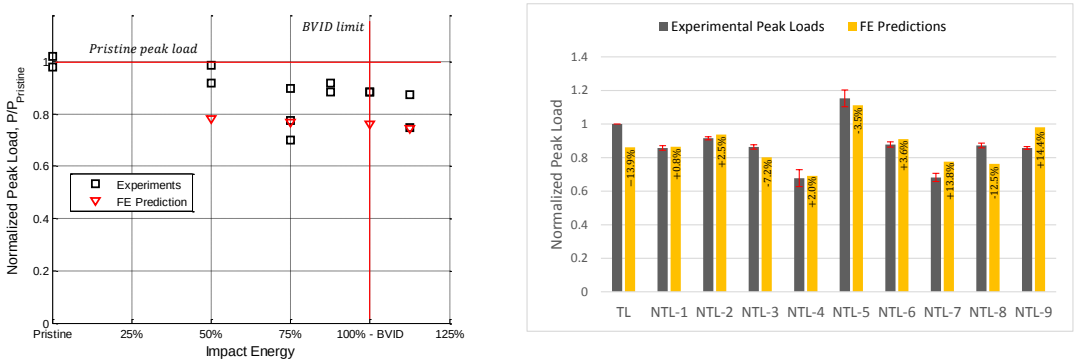

(a) CAI peak load vs. impact energy (b) CAI peak load comparisons for TL and NTL

Figure 6.16: CAI model results compared to experimental data.

the BVID impacts studied here showed limited delaminations in the testing and are therefore not the best candidate for a study of that sort.

6.4.2 BVID CAI Model Results

The CAI experiments presented in Chapter 2.3.2 were modeled using the impact model presented in the previous section. The impact results were imported over to the CAI model as an initial material state using the method described in Chapter 6.2.2. The model showed a very good predictive capability for the CAI event. The TL predictions deviated more from the experimental results, in general, than the NTL predictions. The overall CAI model results are compared to experimental results in Figure 6.16. The BVID study impact cases in Figure 6.16(a) are plotted as a function of the impact energy. The CAI FE model seems to follow the same downwards trend as the experiments do, however the strength reduction is generally greater. While the CAI of the 25% BVID specimens did not show a significant drop in CSAI, maximum reduction of 8%, the model predicted a drop of 22%. The 75% BVID case agreed well with experimental data which had a large scatter and is therefore more forgiving for predictive purposes. The CAI at the BVID limit was under predicted by 12%, when compared to the experimental CSAI. The experiments however had minimal scatter.

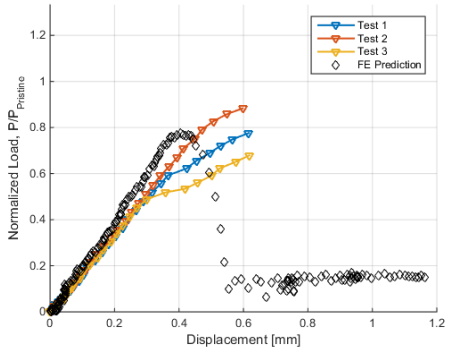

(a) 75% BVID

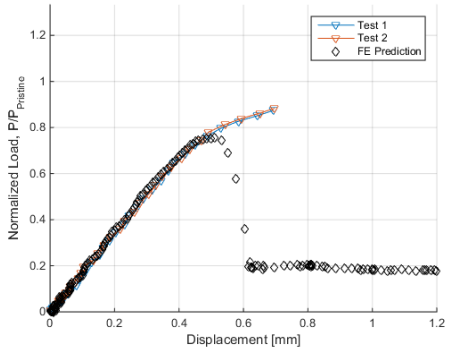

(b) 100% BVID

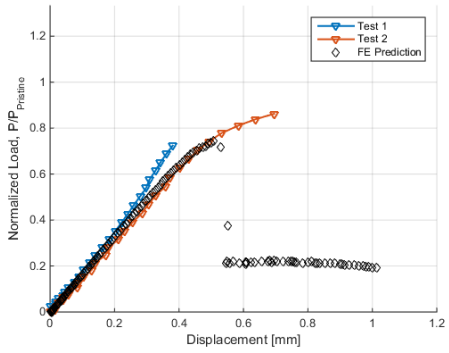

(c) 112.5% BVID

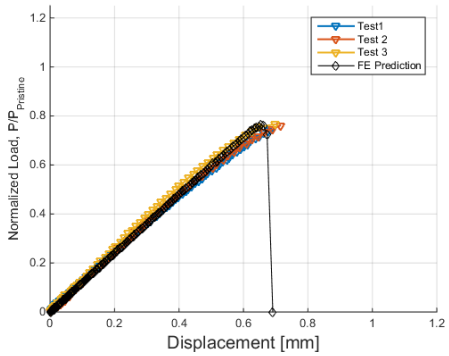

(d) NTL-1

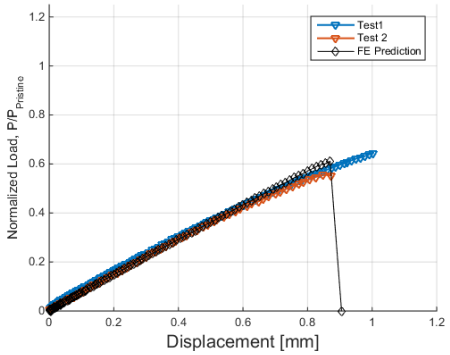

(e) NTL-4

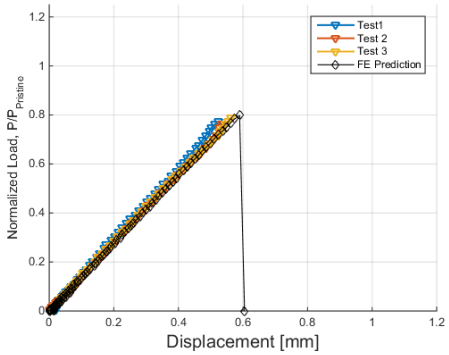

(f) NTL-6

Figure 6.17: CAI load-displacement curves.

The 112.5% case prediction matches the lower experimental bound.

CAI predictions for the NTL specimens are presented in Figure 6.16(b). As previously mentioned, the NTL predictions were in general better than the BVID study CAI predictions as well as the experimental results, showing less variance. One potential reason for the difference in results is that the NTL specimens are in general

more shear dominated due to their layup having more off-axis angles as well as a more dispersed distribution (in most cases). This is also reflected in the lower compressive strengths of the laminates when compared to the TL case. For NTL cases 1-6, the error was seen to range from $0.8\% - 7.2\%$ with respect to the experimental average loads. In some cases it was within the experimental bounds but in others it was outside. The NTL 7-9 cases showed a similar behavior as the TL predictions, showing a error of $12.5\% - 14.4\%$, which is still a very reasonable result.

The load-displacement response for a few chosen cases can be seen in Figure 6.17. The entire set of CAI responses can be seen in Appendix D. The cases were not chosen on a basis of best results but instead for showing different CAI responses and predictions that were seen. From the curves it can be seen that while the TL laminate showed high non-linear behavior prior to failure, the FE model captured this non-linearity up until a pre-mature failure. The FE model stiffness agreed well with experimental results. A stiffening effect was observed in the 75% BVID case which was not seen in those particular experiments. A few of the NTL cases showed a non-linear pre-peak behavior while the rest showed a fairly linear response up until failure.

Furthermore, the CAI results can be seen in detail for the BVID impacted case in Figure 6.18. The load-displacement response has been shown again, now with six specific markings of interest. The first point is at the initiation of loading. The last 3 points are at the loading stages of most interest, point (d) prior to a drastic drop in stiffness and (e) is prior to the final load drop. Point (f) finally shows the predicted failure state of the laminate. Figure 6.18(b) and 6.18(c) show the matrix and fiber failure footprints and a section showing the out-of-plane response during loading, respectively. Color definitions are shown in Figure 6.18(c). It can be seen from all three perspectives that minimal damage growth occurs until point (d). Fiber direction failure initiates early in the top most plies, due to their out-of-plane deformation as

well as full matrix failure. At point (e), failure growth is observed, fiber failure traveling outwards from the center can bee seen. Also noticeable is the buckling of the structure which causes the non-linear response in the load-displacement response. Final failure, as shown in (f), is very representative of what is seen in CAI experiments and was reported in Chapter 2.3.2.

6.5 Conclusion

A robust and efficient computational model for predicting the impact and CAI response of FRPC laminates has been introduced. The model utilizes the EST material model and DCZM elements for capturing the intra-lamina failure modes and inter-laminar failure modes, respectively. Modeling techniques using "local-global" methods for reducing the computational cost without loosing the required fidelity of the models. The required section input properties for the continuum shell elements was introduced, such as the thickness modulus and transverse shear stiffness values. The predicted impact state of the laminate was used as an initial state for the CAI prediction. Thus, the model simulates the impact and CAI experimental procedure virtually. The model was compared against experimental impact data for various impact parameters (mass, energy, velocity, impactor size) as well as two different material systems.

The impact model results were in overall great agreement with experimental data. The model utilized the same non-fiber aligned mesh for capturing the response of multiple different layups including ones with non-traditional ply angles. Pre-peak load-time and load-displacement histories were in excellent agreement with experimental data. The post-peak, impactor rebound, response varied from the experimental data. The effect of this is not very clear and would require further study. Impact damage footprints compared very well with experimental data when compared to ultrasound scan results. Further comparison to microCT data was found to be in good agree-

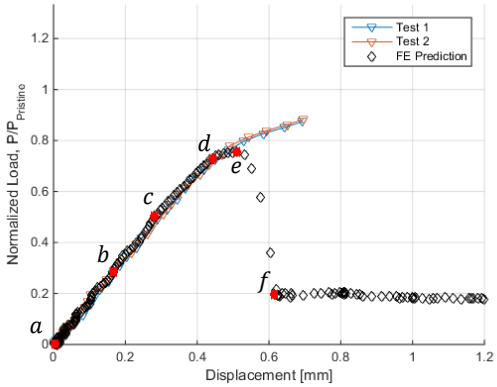

(a) CAI Load-displacement response for BVID case.

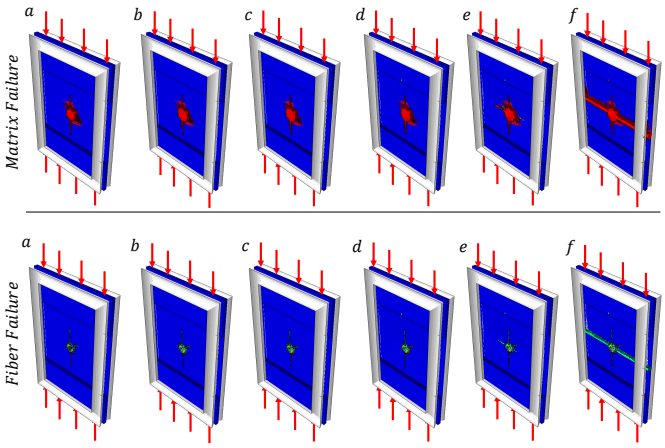

(b) Matrix (top) and fiber (bottom) failure during CAI loading.

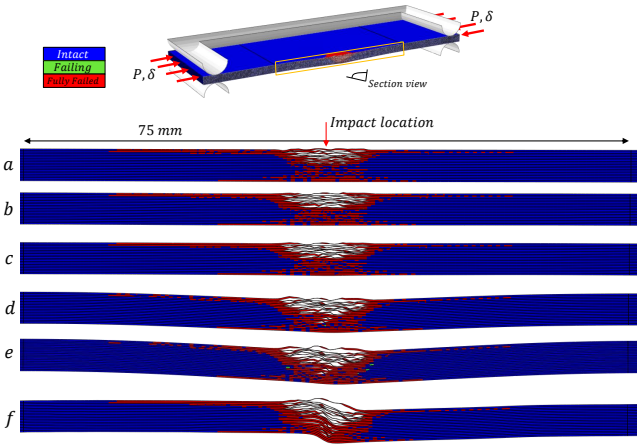

(c) Out-of-plane deformation of a section during loading. Section shows matrix failure.

Figure 6.18: BVID CAI model results details.

ment for both size, shapes and locations of failure. Elevated rate inter-laminar values proved to not have an effect on the model results, since minor delaminations were seen prior to accounting for rate-effects.

CAI predictions were achieved by using the predicted impacted state of the laminate and subjecting it to compressive loading, with the appropriate experimental boundary conditions. Some variance was found between layups. The predicted CSAI was within 7.2% in some cases while others ranged up to 14.4%. Stiffness was captured correctly, the experimental cases that showed a non-linear response were predicted to some extent but improvements and further understanding would be required.

The impact and CAI model has been shown to be successful at predicting the response and damage due to face-on impact and the CSAI of FRPC laminated composites. Future work on improving the model would include capturing the impact rebound correctly by improvements to the compressive residual strengths, permanent deformation due to in-plane failure as well as friction between delaminated surfaces due to debris or powder residue.

CHAPTER VII

Edge-on Impact and CAI Finite Element Modeling & Results

7.1 Introduction

In this chapter, the FE model that was used for face-on impact is utilized for predicting the edge-on impact and CAI response of FRPC laminates. The model is a lamina level shell theory model. EST coupled with DCZM elements allows for capturing lamina level damage and failure in the 1-2 plane and interface (or through-the-thickness) damage and failure, respectively. The model is applicable to laminates of any arbitrary thickness and stacking sequence, not being limited to traditional layup angles of $0°$, $\pm 45°$ and $90°$. The model was initially developed for face-on impact (and CAI) but was later evaluated for edge-on impact predictive capabilities as will be shown in here.

Edge-on impacts are very localized events inducing a combination of delamination and progressive crushing, see Chapter III. Limited numerical modeling of edge-on impacts on FRPC's has been reported in literature even though the edge-on impact is a problem of high interest to industry. It is therefore quite important that edge-on impact modeling is brought into the spotlight and that it gets more attention from academic related research. The author believes that the coupon-level edge-on impact

experimental procedure is beneficial for evaluation of edge-on impact models due to the low manufacturing cost of material coupons (when compared to stiffened panels).

Malhotra et al. [72] used a crude, fully elastic model as a starting point to understand the edge-on impact behavior for glass fiber composites. Ji et al. [57], demonstrated the use of a single shell EST model for capturing the edge-on impact response of a CFRP. The model showed reasonable agreement with experimental results. However, the model was not capable of capturing inter-laminar failure. The model was only verified against low impact energies where delamination was limited. Recently the face-on impact model by Bouvet et al. [11, 13, 47, 101] has been extended to include edge-on impact modeling and the subsequent CAI [85]. Some modifications were made for the model to capture the progressive crushing. Expansion due to swelling was also introduced. The model showed fairly good agreement with experimental results.

In this chapter, the coupon-level edge-on impact problem and CAI will be studied using the same, continuum shell FE model as was introduced for face-on-impact and CAI. The more generic information of the model is described in Chapter VI. Edge-on impact and CAI experimental data presented in Chapter III are used for validation of the model. The edge-on impacts are predicted for the E1, E3 and E5 energy level cases and the subsequent CAI responses. The predictions of the impact event and CAI shows great agreement for the lower energy levels, E1 and E3. The E5 energy level was seen to show good agreement with overall damage extent while the impact response was over predicted and the CSAI under predicted for this case.

7.2 Edge-on Impact and CAI Model

The edge-on impact model is constructed in a similar manner to the face-on impact model presented in Chapter VI. EST material model is used for capturing intra-laminar damage and failure. DCZM elements are used for capturing the inter-laminar

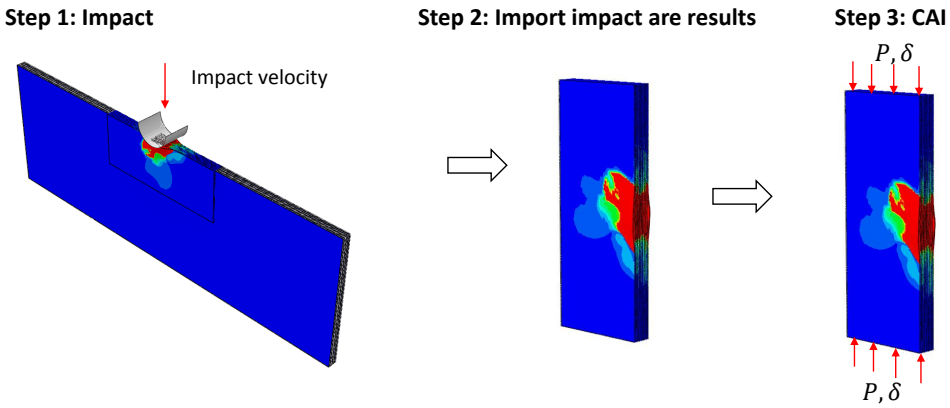

(a) Virtual edge-on impact and CAI steps.

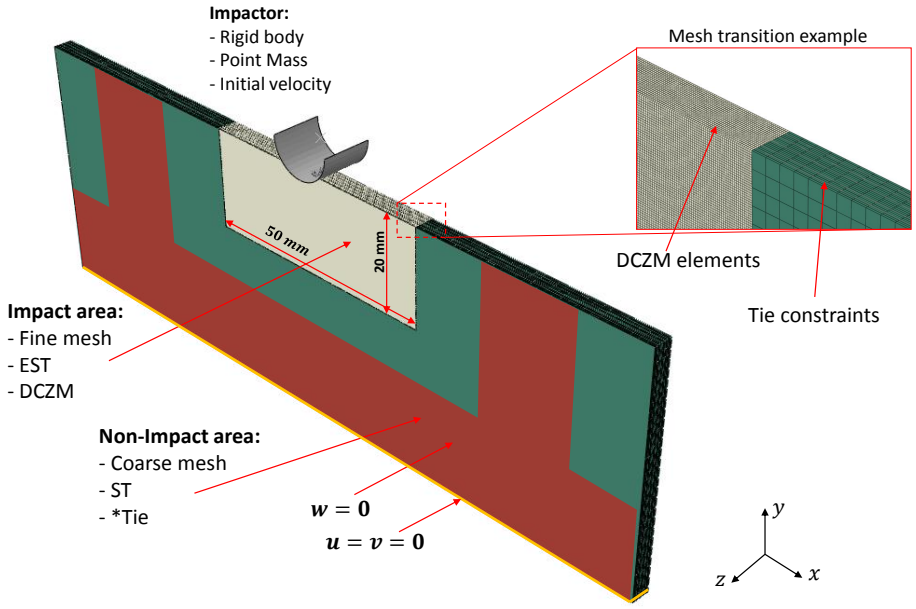

(b) Edge-on impact FE model details.

Figure 7.1: Edge-on impact FE modeling strategy showing steps (a) and model details (b).

failure modes. The "global-local" modeling technique is also utilized in the edge-on impact model. The impact affected area is much smaller than in the face-on impact case. This is due to the impact damage extent as well as the CAI effective specimen size being much smaller. Therefore, in the CAI simulation, only the impact area is imported from the impact results, Figure 7.1(a). The impact area dimensions are 50 mm by 25 mm, Figure 7.1(b).

As in the previous model, the impact area layers are modeled using EST and are connected by DCZM elements. The mesh is refined beyond the CB critical element size limit, Chapter 5.2. An element size of 0.2 mm by 0.2 mm was used in the impact area. Away from the impact area a mesh size of 1.5 mm by 1.5 mm is used and in this region the material model is limited to pre-peak damage only using ST. The shell layers are tied using nodal tie constraints (*TIE).

The specimen dimensions presented in Chapter III are 150 mm by 100 mm. Further study had shown that a reduction of the specimen width by half, down to 50 mm, did not effect the impact response or damage due to how localized the event is. Therefore for saving computational time the impact model was reduced using dimensions of 150 mm by 50 mm. The boundary conditions are seeded on the laminates surface nodes. Out-of-plane displacement is constrained due to the channel as well as L-brackets. The bottom of the laminate is constrained in the y motion. The details of the boundary conditions are shown in Figure 7.1(b). The impactor is modeled using rigid shell elements with a point mass. The impactor is cylindrical with a diameter of 12.7 mm and a mass of 25.13 kg. Surface to surface contact is applied between the impactor and the impact layers, both external and "internal" surfaces. This will allow for friction between the impactor and the delaminated surfaces. Friction coefficient of 0.3 is used for the contact. The edge-on impact simulations were seen to be highly sensitive to the frictional coefficient, as will be discussed later on in the chapter. The residual stiffness in the EST material model was set to 10% of the pristine values.

The continuum shell properties were defined in the same manner as for the face-on impact, Chapter 6.2.1. Importing of the impact damage state for use in the CAI simulation was done in a similar manner as before, Chapter 6.2.2, while there was less data to import in this case. Mass scaling was once again used for the CAI analysis to decrease the computational time. Similar values were used, stable time increment ranged from $1e^{-5} - 2.5e^{-5}$ for any element. Material input properties were also the

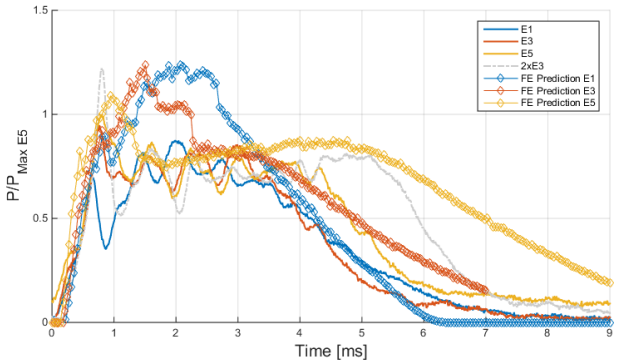

(a) Overall FE vs. experimental comparison

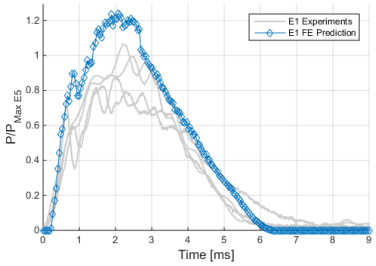

(b) E1 FE prediction vs. experiments

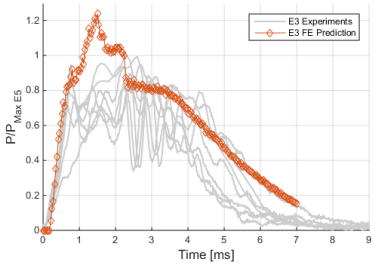

(c) E3 FE prediction vs. experiments

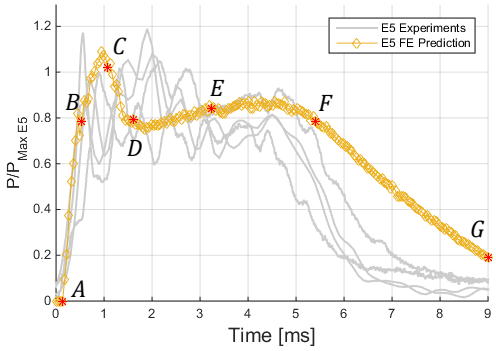

(d) E5 FE prediction vs. experiments with damage interval markings

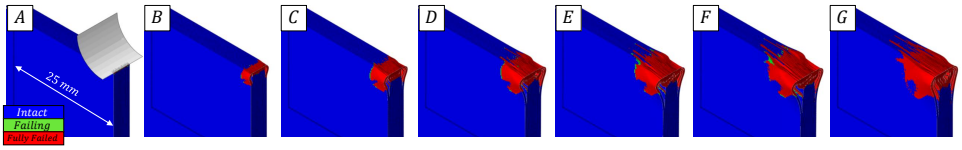

(e) Section showing vertical and horizontal matrix failure evolution for the E5 impact

Figure 7.2: Edge-on impact predictions shown together in (a). E1, E3 and E5 shown separately with multiple experimental impact replicates in (b), (c) and (d), respectively. Matrix failure evolution for E5 is shown in (d).

same as in the face-on impact model, with minor changes to the mode I cohesive law being made. The mode I cohesive law was chosen to be trapezoidal, with $\alpha = 0.8$, as described in Chapter 5.3. This change was in par with the experimental results seen in the mode I inter-laminar testing presented in Chapter IV. Where the mode I response was seen to show effects of the process zone length (as well as the fiber bridging). It was found that to be able to achieve the correct progressive crushing (plateau load) response of the impact experiments, a trapezoidal law was required for a more progressive energy dissipation. The matrix direction compressive failure mode used was the same, a plateau behavior once initiated to simulate continuous crushing. In the case of the edge-on impact this failure mode becomes much more common and would therefore need to be investigated further. Finally, the laminate being studied does only contain two plies with fibers aligned parallel to the impact direction as well as them being on the outside. In the case of there being more of them and in the center of the laminate the response and failure mode will become more dominated by progressive kinking underneath the impactor. In such cases, improvements to the fiber direction compressive failure modes would be essential.

7.3 Impact Model Results

The predicted edge-on impact load-time histories are compared to the experimental data in Figure 7.2. A comparison between the different impact energies is shown in Figure 7.2(a). A trend in the model results can be seen. As the impact energy is increased the transition from the peak load to the crush load is more on par with the experiments. The rebound trend is also captured more accurately for the low energy impacts while the E3 and E5 impact energies have a slower impactor rebound. This behavior is the same as seen in the face-on impact results, yet the effect is greater here due to the more localized failure event causing greater permanent deformation.

Figure 7.2(b), 7.2(c) and 7.2(c) show the predicted impact responses for energies

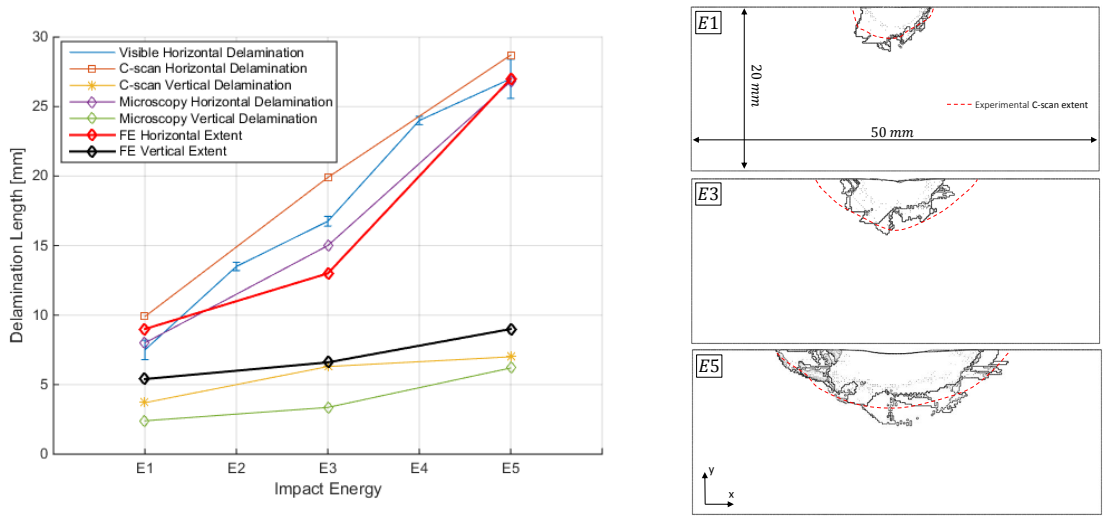

(a) Model failure extent measurements compared to experiments

(b) Full field predicted impact damage extent for E1, E3 and E5 impact energies. C-scan results shown in dotted red.

Figure 7.3: Comparison of model impact damage/failure extent and experimental results.

E1, E3 and E5, respectively, along with the scatter in experimental data. From these results we can see that the load is over predicted for the E1 case while the impact rebound is captured correctly. The impact did not show much failure, both for experiments and prediction, therefore the impact rebound is captured correctly due to the mildly degraded structure. The E3 impacts are already captured more accurately, however the peak load seems to still linger before the crush-load is achieved. Rebound response of the E3 has started to trail off but is quite reasonable. The E5 case shows the best pre-rebound behavior out of the three cases. The peak load drops quite quickly to the crush load. The rebound time is slightly over estimated and the rebound is much slower than the experiments show. Figure 7.2(d) show the evolution of impact damage extent (here shown as intra- matrix failure) during the E5 impact. The time intervals $A-G$ are marked on Figure 7.2(c) for reference. The figures show a section cut through the center of impact, therefore allowing the depth direction extent to be seen as well. The impactor has been removed in stages $B-G$ for better

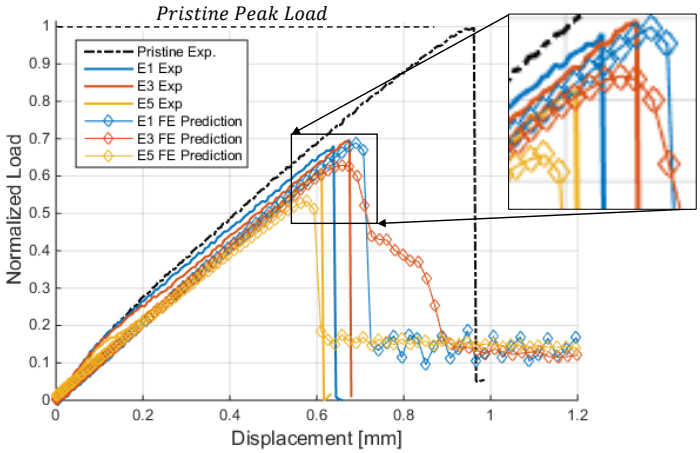

(a) Load-displacement comparison for FE prediction and representative experimental curves

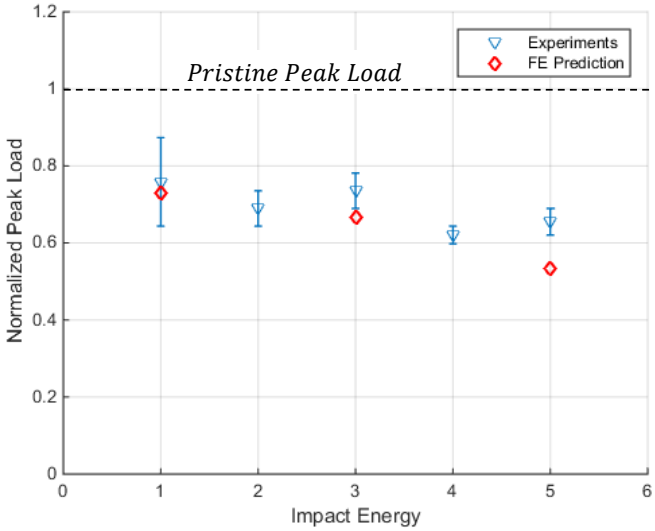

(b) Overall peak load comparisons

Figure 7.4: Comparison of model load-displacement and peak loads with experimental results.

visualization of the horizontal extent. The evolution of damage between the three impact energies are very similar, being only dictated by the total crush distance of the impactor and therefore the E5 case was shown here.

Overall impact damage extent is predicted with a fairly good agreement, Figure 7.3 with experimental results. The vertical extent of damage was over predicted slightly for all impact energies. The horizontal damage extent showed good agreement for the E1 and E5 case and slight deviation for the E3 case. When the predicted impact

damage shape is compared to the experimental C-scan results, Figure 7.3(b), good agreement is seen.

7.4 CAI Results

With the impact model predicting the impact damage extent with a reasonable agreement the CAI predictions can be achieved. The load-displacement response can be seen in Figure 7.4(a). The peak CAI peak loads for different impact energies can be seen in Figure 7.4(b). An outstanding agreement was seen for the CAI mode results. Model stiffness was in excellent agreement with the experimental curves (past the initial compliance of the experimental curves). CAI peak loads were within 10% of the experimental average values of low energies. The E5 case shows a lower value than the experimental results.

The failure progression during loading can be seen in Figure 7.5. The E3 impact case is used here for a reference. Figure 7.5(a) shows the load response with intervals marked from $A - F$. In Figures 7.5(b) and 7.5(c) the matrix/fiber failure and the laminate global response is shown, respectively. From the failure contours it is observed that very little failure occurs prior to the load drop, where a rapid growth of fiber and matrix failure traveling towards the non-impacted side of the specimen can be seen. When the deformation of the structure is looked at, Figure 7.5(c), it can be seen that at the peak load, point C, the specimen buckles to one side. When looked at further it was observed that delamination growth was occurring while no further in-plane failure was seen.

This would lead to the belief that the CAI event is highly sensitive to the delaminations rather than in-plane failure modes. This effect will most likely be highly dependent on the stacking sequence of the laminate. The laminate used in this study had a high percentage of plies with the fiber direction orientated in the same direction as the CAI loading. That is, perpendicular to the impact direction. Fiber

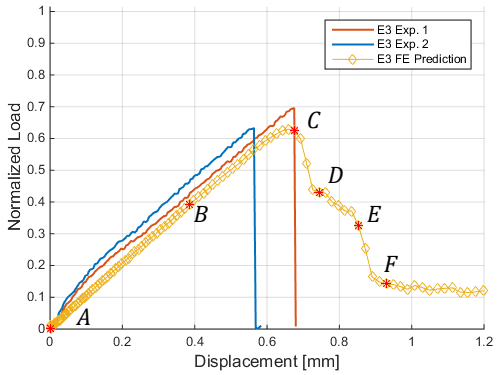

(a) Load-displacement for the E3 impact case

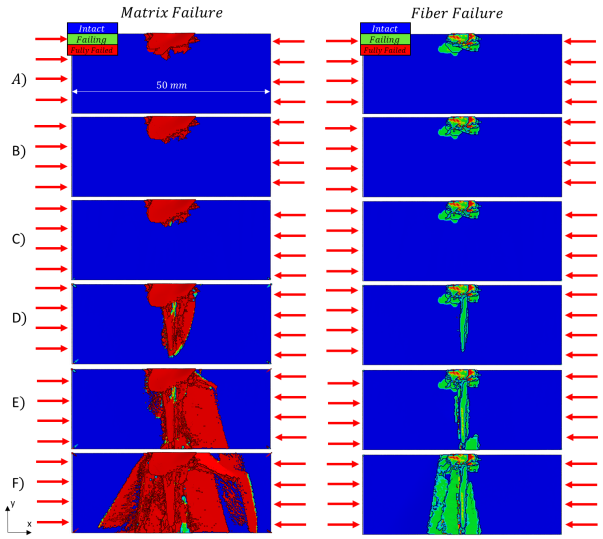

(b) Matrix and fiber failure during CAI loading

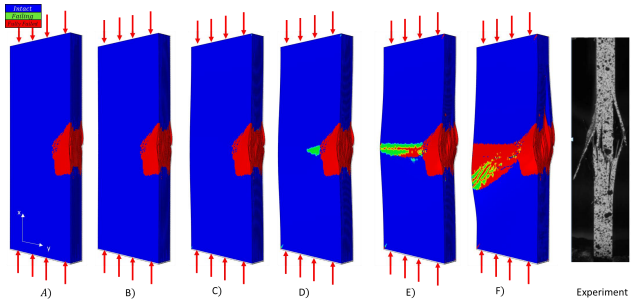

(c) Deformation during loading. Showing matrix failure.

Figure 7.5: Comparison of model load-displacement and peak loads with experimental results.

failure observed in the impact event was therefore minimal, resulting in the biggest compression instability coming from local buckling of the delaminated layers. For a further conclusion the E3 model was run without importing the in-plane failure state of the impact event, only updating the delaminations. The peak load was found to be within 0.1% of the previous result, and stiffnesses also matched. It is therefore clear that the CAI event following an edge-on impact in the BVID regime is most sensitive to the extent of delamination and not to in-plane failure.

7.5 Conclusion

The impact model introduced in Chapter VI for predicting face-on impact and CAI has been evaluated for edge-on impact and CAI modeling. EST material model and DCZM elements were once more used for intra-laminar and inter-laminar failure modeling, respectively. CAI predictions are done using the impact model results as initial data. Results are imported and act as the initial condition for the CAI. The experiments in Chapter III were used for comparisons. The E1, E3 and E5 energy levels were used as the main subjects of the study, giving a range of impact energies and damage extent.

The model proved largely successful at capturing the pre-peak impact response and impact damage extent. The post-peak response differed from experiments in a similar manner to the face-on impact. While the model captures the extent of damage, the compressive failure modes are not captured with the same fidelity as the face-on impact as would be desired. Due to shell elements being used (plane stress) the through-the-thickness compressive failure modes and resultant "slipping" cannot be accurately implemented. However, further improvements to the EST material model to include modeling the residual strength due to constrained in-plane crushing for both matrix (mode I and mode II) and fiber kinking is recommended for future study and this detail should lead to better agreement in failure mode predictions.

The CAI event was predicted very well. Excellent agreement was seen between the CAI model predictions and the experiments. Peak loads were captured within 10% of the average experimental results for the lower energy impacts. E5 impact was off from the average experimental value by roughly 22%. The CAI event showed minimal in-plane failure growth prior to the load drop. The softening and reason for the load drop was found to be due to delamination growth. Delaminations grew from the impacted side of the specimen to the non-impacted side. This resulted in global buckling of the specimen, leading to a catastrophic fiber failure in the 0° layers. The delamination sensitivity of the model was further tested by importing only the delaminated state and no in-plane damage/failure from the EST material model. The CAI response was seen to be identical, within 0.1% of the one with in-plane damage/failure imported. It was therefore concluded that the delamination state of the laminate is indeed the most influential failure mode in influencing the CAI strength.

Future work on the model, which would improve the face-on impact model as well, would include capturing the impact rebound correctly by improvements to the compressive residual strengths, permanent deformation due to in-plane failure as well as friction between delaminated surfaces due to debris or powder residue.

CHAPTER VIII

Concluding Remarks

In this thesis, the response of FRPC laminates subject to low-velocity impact has been investigated experimentally, and numerically using a lamina level FE model with discrete cohesive layers to capture delamination. Low-velocity impact studies with a focus on impacts in the BVID regime were conducted for face-on and edge-on impact. While face-on impact has been widely investigated, and industry standards have been developed, edge-on impact on FRPC's has seen limited representation in literature publications. Edge-on impact is most commonly related to impact on a stiffened panel stringer. Due to the high cost of manufacturing skin-stringer panels for testing, it is clear that a standardized coupon-level experimental method would be highly beneficial. A novel method for conducting coupon-level edge-on impact and CAI was therefore introduced. Impact FE models most commonly use material and fracture properties measured at quasi-static rates while local strain rates can be in the excess of 100 strain/s as well as interface separations (inter-laminar fracture) exceeding 1000 mm/s, locally. It was therefore desired to study the rate effects of inter-laminar fracture. A comprehensive finite element model using lamina level progressive damage and failure material models coupled with discrete cohesive elements was developed for predicting the face-on and edge-on impact events. A continuum shell based model for computational efficiency, coupled with discrete cohesive elements for through-the-

thickness failure modes was seen to be capable of capturing the important failure modes observed in composites subject to low-velocity impact.

Experimental results for various face-on impacts were investigated in detail for two different FRPC material systems. The effect of impact mass and velocity was studied, within the low-velocity impact regime. Impact energy was kept constant while varying the mass. There was no notable difference seen between the different velocity/mass test parameters, within the tested regime. A BVID study was conducted on TL coupons where the impact energy was varied to establish the BVID energy limit. Numerous NTL coupons were then tested at the BVID limit to be used for FE model validation purposes. An extensive post-impact inspection of the coupons was conducted using ultrasound and microCT scanning methods. The results revealed that for model validation and comparisons, ultrasound scanning is insufficient. The method produces the overall damage footprint along with some delamination shapes, which is valuable. However for development of progressive damage and failure models for impact the details and information gathered from microCT scanning is invaluable. MicroCT scans were shown to capture ply-by-ply damage extent, detailed delamination patterns, matrix splitting, fiber rupture, and the interaction of the aforementioned modes. CAI experiments were carried out on the BVID study impact coupons to establish the CSAI in the BVID regime. Impacts at or below the BVID limit were found to reduce the compressive strength of the coupon by up to 30%. It was therefore concluded that an impact at or below the BVID limit can have a significant effect on the load carrying capability of the structure. By factoring in damage growth due to continued service loads, the impact damage growth (due to fatigue) could eventually lead to a catastrophic structural failure.

A novel method for conducting coupon-level edge-on impact on FRPC laminates at various angles was introduced. A BVID study was conducted using the same material system as in the face-on impact BVID study. Impacts at 0° and 45° angles

with respect to the impacted edge were carried out at a range of energy levels to establish the BVID limit. Impact damage due to a 0° edge-on impact was found to be a highly localized event due to the laminate being constrained from globally deforming (bending). A detailed microscopic study on the 0° impacted specimens was presented. Failure mechanisms observed were very rich for the higher energies tested. Mechanisms observed were of the splaying and fragmentation nature where the outer most layers bulge out due to mode I delaminations and the center layers experience fragmentation due to localized crushing. The BVID limit for 0° was found to be very low due to permanent deformations on the edge being highly visible. The 45° impacts showed a completely different response. The impact was soft and forgiving and resembled the face-on impact more than the 0° impact case. At first glance the impact damage was seen to be minimal, however with further ultrasound inspection the damage extent was seen to be slightly lower but on par with the 0° impacts. Industry testing standards for compression after impact proved to be insensitive to the edge-on impact damage due to the size of the coupon and localized impact damage. A method for conducting CAI using a modified CLC fixture was introduced. The specimen width was chosen to be of a size larger than the impact damage caused by the BVID impact, yet relatively small so that impact damage sensitivity would be achieved. Both the 0° and 45° impact cases were seen to be sensitive to compressive loading using the adjusted CLC test setup. Compressive strength was seen to drop by close to 40% in some cases.

Rate dependence of mode I and mode II inter-laminar fracture toughness of FRPC laminates was investigated by conducting testing at elevated rates. Quasi-static and intermediate rate testing up to 100 mm/s were performed on a hydraulic load frame. Testing at elevated rates were conducted on a drop tower test apparatus, where loading rates of up to 3600 mm/s were achieved. An improved wedge-insert fracture method for conducting mode I fracture at elevated rates was introduced. Frictional

effects caused by contact between the wedge and the crack surface has been removed by simply inserting two wedges between the rollers of a conventional DCB specimen orientated vertically. A simple correction factor was introduced to the MBT fracture toughness calculation to account for the axial load applied by the wedges. Kinetic energy contributions were also included in the G_{IC} calculations. The method was verified against established standards at quasi-static rates, and exceptional agreement was achieved. The method was tested at rates up to 3600 mm/s and has been proven to be a viable method for conducting mode I inter-laminar fracture at elevated rates. A downward trend for G_{IC} was seen with increasing rate as well as a drastic reduction in the effect of bridging. Mode II interlaminar fracture was conducted using the established ENF test method. Testing was conducted at up to 2800 mm/s. G_{IIC} calculations were done using kinetic energy contributions. An increase in G_{IIC} was observed up to a loading rate of 1500 mm/s, beyond that a decreasing trend was observed. Testing at rates in excess of 3000 mm/s is recommended.

A robust and efficient FE modeling approach for predicting impact and CAI on FRPC laminates was introduced. A lamina level FE model utilizing Reissner-Mindlin plate theory (shell elements) for modeling each individual ply was introduced. A progressive damage and failure material model, EST, is used for capturing the full field intra-laminar damage (pre-peak) and failure (post-peak) in the 1-2 plane. Inter-laminar failure (delaminations), or through-thickness, is captured by utilizing discrete nodal connection cohesive elements (DCZM elements) for tying together the individual shell layers. The combination of plane stress shell elements and discrete cohesive elements enables the model to capture the most important impact failure mechanisms. While the intra-laminar through-thickness failure modes, such as the 2-3 shear which is a highly reported failure mode in impacted composites. A hypothesis was made that with the combination of damage and failure in the 1-2 plane and interfacial delaminations, the effect of 2-3 shear failure and delamination migration could be

captured.

Using the modeling methods that were previously described, a face-on impact and CAI model was developed. An impact model using the local-global modeling method was built for capturing the impact event and subsequently the CAI response using the same FE model. The model was found to be successful at predicting the impact response for the impacts reported in earlier chapters. An exceptional agreement was seen in the pre-peak response while the rebound (post-peak) response was not captured correctly in the lieu of extensive impact damage. Impact damage extent as well as location, type and shapes of damage/failure predicted by the model was in excellent agreement with experimental results, including both ultrasound and microCT scans. Furthermore, the model proved to be capable of capturing the impact response of TL and NTL laminates subject to BVID impact and CAI, all while using a non fiber-aligned mesh. CAI predictions were achieved by importing the impact damage/failure state of the impact model and using it as the initial state prior to compressive loading. Some variance in error between the experimental post-impact strengths and predicted values was seen in the model. While some cases were predicted to great accuracy of within 1%, the end result was that half the laminate predictions were within 7.2% while the other half ranged up to 14.4% at most. The conclusion was that the model is highly capable of capturing the low-velocity impact and CAI response of FRPC laminates of any arbitrary stacking sequence.

Edge-on impact (0°) predictions using the aforementioned FE model were in overall good agreement with experimental data. Due to the localized failure mechanism of the edge-on impact event being (highly three dimensional), the shell models predicted failure modes that did not resemble the experimental results to the same extent as the face-on impact model. Progressive crushing underneath the impactor causes mode I delaminations at the outer interfaces while the midplane plies experience in-plane compressive loads. In-plane compressive loads then lead to 3D failure modes such

as 2-3 shear and out-of-plane fiber kinking which a shell model is unable to capture. However, the failure mode which seemed to be the most dominant when it came to predicting the CSAI was found to be the delamination modes of failure. This mode of failure was captured quite nicely by the impact model. As a result the CSAI showed a very good agreement with experimental results.

8.1 Best Practices and Modeling Guidelines

The modeling guidelines and best practices, as experienced through the studies presented in this thesis, are provided in this section. The first thing to note are the dimensions of the problem, and to evaluate the approximate impact damage footprint. For the BVID regime, the models provided in this thesis yield fairly accurate representations of the damage footprint. The "local" area, or "impact" area, should be meshed "finely" so that the impact event will be captured properly as explained later. For experimental studies, any boundary effects that could be caused at the local-global boundary should be minimized, and for this, the models presented can be used to estimate the size of the impact damage footprint. The experimental supports should be modeled as accurately as possible. The use of rigid body elements and contact definitions is recommended over the application of nodal boundary conditions on the laminates surface.

Using continuum shell elements instead of the conventional shell elements is required (unless the cohesive element accounts for rotational degrees of freedom) so that the top and bottom surfaces of the lamina are represented correctly. This will allow for the interfacial slip to be captured more accurately. Furthermore, the shell section properties should be defined in the appropriate manner, as described in the ABAQUS manual, as well as Chapter 6.2 of this thesis.

The mesh should be chosen with respect to the desired results and the size of the model. The mesh size should adhere to the critical element lengths of the CB

formulation (to prevent snap-back and unstable behaviour due to sudden loss in stiffness). The element size should be chosen to be below the CB limit. However, the commonly referred to factor of being 10 times smaller than the CB limit is difficult to enforce when the problem becomes large due to a high ply count and therefore cohesive interfaces. The critical element length due to transverse (matrix) compression loading is typically very small due to the high strain to failure. The fracture toughness for transverse (matrix) compression is also assumed to be the same as the value acquired from quasi-static interlaminar mode I fracture. This value is most likely too small as well as the residual strength of an element (due to friction in the $\approx 52^{\circ}$ fracture plane as well as confinement due to adjacent layers). Therefore, for the study presented in this thesis, a plateau stress was implemented for the in-plane mode I compressive failure of the matrix. The results were not seen to be sensitive to this assumption.

The combination of EST+DCZM is capable of capturing the important failure mechanisms that are involved in face-on impact. The edge-on impact model requires some improvements to the compressive failure modes. This is needed so that progressive crushing can be captured. Some details on improvements is given in the "Future Work" section below. Furthermore, the rebound of the model was overall not in good agreement with the experimental data. It is clear that further implementation of viscoelastic behavior and/or permanent strain in the model would be essential for capturing the rebound event, and this is also mentioned in the "Future Work" section below.

For the CAI simulation, the main recommendation which arises due to ABAQUS limitations related to the *Import command, is that a high memory node is used. This is due to the pre-processing taking a lot of memory and only utilizing 1 processor of node. By using a high memory node each processor acquires more memory and therefore you can use more processors overall. Mass scaling should be used carefully so that the kinetic energy in the system is much smaller than the total strain energy of

the system. The boundary conditions need to be enforced correctly in the CAI model, and it may require importing of supports that were not used in the impact model. In the studies presented here, the roller boundary support of the impact model was used for the CAI knife supports as well, although the radius of the contact surface is larger. This led to good agreement with the experimental results.

8.2 Unique Contributions in this Thesis

The impact failure mechanisms in laminates of industry standards are rich and intriguing. The damaged/failed state of the structure shows a combination of interacting intralaminar (fiber and matrix) and interlaminar (delamination) failure modes. The interaction of in-plane and out-of-plane damage and failure modes is a subtle thing but of very high importance for capturing the impact induced damaged correctly. It is therefore necessary to develop a computational tool that is able to capture these effects accurately. A secondary requirement arrives from the industry, where computational time is one of the biggest factors. High-fidelity experimental data is of high importance for accurately validating and improving the developed impact model. The thesis focuses on both the experimental and numerical investigation of low-velocity face-on and edge-on impact of FRPC's, with the main focus on BVID events. The unique contributions of the thesis are as follows:

1. Detailed experimental (real time) results for face-on and edge-on impact and CAI of aerospace laminates has been conducted. Different lay-ups and material systems were investigated. In-situ out-of-plane deformations were captured using high speed imagery and 3D DIC methods. Detailed post impact CT scans showing detailed interior damage mechanisms.

2. Introduced a new experimental method for conducting coupon level edge-on impact and CAI. The method allows for a drastic reduction in experimental costs

(material, setup and preparation). Evaluation of the edge-on impact damage on the stringer of a stiffened panel is captured using a simple laminate coupon.

3. Developed a new experimental method for quasi-static, intermediate and elevated rate mode I fracture characterization using a modified wedge-insert fracture experimental configuration. Detailed analysis and validation of the method were conducted.

4. Introduced a new robust and efficient, finite element based, mesh objective formulation and model that virtually predicts the face-on impact response and CSAI of FRPC's. A continuum shell based model utilizing an in-plane progressive damage and failure material model and discrete cohesive elements was introduced. The model successfully captured several failure mechanisms accurately, such as top face kinking, delamination jumps, and moderate interaction between intra- and inter-laminar failure modes, in a unified model.

5. Extended the shell element model to predict edge-on impact responses and CSAI of FRPC's. Limited FE modeling of edge-on impact has been reported in literature, especially for realistic aerospace laminates. The model showed good promise for capturing the edge-on response, as well as showing good agreement for CSAI.

8.3 Future Work

The thesis presented extensive experimental work using both existing techniques as well as introducing novel methods. A new FE modeling approach for capturing face-on and edge-on impact of FRPC's as well as predicting the CSAI was introduced. However, as with any research related work, there is always more to be understood and more detail to be attained. In the following paragraphs some proposed work is

introduced, this is by no means an exhaustive list of the directions or inclusion the future work could entail.

Face-on Impact: Further experimental study on NTL with dispersed stacking sequences. It would be beneficial to come up with simplified layups for detailed study of the intra-inter interaction between different ply to ply mismatch angles.

Edge-on Impact: Further study using the proposed coupon-level edge-on impact configuration including impacts of higher energy, spherical impactors and different impact angles. Further validation and correlation studies of the CLC method for acquiring the CSAI, mainly investigating the relation between the coupon level compression response and sensitivity to the impact damage w.r.t. the large structure (skin-stringer sub-component level experiments).

Rate Dependence of Inter-laminar Fracture: A good baseline study has been presented in this thesis. The MWIF experimental procedure has been shown to be successful at capturing mode I fracture at elevated rates. Further increase in loading rate would require some improvements of how the load signal is acquired. Since at the highest rates tested the load signal became difficult to extract. Furthermore, the method can be extended for use with high-rate testing. The same goes for mode II testing, increased loading rates as well as different boundary conditions could be investigated, such as investigating the effect of global bending by reducing the distance between the bottom roller supports. A FE study and inverse analysis to investigate the cohesive law behavior at increased loading rates would be essential for gaining more understanding into the fracture characteristics. The study would also give valuable insight and correlation between applied loading rate and the local crack tip separation rate.

FE Impact Model: The main issue with the face-on impact model was the rebound, although it was not seen to be necessary to capture the rebound correctly since the damage extent and failure mechanisms were in excellent agreement with

experimental data. The model requires additional work to accurately capture the progressive crushing that occurs in the edge-on impact event. Below are a few additional implementations that would be beneficial for both face-on and edge-on impact, in no particular order.

1. Residual strain implementation and/or relaxation dampening to capture permanent deformations as well as frictional effects between delaminated surfaces (due to debris and rough fracture surfaces) for capturing the slower rebound of the laminate.

2. Residual strength for compressive modes of failure; this would allow for capturing progressive compressive failures (kinking etc.)

3. Degradation of the continuum shell transverse shear stiffness values w.r.t. in-plane degradation would allow for more accurately capturing the through-the-thickness displacement mismatch due to in-plane failure modes such as ply splitting.

4. Direct interaction between intra- and inter-laminar failure modes.

5. Implement an adaptive cohesive law into the DCZM element formulation to account for the local loading rates. This would be a combined effort with the rate dependence inter-laminar fracture work mentioned above.

Furthermore, with the model being validated and showing excellent predictive capabilities for face-on impact. A study focused on improving the impact response can be done, such as investigating the effect of the layup, ply stacking, strengthening the top surface to minimize compressive failure and/or internal damage and failure.

Lastly, comparisons to a 3D FE model using similar modeling approaches (ST+CB) extended to the through-the-thickness dimension would be beneficial to understand

the upsides and down sides of the 3D model and the shell model. A fiber orientated mesh comparison would also be beneficial for comparisons.

APPENDICES

APPENDIX A

Matrix Crack-Delamination Interaction In Sandwich Composite Beams

A.1 Introduction

Modeling the impact dynamic response in composites, using finite element based approaches can be computationally expensive due to complex failure mechanisms and interactions amongst them during the damage and failure event. Previous studies have found comparable load-displacement responses, and similar damage distributions and force levels between quasi-static and low-velocity impact tests [97, 140]. The failure observed in multi-ply cross ply composite laminates subject to low velocity impact has been reported [62] and it has been observed that a characteristic failure mechanism is the interaction between transverse matrix cracking and delamination. Thus, it is of interest to study this failure mode in isolation. Because of the similarity between failure mechanisms in a multi-layered composite laminate and those that occur in a sandwich panel, under flexural response, it is expedient to investigate failure mode interaction and progression in a sandwich panel, where the flexural rigidity of the specimen can be tailored to experimental requirements. The impact response of

sandwich panels display transverse shear failure and delamination which is similar to failure observed in multi-layered laminates subjected to similar loading conditions.

Experimental and computational results on the flexural response and failure of sandwich composite beams under quasi-static and dynamic three point bend loading are presented in this paper. The motivation for this study is to clearly understand the interaction between different failure mechanisms, in this case the shear failure of the core and the delamination of the interface. Sandwich composites with two significantly different materials with respect to mechanical behavior (face sheet and core) can be expected to have a relatively neat failure mechanism. This study could therefore prove very useful for developing modeling strategies to understand failure in laminated composites subject to low-velocity impact since laminated composites that often contain stacking sequences of (0/90/0) show transverse cracking in the 90 layers which lead to delaminations at the adjacent interfaces, a mechanism that is comparable to the failure initiating in the core of a sandwich structure leading to delamination at the face sheet-core interface.

A.2 Experimental Results

Three point bend tests were performed on a sandwich composite beam both statically and dynamically, the dimensions of the specimen (Table A.1) and test fixture (Figure A.1) were held constant for both events. The sandwich composite beam that was studied in this research has face sheets composed of 8 plies of T300B-3K plain woven carbon fiber laminae with a stacking sequence $(-45/45)_4$, and the face sheets are impregnated with Epon 862 epoxy. The core material used is LAST-A-FOAM-FR-6710, which is a brittle foam. The core thickness was chosen to be 12.7 mm thick.

Rubber pads were used between the rollers and the specimen to prevent stress localization which would result in indentation and crushing of the core under the

roller (these results were found in preliminary testing that was done). The material used for the rubber pads was ultra-strength neoprene rubber with durometer 60A. During loading the rubber pads can be seen deforming excessively, making it seem as if the core is getting crushed underneath the roller, however with close observation it was concluded that the core is not getting crushed, the rubber pads are deforming out-of-plane and creeping over the face sheets.

The static tests were performed on an MTS loading machine with a loading rate of 0.01 mm/second, this provides quasi-static loading conditions. The event was recorded at 1 frame every 5 seconds with a Nikon D5300 digital camera equipped with a 105 mm lens. The dynamic testing was conducted in a drop tower with an impact mass of 25.13 kg, different energy levels of impact were studied to establish the impact energy needed to fail the sandwich structure. The impact energy of interest proved to be 10 joules, the energy level gives repeatable failure in the structure as

Figure A.1: Three-point bend fixture.

Table A.1: Key dimensions in experiments.

Beam length	250 mm
Span length	152.4 mm
Beam width	24 mm
Face-sheet thickness	1.9 mm
Core thickness	12.7 mm
Top roller diameter	12.7 mm
Bottom roller diameter	7.9 mm

well as being close to the minimum required energy to produce failure. The impact event was captured using a Photron SA-2 high-speed camera recording at a rate of 25,000 frames per second with a resolution of 1024 pixels by 248 pixels.

Digital Image Correlation (DIC) techniques were used to obtain full field surface displacement and strain fields during the loading event. Due to the large deflection of the rubber pads, the displacement was collected digitally from the DIC data, where the vertical displacement is calculated from the difference between the displacement at the bottom rollers and at the top roller. This is done at the centerline of the sandwich beam, a schematic is shown in Figure A.2.

Multiple tests were done to make sure repeatability was established. Typical experimental load-displacement response plots can be seen in Figure 1.3(a), for quasi-static and dynamic loading, respectively. It can be seen from the static load-displacement response that after an initial fairly linear response, nonlinearity sets in due to the non-linear stress-strain response of the core material [127]. This non-linear behavior is not present in the impact response of the sandwich beam, because the center displacement of the impact case is smaller than the corresponding quasi-static case, resulting in core shear strains that are smaller.

The peak load for the impacted structure is also lower than for the quasi-statically

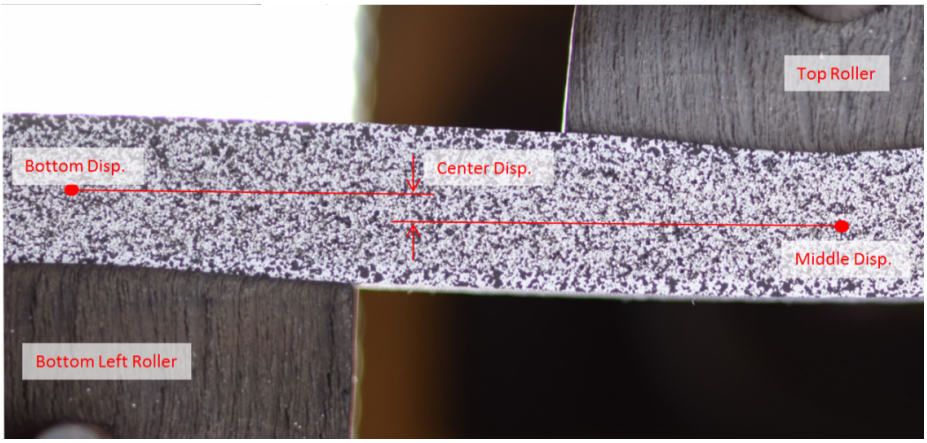

Figure A.2: The definition of center displacement.

loaded specimen as well as the stiffness being lower. The failure modes for the quasi-static and dynamic cases are in good agreement with each other, both of the tests show a highly catastrophic failure. With the use of the high-speed cameras the failure event can be seen more clearly. The structure can be seen going from no failure to complete failure in under 0.2 milliseconds, during which 5 frames showing the initiation and propagation, see Figure A.4 of the failure event is captured. The initial failure is due to high shear stress in the core, and the location of shear failure showed consistency

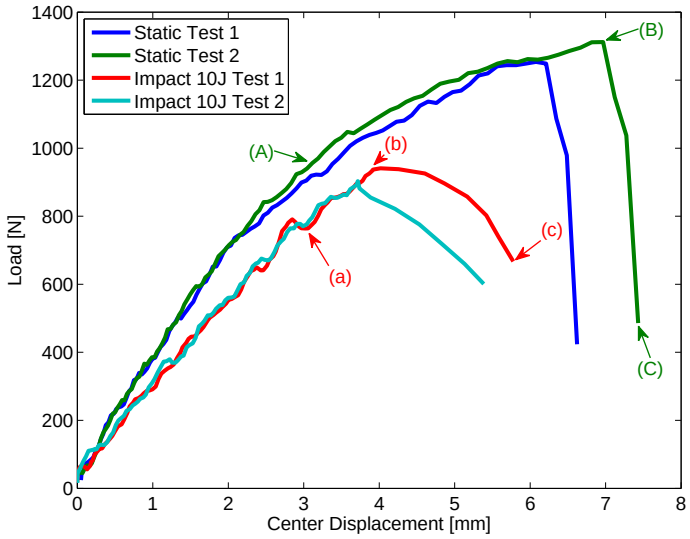

(a) Load-displacement response of quasi-static three-point bend and 10J impact tests

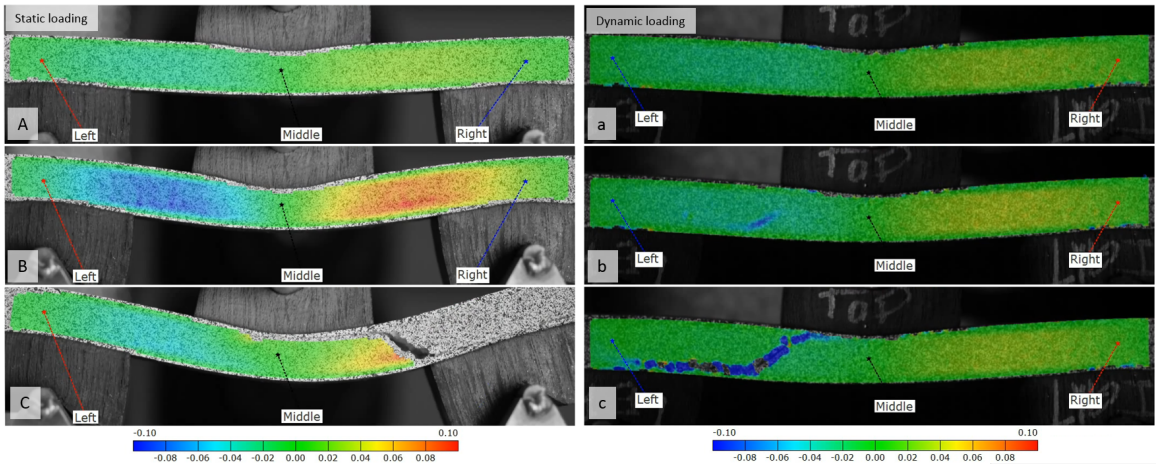

(b) DIC results of transverse shear strain: quasi-static three-point bend test (left) and 10J impact test (right)

Figure A.3: Representative experimental results.

between tests. Figure 1.3(b) shows the strain progression as well as the onset of failure captured in the dynamic case. The quasi-static failure progression was not captured with the rate at which the cameras were recording. From the high-speed cameras the failure can be seen to initiate in the core close to the lower face sheet and then a crack propagates through the core at an angle of 45°. Once the crack reaches the face sheets, initially the lower one, it starts a delamination that grows very rapidly along the face-sheet-core interface. The delamination crack that formed at the bottom interface propagates all the way through to the edge while the delamination at the top interface arrests slightly to the side of the roller, opposite to the side where the core has cracked.

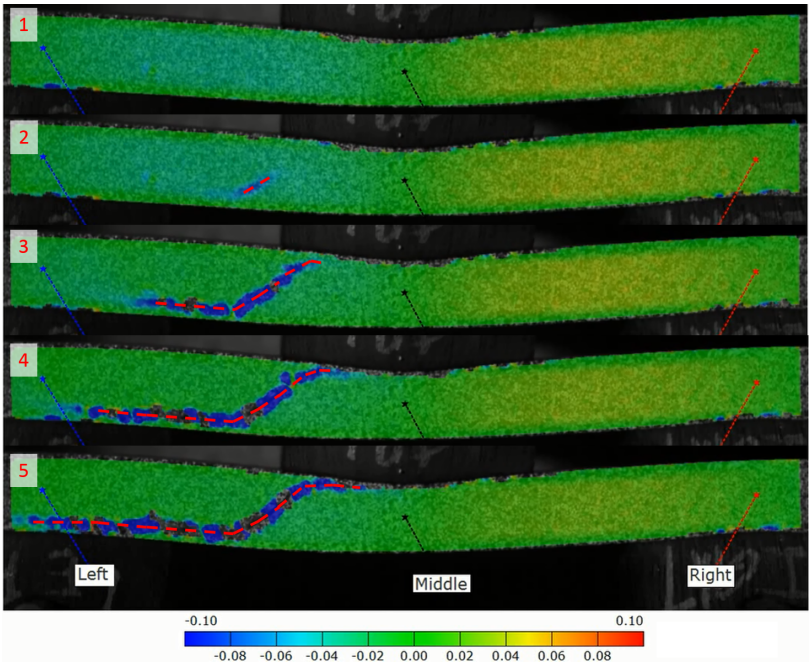

Figure A.4: The failure event for the 10J impact. The interval between each picture is 0.04 milliseconds where the first image shows no damage. The dashed red line represents cracks.

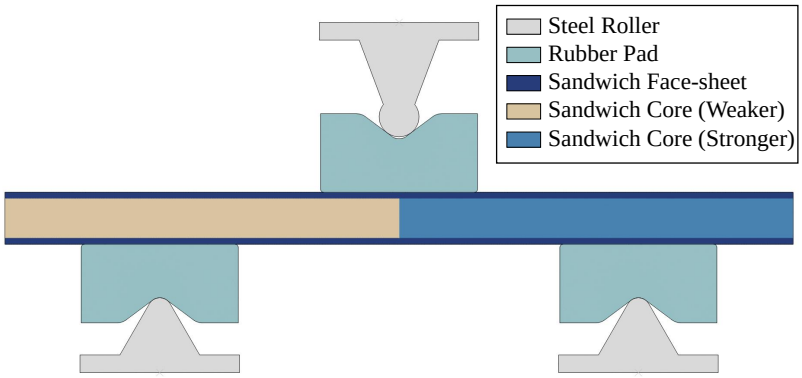

Figure A.5: 2D plane-strain FE model of the sandwich composite with *imperfect* core

A.3 Finite Element (FE)-based Simulation

A.3.1 Modeling Details

The 2D plane strain configuration of the tests, as shown in Figure A.5, was analyzed using the finite element method, [98]. The steel rollers, rubber pads and sandwich beam were modeled by four-noded plane-strain continuum elements with reduced integration (CPE4R), using the commercial software, ABAQUS. A friction coefficient of 0.5 was assigned to all contacts. The friction coefficient was acquired from estimates provided in engineering hand books for hard rubber to steel contact.

The element size of the core and face-sheets are 0.5 mm $\times$ 0.3 mm and 0.5 mm $\times$ 0.2 mm respectively. The face-sheet and the foam core mechanical properties are shown in Tables A.2 and A.3 respectively. The foam core shear non-linearity is shown in Figure A.6, and in this study only the foam core had a failure criterion defined. The evolution of core failure was modeled by using the Smeared Crack Approach (SCA), which has been adapted from the study by Heinrich and Waas [46], who extended the original formulation of Rots et al. [102]. The 2D formulation of the SCA for an isotropic material as presented in [138] and implemented through the user subroutine VUMAT, was used in the present study. Detailed information on the formulation of the 2D isotropic SCA can be seen in the following subsection (Section 3.2). An

Table A.2: Mechanical properties of the face-sheets.

Density, ρ	1450 kg/m^3
Young's modulus, E	48.1 GPa
Poisson's ratio, ν	0.21

Table A.3: Mechanical properties of the foam core.

Density, ρ	160 kg/m^3
Young's modulus, E	86 MPa
Poisson's ratio, ν	0.3
Tensile strength, X_T (static)	1.32 MPa
Tensile strength, X_T (dynamic)	1.10 MPa
Mode I energy release rate, G_{Ic}	0.05 N/mm

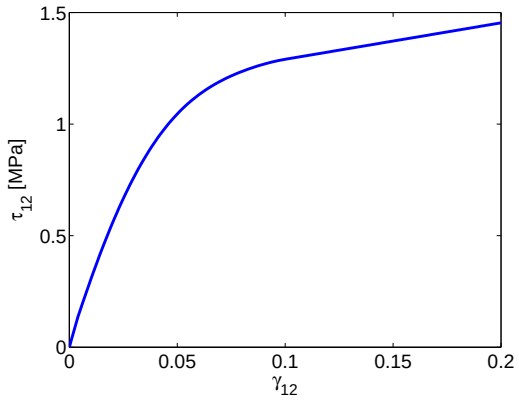

Figure A.6: Nonlinear shear stress-strain relation for the sandwich core material.

exponential traction separation law for the smeared crack strain has been adopted. The failure initiation criterion used is the maximum tensile principle stress, of which the critical value is denoted as X_T. In experiments, the crack randomly occurs on either side of the top roller, and the failure initiation is caused by slight asymmetry in the strength properties of the core which are not homogeneous. Therefore, we introduced a *imperfect* model for the foam core, where the right half is 1.1 times stronger than the left half, in terms of critical tensile principle stress. Due to this choice, the core shear crack will always initiate in the left half, a slightly higher critical value will not significantly influence the crack propagation once the crack reaches the right half.

The density of the rubber pads is 1100 kg/m^3. To achieve a better understanding

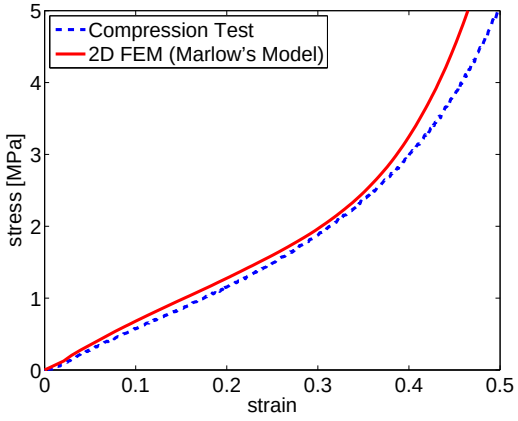

Figure A.7: The stress-strain curve from a compression test on a long rubber specimen and FEM simulation of the test using CPE4 element and Marlow's hyperelastic model.

of the mechanical properties of rubber pad material, uniaxial compression tests were performed on a wide rubber specimen. The dimension of the rubber specimen is 25.94 mm (L) $\times$ 136.15 mm (W) $\times$ 23.90 mm (H). The rubber was loaded in the thickness direction (H). The rubber specimen is wide enough so that it can be considered to satisfy plane-strain conditions. A 2D FE simulation was adopted to simulate the compression test. The cross-section of the rubber specimen was modeled by using continuum plane-strain elements (CPE4). Marlow's hyper-elastic model was used [28]. The Poisson's ratio of the rubber was set as 0.495. As shown in Figure A.7, the 2D FE model gives good agreement with the experimental results.

The steel rollers were modeled as rigid bodies. The impactor mass, 25.13 kg, was assigned as a point mass to the reference point of the top center roller. The quasi-static loading was simulated as a displacement controlled loading at the top center roller with loading rate 25 mm/s. The loading rate was chosen by considering the balance of precision and computational cost. Impact energy was applied to the model by specifying an initial velocity of the top center roller. The initial velocity for the 10J impact is 0.89 m/s.

A.3.2 2D Isotropic Smeared Crack Approach Formulation

A 2D isotropic smeared crack approach was utilized to capture the post-peak failure of the sandwich foam core. The method was implemented as a user material subroutine (VUMAT) in the commercial FE solver, ABAQUS Explicit. Pre-peak behaviour is governed by a nonlinear elasticity model in which the normal stress-strain relation is linear but the shear stress-shear strain relation is non linear. It is possible to implement any type of pre-peak continuum model, such as J2-plasticity or continuum damage mechanics. In the present case the non-linear shear response of the foam core is modeled using a polynominal representation between shear stress and shear strain (Figure 6). Post-peak behaviour is modeled by the SCA method. The SCA method assumes that macroscopic cracks are smeared over a finite element (in which the crack resides) in the form of macroscopic strain softening. The formulation of the 2D method will now be covered.

In the post-peak regime the total strain is represented as a sum of the continuum strain, $\boldsymbol{\varepsilon}^{co}$, and crack strain, $\boldsymbol{\varepsilon}^{cr}$.

$$\boldsymbol{\varepsilon} = \boldsymbol{\varepsilon}^{co} + \boldsymbol{\varepsilon}^{cr} \tag{A.1}$$

The global crack strain, $\boldsymbol{\varepsilon}^{cr}$, can be related to the local co-ordinate crack strain, $\boldsymbol{e}^{cr}$, through the transformation matrix N. The transformation matrix is found by using the Rankine criterion for maximum principal stress. The Rankine criterion for maximum principle stress is also used to evaluate the crack onset and crack direction.

$$\boldsymbol{\varepsilon}^{cr} = \boldsymbol{N}\boldsymbol{e}^{cr} = \boldsymbol{N} \begin{bmatrix} \varepsilon^{cr}_{norm} \\ \gamma^{cr}_{tang} \end{bmatrix} \tag{A.2}$$

Where ε^{cr}_{norm} and γ^{cr}_{tang} are the crack strain components normal and tangential to the crack edge, respectfully. In a similar manner the global stress state, σ, can be

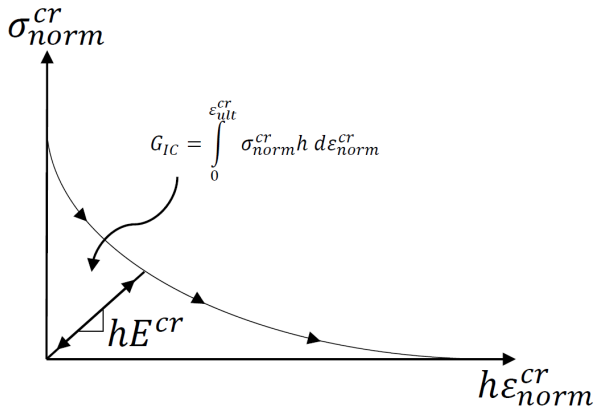

Figure A.8: Traction-separation law dictates the crack interface stiffness.

transformed to give the tractions on the cracks edge where, like previously, σ_{norm}^{cr} and τ_{tang}^{cr} are the normal and tangential stress components on the crack edge.

$$\boldsymbol{s}^{cr} = \begin{bmatrix} \sigma_{norm}^{cr} \\ \tau_{tang}^{cr} \end{bmatrix} = \boldsymbol{N}^T \boldsymbol{\sigma} \tag{A.3}$$

The crack interface (local) stresses are related to the local strains through a secant stiffness matrix, D^{cr}, and a damping matrix, D^{da}, by the following relation

$$\boldsymbol{s}^{cr} = \boldsymbol{D}^{cr}\boldsymbol{e}^{cr} + \boldsymbol{D}^{da}\dot{\boldsymbol{e}}^{cr} \tag{A.4}$$

By adding the damping matrix the crack propagation becomes a time dependent property. By doing so the simulation can be stabilized and oscillations due to sudden loss of stiffness are reduced. The crack (local) strain rate, $\dot{e}^{cr}$, is approximated from the previous time step using finite differences.

$$\dot{\boldsymbol{e}}^{cr} \approx \frac{\boldsymbol{e}^{cr}(t+\Delta t) - \boldsymbol{e}^{cr}(t)}{\Delta t} = \frac{\boldsymbol{e}^{cr} - \boldsymbol{e}_{old}^{cr}}{\Delta t} \tag{A.5}$$

The crack interface stresses can now be expressed as the following;

$$\boldsymbol{s}^{cr} = \boldsymbol{D}^{cr}\boldsymbol{e}^{cr} + \frac{1}{\Delta t}\boldsymbol{D}^{da} - \frac{1}{\Delta t}\boldsymbol{D}^{da}\boldsymbol{e}_{old}^{cr} \tag{A.6}$$

By expanding the above equation, it follows that,

$$\begin{bmatrix} \sigma^{cr}_{norm} \\ \tau^{cr}_{tang} \end{bmatrix} = \begin{bmatrix} E^{cr} & 0 \\ 0 & G^{cr} \end{bmatrix} \begin{bmatrix} h\varepsilon^{cr}_{norm} \\ h\gamma^{cr}_{tang} \end{bmatrix}$$
$$+\frac{1}{\Delta t} \begin{bmatrix} \eta & 0 \\ 0 & \eta \end{bmatrix} \begin{bmatrix} h\varepsilon^{cr}_{norm} \\ h\gamma^{cr}_{tang} \end{bmatrix} - \frac{1}{\Delta t} \begin{bmatrix} \eta & 0 \\ 0 & \eta \end{bmatrix} \begin{bmatrix} h\varepsilon^{cr}_{norm} \\ h\gamma^{cr}_{tang} \end{bmatrix}_{old} \tag{A.7}$$

where E^{cr} and G^{cr} are the crack tensile and shear secant stiffness, respectfully. The crack secant stiffness is a function of the normal crack strain, ε^{cr}_{norm}, and not the shear crack strain, γ^{cr}_{tang}, and is therefore mode I dominated. In the above equation it can be seen that the strains are related to a characteristic length scale, h. This provides the relation between the effective stress-strain relation and the traction-separation law. By the manner in which the crack separation is related to the element level smeared strain, the correct strain energy is dissipated for each element that enters the post-peak regime, ensuring mesh objectivity. The traction-separation law used for the unloading of the element can be seen in Figure A.8.

To relate the crack strain to the total elastic strain we first define the constitutive relation for the continuum as

$$\boldsymbol{\sigma} = \boldsymbol{D}^{co}\boldsymbol{e}^{co} \tag{A.8}$$

By combining the equations above, an implicit relationship between the crack strain and the elastic strain exists

$$\boldsymbol{e}^{cr} = \left[\boldsymbol{D}^{cr} + \boldsymbol{N}^T\boldsymbol{D}^{co}\boldsymbol{N} + \frac{1}{\Delta t}\boldsymbol{D}^{da}\right]^{-1}\left[\boldsymbol{N}^T\boldsymbol{D}^{co}\boldsymbol{\varepsilon}^{co,cr} + \frac{1}{\Delta t}\boldsymbol{D}^{da}\boldsymbol{e}^{cr}_{old}\right] \tag{A.9}$$

The relation between total stress and total strain can now be found, as follows;

$$\boldsymbol{\sigma} = \Big[\boldsymbol{D}^{co} - \boldsymbol{D}^{co}\boldsymbol{N}\Big(\boldsymbol{D}^{cr} + \boldsymbol{N}^T\boldsymbol{D}^{co}\boldsymbol{N} + \frac{1}{\Delta t}\boldsymbol{D}^{da}\Big)^{-1}\boldsymbol{N}^T\boldsymbol{D}^{co}\Big]\boldsymbol{\varepsilon}^{co,cr} - \frac{1}{\Delta t}\Big[\boldsymbol{D}^{cr} + \boldsymbol{N}^T\boldsymbol{D}^{co}\boldsymbol{N} + \frac{1}{\Delta t}\boldsymbol{D}^{da}\Big]^{-1}\boldsymbol{D}^{da}\boldsymbol{e}^{cr}_{old} \tag{A.10}$$

For a more detailed description on the numerical implementation of the SCA method (3D isotropic model and 2D orthotropic model) the reader is referred to Heinrich and Waas [46].

A.3.3 Results

The computed load-displacement responses from the quasi-static simulations are compared against experimental results, as shown in Figure A.9. Two different displacements are reported. Figure 1.9(a) uses the roller displacement, which is the one commonly reported in literature. A new approach to measuring the displacement is considered to eliminate the large deformation influenced by the rubber pads. The center displacement is used to plot a secondary load-displacement response in Figure 1.9(b). The center displacement, defined in Figure A.2, will provide more information on the flexural response of the sandwich structure, including material non-linearity. The FE model shows good agreement with experiments on the flexural response of the structure as well as capturing the peak load, and the location of failure initiation and propagation.

The low velocity impact simulations are compared against the experimental results, the load-time history as well as the load-displacement response are compared, as shown in Figure A.11. The load-time history from the FE model agrees well with experimental results. The peak load predictions are in good agreement with experimental peak loads. From the load-displacement response, where the displacement is the center deflection of the structure (Figure A.2), it can be seen that the experimental results are softer than the model predictions. The experimental results show overall

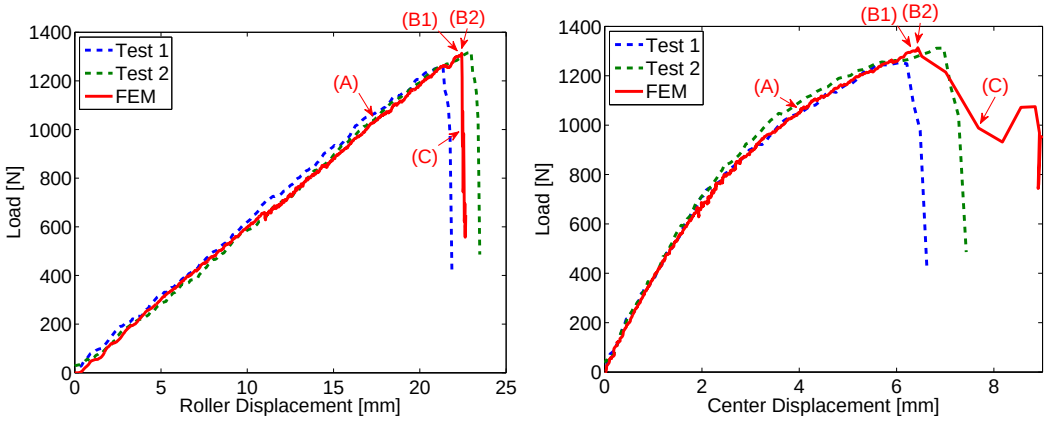

(a) Roller displacement (b) Center displacement

Figure A.9: Comparisons of load-displacement response between experiments and FEM simulation of quasi-static test.

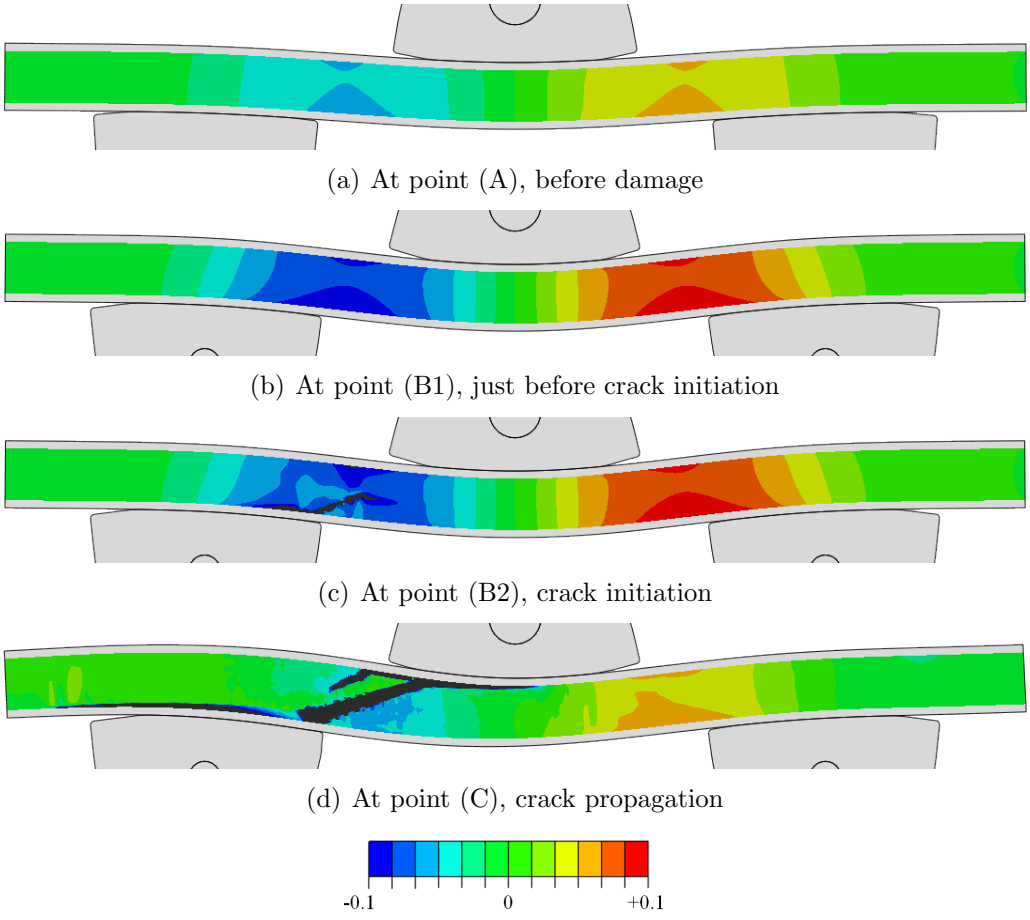

(a) At point (A), before damage

(b) At point (B1), just before crack initiation

(c) At point (B2), crack initiation

(d) At point (C), crack propagation

Figure A.10: Transverse shear strain distribution from FEM simulation of quasi-static test. The colorbar is scaled so that a comparison against experiments can be made. The black color shown is out of the colorbar range.

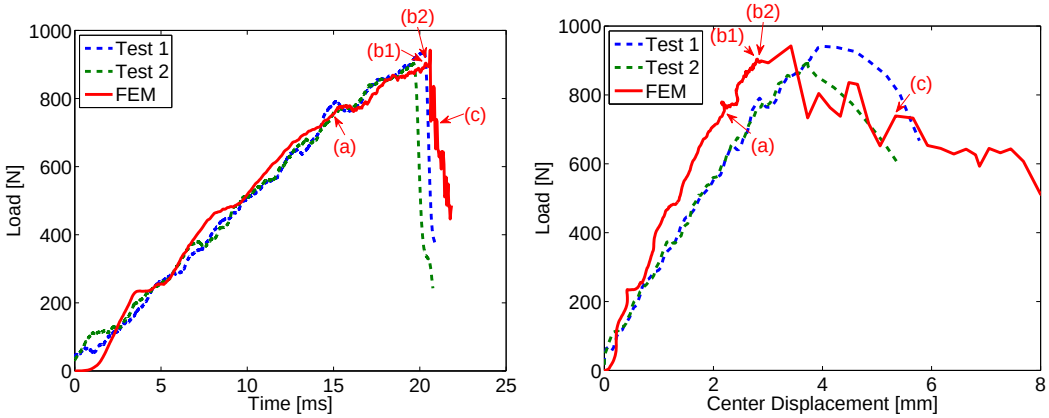

(a) Load-time history. (b) Load-displacement response

Figure A.11: Comparisons of load history and load-displacement response between experiments and FEM simulation of 10J impact.

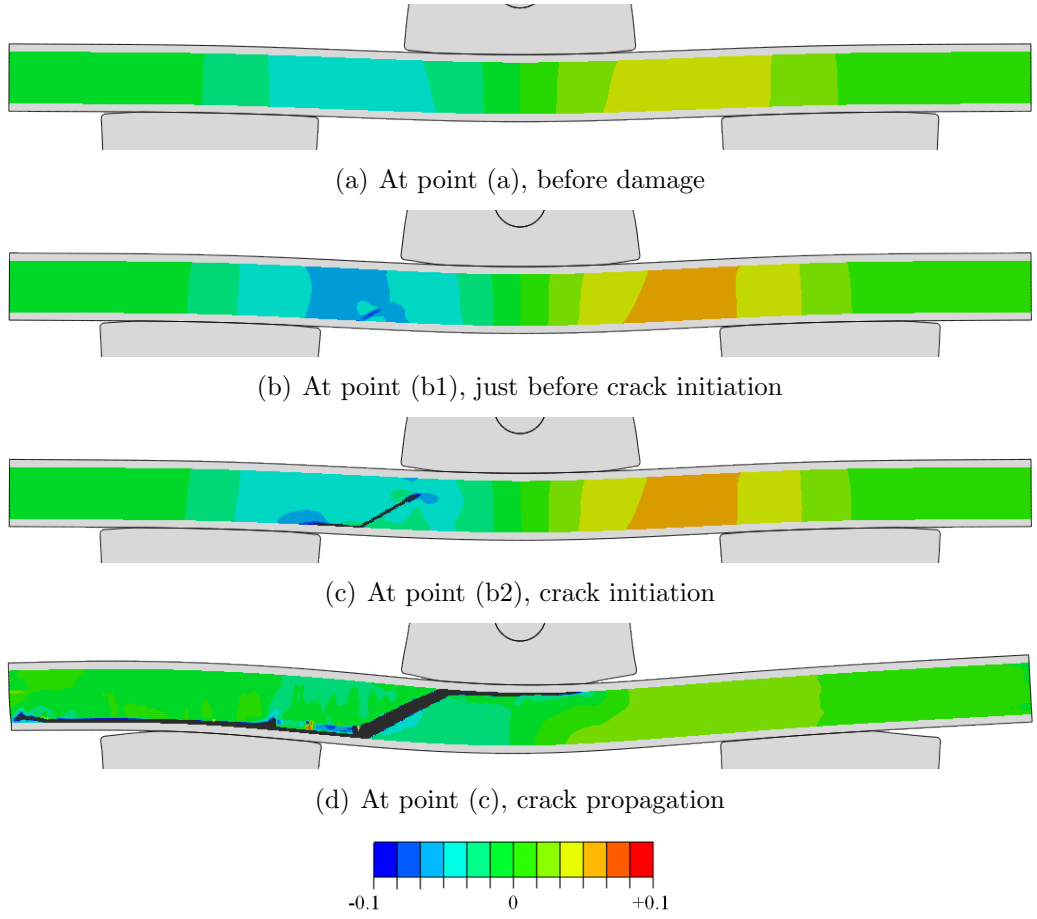

(a) At point (a), before damage

(b) At point (b1), just before crack initiation

(c) At point (b2), crack initiation

(d) At point (c), crack propagation

Figure A.12: Transverse shear strain distribution from FEM simulation of 10J impact. The colorbar is scaled so that comparison against experiment is feasible. The black color shown is out of the colorbar range.

rate softening in stiffness which is not captured by the FE model. The reason for this softening could be due to micro cracking in the foam core almost instantaneously as the structure gets loaded. This would result in an overall stiffness softening rather than a progressive softening response. Further investigations which are beyond the scope of this paper are needed to investigate this hypothesis.

The evolution of core failure and interface delamination for the quasi-static simulation is shown in Figure A.10 and for the dynamic simulation in Figure A.12, in terms of transverse shear strain, noting that the bound for the color contours is ± 0.1 so that it can be compared to the DIC results measured in experiments. The black color region in Figure A.10 and A.12 demonstrates that the absolute transverse shear strain is larger than 0.1. In the SCA, the secant modulus is degraded when the finite element reaches the critical stress and enters the post-peak strain softening zone, where the tangent stiffness is negative [138]. In the progression of failure, the crack strain will replace the continuum strain as the dominant one. Therefore, the black color region can be considered as the crack. The failure initiation and propagation from the experiments were captured, and the events are quite similar and will be described as follows. The crack in the core initiates near the interface between the core and lower face-sheet with a 45° angle. It is worth noting that a small delamination occurs at the lower interface immediately after the small core crack initiates, starting from the core crack tip, which was also captured by the high-speed video in the impact experiments. Once the crack has been initiated, it propagates through the core at a 45° angle as well as delaminations traveling rapidly to either side at a 135° angle, with respect to the core crack, resulting in a zig-zag shaped final failure of the structure. This zig-zag shaped failure, caused by the interaction of the matrix crack and the subsequent delamination is characteristic of the failure mode reported in many publications that deal with impact damage in composites.

A.4 Conclusion

Experimental and computational results for a sandwich composite beam under three point bending, both under quasi-static conditions as well as low velocity impact, have been presented. Detailed insight has been obtained into the failure mechanisms observed in the experiments. These details were captured in a 2D FE model by implementing failure mechanics using the smeared crack approach. The FE model captures the flexural response of the static experiments as well as the onset of failure. The dynamic simulations also show good agreement. In particular, the sequence of physical events observed in the experiments are accurately captured by the modeling framework that is presented. Matrix cracking initiates first, locally. Then, this initiated crack propagates and intersects an interface, at which time delamination is seen to initiate. This sequence of events is well captured in a computationally efficient manner by the study presented here. Extensions of these findings to understand the initiation and propagation of damage and failure during an impact event in a laminated composite (which will require more computational resources) will be useful.

APPENDIX B

Face-on Impact microCT Images

The following appendix contains higher resolution microCT images from the impact experiments conducted in Chapter II. The slices, due to the scanning method, get influenced by adjacent layers. The images have been chosen here to represent the damage extent traveling through the thickness of the specimen. The interface number and major fiber direction of the plies showing damage has been noted. The orientation can be seen in the first figure for each test.

Figure B.1-B.5 show the results from the High-Fidelity Impact Study presented in Chapter 2.2. Layup: $[0/45/0/90/0/-45/0/45/0/-45]_s$

Figure B.6-B.10 show the results from the BVID Impact Study presented in Chapter 2.2. Layup: $[45/90/-45/0_2/-45/0/45/0/45/-45/0/45/0/-45/0_2/-45/90/45]$

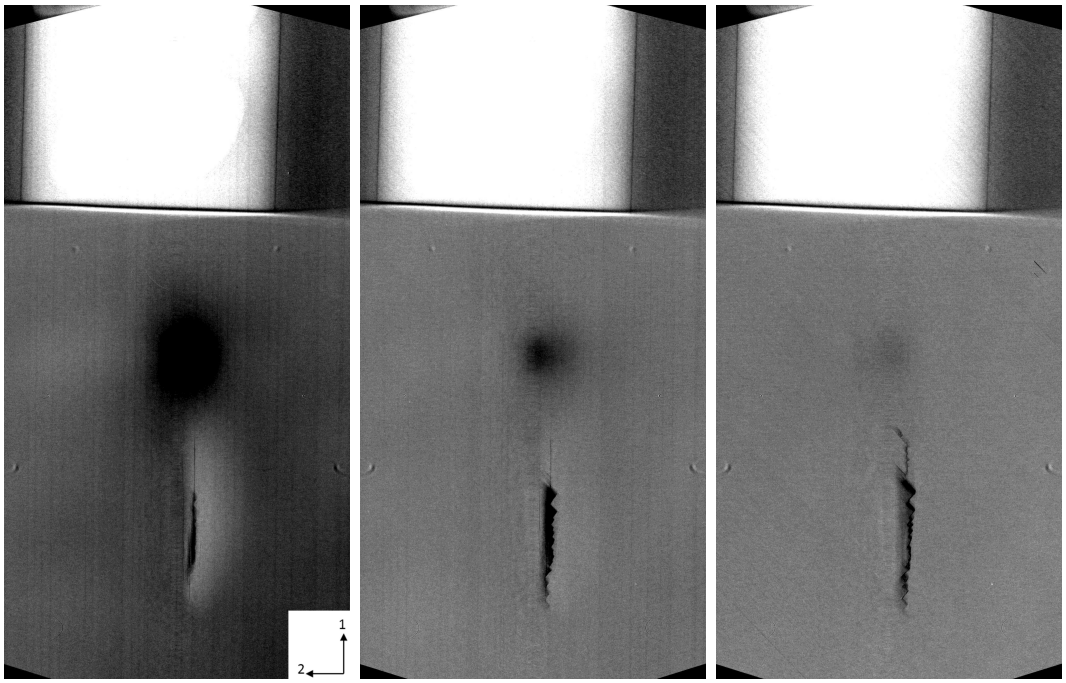

(a) Interface 1: 0/45 (b) Interface 1: 0/45 (c) Interface 2: 45/0

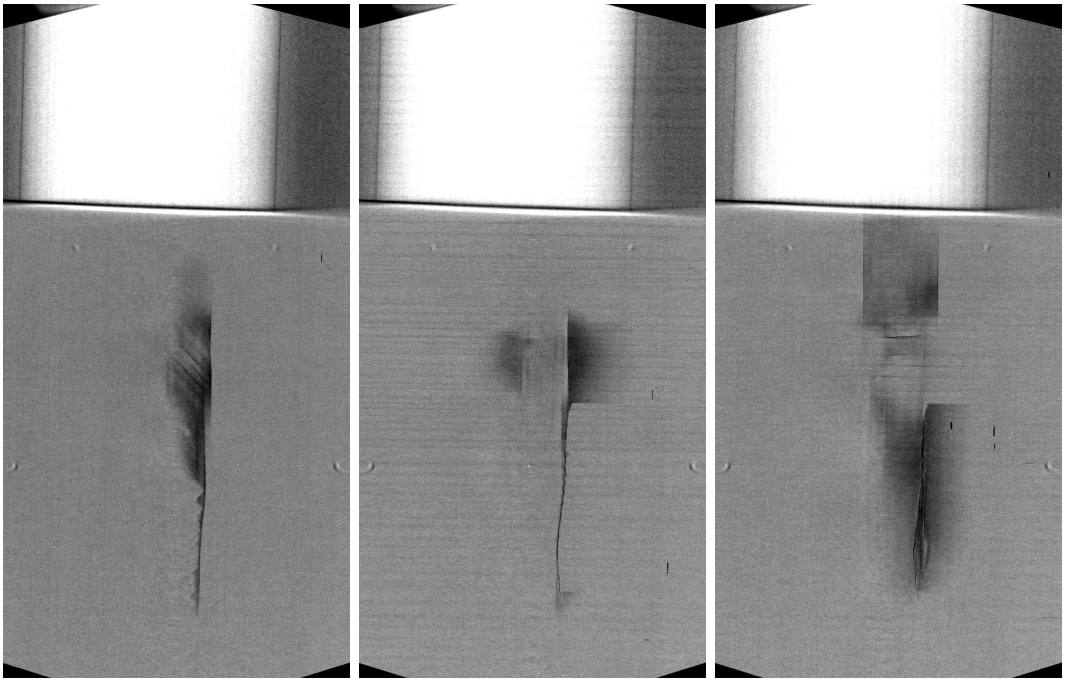

(d) Interface 2: 45/0 (e) Interface 3: 0/90 (f) Interface 4: 90/0

Figure B.1: MicroCT results for interfaces 1-4.

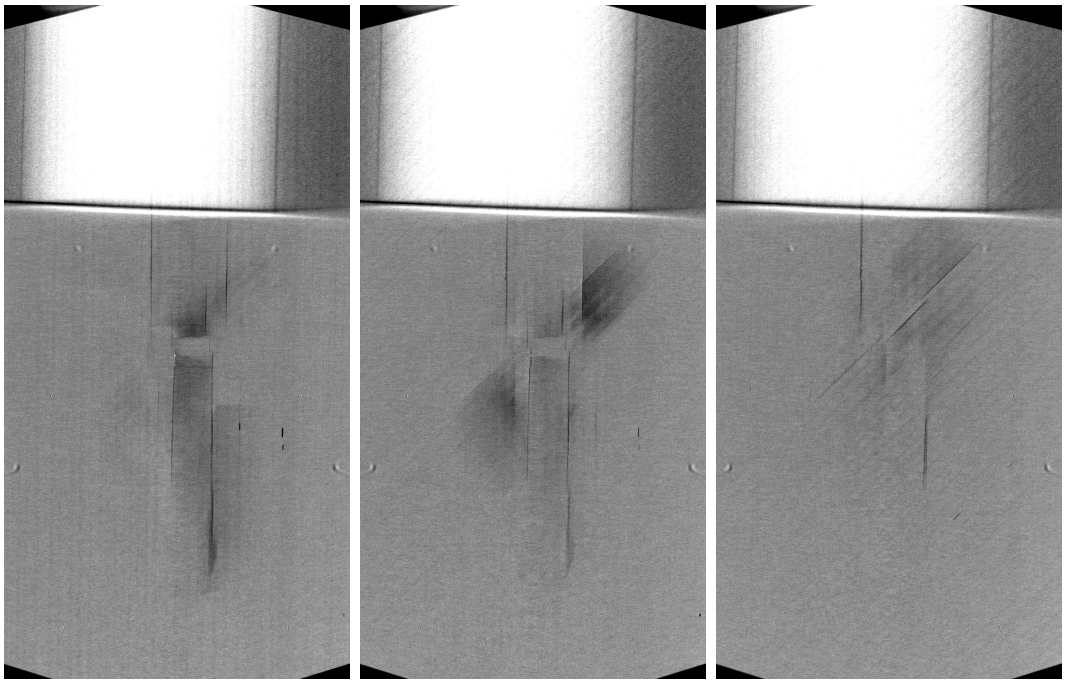

(a) Interface 5: 0/-45 (b) Interface 5: 0/-45 (c) Interface 6: -45/0

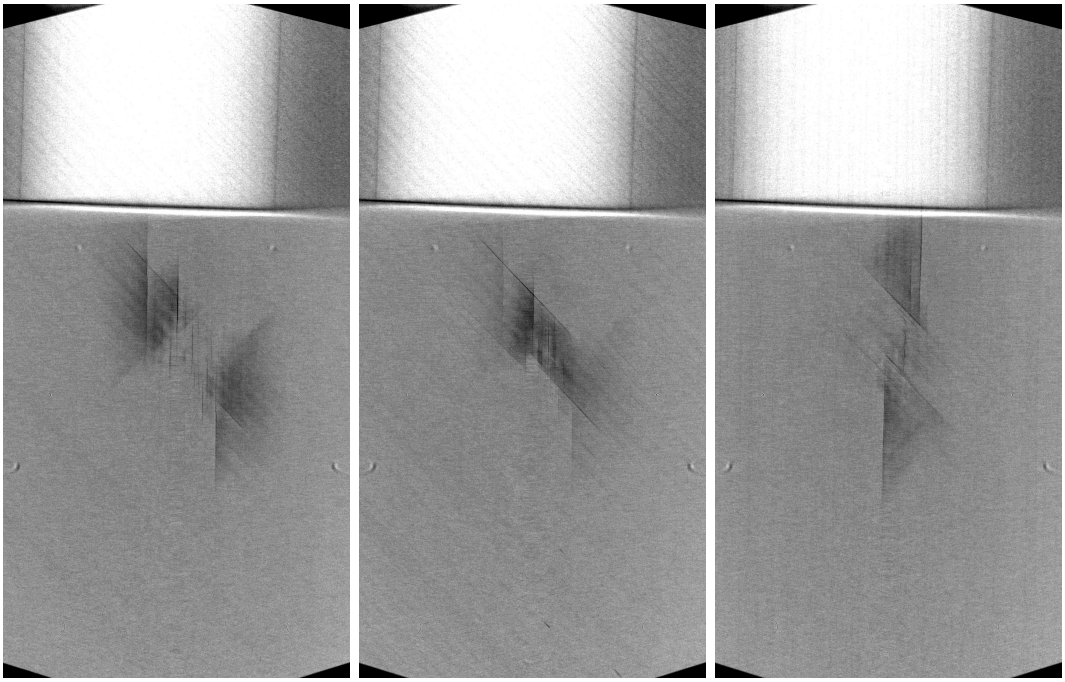

(d) Interface 7: 0/45 (e) Interface 8: 0/45 (f) Interface 9: 45/0

Figure B.2: MicroCT results for interfaces 5-9.

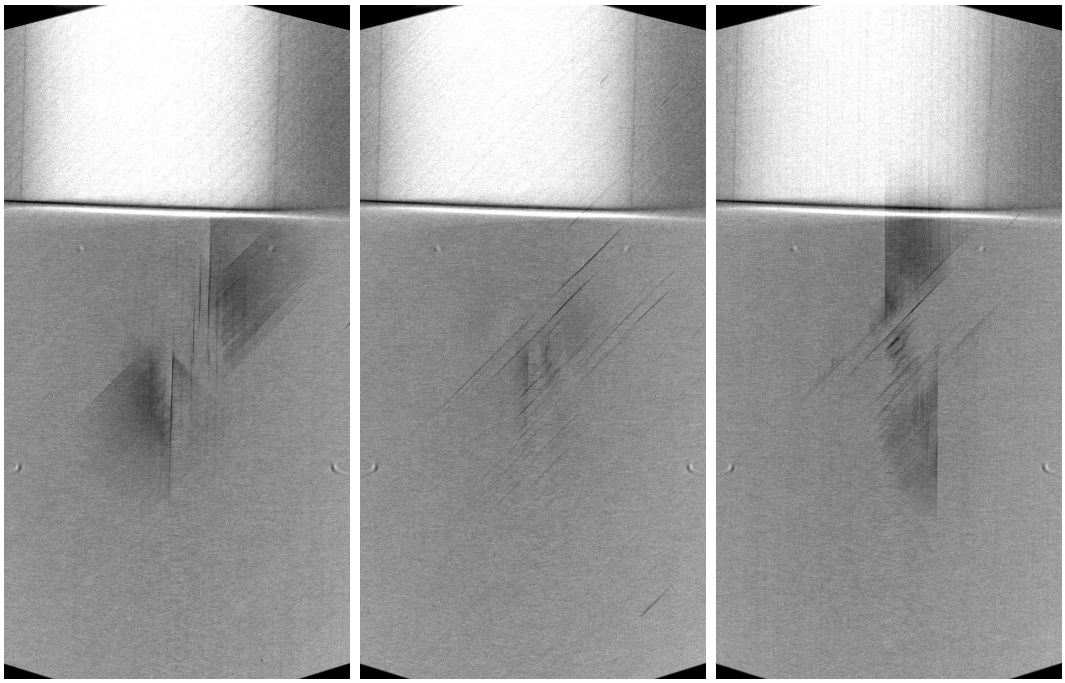

(a) Interface 10: 0/-45x2 (b) Interface 11: -45x2/0 (c) Interface 11: -45x2/0

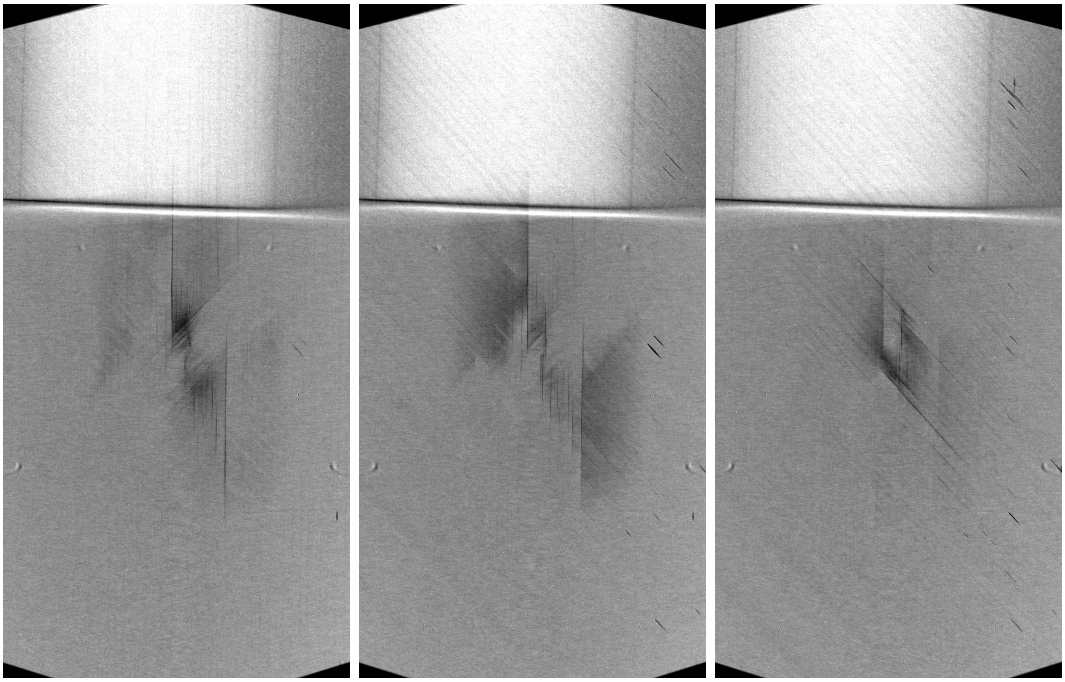

(d) Interface 12: 0/45 (e) Interface 12: 0/45 (f) Interface 13: 45/0

Figure B.3: MicroCT results for interfaces 10-13.

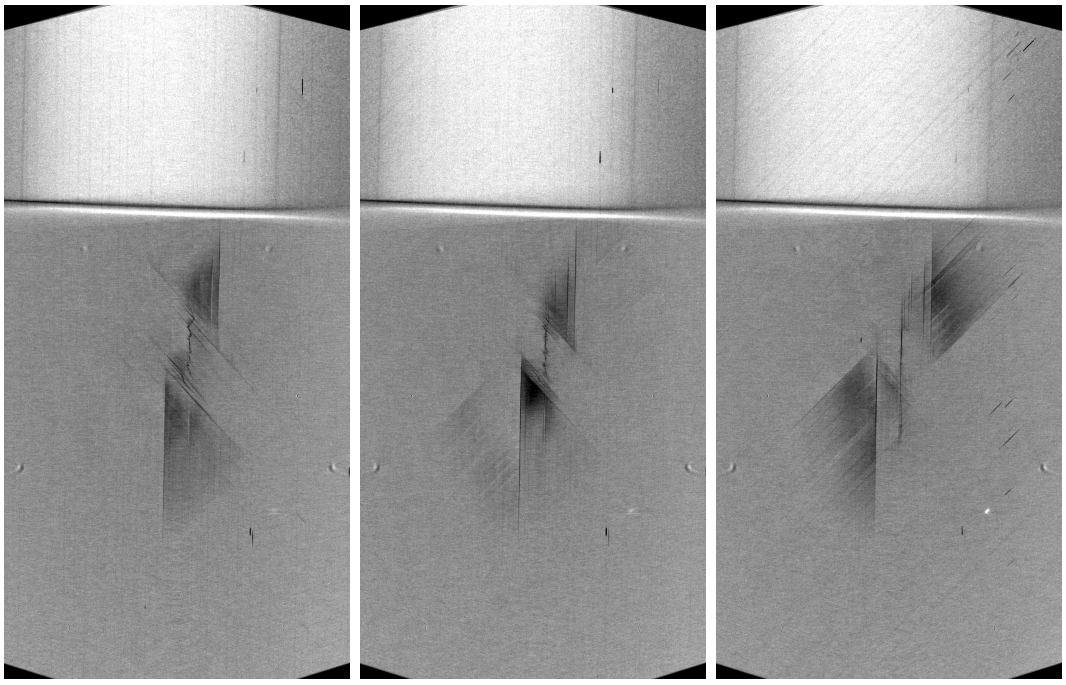

(a) Interface 13: 45/0 (b) Interface 13-14: 45/0/-45 (c) Interface 14: 0/-45

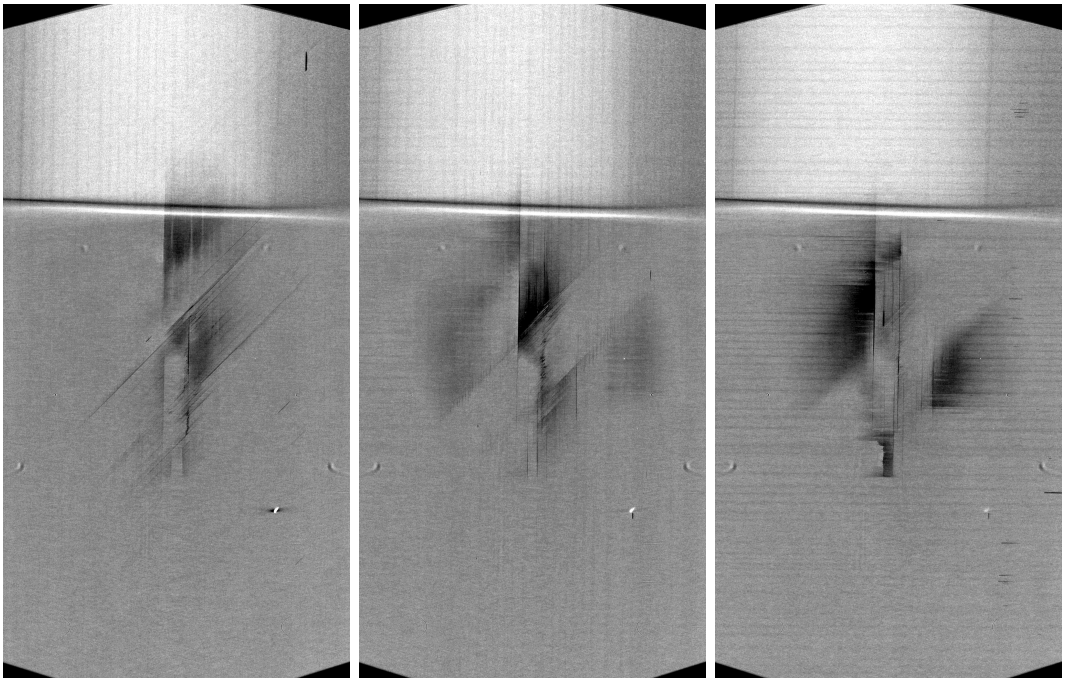

(d) Interface 15: -45/0 (e) Interface 15-16: -45/0/90 (f) Interface 16: 0/90

Figure B.4: MicroCT results for interfaces 13-16.

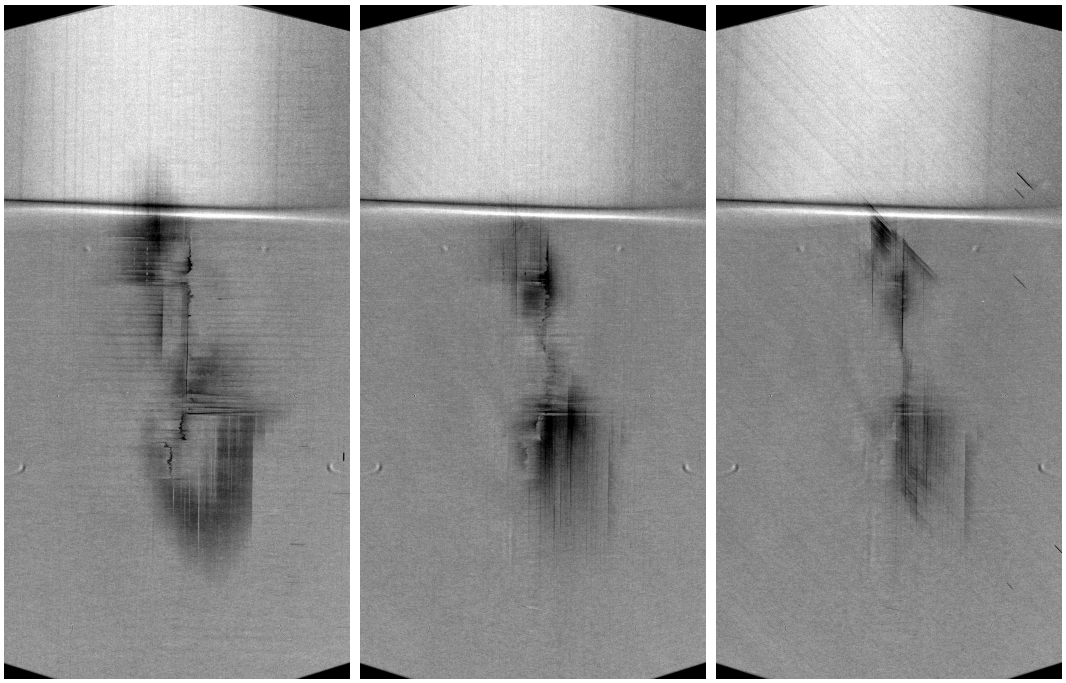

(a) Interface 17: 90/0 (b) Interface 17: 90/0 (c) Interface 18: 0/45

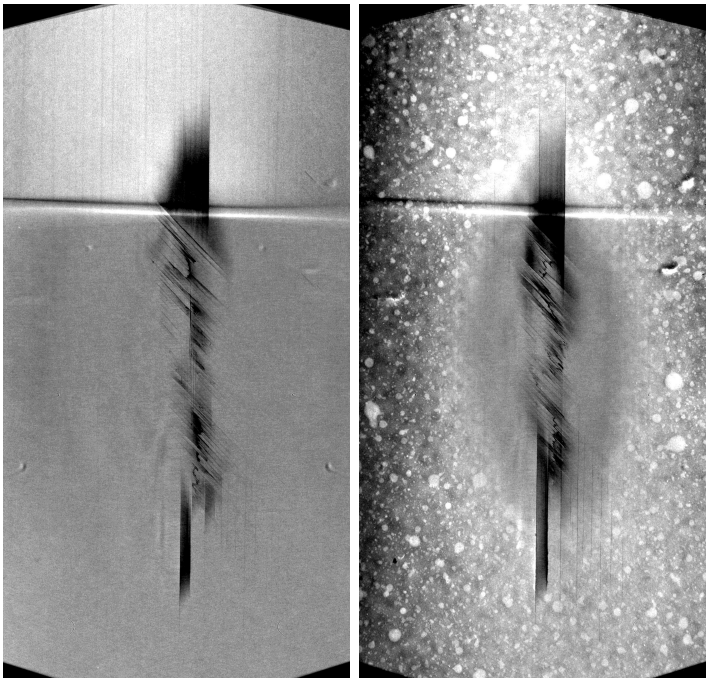

(d) Interface 19: 45/0 (e) Interface 19: 45/0

Figure B.5: MicroCT results for interfaces 17-19.

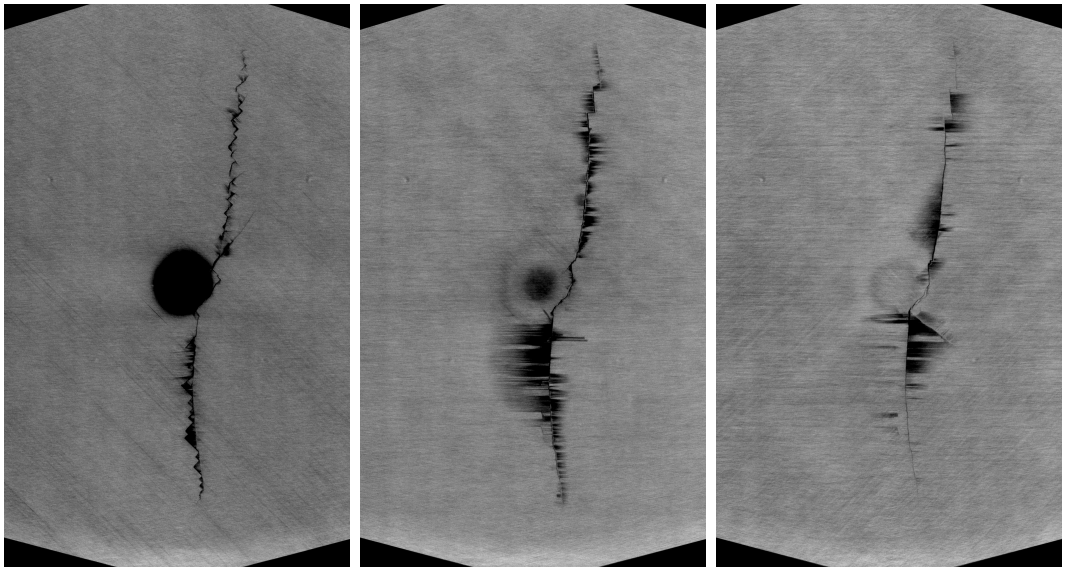

(a) Ply 1: 45 (b) Ply 2: 90 (c) Interface 2: 90/-45

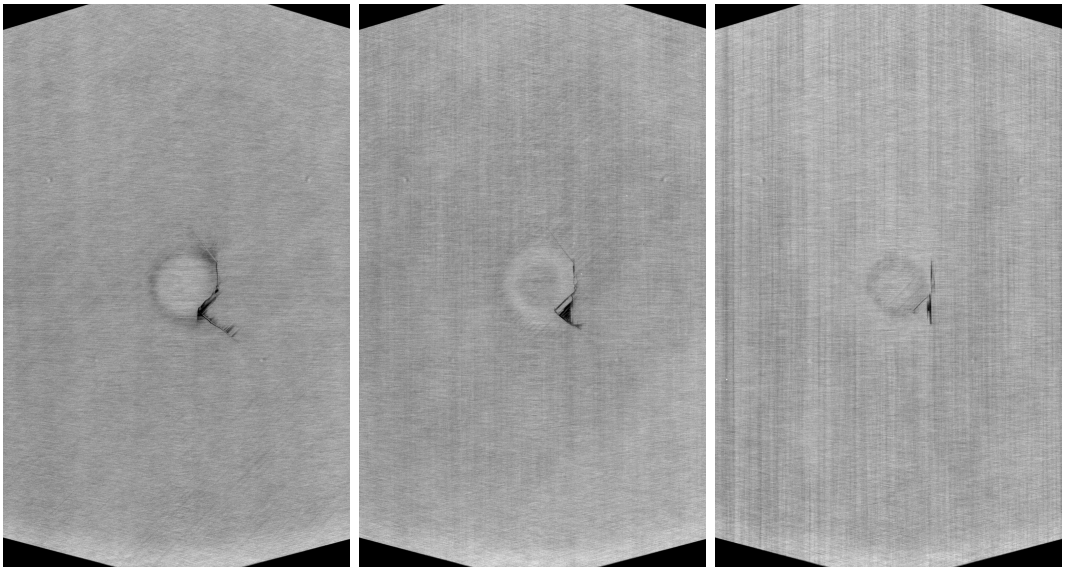

(d) Interface 3: -45/0x2 (e) Interface 3: -45/0x2 (f) Interface 4: 0x2/-45

Figure B.6: MicroCT results for interfaces 1-4.

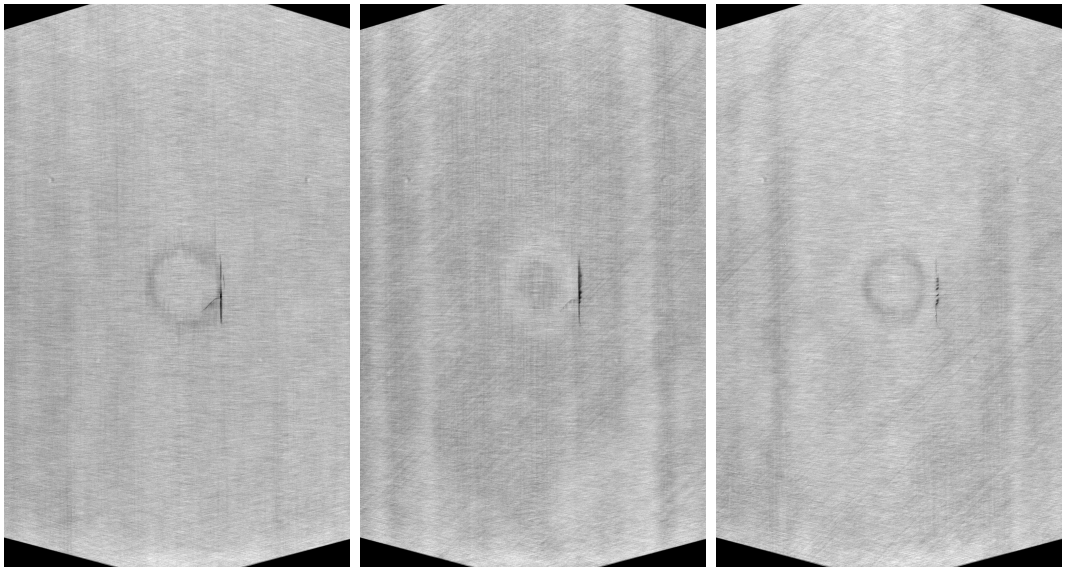

(a) Interface 5: -45/0 (b) Interface 5: -45/0 (c) Interface 5: -45/0

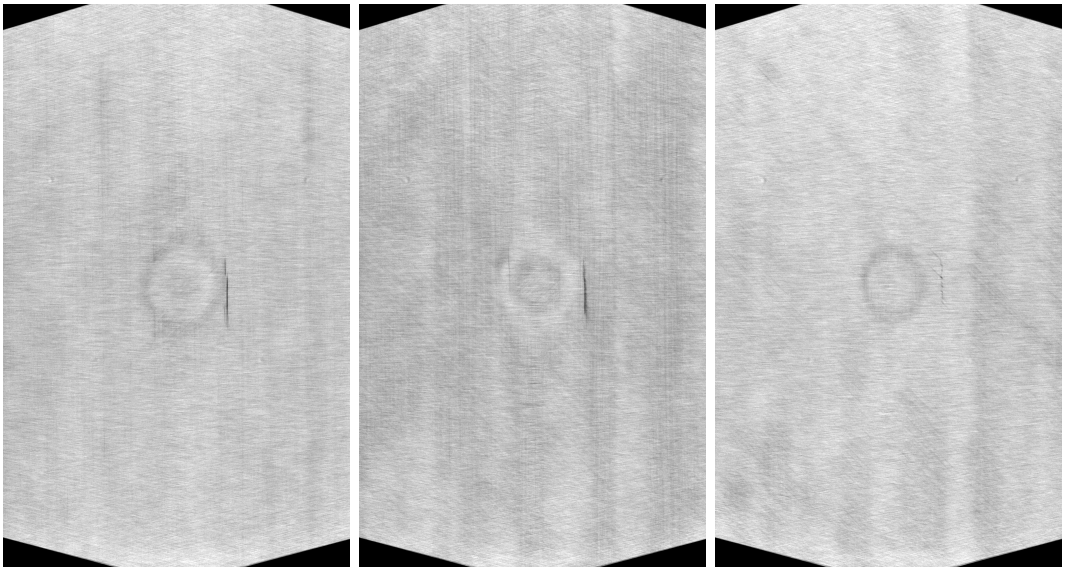

(d) Interface 5-6: -45/0/45 (e) Interface 7: 0/45 (f) Interface 8: 45/0

Figure B.7: MicroCT results for interfaces 5-8.

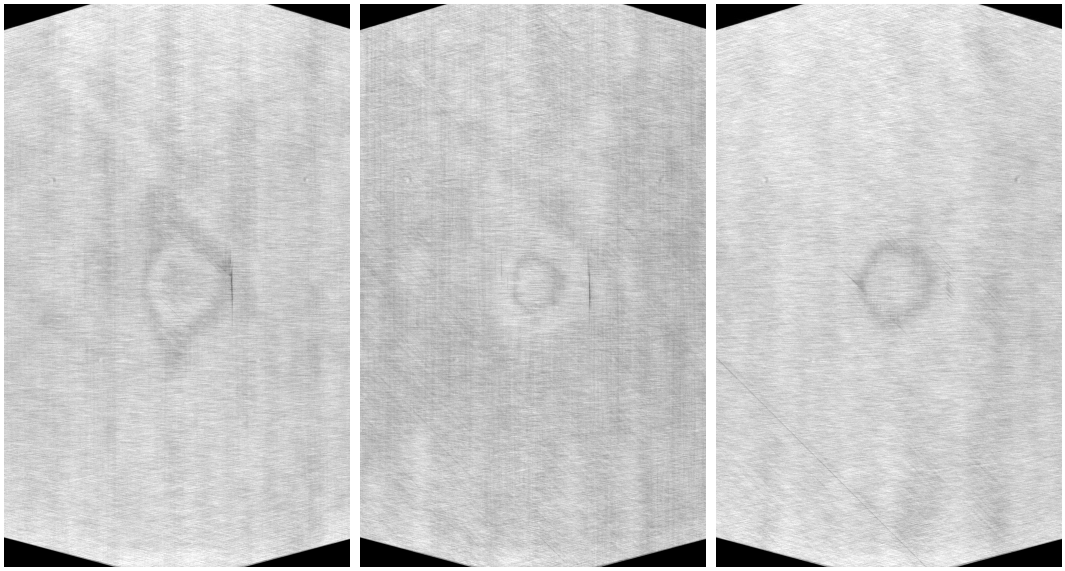

(a) Interface 8: 45/0 (b) Interface 9: 0/45 (c) Interface 9: 0/45

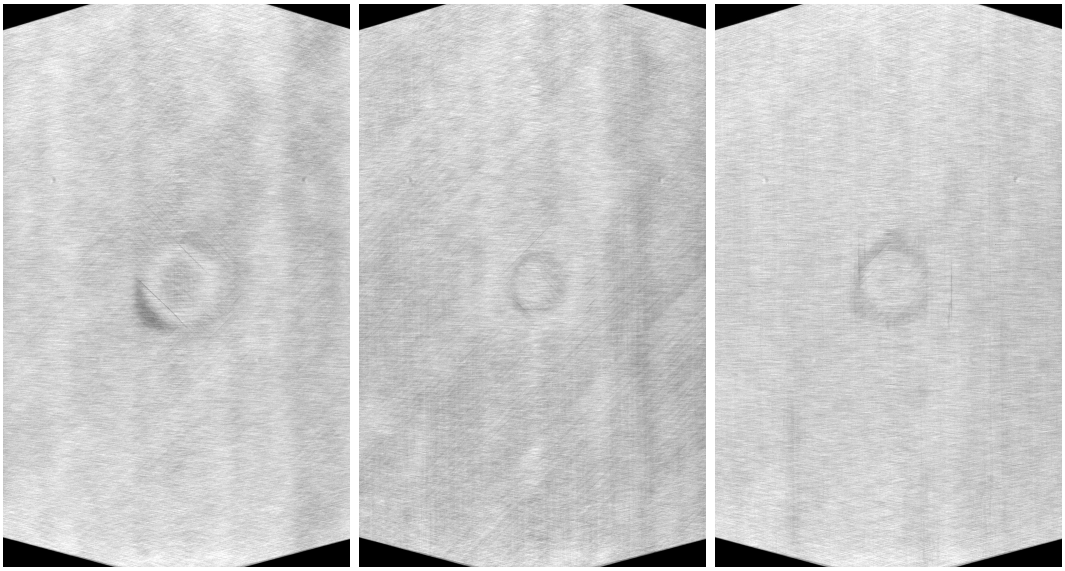

(d) Interface 10: 45/-45 (e) Interface 10: 45/-45 (f) Interface 11: -45/0

Figure B.8: MicroCT results for interfaces 8-11.

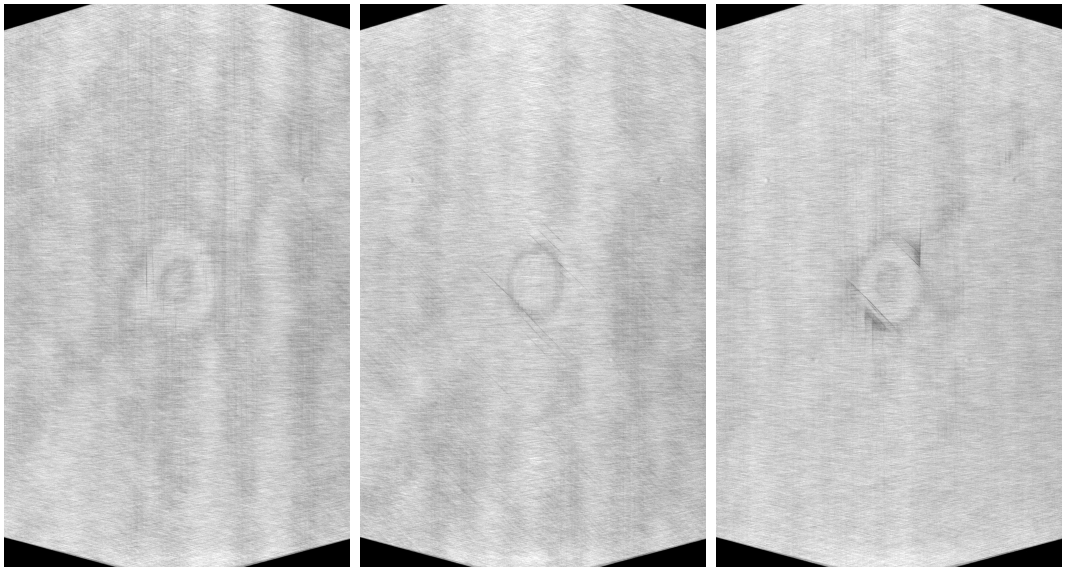

(a) Interface 12: 0/45 (b) Interface 12: 0/45 (c) Interface 13: 45/0

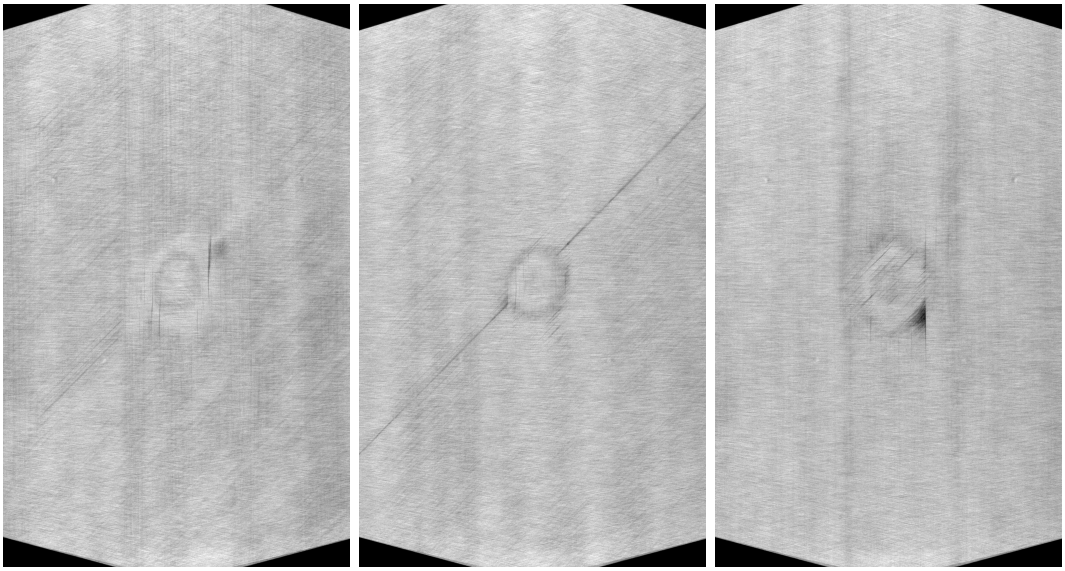

(d) Interface 14: 0/-45 (e) Interface 14: 0/-45 (f) Interface 15: -45/0x2

Figure B.9: MicroCT results for interfaces 12-15.

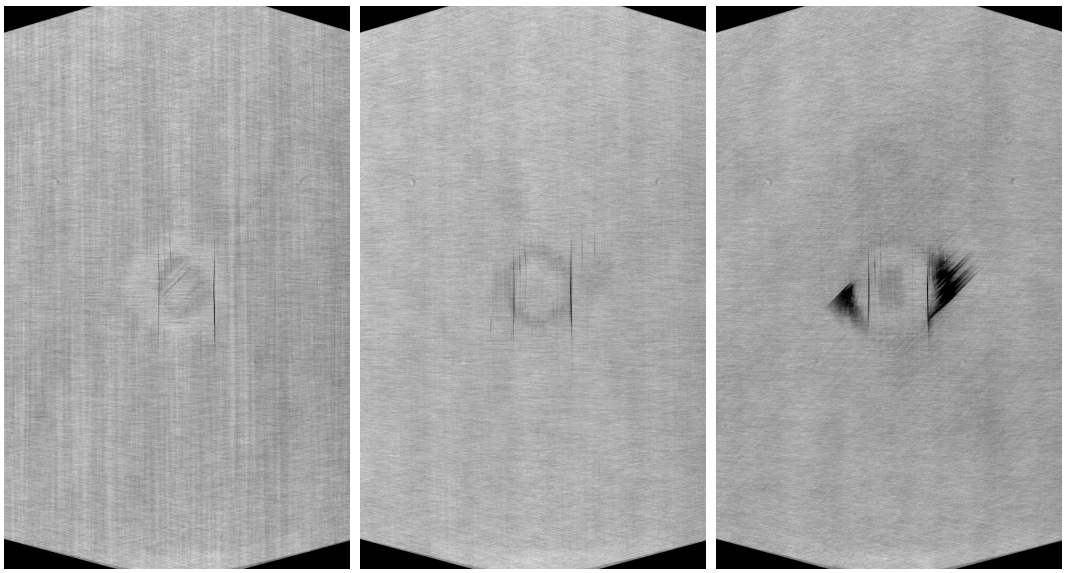

(a) Interface 15: -45/0x2 (b) Interface 15-16: -45/0x2/-45 (c) Interface 16: 0x2/-45

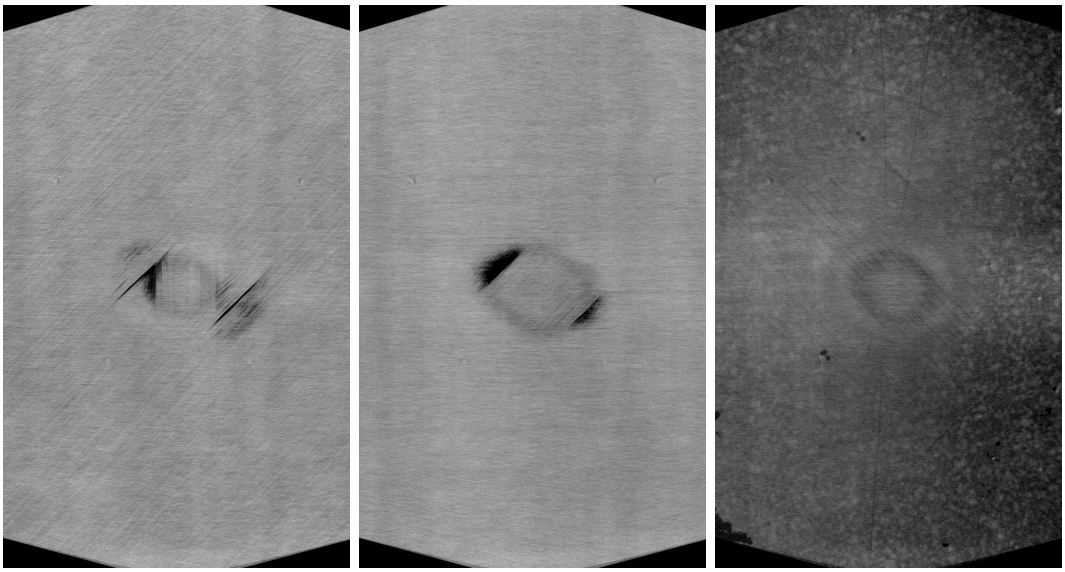

(d) Interface 17: -45/90 (e) Interface 18: 90/45 (f) Ply 20: 45

Figure B.10: MicroCT results for interfaces 15-19.

APPENDIX C

Material Characterization

C.1 Inter-laminar Properties for EST

The majority of the EST input properties are gathered from experimental data. The experimental testing needed to gather the input properties is summarized in the chapters below. The chapters are divided into different experimental procedures which then discuss the parameters acquired.

C.1.1 Crossply Tension

Testing of a $[90_2/0_2]_s$ specimen will allow for measuring the longitudinal modulus, E_{11}. The modulus should be measured roughly mid-way through the test and up to the failure point, this is done to ensure that the 90° layers have fully saturated and no longer carry any load. The longitudinal modulus would be twice the stiffness of the $[90_2/0_2]_s$ experiment at that point, this is due to the 90° layers not carrying any load and therefore the effective gage section area only being that of the 0°, or half of the total area of the $[90_2/0_2]_s$ coupon. Relevant ASTM standards: D3518 [5] and D3039 [115]. The longitudinal/fiber direction failure strain, X_{11}^T, can also be measured with

good accuracy from the $[90/0]_s$ tests. This would be the ultimate failure strain of the coupon. Good agreement has been shown between unidirectional tension and the crossply tension.

C.1.2 Unidirectional Tension

Tension of [0] coupons will allow for measuring the longitudinal/fiber failure strain, X_{11}^T, as well as the poissons ratio, v_{12}. Recommended layup: $[0]_8$. Relevant ASTM standards: D3518 [5] and D3039 [115].

C.1.3 $[\pm 45]_s$ Tension

Tension testing of $[\pm 45]_s$ coupons will result in acquiring the shear modulus, G_{12}, as well as the lamina shear failure strain, Z. Recommended layup: $[+45/-45]_{4s}$. The shear modulus should be measured early on in the experiment, prior to micro damage accumulating, it is recommended that either the loading rate is very low or the strain recordings are done at a reasonably high rate (10Hz or higher). Relevant ASTM standards: D3518 [5] and D3039 [115].

The test can also be used to esimate the longitudinal compressive strength, X_{11}^C, using Consideres construction. The fiber mis-alignment angle would need to be measured.

C.1.4 Transverse Tension and Compression

Tension and compression testing of [90] coupons will give the tension and compressive strain to failure in the transverse direction, Y_{22}^T and $Y22^C$, respectfully. Recommended layup is $[0]_{24}$ for tension and $[0]_{32}$ for compression. Relevant ASTM standards: D3518 [5] and D3039 [115] and D3410 [117].

C.1.5 Single Edge Notched Tension (SENT)

SENT testing of $[90/0]_s$ notched specimens is required for inverse finite element analysis to back out the longitudinal/fiber direction fracture toughness in tension, G^f_{IT}.

C.1.6 Interlaminar Fracture Testing

Intra-laminar fracture toughness for the matrix is assumed to be the same as inter-laminar properties gathered from ASTM D5528 [116] standard for Mode I Interlaminar fracture testing. and ASTM D7905 [118] standard for Mode II Interlaminar fracture testing. Therefore, $G^{Interlaminar}_{IC} = G^m_{IT}$. In a similar manner the mode II fracture toughness is, $G^{Interlaminar}_{II} = G^m_{II}$.

C.1.7 Fracture Toughness for the Compression Modes

Failure of a lamina under longitudinal compression occurs due to kink band formation or local buckling and the transverse compression of a lamina occurs due to shear band formation. Both these physcial mechanisms are not captured correctly in the EST-DCZM model, but their net effect is captured using crack band modeling. The fracture toughness associated with these modes are not physcial and hence cannot be determined accurately. In reality, both kink band formation and shear band formation leads to non-zero residual stress. Current version of EST cannot model this. Hence it is recommended to use high fracture toughness values for these modes to indirectly account for the residual strength that can arise.

C.1.8 Schapery Micro-damage Functions

The Schapery micro-damage functions are acquired through experimental procedures. Sicking and Schapery [106, 112] recommended the use of $[\pm 45^\circ]$ angle-ply laminates to acquire the shear micro-damage function, g_s. The $[\pm 45^\circ]$ angle-ply spec-

imens show the greatest sensitivity to G_{12}. For the transverse micro-damage function in tension, e_{st}, a unidirectional 15° off-axis specimen is recommended. This layup will result in the matrix (transverse direction) to be in tension with respect to the local lamina frame. For the transverse micro-damage function in compression, e_{sc}, a [±30°] angle-ply laminate is recommended. This layup results in the matrix (transverse direction) to be loaded in compression with respect to the local lamina frame. Below, the procedure to establish the micro-damage functions through an experimental procedure will be described.

The experimental data gathered from the three suggested test setups will be the same. The experiments will give the laminate level stress in the loading direction, σ_x, the laminate level strains, ϵ_x, ϵ_y and $\gamma_x y$, as well as the total energy dissipated due to micro-damage, S. From the [±45°] test the shear micro-damage function first needs to be obtained and then by applying that knowledge to the [±30°] and [+15°] experimental results the transverse micro-damage functions in tension and compression can be found.

C.1.9 Shear Micro-damage Function

The experimental results from the [±45°] test can be used to arrive at the shear stress vs. shear strain in the lamina frame, τ_{12} vs. γ_{12}.

$$\tau_{12} = \sigma_{xx}/2 \tag{C.1}$$

$$\gamma_{12} = \epsilon_{11} - \epsilon_{22} \tag{C.2}$$

The [±45°] specimens are shear dominant and therefore the total dissipated energy can be assumed to be related to degradation of the shear moduli. For each increment of the test the secant moduli, G_{12}, and the dissipated energy, S, can be calculated.

The pristine shear modulus, G_{120}, is found to be the value of G_{12} prior to non-linearity being observed (S0). Now the shear micro-damage function can be found by plotting $g_s = G_{12}/G_{120}$ vs. S and arriving at the relation between the secant moduli and micro-damage.

C.1.10 Transverse Micro-damage Functions

Tensile experiments of the $[\pm 30°]$ and $[+15°]$ specimens will provide the same experimental data as the previous test. First the lamina level strains can be backed out

$$\begin{bmatrix} \epsilon_{11} \\ \epsilon_{22} \\ \gamma_{12} \end{bmatrix} = \begin{bmatrix} c^2 & s^2 & cs \\ s^2 & c^2 & -cs \\ -2cs & -2cs & c^2 - s^2 \end{bmatrix} \begin{bmatrix} \epsilon_x \\ \epsilon_y \\ \gamma_{xy} \end{bmatrix} \tag{C.3}$$

Where $c = cos(\theta)$ and $s = sin(\theta)$. For the $[\pm 30°]$ laminate the assumption that $\gamma_{xy} = 0$ can be made. Now that the lamina level strain are known the lamina level shear stress vs. shear strain response can be found utilizing the shear micro-damage function found from the$[\pm 45°]$ test and the 2D plane stress constitutive law,

$$\begin{bmatrix} \sigma_{11} \\ \sigma_{22} \\ \tau_{12} \end{bmatrix} = \begin{bmatrix} Q_{11} & Q_{12} & 0 \\ Q_{12} & Q_{22} & 0 \\ 0 & 0 & Q_{66} \end{bmatrix} \begin{bmatrix} \epsilon_{11} \\ \epsilon_{22} \\ \gamma_{12} \end{bmatrix} \tag{C.4}$$

Where, after making the assumption that $\nu_{12}\nu_{21} \ll 1$, the constituents are

$$Q_{11} = E_{11} \tag{C.5}$$

$$Q_{22} = E_{22} \tag{C.6}$$

$$Q_{12} = \nu_{12} E_{22} \tag{C.7}$$

$$Q_{66} = G_{12} \tag{C.8}$$

Solving for τ_{12} results in,

$$\tau_{12} = G_{120} g_s(S) \gamma_{12} \tag{C.9}$$

With the lamina level shear response being known, the energy dissipated due to shear micro-damage, S_{12}, can be found and subtracted from the total energy, S, to give the energy dissipation that has yet to be accounted for. This leftover energy will be called the transverse micro-damage energy, S_{22}.

$$S_{22} = S - S_{12} \tag{C.10}$$

Solving Eq. C.4 for σ_{22} results in

$$\sigma_{22} = Q_{12} \epsilon_{11} + Q_{22} \epsilon_{22} \tag{C.11}$$

Now, to stay consistent with the theoretical derivation of Schapery Theory, $Q_{12} = \nu_{12} E_{22}$ is assumed to be constant and non-dependent of S. Therefore the equation for the transverse stress is,

$$\sigma_{22} = \nu_{12} E_{220} \epsilon_{11} + E_{22}(S) \epsilon_{22} \tag{C.12}$$

Where,

$$E_{22}(S) = E_{220} e_s(S) \tag{C.13}$$

With the equation for σ_{22} derived as well as ϵ_{11}, ϵ_{22} and S_{22} being known, a simple iterative method can be used to solve for $E_{22}(S)$ while satisfying the required dissipated energy that is missing, S_{22}. Note that $E_{22}(S)$ is a function of the total energy dissipated. The equation to be iterated at each experimental data point,

$$S_{22} = \int_0^{\epsilon_{22}} \sigma_{22}(x)dx - \sigma_{22}(\epsilon_{22})\epsilon_{22} \tag{C.14}$$

Substituting in for σ_{22} and adjusting the equation for a function to be minimized gives

$$S_{22} - \int_0^{\epsilon_{22}} \big(\nu_{12}E_{220}\epsilon_{11}x + E_{22}(S)x^2\sigma_{22}(x)\big)dx - \frac{1}{2}\big(\nu_{12}E_{220}\epsilon_{11}\epsilon_{22} + E_{22}(S)\epsilon_{22}^2\big) = 0 \tag{C.15}$$

Where ϵ_{11}, ϵ_{22} and S_{22} are unique values for each data point of the experiment. By giving an initial guess for $E_{22}(S) = E_{220}$, this initial guess value should be achieved from testing of unidirectional specimens subject to tension in the transverse direction. $E_{22}(S)$ can now be solved iteratively by minimizing the above equation. Once known the transverse micro-damage function can be found by plotting at $e_s = E_{22}/E_{220}$ vs. S_r , where S_r is the reduced damage variable for the entire energy dissipated.

Alternative approach for determining the transverse microdamage function is by using the +/-45 tension test data and using a micromechanics model. A schematic of the procedure is given in Figure C.1. In-situ matrix shear response is calculated using a concentric cylinder model (CCM) and plasticity theory is used for calculating the equivalent stress-strain response of the matrix. This material behavior is then sued in the matrix material of the RUC (Representative Unit Cell) model and the RUC is subjected to virtual transverse tension test to get the stress-strain response. Transverse micro-damage function can be directly measured using the transverse stress-strain response. More details on the procedure can be found in Ng et al. [77]. The dis-

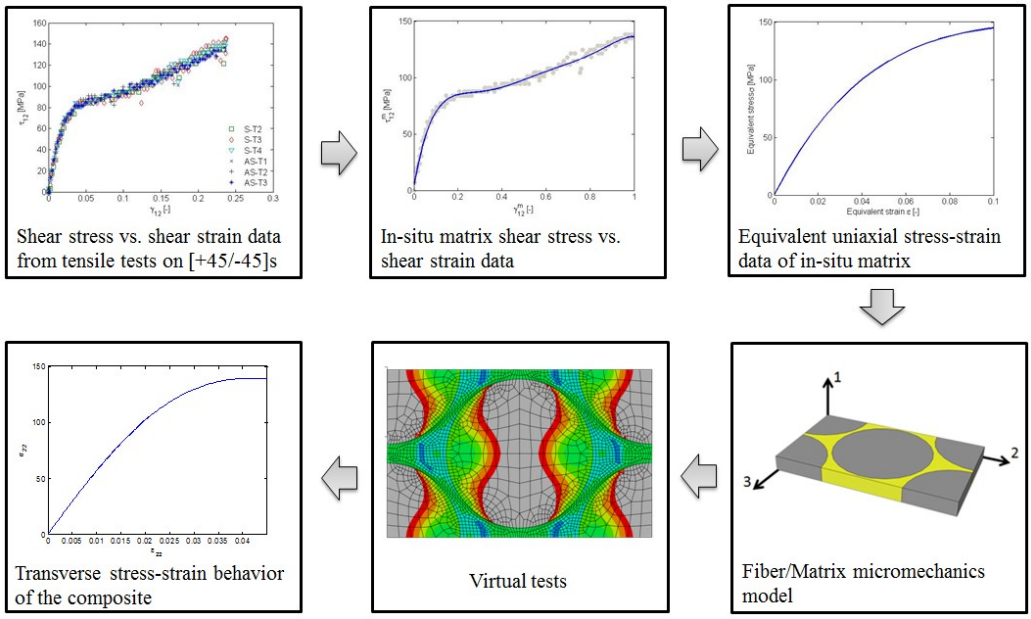

Figure C.1: Micromechanics based prcedure for acquiring transverse Schapery micro-damage functions via. inverse analysis.

advantage of this method is that compressive response cannot be distinguished from the tensile response.

C.2 Intra-laminar Properties for DCZM

Input parameters that need to be defined from experimental testing are the fracture toughness and cohesive strength for mode I, mode II and mode III. The implementation of the DCZM element considers only two different types of modes, peel as mode I and shear as mode II and III. Therefore it is required to get peel and shear fracture toughness and cohesive strengths.

Mode I fracture toughness is acquired by the industry accepted standard for Mode I Interlaminar Fracture, ASTM D5528 [116]. Mode II fracture toughness is acquired by the industry accepted standard for Mode II interlaminar fracture, ASTM D7905 [118]. Mode I cohesive strength can be found using peel-off testing or by numerically backing out it out by FE inverse analysis. Mode II cohesive strength can be found

using an interfacial shear test such as the single lap joint (SLJ) test method and numerically backing it out by FE inverse analysis.

APPENDIX D

Face-on Impact and CAI Model Details

The following appendix contains detailed results from the face-on impact and CAI model.

D.1 CAI Load-Displacement Curves

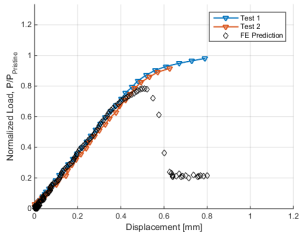

(a) 50% BVID

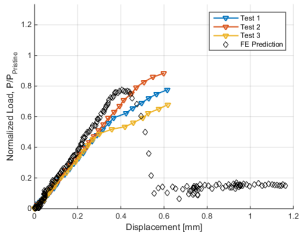

(b) 75% BVID

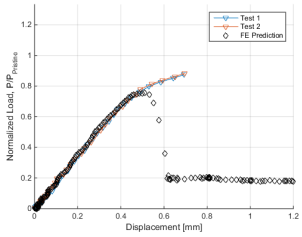

(c) 100% BVID

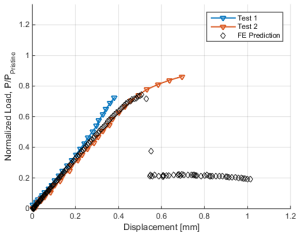

(d) 112.5% BVID

Figure D.1: BVID CAI results.

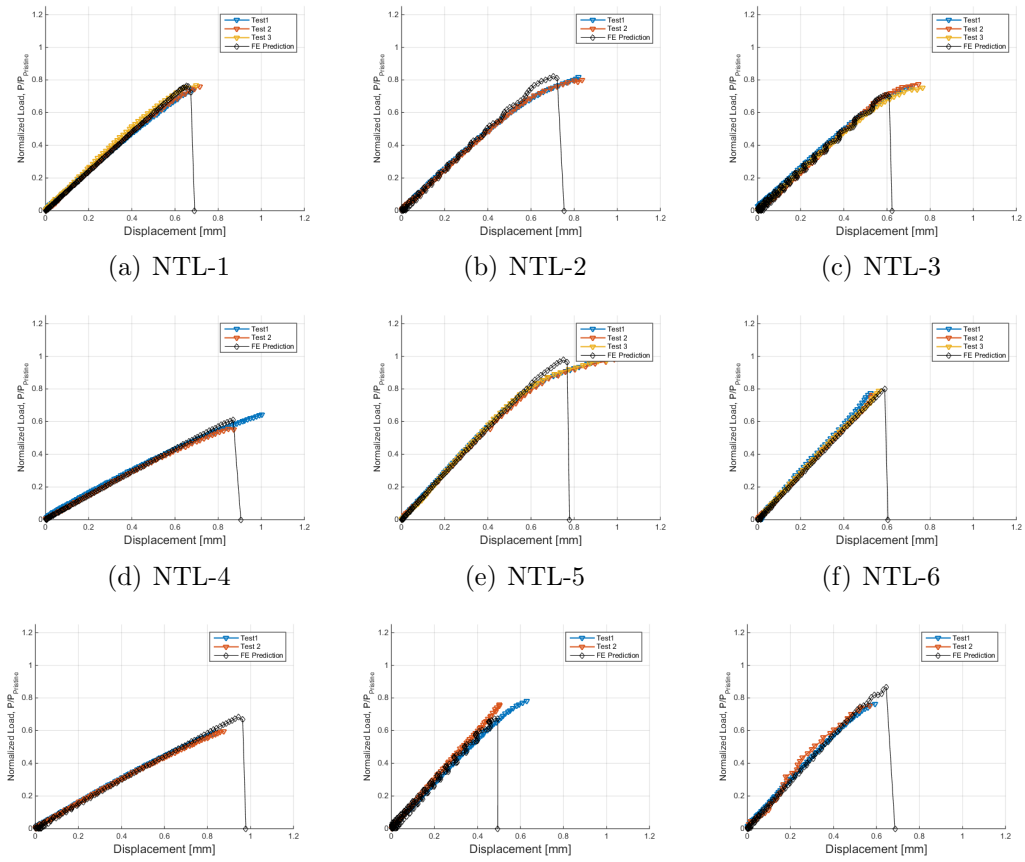

(a) NTL-1 (b) NTL-2 (c) NTL-3

(d) NTL-4 (e) NTL-5 (f) NTL-6

(g) NTL-7 (h) NTL-8 (i) NTL-9

Figure D.2: BVID CAI results.

BIBLIOGRAPHY

BIBLIOGRAPHY

[1] Abaqus. *Abaqus User's Manual*. Dassault Systemes Simulia Corp., 2014.

[2] S Abrate. Impact on laminated composite materials. *Appl Mech Rev*, 44(4):155–190, 1991.

[3] S Abrate. Impact on laminated composites: Recent advances. *Appl Mech Rev*, 47(11):517–554, 1994.

[4] P W Anderson. More is different. *Science*, 177(4047):393–396, 1972.

[5] ASTM ASTM. D3518: Standard test method for in-plane shear response of polymer matrix composite materials by tensile test of a±45 laminate. 2007. *American Society for Testing Materials: West Conshohocken, Pennsylvania*.

[6] O Attia, AJ Kinloch, and FL Matthews. The prediction of fatigue damage growth in impact-damaged composite skin/stringer structures. part i: theoretical modelling studies. *Composites science and technology*, 63(10):1463–1472, 2003.

[7] Shiladitya Basu, Anthony Waas, and Damodar Ambur. A macroscopic model for kink banding instabilities in fiber composites. *Journal of Mechanics of Materials and Structures*, 1(6):979–1000, 2006.

[8] Shiladitya Basu, Anthony M Waas, and Damodar R Ambur. Compressive failure of fiber composites under multi-axial loading. *Journal of the Mechanics and Physics of Solids*, 54(3):611–634, 2006.

[9] Z P Bažant and B H Oh. Crack band theory for fracture of concrete. *Materiaux et constructions*, 16(93):155–177, 1983.

[10] BRK Blackman, JP Dear, AJ Kinloch, H Macgillivray, Y Wang, JG Williams, and P Yayla. The failure of fibre composites and adhesively bonded fibre composites under high rates of test. *Journal of Materials Science*, 30(23):5885–5900, 1995.

[11] C Bouvet, B Castani, M Bizeul, and J J Barrau. Low velocity impact modelling in laminate composite panels with discrete interface elements. *International Journal of Solids and Structures*, 46(14):2809–2821, 2009.

[12] C Bouvet and S Rivallant. Damage tolerance of composite structures under low-velocity impact. *Dynamic Deformation, Damage and Fracture in Composite Materials and Structures*, page 7, 2016.

[13] C Bouvet, S Rivallant, and J J Barrau. Low velocity impact modeling in composite laminates capturing permanent indentation. *Composites Science and Technology*, 72(16):1977–1988, 2012.

[14] D. Broek. *Elementary Engineering Fracture Mechanics*, volume 3. Martinus Nijhoff Publishers, 1982.

[15] Hyung Yun Choi and Fu-Kuo Chang. A model for predicting damage in graphite/epoxy laminated composites resulting from low-velocity point impact. *Journal of composite materials*, 26(14):2134–2169, 1992.

[16] Hyung Yun Choi, Hsi-Yung T Wu, and Fu-Kuo Chang. A new approach toward understanding damage mechanisms and mechanics of laminated composites due to low-velocity impact: Part II-Analysis. *Journal of Composite Materials*, 25(8):1012–1038, 1991.

[17] G Clark and DS Saunders. Morphology of impact damage growth by fatigue in carbon fibre composite laminates. In *Materials Forum*, volume 15, pages 333–342. Pergamon Press, 1991.

[18] Paul Compston, P-YB Jar, PJ Burchill, and K Takahashi. The effect of matrix toughness and loading rate on the mode-ii interlaminar fracture toughness of glass-fibre/vinyl-ester composites. *Composites science and technology*, 61(2):321–333, 2001.

[19] GR Cowper. The shear coefficient in timoshenko's beam theory. ASME, 1966.

[20] Thi D Dang and Stephen R Hallett. A numerical study on impact and compression after impact behaviour of variable angle tow laminates. *Composite Structures*, 96:194–206, 2013.

[21] Isaac M Daniel, Igbal Shareef, and Abdu A Aliyu. Rate effects on delamination fracture toughness of a toughened graphite/epoxy. *Toughened Composites*, 1987.

[22] Paul Davidson and Anthony M Waas. Mechanics of kinking in fiber-reinforced composites under compressive loading. *Mathematics and Mechanics of Solids*, 21(3):667–684, 2016.

[23] G A O Davies and R Olsson. Impact on composite structures. *Aeronautical Journal*, 108(1089):541–563, 2004.

[24] Carlos G Davila, Pedro P Camanho, and Cheryl A Rose. Failure criteria for FRP laminates. *Journal of Composite materials*, 39(4):323–345, 2005.

[25] MFSF De Moura, JPM Gonçalves, AT Marques, and PMS Tavares De Castro. Modeling compression failure after low velocity impact on laminated composites using interface elements. *Journal of Composite Materials*, 31(15):1462–1479, 1997.

[26] M Colin de Verdiere, AA Skordos, M May, and AC Walton. Influence of loading rate on the delamination response of untufted and tufted carbon epoxy non crimp fabric composites: Mode i. *Engineering Fracture Mechanics*, 96:11–25, 2012.

[27] C Devivier, F Pierron, and MR Wisnom. Impact damage detection in composite plates using deflectometry and the virtual fields method. *Composites Part A: Applied Science and Manufacturing*, 48:201–218, 2013.

[28] Royan J DMello and Anthony M Waas. Inplane crush response and energy absorption of circular cell honeycomb filled with elastomer. *Composite Structures*, 106:491–501, 2013.

[29] A Faggiani and B G Falzon. Predicting low-velocity impact damage on a stiffened composite panel. *Composites Part A: Applied Science and Manufacturing*, 41(6):737–749, 2010.

[30] Eugene Fang, Xiaodong Cui, and Jim Lua. A phantom paired element based discrete crack network (dcn) toolkit for residual strength prediction of laminated composites. In *AIAA SciTech, 56th AIAA/ASCE/AHS/ASC Structures, Structural Dynamics, and Materials Conference*, pages 5–9, 2015.

[31] Eugene Fang, Michael Stuebner, and Jim Lua. X-fem co-simulation of delamination and matrix cracking in fiber metal laminated structures under fatigue loading. In *54th AIAA/ASME/ASCE/AHS/ASC Structures, Structural Dynamics, and Materials Conference*, page 1657, 2013.

[32] XJ Fang, ZQ Zhou, BN Cox, and QD Yang. High-fidelity simulations of multiple fracture processes in a laminated composite in tension. *Journal of the Mechanics and Physics of Solids*, 59(7):1355–1373, 2011.

[33] Scott R Finn, Ye-Fei He, and George S Springer. Delaminations in composite plates under transverse impact loads - experimental results. *Composite Structures*, 23(3):191–204, 1993.

[34] Scott R Finn and George S Springer. Delaminations in composite plates under transverse static or impact loads - a model. *Composite Structures*, 23(3):177–190, 1993.

[35] EV González, P Maimí, PP Camanho, CS Lopes, and N Blanco. Effects of ply clustering in laminated composite plates under low-velocity impact loading. *Composites Science and Technology*, 71(6):805–817, 2011.

[36] E Greenhalgh, SM Bishop, D Bray, D Hughes, S Lahiff, and B Millson. Characterisation of impact damage in skin-stringer composite structures. *Composite structures*, 36(3):187–207, 1996.

[37] E Greenhalgh, S Singh, D Hughes, and D Roberts. Impact damage resistance and tolerance of stringer stiffened composite structures. *Plastics, rubber and composites*, 28(5):228–251, 1999.

[38] Emile Greenhalgh and Matthew Hiley. The assessment of novel materials and processes for the impact tolerant design of stiffened composite aerospace structures. *Composites part A: applied science and manufacturing*, 34(2):151–161, 2003.

[39] Emile Greenhalgh, Charlotte Meeks, Andrew Clarke, and James Thatcher. The effect of defects on the performance of post-buckled cfrp stringer-stiffened panels. *Composites Part A: Applied Science and Manufacturing*, 34(7):623–633, 2003.

[40] Peter Gustafson and Anthony Waas. T650/afr-pe-4/fm680-1 mode i critical energy release rate at high temperatures: Experiments and numerical models. In *48th AIAA/ASME/ASCE/AHS/ASC Structures, Structural Dynamics, and Materials Conference*, page 2305, 2007.

[41] Peter Gustafson and Anthony Waas. Efficient and robust traction laws for the modeling of adhesively bonded joints. In *49th AIAA/ASME/ASCE/AHS/ASC Structures, Structural Dynamics, and Materials Conference, 16th AIAA/ASME/AHS Adaptive Structures Conference, 10th AIAA Non-Deterministic Approaches Conference, 9th AIAA Gossamer Spacecraft Forum, 4th AIAA Multidisciplinary Design Optimization Specialists Conference*, page 1847, 2008.

[42] Peter A Gustafson and Anthony M Waas. The influence of adhesive constitutive parameters in cohesive zone finite element models of adhesively bonded joints. *International Journal of Solids and Structures*, 46(10):2201–2215, 2009.

[43] SR Hallett. Three-point beam impact tests on T300/914 carbon-fibre composites. *Composites science and technology*, 60(1):115–124, 2000.

[44] SR Hallett and C Ruiz. Material characterization tests and modelling of carbon fibre T300/914 at impact rates of strain. *Le Journal de Physique IV*, 7(C3):C3–465, 1997.

[45] Zvi Hashin. Failure criteria for unidirectional fiber composites. *Journal of applied mechanics*, 47(2):329–334, 1980.

[46] Christian Heinrich and Anthony M. Waas. Investigation of progressive damage and rracture in laminated composites using the smeared crack approach. *Computers, Materials & Continua*, 35(2), 2013.

[47] N Hongkarnjanakul, C Bouvet, and S Rivallant. Validation of low velocity impact modelling on different stacking sequences of CFRP laminates and influence of fibre failure. *Composite Structures*, 106:549–559, 2013.

[48] JP Hou, N Petrinic, C Ruiz, and SR Hallett. Prediction of impact damage in composite plates. *Composites Science and Technology*, 60(2):273–281, 2000.

[49] Ning Hu, Y Zemba, T Okabe, Cheng Yan, Hisao Fukunaga, and AM Elmarakbi. A new cohesive model for simulating delamination propagation in composite laminates under transverse loads. *Mechanics of Materials*, 40(11):920–935, 2008.

[50] Thomas JR Hughes. *The finite element method: linear static and dynamic finite element analysis*. Courier Corporation, 2012.

[51] D Hull. A unified approach to progressive crushing of fibre-reinforced composite tubes. *Composites science and technology*, 40(4):377–421, 1991.

[52] D Hull and Y B Shi. Damage mechanism characterization in composite damage tolerance investigations. *Composite Structures*, 23(2):99–120, 1993.

[53] Michael W Hyer. *Stress analysis of fiber-reinforced composite materials*. DEStech Publications, Inc, 2009.

[54] Endel V Iarve, Mark R Gurvich, David H Mollenhauer, Cheryl A Rose, and Carlos G Dávila. Mesh-independent matrix cracking and delamination modeling in laminated composites. *International journal for numerical methods in engineering*, 88(8):749–773, 2011.

[55] George R Irwin. Fracture dynamics. *Fracturing of metals*, 152, 1948.

[56] Dawn C Jegley. Behavior of compression-loaded composite panels with stringer terminations and impact damage. *Journal of aircraft*, 35(6):942–948, 1998.

[57] Wooseok Ji, Sunil P Sringeri, Solver I Thorsson, Cyrus J Kosztowny, Anthony M Waas, Mostafa Rassaian, and Salvatore L Liguore. Face-on and edge-on impact response of composite laminates. In *56th AIAA/ASCE/AHS/ASC Structures, Structural Dynamics, and Materials Conference*, page 0956, 2015.

[58] CJ Jih and CT Sun. Prediction of delamination in composite laminates subjected to low velocity impact. *Journal of composite materials*, 27(7):684–701, 1993.

[59] Alastair F Johnson, Anthony K Pickett, and Patrick Rozycki. Computational methods for predicting impact damage in composite structures. *Composites Science and Technology*, 61(15):2183–2192, 2001.

[60] Ashith PK Joseph, Anthony M Waas, and Evan J Pineda. The EST model for predicting progressive damage and failure of open hole bending specimens. *in: 57th AIAA/ASCE/AHS/ASC Structures, Structural Dynamics, and Materials Conference*, pages **CP2016–0730**, 2016.

[61] SP Joshi and CT Sun. Impact induced fracture in a laminated composite. *Journal of Composite Materials*, 19(1):51–66, 1985.

[62] SP Joshi and CT Sun. Impact induced fracture in a laminated composite. *Journal of Composite Materials*, 19(1):51–66, 1985.

[63] J Kalthoff, J Beinert, S Winkler, and J Blauel. On the determination of the crack arrest toughness. In *Fracture 1977, Volume 3, ICF4, Waterloo (Canada) 1977*, 1977.

[64] J-H Kim, Fabrice Pierron, MR Wisnom, and Stéphane Avril. Local stiffness reduction in impacted composite plates from full-field measurements. *Composites Part A: Applied Science and Manufacturing*, 40(12):1961–1974, 2009.

[65] Takayuki Kusaka, Masaki Hojo, Y Mai, T Kurokawa, T Nojima, and S Ochiai. Rate dependence of mode i fracture behaviour in carbon-fibre/epoxy composite laminates. *Composite Science and Technology*, 58(3):591–602, 1998.

[66] Takayuki Kusaka, Masaki Hojo, Shojiro Ochiai, and Tomoaki Kurokawa. Rate-dependent mode ii interlaminar fracture behavior of carbon-fiber/epoxy composite laminates. *Materials science research international*, 5(2):98–103, 1999.

[67] J Lee and C Soutis. A study on the compressive strength of thick carbon fibre–epoxy laminates. *Composites science and technology*, 67(10):2015–2026, 2007.

[68] N Li and PH Chen. Experimental investigation on edge impact damage and compression-after-impact (cai) behavior of stiffened composite panels. *Composite Structures*, 138:134–150, 2016.

[69] CS Lopes, PP Camanho, Z Gürdal, P Maimí, and EV González. Low-velocity impact damage on dispersed stacking sequence laminates. Part II: Numerical simulations. *Composites Science and Technology*, 69(7):937–947, 2009.

[70] CS Lopes, S Sádaba, C González, J Llorca, and PP Camanho. Physically-sound simulation of low-velocity impact on fiber reinforced laminates. *International Journal of Impact Engineering*, 92:3–17, 2016.

[71] CS Lopes, O Seresta, Y Coquet, Z Gürdal, PP Camanho, and B Thuis. Low-velocity impact damage on dispersed stacking sequence laminates. Part I: Experiments. *Composites Science and Technology*, 69(7):926–936, 2009.

[72] A Malhotra, F J Guild, and M J Pavier. Edge impact to composite laminates: experiments and simulations. *Journal of materials science*, 43(20):6661–6667, 2008.

[73] S Mall, GE Law, and M Katouzian. Loading rate effect on interlaminar fracture toughness of a thermoplastic composite. *Journal of Composite Materials*, 21:569–579, 1987.

[74] Michael May. Measuring the rate-dependent mode i fracture toughness of composites - a review. *Composites Part A: Applied Science and Manufacturing*, 81:1–12, 2016.

[75] P Meyer and A M Waas. Fem predictions of damage in continous fiber ceramic matrix composites under transverse tension using the crack band method. *Acta Materialia*, 102:292–303, 2016.

[76] P. Naghipour, S. M. Arnold, E. J. Pineda, B. Stier, L. Hansen, B. A. Bednarcyk, and A. M. Waas. Multiscale static analysis of notched and unnotched laminates using the generalized method of cells. *Journal of Composite Materials*, page DOI: 10.1177/0021998316651708, 2016.

[77] W H Ng, A G Salvi, and A M Waas. Characterization of the in-situ non-linear shear response of laminated fiber-reinforced composites. *Composites Science and Technology*, 70(7):1126–1134, 2010.

[78] Nhung Nguyen and Anthony M Waas. A novel mixed-mode cohesive formulation for crack growth analysis. *Composite Structures*, 156:253–262, 2016.

[79] Nhung Nguyen and Anthony M Waas. Continuum decohesive finite element modeling of in-plane fracture: Mesh-objectivity and sensitivity studies. In *58th AIAA/ASCE/AHS/ASC Structures, Structural Dynamics, and Materials Conference*, 2017.

[80] T Kevin O'Brien, William M Johnston, and Gregory J Toland. Mode ii interlaminar fracture toughness and fatigue characterization of a graphite epoxy composite material. 2010.

[81] J Oliver, AE Huespe, and PJ Sanchez. A comparative study on finite elements for capturing strong discontinuities: E-fem vs x-fem. *Computer methods in applied mechanics and engineering*, 195(37):4732–4752, 2006.

[82] R Olsson. Analytical prediction of large mass impact damage in composite laminates. *Composites Part A: Applied Science Manufacturing*, 32(9):1207–1215, 2001.

[83] R Olsson. Analytical model for delamination growth during small mass impact on plates. *International Journal of Solids and Structures*, 47(21):2884–2892, 2010.

[84] R Olsson. Modelling of impact damage zones in composite laminates for strength after impact. *Aeronautical Journal*, 116(1186):1349–1365, 2012.

[85] Benjamin Ostré, Christophe Bouvet, Clément Minot, and Jacky Aboissière. Finite element analysis of cfrp laminates subjected to compression after edge impact. *Composite Structures*, 153:478–489, 2016.

[86] Ivan Pelivanov, Łukasz Ambroziński, Anton Khomenko, Ermias G Koricho, Gary L Cloud, Mahmoodul Haq, and Matthew ODonnell. High resolution imaging of impacted CFRP composites with a fiber-optic laser-ultrasound scanner. *Photoacoustics*, 4(2):55–64, 2016.

[87] Ivan Pelivanov, Łukasz Ambrozinski, and Matthew ODonnell. Heat damage evaluation in carbon fiber-reinforced composites with a khz a-scan rate fiber-optic pump-probe laser-ultrasound system. *Composites Part A: Applied Science and Manufacturing*, 84:417–427, 2016.

[88] E J Pineda and A M Waas. Numerical implementation of a multiple-isv thermodynamically-based work potential theory for modeling progressive damage and failure in fiber-reinforced laminates. *International Journal of Fracture*, 182(1):93–122, 2013.

[89] Evan J Pineda, Anthony M Waas, Brett A Bednarcyk, Craig S Collier, and Phillip W Yarrington. Progressive damage and failure modeling in notched laminated fiber reinforced composites. *International journal of fracture*, 158(2):125–143, 2009.

[90] Evan Jorge Pineda. *A novel multiscale physics-based progressive damage and failure modeling tool for advanced composite structures*. PhD thesis, NASA Glenn Research Center (University of Michigan), 2012.

[91] Silvestre T Pinho, Carlos G Dàvila, Pedro P Camanho, Lorenzo Iannucci, and Paul Robinson. Failure models and criteria for FRP under in-plane or three-dimensional stress states including shear non-linearity. *NASA/TM-2003-213530*.

[92] SV Potti and CT Sun. Prediction of impact induced penetration and delamination in thick composite laminates. *International Journal of Impact Engineering*, 19(1):31–48, 1997.

[93] P Prabhakar and A M Waas. A novel continuum-decohesive finite element for modeling in-plane fracture in fiber reinforced composites. *Composites Science and Technology*, 83:1–10, 2013.

[94] Pavana Prabhakar and Anthony M Waas. Interaction between kinking and splitting in the compressive failure of unidirectional fiber reinforced laminated composites. *Composite Structures*, 98:85–92, 2013.

[95] A Puck and H Schürmann. Failure analysis of FRP laminates by means of physically based phenomenological models. *Composites Science and Technology*, 58(7):1045–1067, 1998.

[96] Alfred Puck and Helmut Schürmann. Failure analysis of FRP laminates by means of physically based phenomenological models. *Composites Science and Technology*, 62(12):1633–1662, 2002.

[97] H Razi and AS Kobayashi. Delamination in cross-ply laminated composite subjected to low-velocity impact. *AIAA journal*, 31(8):1498–1502, 1993.

[98] Junuthula Narasimha Reddy. *An introduction to the finite element method*, volume 2. McGraw-Hill New York, 1993.

[99] A T Rhead, D Marchant, and R Butler. Compressive strength of composite laminates following free edge impact. *Composites Part A: Applied Science and Manufacturing*, 41(9):1056–1065, 2010.

[100] James R Rice. Inelastic constitutive relations for solids: an internal-variable theory and its application to metal plasticity. *Journal of the Mechanics and Physics of Solids*, 19(6):433–455, 1971.

[101] S Rivallant, C Bouvet, and N Hongkarnjanakul. Failure analysis of CFRP laminates subjected to compression after impact: Fe simulation using discrete interface elements. *Composites Part A: Applied Science and Manufacturing*, 55:83–93, 2013.

[102] JG Rots, P Nauta, GMA Kuster, and J Blaauwendraad. Smeared crack approach and fracture localization in concrete. 1985.

[103] Siva Shankar Rudraraju, Amit Salvi, Krishna Garikipati, and Anthony M Waas. In-plane fracture of laminated fiber reinforced composites with varying fracture resistance: Experimental observations and numerical crack propagation simulations. *International Journal of Solids and Structures*, 47(7):901–911, 2010.

[104] Bhavani V Sankar and Young S Kwon. Indentation-flexure and low-velocity impact damage in graphite epoxy laminates. *Journal of Composites, Technology and Research*, 15(2):101–111, 1993.

[105] R A Schapery. A theory of mechanical behavior of elastic media with growing damage and other changes in structure. *Journal of Mechanics and Physics of Solids*, 38(2):215–253, 1990.

[106] R A Schapery and D L Sicking. On nonlinear constitutive equations for elastic and viscoelastic composites with growing damage. *Mechnical behaviour of materials*, 47:45–76, 1995.

[107] Carl R Schultheisz and Anthony M Waas. Compressive failure of composites, Part I: Testing and micromechanical theories. *Progress in Aerospace Sciences*, 32(1):1–42, 1996.

[108] TA Sebaey, EV González, CS Lopes, N Blanco, P Maimí, and J Costa. Damage resistance and damage tolerance of dispersed CFRP laminates: Effect of the mismatch angle between plies. *Composite Structures*, 101:255–264, 2013.

[109] Jay Shi, Jim Lua, Haim Waisman, Phillip Liu, Ted Belytschko, N Sukumar, and Yu Liang. X-FEM toolkit for automated crack onset and growth prediction. In *49th AIAA/ASME/ASCE/AHS/ASC Structures, Structural Dynamics, and Materials Conference*, page 1763, 2008.

[110] Jianxu Shi, David Chopp, Jim Lua, N Sukumar, and Ted Belytschko. Abaqus implementation of extended finite element method using a level set representation for three-dimensional fatigue crack growth and life predictions. *Engineering Fracture Mechanics*, 77(14):2840–2863, 2010.

[111] Y Shi, C Pinna, and C Soutis. Low-velocity impact of composite laminates: damage evolution. *Dynamic Deformation, Damage and Fracture in Composite Materials and Structures*, page 117, 2016.

[112] D L Sicking. Mechanical characterization of nonlinear laminated composites with transverse crack growth, Ph.D. thesis. *Texas A&M University, College Station, TX*, 163:476–486, 1992.

[113] A J Smiley and R B Pipes. Rate effects on mode i interlaminar fracture toughness in composite materials. *Journal of Composite Materials*, 21(7):670–687, 1987.

[114] AJ Smiley and RB Pipes. Rate sensitivity of mode ii interlaminar fracture toughness in graphite/epoxy and graphite/peek composite materials. *Composites science and technology*, 29(1):1–15, 1987.

[115] ASTM Standard. D3039/d3039m-00. *Standard test method for tensile properties of polymer matrix composite materials*, 2000.

[116] ASTM Standard. D5528-01. *Standard Test Method for Mode I Interlaminar Fracture Toughness of Unidirectional Fiber-Reinforced Polymer Matrix Composites, ASTM International, West Conshohocken, PA*, 2007.

[117] ASTM Standard. D3410. standard test method for compressive properties of polymer matrix composite materials with unsupported gage section by shear loading, 2008.

[118] ASTM Standard. D7905/d7905m–14. *Standard Test Method for Determination of the Mode II Interlaminar Fracture Toughness of Unidirectional Fiber-Reinforced Polymer Matrix Composites*, 2014.

[119] C Sun, M D Thouless, A M Waas, J A Schroeder, and P D Zavattieri. Ductile-brittle transitions in the fracture of plastically-deforming, adhesively-bonded structures. part i: Experimental studies. *International Journal of Solids and Structures*, 45(10):3059–3073, 2008.

[120] C Sun, M D Thouless, A M Waas, J A Schroeder, and P D Zavattieri. Rate effects for mixed-mode fracture of plastically-deforming, adhesively bonded structures. *International Journal of Adhesion and Adhesives*, 29(4):434–443, 2009.

[121] C Sun, MD Thouless, AM Waas, JA Schroeder, and PD Zavattieri. Rate effects in mode-ii fracture of plastically deforming, adhesively bonded structures. *International journal of fracture*, 156(2):111–128, 2009.

[122] S Takeda, S Minakuchi, Y Okabe, and N Takeda. Delamination monitoring of laminated composites subjected to low-velocity impact using small-diameter fbg sensors. *Composites Part A: Applied Science and Manufacturing*, 36(7):903–908, 2005.

[123] S I Thorsson. Experimental and numerical investigation of fiber reinforced laminated composites subject to low-velocity impact. Ph.D. thesis. *University of Michigan, Ann Arbor, MI*, 2017.

[124] S I Thorsson, J Xie, J Marek, and A M Waas. Matrix crack interacting with a delamination in an impacted sandwich composite beam. *Engineering Fracture Mechanics*, 163:476–486, 2016.

[125] Solver I Thorsson. Annual and semi-annual Boeing progress reports. University of Michigan, June 2016 and December 2016.

[126] Solver I Thorsson, Akinori Yoshimura, Anthony M Waas, and Mostafa Rassaian. Prediction of low-velocity face-on impact response of composite laminates using high-fidelity finite element modeling techniques. In *57th AIAA/ASCE/AHS/ASC Structures, Structural Dynamics, and Materials Conference*, page 2184, 2016.

[127] Jie Wang, Anthony M Waas, and Hai Wang. Experimental and numerical study on the low-velocity impact behavior of foam-core sandwich panels. *Composite Structures*, 96:298–311, 2013.

[128] J Wiegand, A Hornig, R Gerlach, C Neale, N Petrinic, and W Hufenbach. An experimental method for dynamic delamination analysis of composite materials by impact bending. *Mechanics of Advanced Materials and Structures*, 22(5):413–421, 2015.

[129] JFM Wiggenraad, X Zhang, and GAO Davies. Impact damage prediction and failure analysis of heavily loaded, blade-stiffened composite wing panels. *Composite structures*, 45(2):81–103, 1999.

[130] Jerry G Williams, Melvin S Anderson, Marvin D Rhodes, James H Starnes Jr, and W Jefferson Stroud. Recent developments in the design, testing and impact-damage tolerance of stiffened composite panels. In *Fibrous Composites in Structural Design*, pages 259–291. Springer, 1980.

[131] D Xie and A M Waas. Discrete cohesive zone model for mixed-mode fracture using finite element analysis. *Engineering Fracture Mechanics*, 73(13):1783–1796, 2006.

[132] Jiawen Xie and Anthony M Waas. Predictions of delamination growth for quasi-static loading of composite laminates. *Journal of Applied Mechanics*, 82(8):081004, 2015.

[133] Shuangyan Xu and David A Dillard. Determining the impact resistance of electrically conductive adhesives using a falling wedge test. *IEEE Transactions on Components and Packaging Technologies*, 26(3):554–562, 2003.

[134] Shigeki Yashiro, Keiji Ogi, Tsukasa Nakamura, and Akinori Yoshimura. Characterization of high-velocity impact damage in CFRP laminates: Part I–Experiment. *Composites Part A: Applied Science and Manufacturing*, 48:93–100, 2013.

[135] Shigeki Yashiro, Keiji Ogi, Akinori Yoshimura, and Yoshihisa Sakaida. Characterization of high-velocity impact damage in CFRP laminates: Part II–Prediction by smoothed particle hydrodynamics. *Composites Part A: Applied Science and Manufacturing*, 56:308–318, 2014.

[136] D Zhang, A M Waas, and C F Yen. Progressive damage and failure response of hybrid 3D textile composites subjected to flexural loading, Part I:Experimental studies. *International Journal of Solids and Structures*, 75:309–320, 2015.

[137] D Zhang, A M Waas, and C F Yen. Progressive damage and failure response of hybrid 3D textile composites subjected to flexural loading, Part II:Mechanics based multiscale computational modeling of progressive damage and failure. *International Journal of Solids and Structures*, 75:321–335, 2015.

[138] Dianyun Zhang, Anthony M Waas, and Chian-Fong Yen. Progressive failure analysis on textile composites. In *55th AIAA/ASMe/ASCE/AHS/SC Structures, Structural Dynamics, and Materials Conference*, 2014.

[139] X Zhang, F Bianchi, and H Liu. Predicting low-velocity impact damage in composites by a quasi-static load model with cohesive interface elements. *Aeronautical Journal*, 116(1186):1367–1381, 2012.

[140] X Zhang, F Bianchi, and H Liu. Predicting low-velocity impact damage in composites by a quasi-static load model with cohesive interface elements. *Aeronautical Journal*, 116(1186):1367–1381, 2012.